THE VERSATILE ROLE OF NICOTINAMIDE ADENINE DINUCLEOTIDE IN IMMUNITY

EDITED BY: Björn Rissiek, Andreas H. Guse, Sahil Adriouch and
Santina Bruzzone

PUBLISHED IN: Frontiers in Immunology

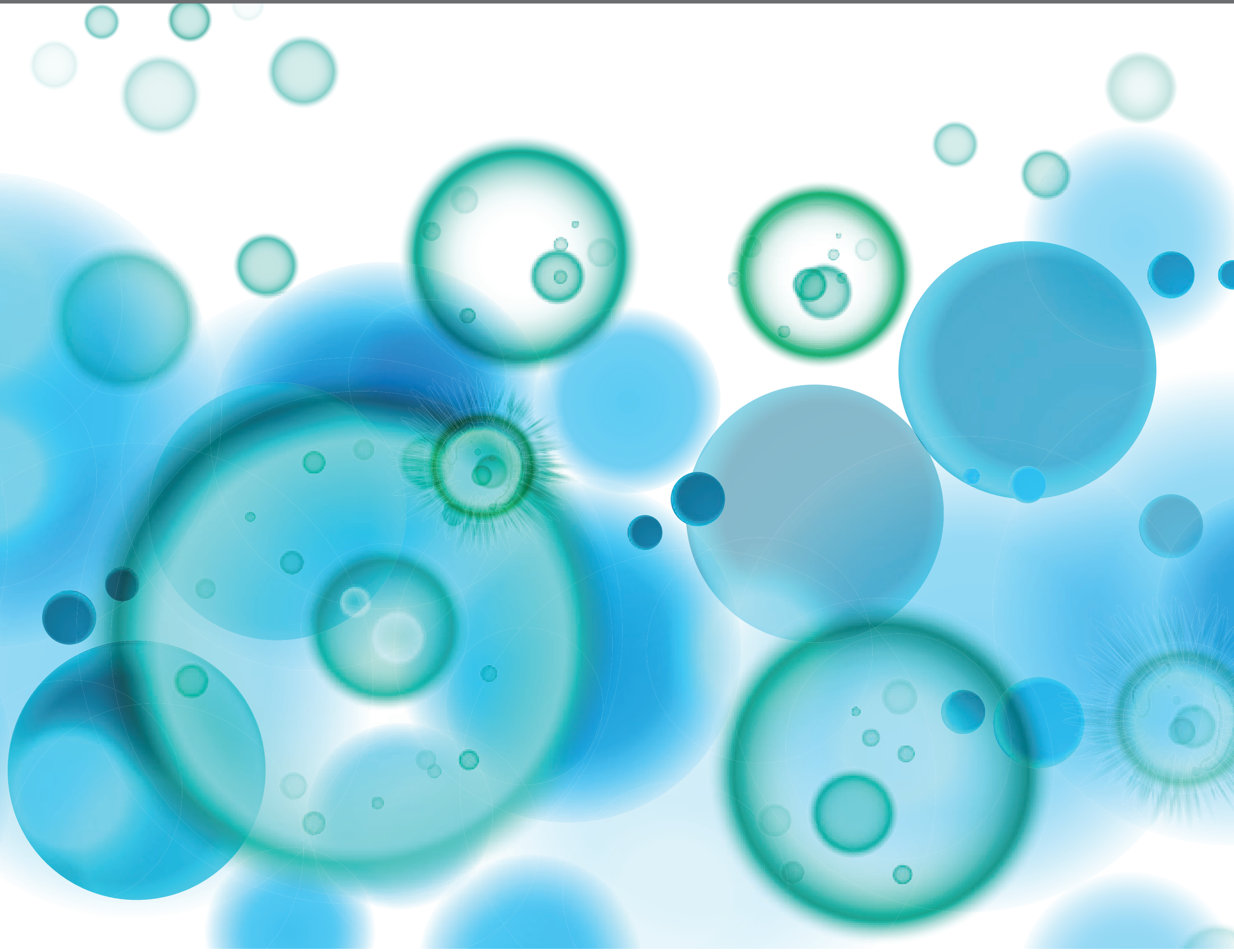

frontiers Research Topics

ISSN 1664-8714
ISBN 978-2-88974-085-7
DOI 10.3389/978-2-88974-085-7

About Frontiers

Frontiers is more than just an open-access publisher of scholarly articles: it is a pioneering approach to the world of academia, radically improving the way scholarly research is managed. The grand vision of Frontiers is a world where all people have an equal opportunity to seek, share and generate knowledge. Frontiers provides immediate and permanent online open access to all its publications, but this alone is not enough to realize our grand goals.

Frontiers Journal Series

The Frontiers Journal Series is a multi-tier and interdisciplinary set of open-access, online journals, promising a paradigm shift from the current review, selection and dissemination processes in academic publishing. All Frontiers journals are driven by researchers for researchers; therefore, they constitute a service to the scholarly community. At the same time, the Frontiers Journal Series operates on a revolutionary invention, the tiered publishing system, initially addressing specific communities of scholars, and gradually climbing up to broader public understanding, thus serving the interests of the lay society, too.

Dedication to Quality

Each Frontiers article is a landmark of the highest quality, thanks to genuinely collaborative interactions between authors and review editors, who include some of the world's best academicians. Research must be certified by peers before entering a stream of knowledge that may eventually reach the public - and shape society; therefore, Frontiers only applies the most rigorous and unbiased reviews.
Frontiers revolutionizes research publishing by freely delivering the most outstanding research, evaluated with no bias from both the academic and social point of view. By applying the most advanced information technologies, Frontiers is catapulting scholarly publishing into a new generation.

What are Frontiers Research Topics?

Frontiers Research Topics are very popular trademarks of the Frontiers Journals Series: they are collections of at least ten articles, all centered on a particular subject. With their unique mix of varied contributions from Original Research to Review Articles, Frontiers Research Topics unify the most influential researchers, the latest key findings and historical advances in a hot research area! Find out more on how to host your own Frontiers Research Topic or contribute to one as an author by contacting the Frontiers Editorial Office: frontiersin.org/about/contact

THE VERSATILE ROLE OF NICOTINAMIDE ADENINE DINUCLEOTIDE IN IMMUNITY

Topic Editors:
Björn Rissiek, University Medical Center Hamburg-Eppendorf, Germany
Andreas H. Guse, University Medical Center Hamburg-Eppendorf, Germany
Sahil Adriouch, Université de Rouen, France
Santina Bruzzone, University of Genoa, Italy

Citation: Rissiek, B., Guse, A. H., Adriouch, S., Bruzzone, S., eds. (2022). The Versatile Role of Nicotinamide Adenine Dinucleotide In Immunity. Lausanne: Frontiers Media SA. doi: 10.3389/978-2-88974-085-7

Table of Contents

frontiers in Immunology

EDITORIAL
published: 29 November 2021
doi: 10.3389/fimmu.2021.810280

Editorial: The Versatile Role of Nicotinamide Adenine Dinucleotide in Immunity

Björn Rissiek[1], Andreas H. Guse[2], Sahil Adriouch[3] and Santina Bruzzone[4]*

[1] Department of Neurology, University Medical Centre Hamburg-Eppendorf, Hamburg, Germany, [2] The Calcium Signaling Group, Department of Biochemistry and Molecular Cell Biology, University Medical Centre Hamburg-Eppendorf, Hamburg, Germany, [3] Normandie University, UNIROUEN, INSERM U1234, Pathophysiology, Autoimmunity, Neuromuscular Diseases and Regenerative THERapies (PANTHER), Rouen, France, [4] Department of Experimental Medicine, University of Genova, Genova, Italy

Keywords: NAD, CD38, ARTC2, ADP-ribosyl transferase, NAADP, AAV (Adeno-associated virus), nanobodies, immunity

Editorial on the Research Topic

The Versatile Role of Nicotinamide Adenine Dinucleotide in Immunity

OPEN ACCESS

Edited and reviewed by:
Silvano Sozzani,
Sapienza University of Rome, Italy

****Correspondence:***
Björn Rissiek
b.rissiek@uke.de

Specialty section:
This article was submitted to
Cytokines and Soluble
Mediators in Immunity,
a section of the journal
Frontiers in Immunology

Received: *06 November 2021*
Accepted: *15 November 2021*
Published: *29 November 2021*

Citation:
Rissiek B, Guse AH, Adriouch S and Bruzzone S (2021) Editorial: The Versatile Role of Nicotinamide Adenine Dinucleotide in Immunity.
Front. Immunol. 12:810280.
doi: 10.3389/fimmu.2021.810280

Nicotinamide adenine dinucleotide (NAD) is a highly abundant intracellular molecule, well known for its role as energy currency. However, intracellularly, NAD and its metabolic products ADP-ribose (ADPR), 2'-deoxy-ADPR (from 2'deoxy-NAD), cyclic ADPR (cADPR) and nicotinic acid adenine dinucleotide phosphate (NAADP) are also important second messengers essential for leukocyte Ca^{2+} signaling (1). Metabolism of these signaling molecules, as well as their exact molecular targets, are still unknown in many aspects, despite their importance in the regulation of innate and adaptive immunity.

Outside of cells, only a few cell surface receptors were identified, i.e. P2Y1 and P2Y11, that can sense extracellular NAD. However, the signaling functions of NAD is broadened by various nucleotide-degrading ecto-enzymes that can generate a variety of other nucleotide metabolites: ecto-CD38 metabolizes NAD into ADPR and cADPR, ecto-nucleotide pyrophosphatases (ENPPs) such as ENPP1 generate adenosine monophosphate (AMP) directly from NAD or from ADPR, thereby providing substrate for CD73-catalyzed adenosine generation and ligands for P1 receptors. Ecto-ADP-ribosyltransferases (ARTCs) utilize extracellular NAD to covalently attach ADPR groups to arginine residues on different cell surface proteins, including P2X7, resulting in a post-translational modification that can significantly affect the function of the modified target (2). In summary, NAD and its metabolites inside and outside of cells can have a remarkable impact on many different regulatory pathways of immunity.

This Research topic comprises 9 articles containing six original research articles, two reviews and one perspective article, all focusing on the role and function of extracellular NAD and intracellular NAD-derived metabolites as modulators of immunity. Three original articles investigated the cell surface ADP-ribosyltransferase ARTC2.2 which utilizes NAD to ADP-ribosylate mainly arginine residues on various cell surface target proteins. Leutert et al. identified several new ARTC2.2. targets on murine T cells. After isolating proteins from T cells incubated with NAD and subsequent mass spectrometry analyses, they identified 93 ADP-ribosylated peptides corresponding to 67 distinct protein. The ecto-5′-nucleotidase CD73 was among the newly identified ARTC2.2 targets and Leutert et al. could demonstrate that ADP-ribosylation of CD73 diminishes its capability to convert adenosine monophosphate into adenosine. Of note, ARTC2.2 also exists in a soluble form, as it can be proteolytically cleaved from the cell surface (3). Based on that Menzel et al. investigated whether cytokines are potential targets for ADP-ribosylation by soluble ARTC2.2. They could demonstrate that several cytokines, such as interferon gamma (IFNγ), interleukin 17A (IL-17A), IL-2 and IL-6 can be ADP-ribosylated by soluble ARTC2.2. For IFNγ Menzel et al. identified the ADP-ribosylation site and revealed that the attachment of the ADP-ribose group diminished IFNγ-induced STAT1 phosphorylation in macrophages. Finally, Gondé et al. presented a methodological approach relying on adeno-associated viral vectors (AAVs) coding for nanobody-based biologics targeting ARTC2.2 or P2X7, a prominent target of ARTC2.2. Following intramuscular injection of AAV coding for ARTC2.2/P2X7 nanobodies, functional modulation of their respective target could be demonstrated *in vivo*. This approach was additionally used to express nanobody-based heavy-chain antibodies, eliciting long-term depletion of T cells expressing high levels of ARTC2.2 or P2X7. This approach extends the available tool box to study ARTC2.2 or P2X7 functions *in vivo* and offers the possibility to modulate the function of ARTC2.2 and/or P2X7, or to deplete cells expressing these targets.

CD38 is another ecto-enzyme utilizing NAD as substrate. It can serve as NAD glycohydrolase or as cyclic ADP-ribose synthase, generating ADP-ribose or cyclic ADP-ribose from NAD, respectively. With their review article, Morandi et al. provide an update on the role of CD38 in the anti-tumor immune response. They highlight the importance of pathways such as the CD38/CD203a-concerted generation of immunosuppressive adenosine from ADP-ribose, the impact of extracellular NAD level on the T cell mediated anti-tumor response and discuss the use of new pharmacological inhibitors of CD38. Along this line, Baum et al. describe in their original article the generation of several new CD38-targeting heavy-chain antibodies. Some of these biologics inhibited CD38 cyclase activity, measured by the inhibition of the conversion of nicotinamide guanine dinucleotide (NGD, an NAD analog) to cyclic guanosine diphosphate ribose (cGDPR). Further, some clones exhibited potent complement-dependent cytotoxicity against CD38-expressing tumor cell lines. Additionally to its role in the anti-tumor immune response, or as target in tumor immunotherapy, CD38 has been attributed both positive and negative modulatory role in autoimmunity, depending on the disease setting (4). In their original article, Martínez-Blanco et al. demonstrate that CD38-deficiency ameliorates disease symptoms in a graft-*versus*-host mouse model for systemic lupus erythematosus (SLE). In their model, *Cd38*$^{-/-}$ mice had lower frequencies of follicular helper T cells, germinal center B cells, plasma cells and T-bet^{+}CD11c^{hi} B cells, and lower levels of anti-ssDNA autoantibodies when compared to WT B6 mice. With this knowledge, new therapeutic strategies based on e.g. CD38-blocking antibodies or pharmacological approaches targeting CD38 enzymatic activity may arise as promising potential option to treat SLE. Furthermore, CD38 is part of a network of intracellular and extracellular enzymes that regulate the synthesis or degradation of NAD. This network is completed by NAD-engaged receptors and NAD-derived metabolites and referred to as NADome. In their review article Audrito et al. highlight the role of the extracellular part of the NADome in immunomodulation and its possible implications for therapeutic approaches.

Inside the cells, NAD is the basis for the production of intracellular second messengers. NAADP, a potent trigger of Ca^{2+} release from intracellular stores (5), can be generated intracellularly in acidic lysosomes in a base-exchange reaction from nicotinamide adenine dinucleotide phosphate (NADP) and nicotinic acid. With their perspective article, Walseth and Guse provide a view back to the discovery of NAADP and forth to the identification of new NAADP receptors, such as HN1L/JPT2. Upon NAADP-induced Ca^{2+} release, Ca^{2+}-microdomain formation occurs at the junctions between the plasma membrane (PM) and the endoplasmic reticulum (ER) in less than a second. In their original article, Gil et al. provide a computational model to describe the evolution of cytosolic and ER Ca^{2+} concentrations in a three-dimensional ER-PM junction.

In summary, the articles published within this Research Topic greatly contribute to further extending our knowledge on NAD and its metabolites as regulators of immunity, both inside and outside of cells.

AUTHOR CONTRIBUTIONS

All authors listed have contribution to this editorial and approved it for publication.

FUNDING

This work was funded by the Deutsche Forschungsgemeinschaft (DFG) (project number 335447717; SFB1328, project A01 to AG) and by a grant from the Agence Nationale de la Recherche (ANR) to SA (ANR-18-CE92-0046).

ACKNOWLEDGMENTS

We thank all contributing authors of this Research Topic and we would like also to acknowledge the work of reviewers for their constructive comments that improved the quality of the articles.

REFERENCES

1. Guse AH. Calcium Mobilizing Second Messengers Derived From NAD. *Biochim Biophys Acta* (2015) 1854:1132–7. doi: 10.1016/j.bbapap.2014.12.015
2. Di Girolamo M, Fabrizio G. Overview of the Mammalian ADP-Ribosyl-Transferases Clostridia Toxin-Like (ARTCs) Family. *Biochem Pharmacol* (2019) 167:86–96. doi: 10.1016/j.bcp.2019.07.004
3. Menzel S, Rissiek B, Bannas P, Jakoby T, Miksiewicz M, Schwarz N, et al. Nucleotide-Induced Membrane-Proximal Proteolysis Controls the Substrate Specificity of T Cell Ecto-ADP-Ribosyltransferase Artc2.2. *J Immunol* (2015) 195:2057–66. doi: 10.4049/jimmunol.1401677
4. Piedra-Quintero ZL, Wilson Z, Nava P, Guerau-de-Arellano M. CD38: An Immunomodulatory Molecule in Inflammation and Autoimmunity. *Front Immun* (2020) 11:597959. doi: 10.3389/fimmu.2020.597959

5. Lee HC, Aarhus R. A Derivative of NADP Mobilizes Calcium Stores Insensitive to Inositol Trisphosphate and Cyclic ADP-Ribose. *J Biol Chem* (1995) 270:2152–7. doi: 10.1074/jbc.270.5.2152

Conflict of Interest: The authors declare that the research was conducted in the absence of any commercial or financial relationships that could be construed as a potential conflict of interest.

frontiers in Immunology

ORIGINAL RESEARCH
published: 08 March 2021
doi: 10.3389/fimmu.2021.642545

ADP-Ribosylation Regulates the Signaling Function of IFN-γ

Stephan Menzel[1]*, Tomas Koudelka[2], Björn Rissiek[3], Friedrich Haag[1], Catherine Meyer-Schwesinger[4], Andreas Tholey[2] and Friedrich Koch-Nolte[1]

[1] Institute of Immunology, University Medical Center Hamburg-Eppendorf, Hamburg, Germany, [2] Institute of Experimental Medicine, AG Systematic Proteome Research and Bioanalytics, Christian-Albrechts-Universität, Kiel, Germany, [3] Department of Neurology, University Medical Center Hamburg-Eppendorf, Hamburg, Germany, [4] Institute of Cellular and Integrative Physiology, University Medical Center Hamburg-Eppendorf, Hamburg, Germany

Murine T cells express the GPI-anchored ADP-ribosyltransferase 2.2 (ARTC2.2) on the cell surface. In response to T cell activation or extracellular NAD$^+$ or ATP-mediated gating of the P2X7 ion channel ARTC2.2 is shed from the cell surface as a soluble enzyme. Shedding alters the target specificity of ARTC2.2 from cell surface proteins to secreted proteins. Here we demonstrate that shed ARTC2.2 potently ADP-ribosylates IFN-γ in addition to other cytokines. Using mass spectrometry, we identify arginine 128 as the target site of ADP-ribosylation. This residue has been implicated to play a key role in binding of IFN-γ to the interferon receptor 1 (IFNR1). Indeed, binding of IFN-γ to IFNR1 blocks ADP-ribosylation of IFN-γ. Moreover, ADP-ribosylation of IFN-γ inhibits the capacity of IFN-γ to induce STAT1 phosphorylation in macrophages and upregulation of the proteasomal subunit ß5i and the proteasomal activator PA28-α in podocytes. Our results show that ADP-ribosylation inhibits the signaling functions of IFN-γ and point to a new regulatory mechanism for controlling signaling by IFN-γ.

Keywords: purinergic signaling, ADP-ribosylation, T cells, interferon-gamma, NAD$^+$

Edited by:
Laura Maggi,
Università degli Studi di Firenze, Italy

Reviewed by:
Enrico Balducci,
University of Camerino, Italy
Stephen Fuller,
The University of Sydney, Australia

***Correspondence:**
Stephan Menzel
s.menzel@uke.de

Specialty section:
This article was submitted to Cytokines and Soluble Mediators in Immunity,
a section of the journal Frontiers in Immunology

Received: *16 December 2020*
Accepted: *10 February 2021*
Published: *08 March 2021*

Citation:
Menzel S, Koudelka T, Rissiek B, Haag F, Meyer-Schwesinger C, Tholey A and Koch-Nolte F (2021) ADP-Ribosylation Regulates the Signaling Function of IFN-γ. Front. Immunol. 12:642545. doi: 10.3389/fimmu.2021.642545

HIGHLIGHTS

- Shed ARTC2.2 ADP-ribosylates several cytokines with a preference for IFN-γ.
- ADP-ribosylation of IFN-γ at Arg128 inhibits its function.
- Our study uncovers a novel pathway to regulate IFN-γ signaling by ADP-ribosylation.

INTRODUCTION

ARTC2.2 is a toxin-related, GPI-anchored ecto-ADP-ribosyltransferase expressed on the surface of murine T cells (1, 2). ARTC2.2 catalyzes arginine-specific ADP-ribosylation of P2X7 and other cell surface proteins in response to NAD$^+$ released from damaged cells (3, 4). Akin to phosphorylation, ADP-ribosylation is a reversible posttranslational modification that regulates the function of target proteins (5, 6). The targets of ADP-ribosylation are mainly ecto-domains of membrane proteins like P2X7, integrins or Fc-gamma-receptors (4, 7). Further, ADP-ribosylation of soluble proteins has been described previously, for example, ARTC1-mediated ADP-ribosylation of HNP-1 reduces the antimicrobial activity of HNP-1 (8).

We previously observed that ARTC2.2 is shed by a metalloprotease following T cell activation as well as upon activation of the P2X7 ion channel (9, 10). Release of ARTC2.2 from the cell surface redirects the enzymatic activity of ARTC2.2 from cell surface bound membrane proteins to soluble proteins in the extracellular milieu (10). We hypothesized that the release of ARTC2.2 from the cell surface into the inflammatory environment has immunoregulatory functions by regulating cytokine signaling. ARTC2.2 is expressed in mice and other rodents. In humans and other primates ARTC2.2 represents a nonfunctional pseudogene (11) but other members of the ADP-ribosytransferase family, for example, ARTC1 are expressed (12).

The goal of this study was to identify potential target cytokines of shed ARTC2.2. Using radio-ADP-ribosylation and mass spectrometry analyses we identified IFN-γ as a major target of shed ARTC2.2. We identified the ADP-ribosylation site on IFN-γ and assessed the effects of ADP-ribosylation on the signaling functions of IFN-γ by flow cytometry and immunoblot analyses. Our results show that ADP-ribosylation inhibits the signaling functions of IFN-γ and point to a new regulatory mechanism for controlling signaling by IFN-γ.

MATERIALS AND METHODS

Mice and cells – C57BL/6 mice were bred at the animal facility of the University Medical Center (UKE). ARTC2$^{-/-}$ mice (13) were backcrossed to C57BL/6 wild-type (WT) mice for more than 12 generations. All animal experiments were performed in accordance with local regulations (registration number ORG153).

DC27.10 lymphoma cells (14), kindly provided by Bernhard Fleischer, Bernhard Nocht Institute for Tropical Medicine, Hamburg, were cultured in RPMI-1640 supplemented with 10% FCS, 2 mM glutamine, 2 mM sodium pyruvate. An expression construct encoding ARTC2.2 (Genebank AJ489297) with an N-terminal FLAG-tag was transfected into DC27.10 lymphoma cells using jetPEI transfection reagent (Q-Biogen) and stable transfectants were obtained by selection of neomycin-resistant cells and cell sorting (4).

Radio-ADP-ribosylation assays – Recombinant cytokines were obtained from Immunotools, recombinant IFNR1-Fc was obtained from R&D Systems. Recombinant murine cytokines (0.1–0.5 μg) and serum proteins from ARTC2−/− mice (50 μg) were incubated with 20 ng shed ARTC2.2 and 1 μM 32P-NAD$^+$ for 20 min. Reactions were stopped by addition of NuPAGE SDS sample buffer and SDS-PAGE was performed using Novex NuPAGE precast 12% Bis-Tris gels (Invitrogen). Gels were stained with Coomassie brilliant blue and dried in cellophane sheets. Dried gels were subjected to autoradiography by exposure of an X-ray film (Hyperfilm, GE-Healthcare) at −80°C.

Purification of ARTC2.2 – Shed ARTC2.2 was purified as described before (10). Briefly, DC27.10 cells stably transfected with ARTC2.2 were treated for 20 min at 37°C with 1 mM ATP. ARTC2.2 was purified from the cell supernatant by affinity chromatography on immobilized anti-FLAG mAb M2 (Sigma) and concentrated via ultra centrifugal filters (Amicon).

Mass spectrometry analyses – Recombinant IFN-γ (1 μg) was incubated with 5 μM NAD$^+$ in the absence or presence of purified shed ARTC2.2 (50 ng) for 60 min at 37°C. After SDS-PAGE, the excised IFN-γ bands were digested with either chymotrypsin or endoproteinase Glu-C (Glu-C). Resulting peptides were separated and analyzed by nano-ion pair reversed phase HPLC coupled online to an Orbitrap LTQ Velos mass spectrometer. Collision-induced dissociation (CID), Higher-energy collisional dissociation (HCD) and MS^3 experiments were used to identify ADP-ribosylation sites.

IFN-γ signaling assays – Recombinant ADP-ribosylarginine hydrolase ARH1 was produced as described previously (15). Murine IFN-γ (1 μg) was ADP-ribosylated by incubation for 60 min at 37°C with 10 μM NAD$^+$ and ARTC2.2 (50 ng). For de-ADP-ribosylation, ADPR-IFN-γ was further incubated with an excess of ARH1 (1 μg) for 60 min at 37°C. For monitoring IFN-γ induced phosphorylation of STAT1 in peritoneal macrophages, C57BL/6 mice were sacrificed and peritoneal macrophages were harvested *via* peritoneal lavage. 2 × 10^5 cells were incubated at 37°C in RPMI containing serial dilutions of IFN-γ, ADPR-IFN-γ or de-ADP-ribosylated IFN-γ (de-ADPR-IFN-γ). After 30 min, cells were washed, fixed with 2% PFA and stained with FITC-conjugated anti-CD11b (mAb M1/70, Biolegend). Cells were then washed, permeabilized at 4°C using Phosflow Perm Buffer III (BD) and stained with anti-phospho STAT1 (mAb pY701, BD PhosFlow) on ice. Cells were washed twice and analyzed by flow cytometry.

For monitoring IFN-γ induced upregulation of immunoproteasome components, terminally differentiated mouse podocytes (16) were incubated for 24 h with IFN-γ, ADPR-IFN-γ or de-ADPR-IFN-γ (100 ng/ml). Cells were harvested and solubilized in tissue protein extraction reagent (TPER, Pierce) for 20 min at 4°C. Clarified lysates were size fractionated on precast SDS-PAGE gels (NuPAGE®, Thermo-Fischer) and blotted onto PVDF membranes. Blots were subjected to immunodetection with antibodies directed against β5i and PA28-α (ab3329, Abcam and #2408, Cell Signaling). Immunodetection of β-actin (clone AC-15, Sigma) was performed as a loading control. Bound antibodies were detected with the enhanced chemiluminescent system (GE Healthcare) using peroxidase-conjugated anti-rabbit Ig or anti-mouse Ig antibodies (Jackson Immunoresearch Laboratories).

RESULTS

Shed ARTC2.2 Preferentially ADP-Ribosylates IFN-γ

The observation that shed ARTC2.2 ADP-ribosylates distinct serum proteins (10) prompted us to determine whether ARTC2.2 preferentially ADP-ribosylates certain cytokines. We

---

Standard Abbreviations: Ab, ATP, LPS, C-terminal, N-terminal, Da, EC$_{50}$, FCS, i.v. IFN, IL, GPI, NAD, mAb.

Abbreviations: ARTC, ADP-ribosyltransferase subgroup related to Clostridial C2/C3 toxins; ARTD, ADP-ribosyltransferase subgroup related to Diphtheria toxin; ARH, arginine ADP-ribosylhydrolase.

therefore incubated shed ARTC2.2 with individual recombinant cytokines in the presence of ^{32}P-NAD$^+$ and monitored covalent incorporation of radioactivity into cytokines by autoradiography after SDS-PAGE (**Figure 1** right panel). The results show that shed ARTC2.2 ADP-ribosylates IFN-γ, IL-2, IL-6, and IL-17 (**Figure 1** without arrow). When incubated with a cocktail of cytokines, ARTC2.2 potently ADP-ribosylates IFN-γ in addition to other cytokines (**Figure 1B**, arrow). Similarly, when incubated in serum spiked with IFN-γ, ARTC2.2 preferentially ADP-ribosylated IFN-γ (**Figure 1C**).

IFN-γ forms a homodimeric bioactive cytokine by a covalent disulfide bridge between the C-terminal cysteine residues (Cys133). Shed ARTC2.2 effectively ADP-ribosylates the native IFN-γ homodimer, as revealed by autoradiography after non-reducing SDS-PAGE (**Figure 1C**). Analysis of IFN-γ under reducing conditions reveals a discernible shift in migration of the IFN-γ band in Coomassie-stained SDS-PAGE after incubation with shed ARTC2.2 and NAD$^+$ (**Figures 1D,E**, lane 2 vs. lane 1), suggesting that ARTC2.2 ADP-ribosylates both molecules of the IFN-γ homodimer, since the presence of ADP-ribosylated and non-ADP-ribosylated IFN-γ should result in two bands after size fractionation by reducing SDS-PAGE. Consistently, pre-ADP-ribosylation of IFN-γ by preincubation with ARTC2.2 and non-radioactive NAD$^+$ for 60 min prevented subsequent incorporation of radiolabel during further incubation with ^{32}P-labeled NAD$^+$ (**Figure 1D**). Addition of recombinant ADP-ribosylarginine hydrolase 1 (ARH1) to ADP-ribosylated IFN-γ caused a shift in migration back to that of native IFN-γ (**Figure 1E**, lane 3), consistent with removal of the ADP-ribose moieties from both molecules of the IFN-γ homodimer. This shift in migration by ADP-ribosylation and de-ADP-ribosylation can be seen in the Coomassie-stained gel without autoradiography (**Figure 1E**).

In order to identify the target arginine for ADP-ribosylation of IFN-γ, we subjected ADP-ribosylated recombinant IFN-γ to LC-MS/MS following in-gel digestion with chymotrypsin and Glu-C (**Figure 2A**). MS^2 analyses revealed a combined sequence coverage of 100% (**Figure 2B** red). Both Higher-Energy Collisional Dissociation (HCD) and Collision Induced Dissociation (CID) of ADP-ribose containing peptides yielded a characteristic MS fingerprint with the major sites of fragmentation occurring at the pyrophosphate bond and the terminal adenine. Manual inspection of the HCD-MS^2 spectra from chymotrypsin-generated peptides revealed a single peptide—R^{126}KRKRSRC^{133}–exhibiting this characteristic ADP-ribose fingerprint with very little peptide-backbone fragmentation (**Figure 2C**). This peptide contains four arginines and the protein's C-terminus. Fragmentation of the ADP-ribose moiety during CID results in the conversion of the ADP-ribosylated arginine to ornithine. The intact ornithine containing peptide can be further isolated in tandem mass spectrometry and subjected to MS^3 analysis for peptide sequencing (17). Applying this strategy to the ADP-ribosylated peptide allowed assignment of ornithine at R128 (**Figure 2D**). Similarly, LC-MS analyses of peptides generated by in-gel digestion with Glu-C resulted in a single peptide - S^{123}SLRKRKRSRC^{133} - exhibiting the characteristic ADP-ribosyl-arginine fragments (**Figure 2B**). A targeted MS^3 experiment again assigned R128 as ornithine (not shown). Together, these results unambiguously identify R128 as the target site of IFN-γ for ADP-ribosylation by ARTC2.2. A model of mouse IFN-γ in complex with IFN-γ receptor 1 (IFNR1) based on the published 3D-crystal structure of human IFN-γ with the *Ectromelia virus* IFN-γ binding protein (pdb code 3bes) (18) indicates that R128 participates in binding to IFNR1 by forming a salt bridge to E174 of IFNR1 (**Figure 2E**).

ARTC2.2-Catalyzed ADP-Ribosylation Inhibits the Signaling Function of IFN-γ

On the basis of the structure model of IFN-γ in complex with IFNR1 (**Figure 2E**), we hypothesized that R128 is not accessible for ADP-ribosylation when IFN-γ is bound to IFNR1. To test this hypothesis, we allowed IFN-γ to form a complex with the recombinant extracellular domain of IFNR1 and analyzed whether IFN-γ is still accessible in this complex for ADP-ribosylation by shed ARTC2.2. The results show that ADP-ribosylation of IFN-γ is blocked in the presence of IFNR1 and that IFNR1 itself is not a target for ADP-ribosylation (**Figure 3A**).

In order to determine whether ADP-ribosylation of IFN-γ impinges on its signaling function, we used two established cellular assays, that is, IFN-γ-induced phosphorylation of signal-transducer-and-activator-of-transcription-1 (STAT1) in macrophages and IFN-γ-induced expression of the immune proteasome component β5i and the proteasomal activator PA28-α in podocytes (**Figures 3B,C**). The results show that ADP-ribosylation reduces potency of IFN-γ to induce phosphorylation of STAT1 in primary peritoneal macrophages by approximately four-fold (**Figure 3B**). De-ADP-ribosylation of IFN-γ with ARH1 restores its original potency to induce STAT1 phosphorylation. Similarly, ADP-ribosylation of IFN-γ inhibits its capacity to induce expression of β5i and PA28-α by murine podocytes (**Figure 3C**, lane 3), whereas de-ADP-ribosylation of IFN-γ by ARH1 restores its capacity to induce expression of β5i and PA28-α (**Figure 3C**, lane 4).

DISCUSSION

Our results confirm that shed ARTC2.2 preferentially ADP-ribosylates secretory proteins (10). To identify possible soluble targets we performed a comparative radio-ADP-ribosylation assay with different cytokines and recombinant soluble ARTC2.2 and ^{32}P-NAD$^+$. In these experiments ARTC2.2 showed a propensity to ADP-ribosylate IFN-γ. Moreover, we identified R128 as the ADP-ribosylation site of IFN-γ and showed that ADP-ribosylation of IFN-γ inhibits its signaling function.

Arginine ADP-ribosylation is a reversible posttranslational protein modification: ARH1 catalyzes hydrolysis of the ADP-ribose residue from arginine (19). Our results show that recombinant ARH1 can de-ADP-ribosylate IFN-γ and thereby restore the signaling capacity of IFN-γ. In this context, it is important to note that ARH1 lacks an N-terminal signal sequence for export from cells by a classical secretion pathway via the ER and Golgi apparatus and, thus, presumably is expressed as a cytosolic enzyme. It remains to be established whether

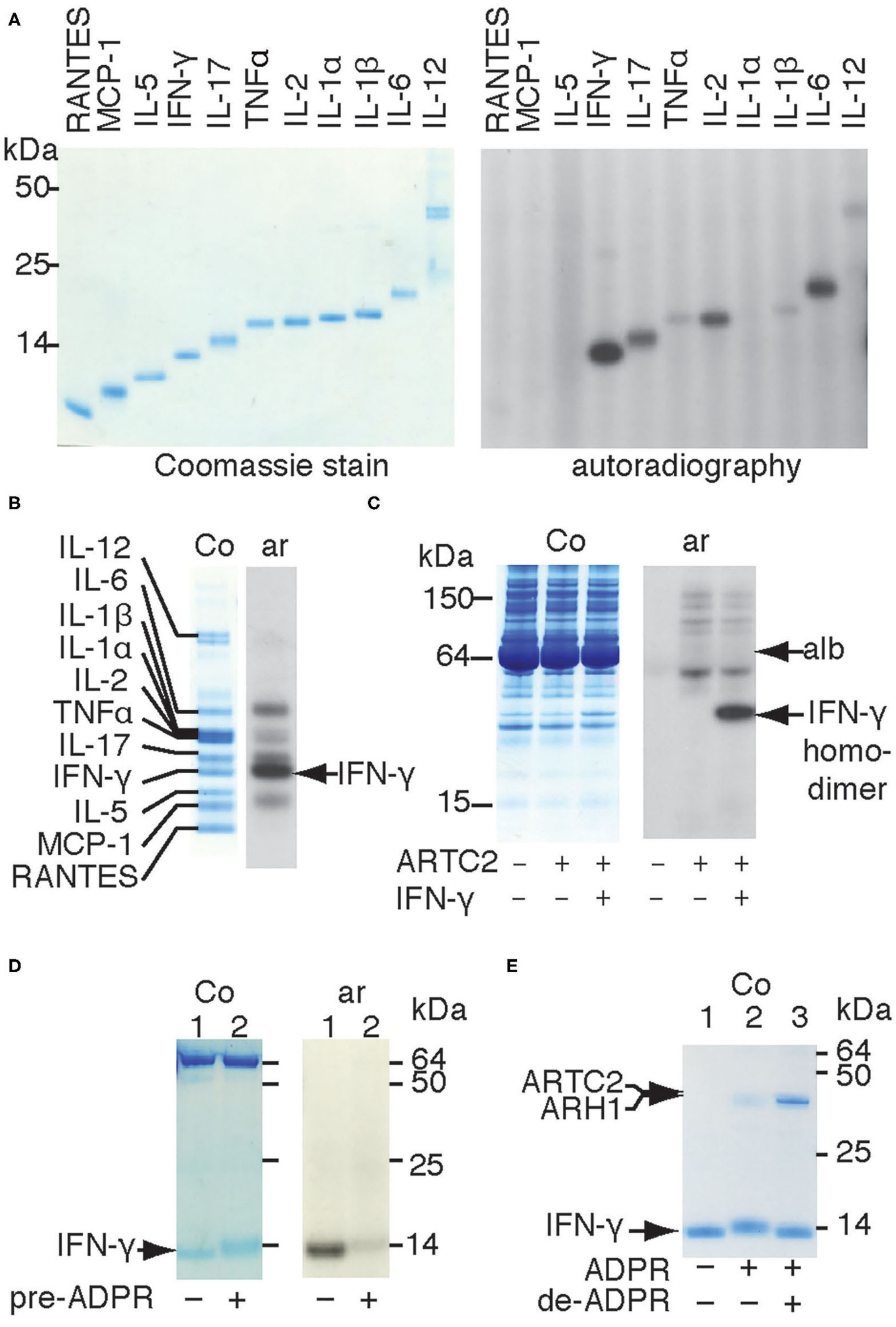

FIGURE 1 | Shed ARTC2.2 preferentially ADP-ribosylates IFN-γ. **(A–D)** Purified shed ARTC2.2 (50 ng) was incubated for 15 min with ^{32}P-NAD$^+$ (1 μM) and **(A)** individual recombinant cytokines (500 ng), **(B)**, a cocktail of cytokines (500 ng each), **(C)**, serum spiked with IFN-γ, or **(D)** IFN-γ that had been pre-ADP-ribosylated or not by incubation for 30 min with shed ARTC2.2 and non-radioactive NAD$^+$. Reactions were stopped by the addition of SDS-PAGE sample buffer. Proteins were size fractionated by SDS-PAGE and stained with Coomassie (Co). ^{32}P-ADP-ribosylated proteins were detected by autoradiography (Ar). The gels in A, B, and D were run under reducing conditions, the gel in C was run under non- reducing conditions. In C, alb indicates the prominent 65 kDa band corresponding to endogenous albumin in murine serum. In D the prominent bands at 65 kDa represents bovine albumin that was added as carrier protein. **(E)** IFN-γ was sequentially ADP-ribosylated then de-ADP-ribosylated as described in the methods. Proteins were analyzed by SDS-PAGE and Coomassie-staining. Results are representative of three or four independent experiments.

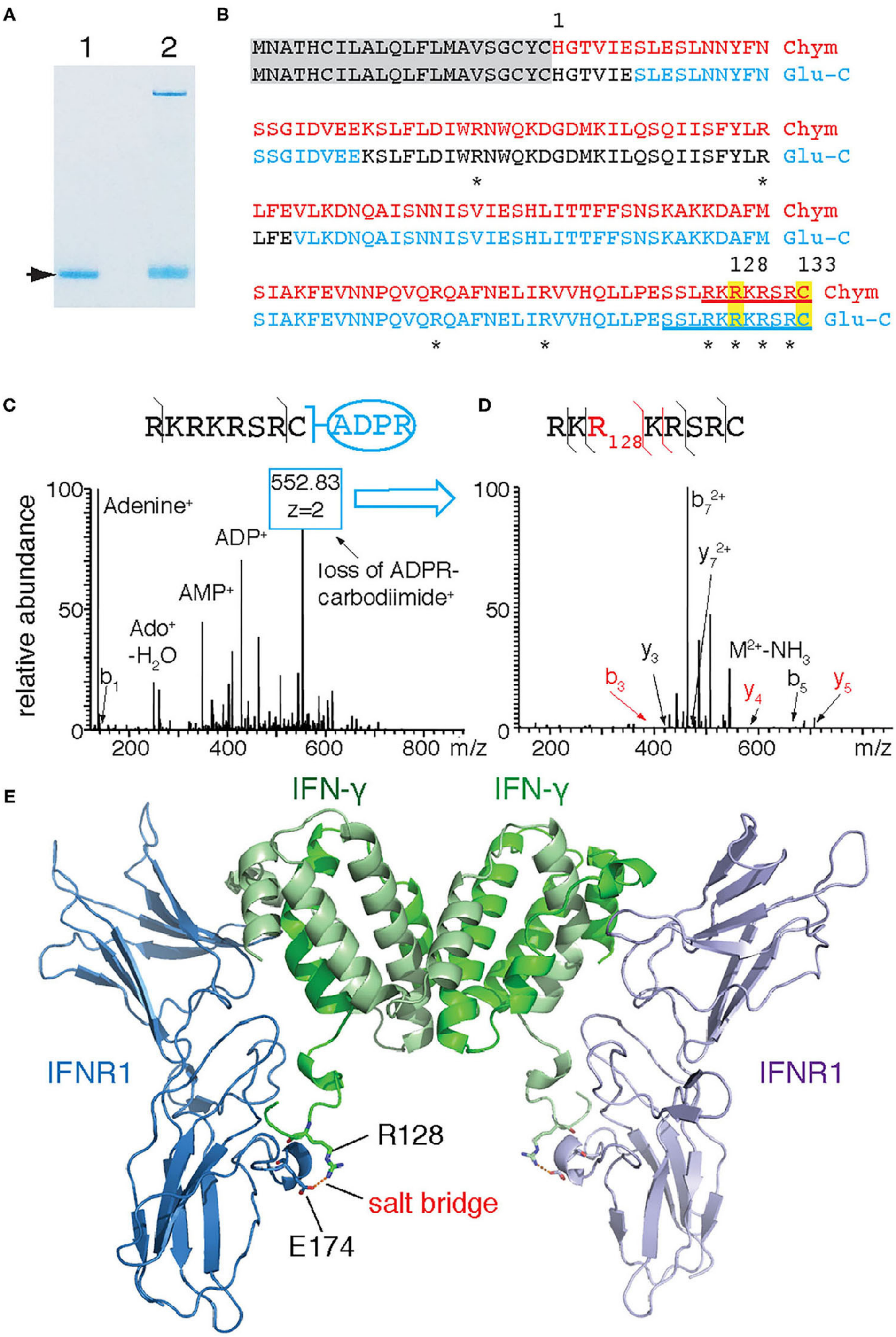

FIGURE 2 | IFN-γ is ADP-ribosylated by ARTC2.2 at R128. **(A)** Recombinant IFN-γ was incubated in the absence (lane 1) or presence (lane 2) of shed ARTC2.2 and NAD^+. Bands corresponding to unmodified and ADP-ribosylated IFN-γ (arrow) were excised from the gel and subjected to in-gel digestion with chymotrypsin or Glu-C protease. **(B)** Peptides identified by MS-MS analyses are indicated in red and blue for chymotrypsin and Glu-C, respectively. Potential target arginine residues for ADP-ribosylation are marked by asterisks. Peptides exhibiting the characteristic ADP-ribose fragmentation fingerprint are underlined. **(C)** HCD-MS^2 spectrum of the ADP-ribose-containing C-terminal peptide generated from IFN-γ by chymotrypsin cleavage, showing the characteristic ADP-ribosyl fragments. The most intense peak corresponds to a fragment resulting from the conversion of ADP-ribosyl-arginine to ornithine (loss of ADP-R-carbodiimide). **(D)** MS^3-CID spectrum of the ornithine-containing peptide generated by MS^2. **(E)** Model of interaction between murine IFN-γ and IFNR1. IFN-γ and IFNR1 were modeled onto the co-crystal structures of human IFN-γ and *Ectromelia virus* IBP^{ECTV} (PDB ID: 3bes) using Swiss Model. Models were aligned to 3bes in Pymol. R128 of IFN-γ and E174 of IFNR1 are presented as sticks with oxygen atoms in red and nitrogen atoms in blue—the corresponding residues in human IFN-γ and IBP^{ECTV} form a salt bridge. The C-terminal amino acids (R132 and C133) of murine IFN-γ could not be modeled since the corresponding residues of human IFN-γ are not visible in 3bes.

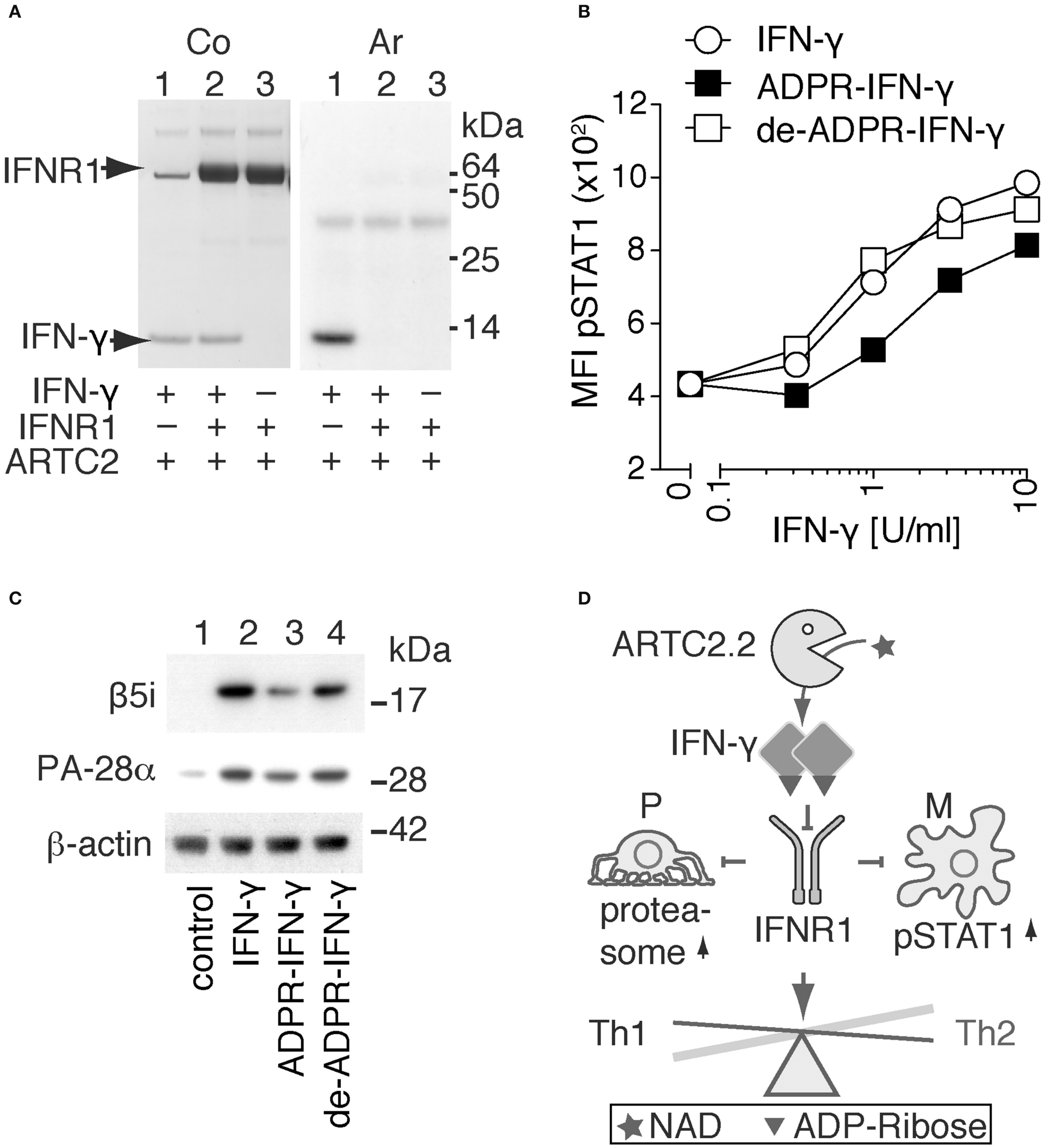

FIGURE 3 | ADP-ribosylation inhibits the signaling function of IFN-γ. **(A)** Recombinant IFN-γ and the ectodomain of IFNR1 were preincubated for 1h at 4°C before addition of shed ARTC2.2 and ^{32}P-NAD^{+}. After further incubation for 15 min, reactions were stopped by addition of SDS-PAGE sample buffer. Proteins were size-fractionated by SDS-PAGE and visualized by Coomassie staining (Co). ADP-ribosylated proteins were detected by autoradiography (Ar). **(B, C)** IFN-γ signaling assays were performed using unmodified IFN-γ, ADP-ribosylated IFN-γ and de-ADP-ribosylated IFN-γ prepared as described in the methods. **(B)** Peritoneal macrophages were incubated for 20 min with serial titrations of IFN-γ, ADP-ribosylated IFN-γ (ADPR-IFN-γ), or de-ADP-ribosylated IFN-γ (de-ADPR- IFN-γ). Cells were then fixed, permeabilized, and stained with a fluorochrome-conjugated mAb against phosphorylated STAT1 (pSTAT1) before flow cytometry analyses. **(C)** Differentiated podocytes were incubated for 24 h in the absence of IFN-γ (control), or presence of either IFN-γ, ADPR-IFN-γ, or de-ADPR-IFN-γ. Cells were washed and lysed in TPER. Insoluble material was removed by centrifugation and solubilized proteins were analyzed by SDS-PAGE and immunoblot analyses. Components β5i of the immunoproteasome and the proteasomal activator PA28-α and β-actin as loading control were detected with appropriate primary and secondary antibodies. Results are representative of three independent experiments. **(D)** Schematic model illustrating the proposed regulation of IFN-γ signaling by ADP-ribosylation. ARTC2.2-catalyzed ADP-ribosylation of IFN-γ inhibits IFNR1 activation and thereby phosphorylation of STAT1 and activation of the immunoproteasome in macrophages (M) and podocytes (P), respectively. By inhibiting IFN-γ signaling, this pathway may tip the balance from a Th1 toward a Th2 response.

ARH1 can be released from cells by non-classical secretion system, for example, analogous to other cytosolic enzymes and cytokines that lack a signal sequence such as adenosine deaminase, PBEF1/NAMPT, IL-1β and IL-18 (20–22).

Using LC-MS/MS, we identified R128 as the target site for ADP-ribosylation by ARTC2.2 (**Figure 2**). This site was confirmed in peptides derived from two different proteases (chymotrypsin, Glu-C). R128 is located in a highly basic region, just five amino acid residues upstream of the C-terminal cysteine. Arginines in other proteins that function as ADP-ribosylation targets of vertebrate ARTCs typically lie in regions with high pKa (23). Consistently, R128 is flanked on either side by lysine and arginine residues. Previous functional and structural studies revealed a crucial role of the C-terminus of IFN-γ for receptor binding and biological activity (18, 24–26). Deletion of the C-terminus or site directed mutagenesis of the basic residues in this region markedly reduce the capacity of IFN-γ to bind to its receptor (24, 26). Importantly, site-directed mutagenesis of R129 of human IFN-γ–that is, the residue corresponding to the R128 ADP-ribosylation site of murine IFN-γ–drastically reduced receptor binding and biological activity (25).

The C-terminus is not resolved in known structures of IFN-γ, either alone or in complex with its receptor, IFNR1 (27, 28). However, R129 of human IFN-γ is visible in the co-crystal structure of IFN-γ bound to IBP^{ECTV}, a viral protein homologous to IFNR1. Interestingly, this residue forms a salt bridge to a conserved aspartic acidic residue in IBP^{ECTV} (18) that corresponds to E174 of IFNR1. It is thus conceivable that a bulky, negatively charged ADP-ribose moiety at R128 would disturb this interaction and lead to reduced biological activity.

IFN-γ is secreted mainly by activated Th1 effector cells and is an important endogenous mediator of immunity and inflammation. It plays a key role in macrophage activation and T cell differentiation (29). Excessive IFN-γ can lead to tissue damage and autoimmunity (26, 30, 31) as illustrated by the severe inflammatory disease in mice deficient in suppressor of cytokine signaling 1 (SOCS1), one of several known attenuators of IFN-γ expression (32). It was also shown that C-terminal truncation of IFN-γ by matrix metalloproteinase 12 controls IFN-γ signaling to resolve inflammation and that this negative feedback mechanism is often defective in autoimmune diseases (26).

Recent studies indicate that the IFN-γ/STAT-1 signaling pathway in macrophages regulates and is regulated also by intracellular ADP-ribosylransferases, for example, ARTD8 and ARTD9 (33–37). Interestingly IFN-γ signaling stimulates the activity of these members of the ARTD family, and these enzymes in turn modulate IFN-γ signaling by ADP-ribosylating STAT1.

ADP-ribosylation provides an additional, posttranslational means for regulating IFN-γ signaling. However, given the locally restricted release of ARTC2.2 and IFN-γ from activated T cells, and of NAD^+ as substrate from lysed or damaged cells, the total amount of ADP-ribosylated IFN-γ *in vivo* is likely to be low. Currently available tools lack the sensitivity to monitor ADP-ribosylation of IFN-γ *in vivo*. ARTC2.2 is expressed in mice and other rodents but is not expressed in humans and other primates which carry a nonfunctional ARTC2.2. pseudogene (11). Since ADP-ribosylation of IFN-γ is mediated by soluble ARTC2.2, it is conceivable that other members of the ADP-ribosytransferase family for example, ARTC1 (7, 12) could replace this function in humans.

Considering that IFN-γ drives differentiation of effector T cells to Th1 cells, and conversely that neutralizing IFN-γ promotes differentiation to Th2 cells, we hypothesize that ADP-ribosylation of IFN-γ might be involved in endogenous regulatory mechanisms to tip the balance from a Th1 to a Th2 immune response and thereby to diminish unwanted autoimmune responses (**Figure 3D**).

In summary, our results uncover a hitherto unrecognized mechanism to control signaling by IFN-γ *via* reversible ADP-ribosylation by the shed ectodomain of ARTC2.2. Our findings point to new avenues for modulating inflammatory reactions by pharmacologically blocking or enhancing ADP-ribosylation of IFN-γ, for example, by suitable decoy-peptides or by targeting recombinant ecto-ADP-ribosyltransferase ARTC2.2 or ADP-ribosylarginine hydrolase ARH1 to IFN-γ at sites of inflammation.

DATA AVAILABILITY STATEMENT

The raw data supporting the conclusions of this article will be made available by the authors, without undue reservation.

ETHICS STATEMENT

The animal study was reviewed and approved by Hamburger Behörde für Gesundheit und Verbraucherschutz, Veterinärwesen/Lebensmittelsicherheit, ORG 153.

AUTHOR CONTRIBUTIONS

SM, FH, CM-S, AT, and FK-N conceived the project. SM and FK-N wrote the manuscript. SM performed the experiments shown in **Figures 1**, **2A,E** and **3A**. TK those in **Figures 2B–D**. BR those in **Figure 3B**. CM-S those in **Figure 3C**. All authors reviewed and approved the manuscript.

FUNDING

This study was supported by grants from the Deutsche Forschungsgemeinschaft SFB877 (projects A5 and Z2) to FK-N, TK, and AT, SFB1328 (project Z02) to FK-N and by the DFG-Cluster of Excellence Precision Medicine in Inflammation, RTF-V to AT.

ACKNOWLEDGMENTS

We thank Fabienne Seyfried, Joanna Schmid, and Gudrun Dubberke for excellent technical assistance. We also thank B. Fleischer, E. Tolosa, and H.W. Mittrücker for critical reading of the manuscript.

REFERENCES

1. Koch F, Thiele HG, Low MG. Release of the rat T cell alloantigen RT-6.2 from cell membranes by phosphatidylinositol-specific phospholipase C. *J Exp Med.* (1986) 164:1338–43. doi: 10.1084/jem.164.4.1338
2. Koch-Nolte F, Petersen D, Balasubramanian S, Haag F, Kahlke D, Willer T, et al. Thiele, Mouse T cell membrane proteins Rt6-1 and Rt6-2 are arginine/protein mono(ADPribosyl)transferases and share secondary structure motifs with ADP-ribosylating bacterial toxins. *J Biol Chem.* (1996) 271:7686–93. doi: 10.1074/jbc.271.13.7686
3. Seman M, Adriouch S, Scheuplein F, Krebs C, Freese D, Glowacki G, et al. Koch-Nolte, NAD-induced T cell death: ADP-ribosylation of cell surface proteins by ART2 activates the cytolytic P2X7 purinoceptor. *Immunity.* (2003) 19:571–82. doi: 10.1016/S1074-7613(03)00266-8
4. Adriouch S, Bannas P, Schwarz N, Fliegert R, Guse AH, Seman M, et al. ADP-ribosylation at R125 gates the P2X7 ion channel by presenting a covalent ligand to its nucleotide binding site. *FASEB J.* (2008) 22:861–9. doi: 10.1096/fj.07-9294com
5. Corda D, Di Girolamo M. Functional aspects of protein mono-ADP-ribosylation. *EMBO J.* (2003) 22:1953–8. doi: 10.1093/emboj/cdg209
6. Feijs KL, Forst AH, Verheugd P, Luscher B. Macrodomain-containing proteins: regulating new intracellular functions of mono(ADP-ribosyl)ation. *Nat Rev Mol Cell Biol.* (2013) 14:443–51. doi: 10.1038/nrm3601
7. Leutert M, Menzel S, Braren R, Rissiek B, Hopp AK, Nowak K, et al. Hottiger, proteomic characterization of the heart and skeletal muscle reveals widespread arginine ADP-ribosylation by the ARTC1 ectoenzyme. *Cell Rep.* (2018) 24:1916–29. e5. doi: 10.1016/j.celrep.2018.07.048
8. Paone G, Stevens LA, Levine RL, Bourgeois C, Steagall WK, Gochuico BR, et al. ADP-ribosyltransferase-specific modification of human neutrophil peptide-1. *J Biol Chem.* (2006) 281:17054–60. doi: 10.1074/jbc.M603042200
9. Kahl S, Nissen M, Girisch R, Duffy T, Leiter EH, Haag F, et al. Metalloprotease-mediated shedding of enzymatically active mouse ecto-ADP-ribosyltransferase ART2.2 upon T cell activation. *J Immunol.* (2000) 165:4463–9. doi: 10.4049/jimmunol.165.8.4463
10. Menzel S, Rissiek B, Bannas P, Jakoby T, Miksiewicz M, Schwarz N, et al. Nucleotide-induced membrane-proximal proteolysis controls the substrate specificity of T cell ecto-ADP-ribosyltransferase ARTC2.2. *J Immunol.* (2015) 195:2057–66. doi: 10.4049/jimmunol.1401677
11. Haag F, Koch-Nolte F, Kuhl M, Lorenzen S, Thiele HG. Premature stop codons inactivate the RT6 genes of the human and chimpanzee species. J Mol Biol. (1994) 243:537–46. doi: 10.1006/jmbi.1994.1680
12. Hottiger MO, Hassa PO, Luscher B, Schuler H, Koch-Nolte F. Toward a unified nomenclature for mammalian ADP-ribosyltransferases. *Trends Biochem Sci.* (2010) 35:208–19. doi: 10.1016/j.tibs.2009.12.003
13. Ohlrogge W, Haag F, Lohler J, Seman M, Littman DR, Killeen N, et al. Generation and characterization of ecto-ADP-ribosyltransferase ART2.1/ART2.2-deficient mice. *Mol Cell Biol.* (2002) 22:7535–42. doi: 10.1128/MCB.22.21.7535-7542.2002
14. Gabert J, Langlet C, Zamoyska R, Parnes JR, Schmitt-Verhulst AM, Malissen B. Reconstitution of MHC class I specificity by transfer of the T cell receptor and Lyt-2 genes. Cell. (1987) 50:545–54. doi: 10.1016/0092-8674(87)90027-4
15. Kernstock S, Koch-Nolte F, Mueller-Dieckmann J, Weiss MS, Mueller-Dieckmann C. Cloning, expression, purification and crystallization as well as X-ray fluorescence and preliminary X-ray diffraction analyses of human ADP-ribosylhydrolase 1. *Acta Crystallogr Sect F Struct Biol Cryst Commun.* (2009) 65:529–32. doi: 10.1107/S1744309109014067
16. Schordan S, Schordan E, Endlich N, Lindenmeyer MT, Meyer-Schwesinger C, Meyer TN, et al. Alterations of the podocyte proteome in response to high glucose concentrations. Proteomics. (2009) 9:4519–28. doi: 10.1002/pmic.200800214
17. Osago H, Yamada K, Shibata T, Yoshino K, Hara N, Tsuchiya M. Precursor ion scanning and sequencing of arginine-ADP-ribosylated peptide by mass spectrometry. Anal Biochem. (2009) 393:248–54. doi: 10.1016/j.ab.2009.06.028
18. Nuara AA, Walter LJ, Logsdon NJ, Yoon SI, Jones BC, Schriewer JM, et al. Walter, structure and mechanism of IFN-gamma antagonism by an orthopoxvirus IFN-gamma-binding protein. *Proc Natl Acad Sci USA.* (2008) 105:1861–6. doi: 10.1073/pnas.0705753105
19. Takada T, Iida K, Moss J. Cloning and site-directed mutagenesis of human ADP-ribosylarginine hydrolase. J Biol Chem. (1993) 268:17837–43. doi: 10.1016/S0021-9258(17)46780-9
20. Friebe D, Neef M, Kratzsch J, Erbs S, Dittrich K, Garten A, et al. Leucocytes are a major source of circulating nicotinamide phosphoribosyltransferase (NAMPT)/pre-B cell colony (PBEF)/visfatin linking obesity and inflammation in humans. *Diabetologia.* (2011) 54:1200–11. doi: 10.1007/s00125-010-2042-z
21. Dubyak GR. P2X7 receptor regulation of non-classical secretion from immune effector cells. Cell Microbiol. (2012) 14:1697–706. doi: 10.1111/cmi.12001
22. Schilling E, Hauschildt S. Extracellular ATP induces P2X7-dependent nicotinamide phosphoribosyltransferase release in LPS-activated human monocytes. *Innate Immun.* (2012) 18:738–44. doi: 10.1177/1753425912439614
23. Laing S, Unger M, Koch-Nolte F, Haag F. ADP-ribosylation of arginine. *Amino Acids.* (2010) 41:257–69. doi: 10.1007/s00726-010-0676-2
24. Lundell D, Lunn C, Dalgarno D, Fossetta J, Greenberg R, Reim R, et al. The carboxyl-terminal region of human interferon gamma is important for biological activity: mutagenic and NMR analysis. Protein Eng. (1991) 4:335–41. doi: 10.1093/protein/4.3.335
25. Haelewyn J, Michiels L, Verhaert P, Hoylaerts MF, Witters R, De Ley M. Interaction of truncated human interferon gamma variants with the interferon gamma receptor: crucial importance of Arg-129. *Biochem J.* (1997) 324(Pt 2):591–5. doi: 10.1042/bj3240591
26. Dufour A, Bellac CL, Eckhard U, Solis N, Klein T, Kappelhoff R, et al. Overall, C-terminal truncation of IFN-gamma inhibits proinflammatory macrophage responses and is deficient in autoimmune disease. Nat Commun. (2018) 9:2416. doi: 10.1038/s41467-018-04717-4
27. Walter MR, Windsor WT, Nagabhushan TL, Lundell DJ, Lunn CA, Zauodny PJ, et al. Crystal structure of a complex between interferon-gamma and its soluble high-affinity receptor. Nature. (1995) 376:230–5. doi: 10.1038/376230a0
28. Randal M, Kossiakoff AA. The structure and activity of a monomeric interferon-gamma:alpha-chain receptor signaling complex. Structure. (2001) 9:155–63. doi: 10.1016/S0969-2126(01)00567-6
29. Abbas AK, Murphy KM, Sher A. Functional diversity of helper T lymphocytes. *Nature.* (1996) 383:787–93. doi: 10.1038/383787a0
30. Baccala R, Kono DH, Theofilopoulos AN. Interferons as pathogenic effectors in autoimmunity. *Immunol Rev.* (2005) 204:9–26. doi: 10.1111/j.0105-2896.2005.00252.x
31. Hu X, Ivashkiv LB. Cross-regulation of signaling pathways by interferon-gamma: implications for immune responses and autoimmune diseases. *Immunity.* (2009) 31:539–50. doi: 10.1016/j.immuni.2009.09.002
32. Alexander WS, Starr R, Fenner JE, Scott CL, Handman E, Sprigg NS, et al. SOCS1 is a critical inhibitor of interferon gamma signaling and prevents the potentially fatal neonatal actions of this cytokine. *Cell.* (1999) 98:597–608. doi: 10.1016/S0092-8674(00)80047-1
33. Higashi H, Maejima T, Lee LH, Yamazaki Y, Hottiger MO, Singh SA, et al. A Study into the ADP-ribosylome of IFN-gamma-stimulated THP-1 human macrophage-like cells identifies ARTD8/PARP14 and ARTD9/PARP9 ADP-ribosylation. *J Proteome Res.* (2019) 18:1607–22. doi: 10.1021/acs.jproteome.8b00895
34. Zhang Y, Mao D, Roswit WT, Jin X, Patel AC, Patel DA, et al. PARP9-DTX3L ubiquitin ligase targets host histone H2BJ and viral 3C protease to enhance interferon signaling and control viral infection. *Nat Immunol.* (2015) 16:1215–27. doi: 10.1038/ni.3279

35. Kunze FA, Hottiger MO. Regulating immunity via ADP-ribosylation: therapeutic implications and beyond. Trends Immunol. (2019) 40:159–73. doi: 10.1016/j.it.2018.12.006

36. Iwata H, Goettsch C, Sharma A, Ricchiuto P, Goh WW, Halu A, et al. PARP9 and PARP14 cross-regulate macrophage activation via STAT1 ADP-ribosylation. *Nat Commun.* (2016) 7:12849. doi: 10.1038/ncomms12849

37. Guo T, Zuo Y, Qian L, Liu J, Yuan Y, Xu K, et al. ADP-ribosyltransferase PARP11 modulates the interferon antiviral response by mono-ADP-ribosylating the ubiquitin E3 ligase beta-TrCP. Nat Microbiol. (2019) 4:1872–84. doi: 10.1038/s41564-019-0428-3

Conflict of Interest: The authors declare that the research was conducted in the absence of any commercial or financial relationships that could be construed as a potential conflict of interest.

frontiers
in Immunology

MINI REVIEW
published: 15 April 2021
doi: 10.3389/fimmu.2021.658263

The Key Role of NAD$^+$ in Anti-Tumor Immune Response: An Update

Fabio Morandi[1]*, *Alberto Leonardo Horenstein*[2] *and Fabio Malavasi*[2]

[1] *Laboratorio Cellule Staminali Post-Natali e Terapie Cellulari, IRCCS Istituto Giannina Gaslini, Genoa, Italy,* [2] *Dipartimento Scienze Mediche, Università di Torino, Centro Ricerche Medicina Sperimentale (CeRMS) and Fondazione Ricerca Molinette Onlus, Torino, Italy*

Nicotinamide adenine dinucleotide (NAD$^+$) is an important molecule that functions as a co-enzyme in numerous metabolic processes. Generated both through *de novo* synthesis and *via* salvage pathways, NAD$^+$ is the substrate for a variety of NAD$^+$-consuming enzymes. Among them is CD38, a cell surface ecto-enzyme widely expressed on different types of cells and endowed with the function of cADP-ribose synthases/NAD$^+$ glycohydrolase. Surface CD38 expression is increased in different hematological and solid tumors, where it cooperates with other ecto-enzymes to produce the immunosuppressive molecule adenosine (ADO). Few studies have explored the correlation of NAD$^+$ levels with T-cell mediated anti-tumor response in preclinical models. We therefore discuss these novel findings, examining the possible contribution of NAD$^+$ depletion, along with ADO production, in the immunosuppressive activities of CD38 in the context of human tumors. Lastly, we discuss the use of pharmacological inhibitors of CD38 and supplementation of different NAD$^+$ precursors to increase NAD$^+$ levels and to boost T cell responses. Such molecules may be employed as adjuvant therapies, in combination with standard treatments, for cancer patients.

Keywords: NAD$^+$, human tumors, immune response, CD38, T cells

OPEN ACCESS

Edited by:
Santina Bruzzone,
University of Genoa, Italy

Reviewed by:
Giovanna Montana,
Institute of Biomedicine
and Molecular Immunology
Alberto Monroy (IBIM), Italy
Silvia Deaglio,
University of Turin, Italy
Nadia Raffaelli,
Marche Polytechnic University, Italy

****Correspondence:***
Fabio Morandi
fabiomorandi@gaslini.org

Specialty section:
This article was submitted to
Cytokines and Soluble
Mediators in Immunity,
a section of the journal
Frontiers in Immunology

Received: *25 January 2021*
Accepted: *25 March 2021*
Published: *15 April 2021*

Citation:
Morandi F, Horenstein AL and
Malavasi F (2021) The Key Role of
NAD$^+$ in Anti-Tumor Immune
Response: An Update.
Front. Immunol. 12:658263.
doi: 10.3389/fimmu.2021.658263

INTRODUCTION

Nicotinamide adenine dinucleotide (NAD$^+$) and its reduced/phosphorylated forms (NADH, NADP$^+$ and NADPH) are key molecules in cellular metabolism and energy production, acting as hybrid-accepting and hybrid-donating co-enzymes in different biological reactions. NAD$^+$ and NADH are then inter-converted by hybrid transfer and not consumed (1). NAD$^+$ can be generated *de novo* starting from tryptophan, which is converted to N-formylkynurenine by indoleamine dioxygenase or tryptophan dioxygenase. Other enzymes are involved in converting N-formylkynurenine to nicotinic acid mononucleotide (NaMN), which is adenylated by adenyl-transferases to generate nicotinic acid adenine dinucleotide (NaAD), finally converted to NAD$^+$ by NAD$^+$ synthetase (1). NAD$^+$ can also be obtained through different salvage pathways, starting from nicotinic acid (Na) which is converted to NaMN by Na phosphoribosyltransferase (Naprt) or starting from nicotinamide (Nam) and nicotinamide riboside (NR). The latter are converted to nicotinamide mononucleotide (NMN) by Nam phosphoribosyltransferase (Nampt or PBEF) and nicotinamide riboside kinases (NamRK), respectively. NMN is finally converted to NAD$^+$ by adenyl-transferases (1). In contrast with metabolic reactions, NAD$^+$ is consumed during its conversion to Nam by different enzymes involved in process related to gene expression, Ca2$^+$ mobilization, cell death and aging (1). These enzymes are defined as NAD$^+$-dependent ADP-ribosyl transferase, and include i) ADP-ribose transferases or poly(ADP-ribose) polymerases, (ii) cADP-ribose synthases and (iii) sirtuins (NAD$^+$-dependent protein deacetylases) (1).

INHIBITION OF ANTI-TUMOR IMMUNITY

The Role of cADP-ribose Synthases/NAD$^+$glycohydrolase

CD38 and its homologue CD157 belong to the family of cADP-ribose synthases/NAD$^+$ glycohydrolases. CD38 is also part of an alternative ecto-enzymatic pathway, which involves CD203a/ENPP1 and CD73, to produce adenosine (ADO) and inosine (INO) (2, 3). CD38 expression and its role in the inhibition of anti-tumor immune response has been described in solid (4) and hematological (5–8) tumors. CD38 expression is increased during inflammation and tumor transformation, and is paralleled by CD73 up-regulation (9, 10). In chronic lymphocytic leukemia (CLL), increased CD38 expression is associated with unfavorable prognosis (11), along with T cell inhibition (12). Taken together, these observations suggest that increased CD38 expression is directly related to anti-tumor immune response suppression and/or inhibition of migration (13). Indeed, CD38^{hi} CLL cells have high NAD$^+$ glycohydrolase enzymatic activity that leads to ADO production (11) (through the concerted activity of CD203a/ENPP1 and CD73) and, more importantly, to extracellular NAD$^+$ consumption.

The role of CD38 in tumor-mediated inhibition of T cell functions has been extensively studied in the multiple myeloma (MM) model, where malignant plasma cells (PC) grow in a hypoxic bone marrow (BM) niche (6, 14). The niche contains a purinome, represented by different molecules interacting with extracellular nucleotides, including channels, transporters, catabolizing enzymes, intermediate products and receptors. As a result of the activity of this complex network, ADO is produced by canonical and alternative enzymatic pathways, starting from ATP or NAD$^+$, respectively (3, 14). In the canonical pathway, CD39 converts extracellular ATP to AMP, whereas in the alternative pathway CD38 converts β-NAD$^+$ to ADPR and Nam and CD203a/ENPP1 converts ADPR to AMP. Finally, both pathways converge to CD73, which de-phosphorylates AMP to ADO (2). The expression of ectoenzymes belonging to alternative pathway is discontinuous in the MM niche, since PC express CD38, whereas CD203a and CD73 are detectable at very low expression (15). However, the latter molecules are highly expressed by osteoblasts, osteoclasts and BM stromal cells, thus confirming the existence of the complete pathway within BM niche (6, 14). ADO exerts immunosuppressive functions, by i) inhibiting tumor cell lysis by T and NK cells, ii) inducing M2 macrophages and tolerogenic dendritic cells (DC) and iii) inducing Treg expansion (6). In this context, NAD$^+$ consumption in the BM niche may account for additional immunosuppressive feature of CD38, since the alternative pathway is more active than the canonical counterpart in hypoxic conditions and at a low pH (14). Accordingly, therapeutic anti-CD38 mAbs Daratumumab and Isatuximab are able to modulate the NAD$^+$ glycohydrolase enzymatic activity of CD38, likely affecting ADO production on the one hand, and NAD$^+$consumption on the other (6, 16). The degree of modulation is significantly different, Isatuximab scoring the highest level (15, 17).

We elsewhere described the expression and function of ADO generation pathways in primary melanoma cells (18). In these tumor cells, CD38 and CD73 expression was constantly detected, whereas CD39 and CD203a were highly expressed in some primary melanoma cells, and low to absent in the others. Accordingly, ADO production was different, depending on the expression of each ectoenzyme (18). Melanoma cells inhibited T cell proliferation, and such inhibition was only partially reverted using inhibitors of ADO receptors: this suggests that other mechanisms may be involved. In this regard, T cell proliferation was restored by using kuromanin, a specific CD38 inhibitor, providing indirect evidence for the central role played by CD38 in melanoma-mediated immunosuppression (18). We hypothesize that NAD$^+$ consumption may represent an additional immunosuppressive mechanism in *in vitro* experiments and may also represent a strategy enacted by melanoma cells *in vivo* in the tumor microenvironment to inhibit anti-tumor immune response. In this context, inoculation of Nam in a mouse model of melanoma significantly increased anti-tumor immune response through the induction of IFN-γ secretion (19). In addition, in preclinical models of melanoma, mice receiving Nam displayed a higher T cell infiltration within the tumor than those receiving placebo (20). Taken together, these studies support the role of NAD$^+$ as an essential cofactor for anti-tumor T cell response in melanoma.

Recent studies showed that some purinergic ectoenzymes metabolize cyclic dinucleotides, such as 2',3'cyclic GMP-AMP (cGAMP) (21). CD203a/ENPP1 metabolizes cGAMP generating AMP and GMP (22). cGAMP is an activator of the stimulator of interferon genes (STING), which stimulate innate immunity. In brief, cyclic GMP-AMP synthase (cGAS) senses DNA released from tumors and catalyzes the conversion of GTP and ATP to cGAMP, which subsequently activates STING to activate the transcription of type 1 IFN and other cytokines, and by activating DC (21). Links between the cGAS-STING pathway with CD203a/ENPP1 and NAD$^+$ have recently emerged whereby the hydrolysis of cGAMP by CD203a/ENPP1 attenuates cGAS-STING signaling and NAD$^+$ cleavage (23, 24). Indeed, bacterial STING, containing a NADase-TIR domain, recognizes cyclic dinucleotides in a conformation similar to cGAMP in complex with human STING, allowing for β-NAD$^+$ hydrolysis (22). NAD$^+$ cleavage activity of bacterial TIR domains is conserved in the mammalian SARM1 (sterile alpha and TIR motif containing 1) NAD$^+$-glycohydrolase (23, 25). In mice, high cGAMP correlated with high anti-tumor activity, by a direct triggering of the STING-dependent pathway. Consequently, inhibitors of CD203a/ENPP1 (26) could have anti-tumor activity by inhibiting the conversion of extracellular β-NAD$^+$ to ADO and by inhibiting cGAMP degradation and, therefore, the secretion of SASP (senescent-associated secretory phenotype) factors which were found to increase CD38 expression (27, 28). All these findings are schematized in **Figure 1**.

The Direct Role of NAD$^+$

Recently, several reports investigated whether NAD$^+$ might play a direct role in modulating anti-tumor immune response. In particular, extracellular levels of NAD$^+$ are relevant for T cell functions. A study compared the metabolic activity of a hybrid T cell population with characteristics of both Th1 and Th17 cells, referred to as Th1/17 cells, to Th1 and Th17 cells (29). Indeed, Th1/17 cells display a unique metabolic phenotype, with high glutaminolysis and medium levels of glycolysis. The study showed that Th1/17 cells expressed 34 times more intracellular NAD$^+$ levels than Th17 cells, due to glutaminolysis. In addition, NAD$^+$ depletion, obtained through pharmacological inhibition of Nampt using FK866, downregulated IFN-γ/IL-17$^+$ cells in Th1/17 cells. More importantly such cells, adoptively transferred to tumor-bearing mice, failed to control tumor growth unlike untreated cells, thus demonstrating that NAD$^+$ is essential for anti-tumor activity of Th1/17 cells (29). Sirt1, a NAD$^+$-dependent protein deacetylase, is a key factor, being higher in Th1/17 cells than in other subsets. Moreover, cells treated with Sirt1 inhibitors and Sirt-1-KO T cells displayed fewer IL-17$^+$ cells. Accordingly, tyrosinase-reactive hybrid Th1/17 cells differentiated *ex vivo* in the presence of Ex527 (Sirt1 inhibitor) displayed a lower anti-tumor activity than untreated cells in a murine melanoma model. Similar results were obtained using Sirt$^{fl/fl}$CD4^{Cre} mouse splenic T cells retrovirally transduced with TRP-1 TCR and programmed to the hybrid Th1/17 phenotype. These findings confirmed that Sirt1 deacetylase activity is required for Th1/17 cells anti-tumor functions (29). While investigating the target of Sirt1 activity, the researchers found a reduced acetylation status in Th1/17 cells, which is partially

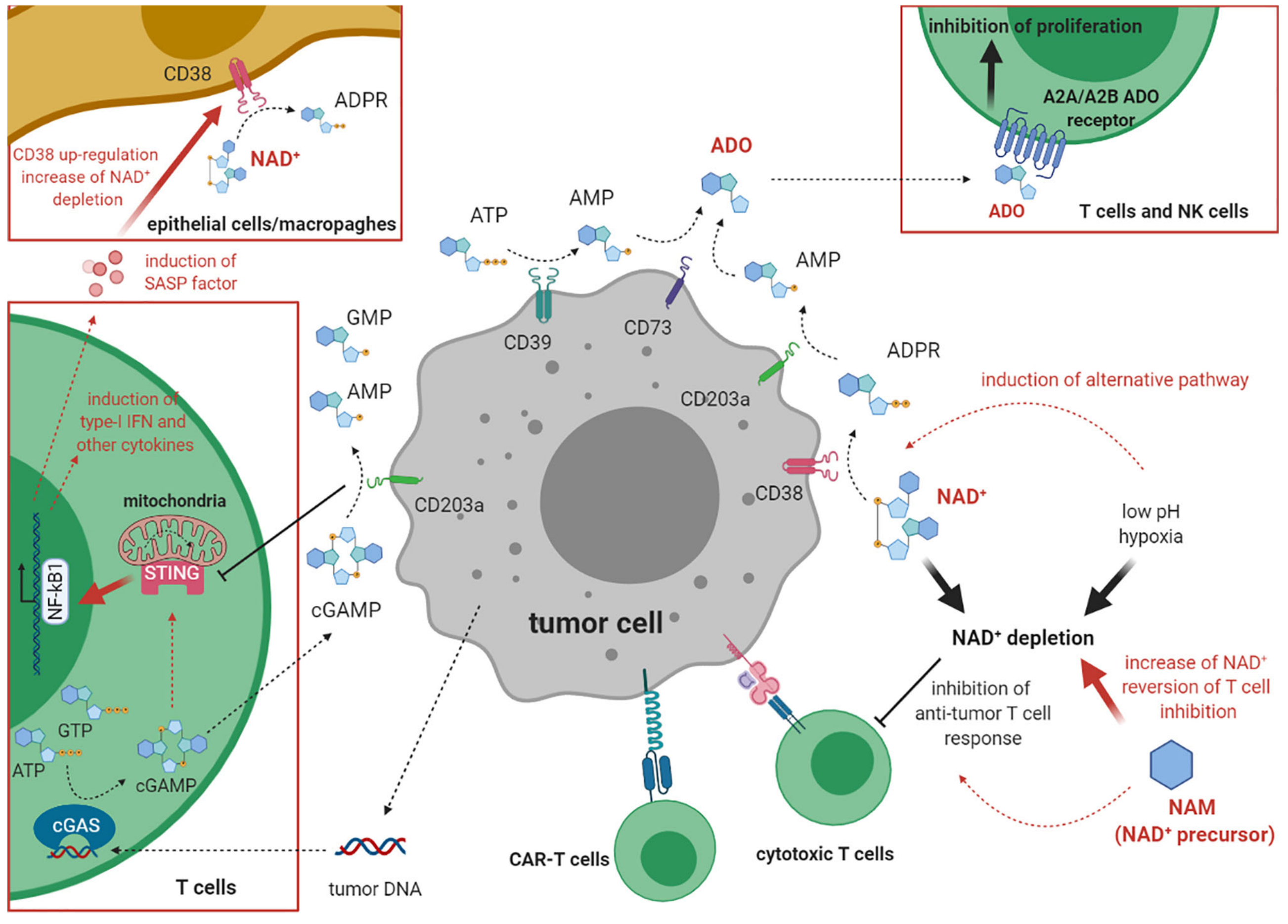

FIGURE 1 | The role of cADP ribose synthase and cGAS/STING pathway in the inhibition of anti-tumor immune response. This cartoon describes the mechanism(s) underlying the inhibition of the immune response against tumor cells by CD38. On one hand, CD38 co-operates with other ectoenzymes (CD203a/ENPP1, CD73, CD39) in the production of the immunosuppressive molecule ADO. On the other hand, CD38 depletes NAD$^+$ from the extracellular environment, especially in conditions with low pH and hypoxia, thus inhibiting tumor cell lysis. cGAS (on the left) metabolizes 2',3'cyclic GMP-AMP (cGAMP) dinucleotide also acting as modulator of the immune system. Hydrolysis of cGAMP by CD203a/ENPP1 attenuates cGAS-STING signaling and the cleavage of NAD$^+$.

reverted when NAD$^+$ levels are decreased using pharmacological inhibitors. In particular, they analyzed *Foxo1*, a transcription factor involved in the responses of memory T cells, which is regulated by phosphorylation and acetylation. *Foxo1* phosphorylation, which correlated with its internalization and degradation, was found to be the highest in Th17 cells, and at medium levels in Th1/Th17 cells. In contrast, *Foxo1* acetylation, which attenuates its function, is reduced in both Th1 and Th1/17 cells. Thus, the transcriptional activity of *Foxo1* is the highest in Th1/17 cells due to phosphorylation/acetylation balance, which leads to higher levels of the *Foxo1* target genes *Klf2* and *Ccr7* in Th1/17 cells than in Th17 and Th1 cells. This implies an increased Th1/17 cells homing to the lung, liver, spleen, and lymph nodes after adoptive transfer. Lastly, pharmacological inhibition of NAD$^+$ and Sirt1 leads to direct inhibition of *Klf2* and *Ccr7*, thus confirming that the NAD$^+$-Sirt1 axis regulates differentiation, migration, effector functions and the anti-tumor response of Th1/17 cells (29).

The role of NAD$^+$ in the metabolic reprogramming of T cells and in T-cell mediated anti-tumor immune response was further demonstrated using CD38^{KO} cells. Such cells lack CD38 NAD-ase activity, and consequently have higher levels of NAD$^+$ and Sirt1 activity. Moreover, they display enhanced expression of the glutaminolysis pathway and of the mitochondrial biogenesis regulator PGC1a, thus confirming a metabolic phenotype similar to that of Th1/17 cells. More importantly, they controlled tumor growth in animal models more efficiently than wild-type cells, with an increased cytokine production within the tumor microenvironment. These observations suggested that CD38 loss, and consequent extracellular NAD$^+$ increase, is the key to implement anti-tumor activity of T cells *in vivo*. This conclusion was reinforced by additional studies were T cells were treated with TGF-β (which mimics tumor immune suppression) and then with anti-CD38 antibody (29). Such cells were lower in CD38 expression and higher in cytokine production and Sirt1 activity than untreated cells. Accordingly, tumor-bearing mice undergoing adoptive transfer of T cells after anti-CD38 treatment had longer survival times and better control of tumor growth than mice treated with anti-CD38 or T cells alone (29).

The role of Sirt2 in the differentiation of effector memory T cells (TEM) was analyzed in breast cancer patients (30). Patients express lower levels of Sirt2 in T lymphocytes than the controls, and patients with high levels of Sirt2 exhibited a higher percentage of TEM than patients with low Sirt2 expression. The percentage of TEM was highest in patients with the worst prognosis, since such cells differentiate from naïve T cells and are mobilized to exert an anti-tumor response. The role of Sirt2 was unambiguously demonstrated in Sirt2$^{-/-}$ mice, where naïve T cells were more abundant than TEM. Sirt2 acted through the GSK-3β deacetylation (30). This study confirmed that Sirt2, a NAD$^+$ dependent deacetylase, is pivotal in the differentiation of naïve T cells to TEM. Thus, high levels of NAD$^+$ in the tumor microenvironment are required for Sirt2 activation and, in turn, for T cell differentiation and for achieving powerful anti-tumor immune response. In contrast, NAD$^+$ depletion, as observed in different human tumors, may lead to immune suppression.

A novel study analyzed the role of NAD$^+$ in the activation of the anti-tumor T cell response (31). Genetic and metabolic analysis of the Jurkat T-ALL cell line allowed the genes involved in T cell activation to be identified. Nampt was proved as a key factor for T cell activation in both analysis, and three compounds known to target Nampt (FK866, STF-118804, and GMX1178) as the most disruptive to T cell activation (31). Accordingly, FK866 was able to inhibit T cell activation, as witnessed by the downregulation of CD69, CD25 and ICOS activation markers, inhibition of calcium flux and phosphorylation of signaling proteins. Interestingly, NAD$^+$ intracellular levels were restored by adding NAD$^+$ to the culture medium, thus suggesting that T cells are able to uptake NAD$^+$ from the environment. This was able to restore T cell activation, confirming that high NAD$^+$ levels are essential for T cell activation (31). Appealing results were obtained by comparing the NAD$^+$ levels of tumor infiltrating lymphocytes (TIL) and peripheral blood lymphocytes (PBL), in samples from ovarian cancer patients and from melanoma preclinical models. NAD$^+$ levels were significantly lower in TIL than in PBL, thus suggesting that the tumor microenvironment induced NAD$^+$ depletion in infiltrating lymphocytes. Accordingly, the authors observed an increased nicotinate and nicotinamide metabolism KEGG pathway in TIL as compared to PBL (31). The salvage NAD$^+$ synthesis pathway represents the principal source of NAD$^+$ in T cells, since *Nampt* knockdown induced a decrease of about 50% of intracellular NAD$^+$ levels (31). Pathways regulated by NAD$^+$ in T cells were also analyzed, revealing that inhibition of NAD$^+$ synthesis by FK866 altered the levels of metabolites belonging to the glutaminolysis, glycolysis and citric acid cycle pathways, thus affecting mitochondrial oxidative phosphorylation, both in Jurkat cells and in PBL. Also here it was confirmed significant decreases in lactate, citric acid, succinic acid and oxoglutaric acid, along with an increase in glucose and glutamine. As a final result, NAD$^+$ deprivation reduced the number of mitochondria and their respiratory capacity, leading to lower ATP levels in T cells (31). Notably, this study analyzed the role of NAD$^+$ in CAR-T cell functions against solid tumors. It was confirmed that NAD$^+$ depletion by FK866 decreased *ex vivo* cytotoxic potential of CD19-41BB CAR T cells, through the downregulation of Granzyme B, IL-2 and IFN-γ secretion. In contrast, increased NAD$^+$ intracellular levels (achieved by Nampt overexpression) enhanced tumor cell killing by CAR T cells (31). In line are the results obtained *in vivo* using mice subcutaneously inoculated with K562-CD19 tumor cells and then treated with CD19-41BB CAR T cells. A cohort of mice underwent intraperitoneal injection of Nam, which increased NAD$^+$ intracellular levels in CAR T cells, about as much as NAD$^+$ itself. This cohort showed an increased number of tumor-free mice, prolonged survival rates and a higher percentage of lymphocytes infiltrating the tumor, as compared to mice treated with CAR T cells alone. A reasonable conclusion is that supplementation with NAD$^+$ precursors may increase tumor killing and CAR T cell therapeutic functions (31). Furthermore, Nam supplementation may increase the success of therapeutic strategies based on the blockade of immune checkpoints (ICB). Mice inoculated with B16F10 and MC38 tumor cell lines were then treated with anti-PD1 and anti-CTLA4, respectively, in the presence (or absence) of Nam supplementation. In both cases, the therapeutic effect of ICB was increased in mice inoculated with Nam, showing limited tumor growth and longer survival. Infiltration of T lymphocytes in the tumor was also increased, thus indicating that Nam was able to activate the anti-tumor T cell response (31). Similar results have been obtained in a mouse model of melanoma (19), where Nam administered alone as a therapeutic agent reduced tumor growth and prolonged the survival of mice. Higher levels of IFN-γ-producing cells were found in the peripheral blood of mice treated with Nam than in untreated mice. In addition, different cytokines/chemokines were modulated in Nam-treated mice (but not in untreated mice), including an increase of IL-5 and Eotaxin and a decrease of IL-10, IL-12, IL-3 and RANTES. Thus, Nam treatment is able to increase IFN-γ secretion, which is pivotal for the anti-tumor immune response, and to modulate the balance of cytokine/chemokine in the periphery (19). These studies confirmed the role of NAD$^+$ in the activation of anti-tumor T cell response and clarified one of the mechanisms underlying T cell inactivation after NAD$^+$ depletion, centered on metabolic reprogramming. More importantly, NAD$^+$ and its precursors have been proposed as an adjuvant therapeutic strategy to improve the clinical outcome of adoptive T cell therapy in patients with solid tumors.

The effects of NAD$^+$ deprivation was analyzed on different T cell subsets and on different types of T cell response (32). Nampt serum levels were higher in transplanted patients with acute severe GvHD than in those with no signs of GvHD. Furthermore, Nampt was predominantly expressed by T lymphocytes in colonic sections of patients, and the same results were observed in mice receiving allogenic BM transplantation. Furthermore, mice receiving allogeneic BMT and treated with FK866 were clinically protected against GvHD, as witnessed by a

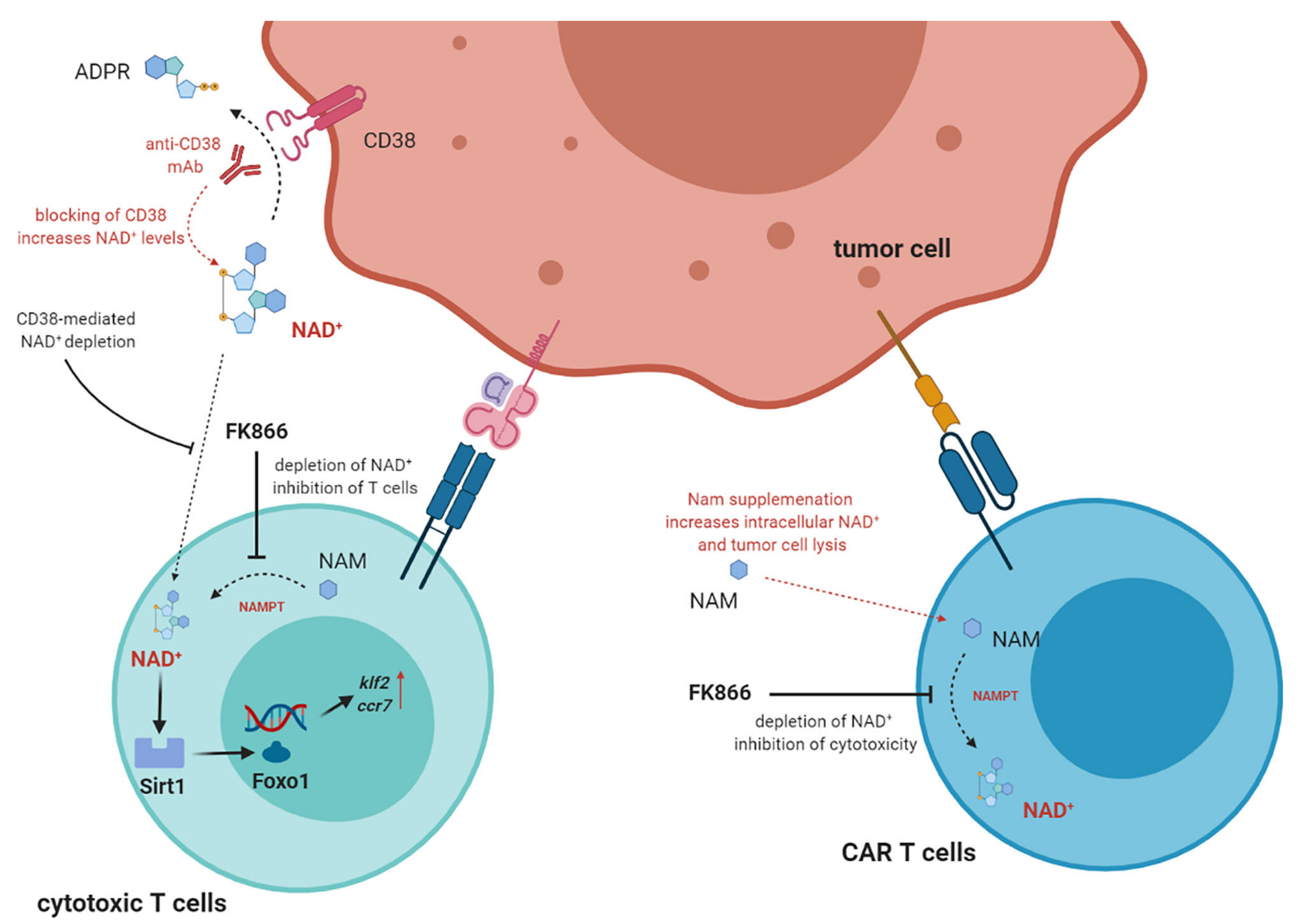

FIGURE 2 | The direct role of NAD$^+$ in T cell function. In T cells NAD$^+$ intracellular levels are increased by NAMPT (nicotinamide phosphoribosyltransferase) which converts NAM to NAD$^+$. High intracellular levels of NAD$^+$ correlated with high activity of Sirt1 deacetyase activity, which in turn activate *Foxo1*and increase the expression of downstream genes *Klf2* and *Ccr7*. These effects correlated to the increase of T cell functions, including tumor cell lysis. NAD$^+$ can be uptake from extracellular space, where it may be depleted by CD38 enzymatic activity. Thus, mAbs targeting CD38 may block NAD$^+$depletion and increase T cell functions. Supplementation of NAM may also augment NAD$^+$ levels, thus increasing tumor cell lysis. On the other hand, NAMPT inhibitors block the conversion of NAM to NAD$^+$, thus inhibiting T cell functions.

decreased weight loss, reduced clinical GvHD scores, normal colon length and reduced histological severity scores in colon and liver (32). Accordingly, mice treated with FK866 showed fewer donor T cells and more Tregs in spleen and liver than untreated mice. Worth noting, memory T cells and other immune cell populations, including monocytes, macrophages, DC and NK cells, were not affected by FK866 treatment. Such treatment induced apoptosis in donor-derived T cells in spleen and liver. In addition, no effects were observed in mice receiving syngenic BMT, thus suggesting that inhibition of Nampt only affects alloreactive T cells (32). Upon TCR stimulation, Nampt mRNA was upregulated in effector cells but not in Tregs: these effects were paralleled by increased intracellular NAD^+ levels. In line with this observation, FK866 treatment reduced viability and downregulated IFN-γ and TNF-α production only in effector T cells, mediated by NAD^+ depletion. In contrast, FK866 significantly up-regulated FoxP3 expression in Tregs, through the inhibition of Sirt1-mediated acetylation, thus increasing their regulatory functions (32). Lastly, the authors setup a graft-versus-leukemia (GvL) experimental model, where mice underwent syngenic or allogenic BMT and then inoculated with leukemia or lymphoma cell lines. Mice receiving syngenic BMT rapidly developed metastatic tumors, and tumor spread was abrogated with FK866 treatment, thus suggesting a direct anti-tumor effect of this molecule. In contrast, mice receiving allogeneic BMT display a limited tumor burden (due to GvL) and a severe GvHD. In these mice, FK866 treatment reduced GvHD and suppressed tumor growth. The study demonstrated that FK866 abrogated tumor cell proliferation by depleting intracellular NAD^+ (32). Thus, NAD^+ is necessary for T cell proliferation and T cell responses. Targeting NAD^+ salvage pathway may be useful for the treatment of GvHD in transplanted patients, since Nampt activity and NAD^+ levels are the highest in allogeneic T cells, without affecting GvL and anti-tumor activity. **Figure 2** describes the role of NAD^+ in anti-tumor T cell responses.

DISCUSSION

This mini review reports on recent evidence highlighting the role of NAD^+ as a key factor in the anti-tumor T cell response. To date, a handful of studies indicate that NAD^+ administration may boost the anti-tumor activity of canonical and engineered T cells in preclinical models of human tumors. NAD^+ depletion brought about by immunosuppressive mechanisms, which involve NAD^+-consuming enzymes, may dampen T cell functions. Based on these findings, it appears that CD38 immunosuppressive activity in human solid and hematological tumors, which hinges upon the production of the inhibitory molecule ADO, might exploit NAD^+ consumption as well. This feature is more relevant in the specific microenvironment of the BM niche in MM, which is characterized by hypoxia and low pH, thus rendering the alternative pathway (which consumes NAD^+) more effective than the canonical one. In conclusion, NAD^+ balance must be taken into account in the treatment of cancer patients, and enzymes involved in NAD^+ synthesis and catabolism may represent novel targets for adjuvant therapies, contributing to the success of adoptive T cell therapies. Indeed, recent studies have addressed the efficacy of CD38 inhibitors (i.e. kuromanin) in preclinical models of CLL (33, 34) in combination with standard therapies. In addition, Nam has been administered in combination with radiotherapy or chemotherapy to patients with different solid tumors, obtaining promising effects (35). Thus, pharmacological interventions aimed at restoring NAD^+ levels may increase the efficacy of standard therapies for patients with solid and hematological tumors. In this line, other NAD^+ precursors, such as NR and NMN, have been recently proposed to revert NAD^+ depletion in multiple organ fibrosis (36) and aging (37), respectively. Finally, five clinical studies using Nam as adjuvant therapy are currently ongoing for cancer patients (www.clinicaltrials.gov).

AUTHOR CONTRIBUTIONS

FMo wrote the manuscript, AH and FMa critically revised the original draft. All authors contributed to the article and approved the submitted version.

FUNDING

This work was supported by Ministero della Salute, Progetti di Ricerca Corrente and "CD38 Project", Fondazione Ricerca Molinette, Torino, Italy.

ACKNOWLEDGMENTS

Figures were created with BioRender.com. We thank the developers for sharing excellent tools. We also thank Laura McLean, Lecturer at the University of Torino, for the excellent English revision of the manuscript.

REFERENCES

1. Belenky P, Bogan KL, Brenner C. NAD+ metabolism in health and disease. *Trends Biochem Sci* (2007) 32(1):12–9. doi: 10.1016/j.tibs.2006.11.006
2. Horenstein AL, Chillemi A, Zaccarello G, Bruzzone S, Quarona V, Zito A, et al. A CD38/CD203a/CD73 ectoenzymatic pathway independent of CD39 drives a novel adenosinergic loop in human T lymphocytes. *Oncoimmunology* (2013) 2(9):e26246. doi: 10.4161/onci.26246
3. Ferretti E, Horenstein AL, Canzonetta C, Costa F, Morandi F. Canonical and non-canonical adenosinergic pathways. *Immunol Lett* (2019) 205:25–30. doi: 10.1016/j.imlet.2018.03.007
4. Konen JM, Fradette JJ, Gibbons DL. The Good, the Bad and the Unknown of CD38 in the Metabolic Microenvironment and Immune Cell Functionality of Solid Tumors. *Cells* (2019) 9(1):52. doi: 10.3390/cells9010052
5. Burgler S. Role of CD38 Expression in Diagnosis and Pathogenesis of Chronic Lymphocytic Leukemia and Its Potential as Therapeutic Target. *Crit Rev Immunol* (2015) 35(5):417–32. doi: 10.1615/CritRevImmunol.v35.i5.50

6. Horenstein AL, Bracci C, Morandi F, Malavasi F. CD38 in Adenosinergic Pathways and Metabolic Re-programming in Human Multiple Myeloma Cells: In-tandem Insights From Basic Science to Therapy. *Front Immunol* (2019) 10:760. doi: 10.3389/fimmu.2019.00760
7. Malavasi F, Deaglio S, Funaro A, Ferrero E, Horenstein AL, Ortolan E, et al. Evolution and function of the ADP ribosyl cyclase/CD38 gene family in physiology and pathology. *Physiol Rev* (2008) 88(3):841–86. doi: 10.1152/physrev.00035.2007
8. Vaisitti T, Audrito V, Serra S, Bologna C, Brusa D, Malavasi F, et al. NAD+-metabolizing ecto-enzymes shape tumor-host interactions: the chronic lymphocytic leukemia model. *FEBS Lett* (2011) 585(11):1514–20. doi: 10.1016/j.febslet.2011.04.036
9. Resta R, Yamashita Y, Thompson LF. Ecto-enzyme and signaling functions of lymphocyte CD73. *Immunol Rev* (1998) 161:95–109. doi: 10.1111/j.1600-065X.1998.tb01574.x
10. Zhou P, Zhi X, Zhou T, Chen S, Li X, Wang L, et al. Overexpression of Ecto-5'-nucleotidase (CD73) promotes T-47D human breast cancer cells invasion and adhesion to extracellular matrix. *Cancer Biol Ther* (2007) 6(3):426–31. doi: 10.4161/cbt.6.3.3762
11. Damle RN, Wasil T, Fais F, Ghiotto F, Valetto A, Allen SL, et al. Ig V Gene Mutation Status and CD38 Expression As Novel Prognostic Indicators in Chronic Lymphocytic Leukemia: Presented in part at the 40th Annual Meeting of The American Society of Hematology, held in Miami Beach, FL, December 4-8, 1998. *Blood* (1999) 94(6):1840–7. doi: 10.1182/blood.V94.6.1840.418k06_1840_1847
12. Ramsay AG, Johnson AJ, Lee AM, Gorgün G, Le Dieu R, Blum W, et al. Chronic lymphocytic leukemia T cells show impaired immunological synapse formation that can be reversed with an immunomodulating drug. *J Clin Invest* (2008) 118(7):2427–37. doi: 10.1172/JCI35017
13. Malavasi F, Deaglio S, Damle R, Cutrona G, Ferrarini M, Chiorazzi N. CD38 and chronic lymphocytic leukemia: a decade later. *Blood* (2011) 118(13):3470–8. doi: 10.1182/blood-2011-06-275610
14. Horenstein AL, Chillemi A, Quarona V, Zito A, Roato I, Morandi F, et al. NAD$^+$-Metabolizing Ectoenzymes in Remodeling Tumor-Host Interactions: The Human Myeloma Model. *Cells* (2015) 4(3):520–37. doi: 10.3390/cells4030520
15. Malavasi F, Faini AC, Morandi F, Castella B, Incarnato D, Oliviero S, et al. Molecular dynamics of targeting CD38 in multiple myeloma. *Br J Haematol* (2021). doi: 10.1111/bjh.17329
16. van de Donk N. Immunomodulatory effects of CD38-targeting antibodies. *Immunol Lett* (2018) 199:16–22. doi: 10.1016/j.imlet.2018.04.005
17. Martin TG, Corzo K, Chiron M, Hvd V, Abbadessa G, Campana F, et al. Therapeutic Opportunities with Pharmacological Inhibition of CD38 with Isatuximab. *Cells* (2019) 8(12):1522. doi: 10.3390/cells8121522
18. Morandi F, Morandi B, Horenstein AL, Chillemi A, Quarona V, Zaccarello G, et al. A non-canonical adenosinergic pathway led by CD38 in human melanoma cells induces suppression of T cell proliferation. *Oncotarget* (2015) 6(28):25602–18. doi: 10.18632/oncotarget.4693
19. Scatozza F, Moschella F, D'Arcangelo D, Rossi S, Tabolacci C, Giampietri C, et al. Nicotinamide inhibits melanoma in vitro and in vivo. *J Exp Clin Cancer Res* 39(1):211. doi: 10.1186/s13046-020-01719-3
20. Malesu R, Martin AJ, Lyons JG, Scolyer RA, Chen AC, McKenzie CA, et al. Nicotinamide for skin cancer chemoprevention: effects of nicotinamide on melanoma in vitro and in vivo. *Photochem Photobiol Sci* (2020) 19(2):171–9. doi: 10.1039/C9PP00388F
21. Kato K, Nishimasu H, Oikawa D, Hirano S, Hirano H, Kasuya G, et al. Structural insights into cGAMP degradation by Ecto-nucleotide pyrophosphatase phosphodiesterase 1. *Nat Commun* (2018) 9(1):4424. doi: 10.1038/s41467-018-06922-7
22. Balka KR, De Nardo D. Molecular and spatial mechanisms governing STING signalling. *FEBS J* (2020). doi: 10.1111/febs.15640
23. Morehouse BR, Govande AA, Millman A, Keszei AFA, Lowey B, Ofir G, et al. STING cyclic dinucleotide sensing originated in bacteria. *Nature* (2020) 586 (7829):429–33. doi: 10.1038/s41586-020-2719-5
24. Onyedibe KI, Wang M, Sintim HO. ENPP1, an Old Enzyme with New Functions, and Small Molecule Inhibitors-A STING in the Tale of ENPP1. *Molecules* (2019) 24(22):4192. doi: 10.3390/molecules24224192
25. Katsyuba E, Romani M, Hofer D, Auwerx J. NAD+ homeostasis in health and disease. *Nat Metab* (2020) 2(1):9–31. doi: 10.1038/s42255-019-0161-5
26. Sharma M, Thode T, Weston A, Kaadige MR. Development of Enpp1 Inhibitors as a Strategy to Activate Stimulator of Interferon Genes (STING) in Cancers and Other Diseases. *Int J Cell Sci Mol Biol* (2018) 5(1). doi: 10.19080/IJCSMB.2018.05.555655
27. Chini C, Hogan KA, Warner GM, Tarragó MG, Peclat TR, Tchkonia T, et al. The NADase CD38 is induced by factors secreted from senescent cells providing a potential link between senescence and age-related cellular NAD (+) decline. *Biochem Biophys Res Commun* (2019) 513(2):486–93. doi: 10.1016/j.bbrc.2019.03.199
28. Covarrubias AJ, Kale A, Perrone R, Lopez-Dominguez JA, Pisco AO, Kasler HG, et al. Senescent cells promote tissue NAD+ decline during ageing via the activation of CD38+ macrophages. *Nat Metab* (2020) 2:1265–83. doi: 10.1038/s42255-020-00305-3
29. Chatterjee S, Daenthanasanmak A, Chakraborty P, Wyatt MW, Dhar P, Selvam SP, et al. CD38-NAD(+)Axis Regulates Immunotherapeutic Anti-Tumor T Cell Response. *Cell Metab* (2018) 27(1):85–100 e8. doi: 10.1016/j.cmet.2017.10.006
30. Jiang C, Liu J, Guo M, Gao X, Wu X, Bai N, et al. The NAD-dependent deacetylase SIRT2 regulates T cell differentiation involved in tumor immune response. *Int J Biol Sci* (2020) 16(15):3075–84. doi: 10.7150/ijbs.49735
31. Wang Y, Wang F, Wang L, Qiu S, Yao Y, Xiong X, et al. Potentiating the anti-tumor response of tumor infiltrated T cells by NAD+ supplementation. *bioRxiv* (2020) 2020.03.21.001123. doi: 10.1101/2020.03.21.001123
32. Gerner RR, Macheiner S, Reider S, Siegmund K, Grabherr F, Mayr L, et al. Targeting NAD immunometabolism limits severe graft-versus-host disease and has potent antileukemic activity. *Leukemia* (2020) 34(7):1885–97. doi: 10.1038/s41375-020-0709-0
33. Manna A, Kellett T, Aulakh S, Lewis-Tuffin LJ, Dutta N, Knutson K, et al. Targeting CD38 is lethal to Breg-like chronic lymphocytic leukemia cells and Tregs, but restores CD8+ T-cell responses. *Blood Adv* (2020) 4(10):2143–57. doi: 10.1182/bloodadvances.2019001091
34. Manna A, Aulakh S, Jani P, Ahmed S, Akhtar S, Coignet M, et al. Targeting CD38 Enhances the Antileukemic Activity of Ibrutinib in Chronic Lymphocytic Leukemia. *Clin Cancer Res Off J Am Assoc Cancer Res* (2019) 25(13):3974–85. doi: 10.1158/1078-0432.CCR-18-3412
35. Nikas IP, Paschou SA, Ryu HS. The Role of Nicotinamide in Cancer Chemoprevention and Therapy. *Biomolecules* (2020) 10(3):477. doi: 10.3390/biom10030477
36. Shi B, Wang W, Korman B, Kai L, Wang Q, Wei J, et al. Targeting CD38-dependent NAD(+) metabolism to mitigate multiple organ fibrosis. *iScience* (2021) 24(1):101902. doi: 10.1016/j.isci.2020.101902
37. Chini CCS, Peclat TR, Warner GM, Kashyap S, Espindola-Netto JM, de Oliveira GC, et al. CD38 ecto-enzyme in immune cells is induced during aging and regulates NAD(+) and NMN levels. *Nat Metab* (2020) 2(11):1284–304. doi: 10.1038/s42255-020-00298-z

Conflict of Interest: The authors declare that the research was conducted in the absence of any commercial or financial relationships that could be construed as a potential conflict of interest.

The reviewer SD declared a shared affiliation with the authors AH and FMa to the handling Editor.

frontiers
in Immunology

ORIGINAL RESEARCH
published: 28 April 2021
doi: 10.3389/fimmu.2021.659790

Three-Dimensional Model of Sub-Plasmalemmal Ca^{2+} Microdomains Evoked by the Interplay Between ORAI1 and $InsP_3$ Receptors

Diana Gil[1], Andreas H. Guse[1] and Geneviève Dupont[2]*

[1] The Ca^{2+} Signalling Group, Department of Biochemistry and Molecular Cell Biology, University Medical Center Hamburg-Eppendorf, Hamburg, Germany, [2] Unit of Theoretical Chronobiology, Faculté des Sciences CP231, Université Libre de Bruxelles (ULB), Brussels, Belgium

Ca^{2+} signaling plays an essential role in T cell activation, which is a key step to start an adaptive immune response. During the transition from a quiescent to a fully activated state, Ca^{2+} microdomains characterized by reduced spatial and temporal extents are observed in the junctions between the plasma membrane (PM) and the endoplasmic reticulum (ER). Such Ca^{2+} responses can also occur in response to T cell adhesion to other cells or extracellular matrix proteins in otherwise unstimulated T cells. These non-TCR/CD3-dependent Ca^{2+} microdomains rely on D-*myo*-inositol 1,4,5-trisphosphate (IP_3) signaling and subsequent store operated Ca^{2+} entry (SOCE) *via* the ORAI/STIM system. The detailed molecular mechanism of adhesion-dependent Ca^{2+} microdomain formation remains to be fully elucidated. We used mathematical modeling to investigate the spatiotemporal characteristics of T cell Ca^{2+} microdomains and their molecular regulators. We developed a reaction-diffusion model using COMSOL Multiphysics to describe the evolution of cytosolic and ER Ca^{2+} concentrations in a three-dimensional ER-PM junction. Equations are based on a previously proposed realistic description of the junction, which is extended to take into account IP_3 receptors (IP_3R) that are located next to the junction. The first model only considered the ORAI channels and the SERCA pumps. Taking into account the existence of preformed clusters of ORAI1 and STIM2, ORAI1 slightly opens in conditions of a full ER. These simulated Ca^{2+} microdomains are too small as compared to those observed in unstimulated T cells. When considering the opening of the IP_3Rs located near the junction, the local depletion of ER Ca^{2+} allows for larger Ca^{2+} fluxes through the ORAI1 channels and hence larger local Ca^{2+} concentrations. Computational results moreover show that Ca^{2+} diffusion in the ER has a major impact on the Ca^{2+} changes in the junction, by affecting the local Ca^{2+} gradients in the sub-PM ER. Besides pointing out the likely involvement of the spontaneous openings of IP_3Rs in the activation of SOCE in conditions of T cell adhesion prior to full activation, the model provides a tool to investigate how Ca^{2+} microdomains extent and interact in response to T cell receptor activation.

Keywords: non-TCR/CD3-dependent microdomains, Calcium Signaling, T-cells, COMSOL, computational model, Store operated calcium entry (SOCE)

Edited by:
Khaled Machaca,
Weill Cornell Medicine-Qatar,
Qatar

Reviewed by:
Alexei Tepikin,
University of Liverpool,
United Kingdom
Ghanim Ullah,
University of South Florida,
United States

***Correspondence:**
Geneviève Dupont
gdupont@ulb.ac.be

Specialty section:
This article was submitted to Cytokines and Soluble Mediators in Immunity, a section of the journal Frontiers in Immunology

Received: *28 January 2021*
Accepted: *06 April 2021*
Published: *28 April 2021*

Citation:
Gil D, Guse AH and Dupont G (2021) Three-Dimensional Model of Sub-Plasmalemmal Ca^{2+} Microdomains Evoked by the Interplay Between ORAI1 and $InsP_3$ Receptors. Front. Immunol. 12:659790. doi: 10.3389/fimmu.2021.659790

INTRODUCTION

T cell stimulation initiates a cascade of intracellular events among which increases of the free cytosolic Ca^{2+} concentration (C_C), having well-defined spatio-temporal characteristics, play a crucial role. In particular, Ca^{2+} controls many processes that are essential for an adaptive immune response such as transcriptional activation, proliferation, differentiation or secretion of cytokines (1). As in most non-excitable cells, the classical model for Ca^{2+} signaling in T cells considers as first step the formation of D-*myo*-inositol 1,4,5-trisphopshate (IP_3) and subsequent activation of IP_3R (2). Another Ca^{2+} mobilizing second messenger, nicotinic acid adenine dinucleotide phosphate (NAADP) has been shown to be also involved through its action on type 1 ryanodine receptor (RYR1) (3, 4). Both IP_3R and RyR1 release Ca^{2+} from the endoplasmic reticulum (ER), which results in a significant decrease of the luminal Ca^{2+} concentration and thereby stimulates capacitative or store operated Ca^{2+} entry (SOCE) (see (5) for review) *via* the ORAI/STIM system. The Ca^{2+} filling state of the ER is indeed detected by Ca^{2+} sensors stromal interaction molecules 1 (STIM1) and 2 (STIM2) located in the ER membrane (6, 7). Upon a decrease in ER Ca^{2+}, Ca^{2+} dissociates from STIMs and STIM molecules aggregate and move to so-called “junctional spaces”. These junctions, also called “puncta”, are regions of the cell where the ER is located in close proximity of the plasma membrane (PM), thereby creating a 10-20 nm gap of cytosol between the two membranes (8). There, STIM molecules can recruit ORAI1 to form active Ca^{2+} channels that allow Ca^{2+} to enter from the extracellular medium into the cytosol (1, 9). The relation between SOCE and the ER Ca^{2+} concentration (C_S) is non-linear and generally described by a decreasing Hill function of C_S, with a K_D for half activation of the order of ~200 μM when it depends on the dissociation of Ca^{2+} from STIM1 and of ~400 μM when it depends on the dissociation of Ca^{2+} from STIM2 (6, 10, 11). Since resting C_S is in the range 400-600 μM depending on the cell type (12), STIM1 is activated only upon conditions of massive ER depletion, while STIM2 has a greater sensitivity to small decreases in C_S.

Global Ca^{2+} signaling is often preceded by local Ca^{2+} signals known as “Ca^{2+} microdomains” that occur as a signaling transition state between quiescence and full activation of cells (13). Interestingly, a role for ORAI/STIM proteins in Ca^{2+} microdomains occurring in the process of immune synapse formation was described (14). High-resolution Ca^{2+} imaging revealed that T cell Ca^{2+} microdomains occur as a signaling transition during the first ~15 s following cell activation by TCR/CD3 and show well-defined spatio-temporal dynamics. Such Ca^{2+} increases appear randomly in time and last for 64 ± 3 ms [computed from the data of (4)]. Ca^{2+} microdomains extent on 0.216 μm^2 ± 0.004 and display an average amplitude of 325 ± 11 nM (3, 4). They are initiated by NAADP signaling acting on RYR1 and strongly depend on ORAI1 and both STIM1 and STIM2.

Similar Ca^{2+} microdomains can moreover occur in the absence of T cell activation *via* TCR/CD3 (non-TCR/CD3-dependent Ca^{2+} microdomains). These small signals are more than four times less frequent than those occurring in the first seconds following stimulation and are shorter [44 ± 4 ms, computed from the data of (4)] but display similar amplitudes (290 ± 12 nM). This amplitude is not affected by the absence RYR1, which indicates that NAADP-evoked Ca^{2+} release is not significantly involved in the creation of non-TCR/CD3-dependent Ca^{2+} microdomains. In contrast to TCR/CD3-dependent Ca^{2+} microdomains, the non-TCR/CD3-dependent microdomains rely on T cell adhesion to other cells or proteins of the extracellular matrix (ECM), integrin evoked IP_3 signaling and subsequent SOCE *via* the ORAI/STIM system (15). In these conditions, pre-formed complexes of ORAI1 and both STIM1 and STIM2 have been obtained by FRET experiments and super-resolution microscopy (4, 15).

Non-TCR/CD3-dependent Ca^{2+} microdomains are the signature of a basal, low-level Ca^{2+} entry in resting T cells. How partial and local depletion in C_S allows Ca^{2+} to enter into the cytosol through preformed assembly of ORAI1 and STIM molecules, cannot be resolved experimentally on the single channel level given that current Ca^{2+} imaging systems are characterized by spatial and temporal resolutions in the range of several hundreds of nanometers and tens of milliseconds, e.g. 368 nm and 20 to 25 ms, respectively (3). Here, we used mathematical modelling to further investigate the molecular origin of non-TCR/CD3-dependent Ca^{2+} microdomains. In particular, we quantitatively explored the relation between the Ca^{2+} concentration in a PM junction and in its adjacent ER upon opening of pre-formed ORAI1/STIM2 channels, under different conditions triggering channel opening and for various spatial geometries of the junction.

Mathematical modeling has been much used in the field of Ca^{2+} signaling to help deciphering its sophisticated spatio-temporal organization and its versatility (16). In particular, small-scale Ca^{2+} events corresponding to the spontaneous, stochastic opening of a few IP_3R have been much investigated theoretically (17–22). Similarly, simulations of Ca^{2+} fluxes in realistic geometries have been very useful to explore the relation between microscopic structures and cellular responses in cardiac cells (23, 24).

How SOCE interferes with Ca^{2+} signaling has mainly been investigated in models that do not take the detailed arrangement of the Ca^{2+} stores and fluxes into account. Using an *ad hoc* dependence of the SOC current on ER Ca^{2+} concentration, Ong et al. (25) showed that the re-localization of STIM1 near ORAI1 channels, and thus the status of SOCE, depends on the Ca^{2+} concentration just beneath the ER membrane. A molecular description of a Ca^{2+}-dependent ORAI1-STIM1 binding was introduced by Liu et al. (26), who fitted their model to reproduce data of SOCE activation in human Jurkat leukemic T cells (10). A theoretical study closely based on experimental observations in airway smooth muscle cells enlightened the primary role played by SOCE in the maintenance of agonist induced Ca^{2+} entry (27). A similar, phenomenological description of SOCE was introduced in an extended model of Ca^{2+} signaling and transcription factor activation in T-lymphocytes (28). In another recent study, Yoast et al. (29) used mathematical modelling to back-up their experimental investigation of the relation between the precise composition of ORAI heteromultimers and global Ca^{2+} signaling that differentially activates NFAT-mediated transcriptional responses.

Other mathematical models have focused on the spatial aspects of SOCE-mediated influx, and more especially on the influence of the geometry of the ER-PM junction on the spatio-temporal characteristics of Ca^{2+} entry. These models describe Ca^{2+} signaling in one PM-ER junction. Unequivocal theoretical considerations allowed establishing the highly local character of the ORAI1-mediated Ca^{2+} profile through ORAI1 in a realistic junction geometry (30). A 3D spatial model was developed by Samanta et al. (31) to investigate the effect of clustering within the ER-PM junction of RBL-1 cells. They concluded that ORAI1 clustering increases both the amplitude and the spatial spread of the Ca^{2+} signal in the junction in response to a massive decrease in ER Ca^{2+}. A more detailed description of the junction, taking into account the sub-PM ER and the activity of the SERCAs in the junction, was later developed by McIvor et al. (32). The model allowed to investigate the microscopic patterning of the Ca^{2+} signal in the junction and the replenishment of the ER after significant depletion, in conditions encountered when cells are treated with massive doses of SERCA inhibitors.

In this study, we adapt the model proposed by McIvor et al. (32) to investigate the molecular origin of the non-TCR/CD3-dependent Ca^{2+} microdomains that have been observed in T cells adhering to poly-L-lysine coated surface (4). After describing the mathematical model, we successively simulate situations with and without IP_3Rs in the sub-PM ER membrane. We found that the local ER depletions created by their spontaneous activity are necessary to account for experimental observations about the average amplitude of Ca^{2+} microdomains in T cells. We also used the model to investigate the impact of Ca^{2+} diffusion in the ER and of the distance between ORAI1 channels and found that only the former factor has a significant impact on the characteristics of the Ca^{2+} signals in the PM-ER junction.

DESCRIPTION OF THE MATHEMATICAL MODEL

Our model is based on the realistic 3-dimensional mathematical description of the junction proposed by McIvor et al. (32). In this study, the authors investigated Ca^{2+} dynamics associated with SOCE in conditions corresponding to a significant depletion of the ER, up to $[Ca^{2+}] = 150$ µM. Here, we used a modified version of this model to investigate the origin of the non-TCR/CD3-dependent Ca^{2+} microdomains described by Diercks et al. (4).

Spatial Geometry

Model geometry is shown in **Figure 1**. It represents a portion of ER surrounded by cytoplasm, with the specificity that the ER and

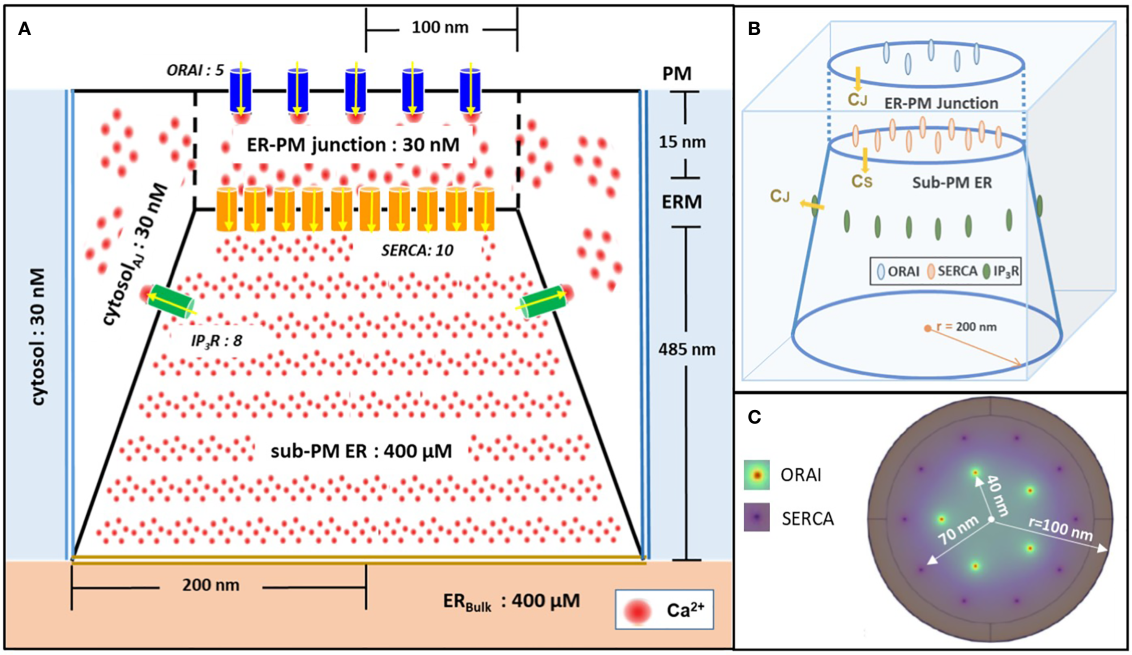

FIGURE 1 | Schematic representation of the model geometry of the ER-PM junction and sub-PM ER used to investigate the origin of the Ca^{2+} microdomains in T cells. **(A)** Frontal diagram showing the dimensions of the cone that represents the sub-PM ER, of the junction and of the portion of the cytosol considered in the simulations. ORAI1 channels are in blue, SERCA pumps in yellow and IP_3Rs in green. Plain lines represent membrane boundaries; dashed lines, fictitious limits between the junction and the cytosol and double lines indicate the limits of the simulated system. The resting Ca^{2+} concentrations considered as initial conditions and boundary conditions in the two compartments are indicated. **(B)** 3D view of the model geometry **(C)** Upper view of the positions of the ORAI1 channels on the PM, in green, and of the ERM, in purple, using COMSOL. Not to scale. This geometry is based on McIvor et al. (32). See text for details.

the PM membranes are very close to one another. The part of the ER that is closest to the PM is called sub-PM ER (25) and is described by a conic domain. The up and bottom faces have diameters of 200 nm and 400 nm, respectively. The depth of the sub-PM is 485 nm (32). The bottom face stands for the sub-PM ER limit, where it coincides with the bulk of the ER (ER_{Bulk}). The sub-PM ER is embedded in a cubic cytosolic domain of 400 nm x 400 nm that includes the ER-PM junction itself, represented as a cylindrical sub-domain of 200 nm in diameter that extends 15 nm from the ER membrane (ERM) up to the PM. The rest of the cube corresponds to the cytosol adjacent to the junction (**Figures 1A, B**). The lateral faces of the cube are in contact with the bulk cytosol of the cell.

We include five ORAI channels on the PM as estimated by Hogan (30) and ten SERCA pumps as proposed by McIvor et al. (32), both placed at the rim of concentric rings with a 40 nm and 70 nm radius, respectively (**Figure 1C**). The corresponding inter-channel distances are thus 47 nm for ORAI1s, as estimated by Samanta et al. (31) and 44 nm for SERCAs. The arrangement of SERCAs as a ring around the ORAI1s in the junction follows the arrangement proposed by Alonso et al. (33). As will be explained in the "Results" section (15), IP_3Rs have to be considered in the simulations to describe junctional Ca^{2+} microdomains in T cells. Thus, a cluster of eight IP_3Rs is included at the boundary between the sub-PM ER and the cytosol. Spatial arrangement of the IP_3Rs is based on the work by Thillaiappan et al. (34), who reported clusters of native immobile 'licensed' IP_3Rs residing alongside the ER-PM junction and facing the PM. The IP_3R inter-channel distance varies from 30 nm up to 200 nm (34–36). We chose 90 nm for symmetry reasons and use the same distance to the ER membrane. Actually, as detailed in the next section, this location simply reflects that IP_3R's colocalize with SOC channels.

Continuous black lines in **Figure 1A** represent membranes and thus correspond to no flux boundary conditions, except across channels and pumps. The black dashed lines represent symbolic boundaries between the ER-PM junction and the cytosol, through which Ca^{2+} actually diffuses freely. Dirichlet boundary conditions corresponding to the initial Ca^{2+} concentrations are imposed at the outer boundaries represented by double bold lines, blue to the cytosol and yellow to ER_{bulk} as in McIvor et al. (32). Thus, we fix the free cytosolic $[Ca^{2+}]$ C_C at 30 nM at the boundaries between the junction and the cytosol. This is in agreement with the brief and local nature of Ca^{2+} microdomains (30). Similarly, because the regulation of SOCE is governed mainly by $[Ca^{2+}]_{ER}$ in close proximity to the junction (25), a constant ER Ca^{2+} concentration equal to 400 μM, corresponding to the Ca^{2+} resting concentration in the bulk of the ER, is imposed at the bottom boundary of the sub-PM ER domain. All parameter values are given in **Table S1**.

Ca^{2+} Dynamics

The model describes the evolutions of Ca^{2+} concentration in the cytosol (C_C) and in the sub-PM ER (C_s). These concentrations obey the diffusion equations

$$\frac{\partial C_C}{\partial t} - D_C \nabla^2 C_C = 0 \ , \tag{1a}$$

$$\frac{\partial C_S}{\partial t} - D_S \nabla^2 C_S = 0 \ , \tag{1b}$$

where D_C and D_S stand for the Ca^{2+} diffusion coefficient in the cytosol and in the ER, respectively. Default values for these coefficients are 220 and 10 $\mu m^2/s$ (32). Ca^{2+} fluxes are taken into account in the boundary conditions that are schematized in **Figure 1**, described in the previous section and detailed in the **Supplementary Information**.

The flux through the ORAI channel is given by Eq. 2, with I_{ORAI} the maximal single channel current, F the Faraday constant, z the charge of a Ca^{2+} ion and A_O the surface of the channel pore:

$$J_{ORAI} = f\left(C_S^{loc}\right) \frac{I_{ORAI}}{F \cdot z \cdot A_o} \tag{2}$$

The function *f*, which takes discrete values between 0 and 1, allows to consider the different opening states of the ORAI1 channel. These states relate to the local concentration of Ca^{2+} around the mouth of the IP_3R (C_S^{loc})

In the model, this concentration was evaluated as the average $[Ca^{2+}]$ in a 108 nm^3 volume surrounding each IP_3R. Each volume is independently sensed by one associated ORAI1 channel. This modelling assumption, through which we explicitly consider SOC channels located in very close proximity of immobile IP_3Rs, is based on considerations described in Thillaiappan et al. (34). Eq. 2 implies that the exact distance between ORAI1's and IP_3R's will not change the outcome of the simulations, as a consequence of the fact that STIM molecules are not modelled explicitly. Function *f* was defined on the basis of the relation between the SOC current and $[Ca^{2+}]_{ER}$ measured by Luik et al. (10) in Jurka T cells, while taking into account that STIM2 has a lower K_D for Ca^{2+} than STIM1. This relation was combined with the results of Li et al. (37) on the graded activation of ORAI1 channels in HEK cells (see **Figure S1** and **Supplementary Information** for a detailed explanation). A similar graded description of the different opening states of ORAI1 depending in that case on the number of STIM1 attached is used in Schmidt et al. (38). Because we investigate conditions of full ER, STIM1 that has a high affinity for Ca^{2+} is not explicitly considered in the present simulations (39).

The flux through the IP_3R is given by Eq. 3, with I_{IP3R} the current through the IP_3R and A_{IP3R} the surface of the channel pore. The second factor allows to scale the current to take the actual gradient across the channel pore into account, where $C_{S,0}$ and $C_{J,0}$ represent resting concentrations of Ca^{2+} in the ER and in the cytosol (40). A unitary IP_3R current of 0.064 pA (41) has been estimated at the baseline concentration difference.

$$J_{IP_3R} = \frac{I_{IP_3R}}{F \cdot z \cdot A_{IP_3R}} \cdot \frac{(C_s - C_C)}{(C_{s,0} - C_{C,0})} \tag{3}$$

The SERCA pumps are considered as bidirectional. We used the same kinetic expression as McIvor et al. (32). As in the latter study, we did not include Ca^{2+} buffering explicitly, given both the short time scales considered and the fact that local Ca^{2+} buffers are near saturation given the high Ca^{2+} concentrations reached around the channel mouths. Values of parameters are taken from McIvor et al. (32) and indicated in **Table S1**. For the processes that were not considered in this previous study, parameter values are discussed in the text and indicated in the figure legends or in the **Supplementary Information**.

To solve the partial differential equations (PDE), we used the finite element method (FEM) and simulation software COMSOL Multiphysics 5.5 (http://www.comsol.com) instead of using Green's functions as it was done in McIvor et al. (32). This choice is based on the considerable extra flexibility and accuracy provided by the software, since it includes a specific physics-controlled domain discretization and solver configuration, which permits geometry modifications or model expansions. The computational capacity of the software also allowed us to rapidly perform a large number of simulations to explore various possible biological situations.

RESULTS

Are ORAI1 Channel Openings Sufficient to Explain Non-TCR/CD3-Dependent Ca^{2+} Microdomains Mechanistically?

Non-TCR/CD3-dependent Ca^{2+} microdomains last for 44 ± 4 ms and reach amplitudes of 290 ± 12 nM (4). Further, such Ca^{2+} microdomains were not decreased in T cells devoid of RYR1 (4). To determine whether ORAI1 channel openings are sufficient to explain non-TCR/CD3-dependent Ca^{2+} microdomains mechanistically, in a first approach, we used our model to predict the amplitude and spatial extent of the changes in junctional $[Ca^{2+}]$ induced by the opening of ORAI1 channels, in the presence of SERCA pumps as schematized in **Figure 1**. IP_3Rs are not considered in these first simulations. The ER is assumed to be full to reproduce the situation of unstimulated T cells in which Ca^{2+} microdomains have been observed. In consequence, ORAI1 channels open at 21% of their full current when attached to Ca^{2+}-unbound STIM2 (**Figure S1**). This situation is assumed to correspond to the spontaneous opening of an ORAI1 channel in the conditions of a full ER, mediated by a pre-formed ORAI1-STIM2 complex from which ER Ca^{2+} spontaneously dissociates due to a random fluctuation. In **Figure 2**, we considered an opening duration of 44 ms, based on the observed lifespan of the microdomains. Opening of one ORAI1 channel leads to a Ca^{2+} increase up to 4 μM at the cytosolic mouth of the channel. Because of the steep Ca^{2+} gradient across the PM, Ca^{2+} increases nearly instantaneously at the channel mouth. When ORAI1 closes, the microdomain disappears as soon as ORAI1 closes, given the small size of the domain respective to the cytosol. The spatial extent around the channel mouth is approx. 40-50 nm in diameter, which much exceeds the dimension of the channel pore, due to diffusion. However, this spatial extent remains significantly below the optical resolution of most current live cell imaging systems, preventing meaningful comparison with experimental data. The amplitude of the average Ca^{2+} increase in the junction is however below the experimentally determined lower limit (**Figures 2C, H**). From these computational results, one can conclude that the experimentally observed microdomains do not correspond to the opening of one ORAI1 channel in the conditions of full ER. If three or more ORAI1 open simultaneously, this creates a Ca^{2+} signal just below the plasma membrane that can be classified as a microdomain, as defined by Diercks et al. (4). For five open channels, the Ca^{2+} signal has an amplitude of 252 nM and a spatial extent of 0.04 μm^2. It is worth noticing that five ORAI1 channels simultaneously open at 21% during 44 ms correspond to the entry of ~300 Ca^{2+} ions in the junction. However, given the small volume of the junction and the high diffusion coefficient of free Ca^{2+} (220 $\mu m^2/s$), the time of residence of an ion in the junction is of the order of 0.045 ms. Because of this small residence time and of the activity of SERCA pumps, average numbers of free Ca^{2+} ions in the microdomain evaluated on the basis of the simulated concentrations thus remain smaller than one.

The Ca^{2+} signals created by the simultaneous opening of five ORAI1 channels are thus not compatible with the average amplitude of 300 nM observed experimentally. This indicates that even in the unlikely situation of a simultaneous opening of the five ORAI1 channels of the junction in conditions of a full ER, the amount of Ca^{2+} entering in the simulated junction is too small to account for experimental observations (Anim. S1). Indeed, SERCA pumps, which may in principle attenuate the Ca^{2+} increase, have a very limited activity in these conditions. The maximal Ca^{2+} concentration at the ER mouth of simulated pumps does not exceed 402 μM. In conclusion, simulations of the Ca^{2+} fluxes in and out the PM-ER junction show that the spontaneous opening of ORAI1 channels in a conductance state that corresponds to a full ER cannot account for the non-TCR/CD3-dependent Ca^{2+} microdomains observed in T cells.

Concerted Activity of IP_3R and ORAI1 Channels Mimics Non-TCR/CD3-Dependent Ca^{2+} Microdomains

Junctional small-scale Ca^{2+} increases thus probably involve an ER-related component. RYRs are not significantly involved in the formation of non-TCR/CD3-dependent microdomains in T cells (4). We thus explored the possible involvement of IP_3Rs. It is indeed well known that in resting cells, some IP_3R can open in the presence of the basal IP_3 concentration to release luminal Ca^{2+} and create short-lived blips or puffs of Ca^{2+} in the cytoplasm (13, 42). Thillaiappan et al. (34) have shown that Ca^{2+} puffs occur nearly exclusively at immobile puncta close to the PM and proposed that these IP_3Rs may provide local ER depletion closest to the PM where SOCE can occur. We thus reasoned that Ca^{2+} microdomains in T cells may be associated with the opening of immobile IP_3Rs located close to the junctions, either spontaneously or due to receptors other than TCR/CD3. Indeed, evidence for integrin evoked IP_3 was obtained

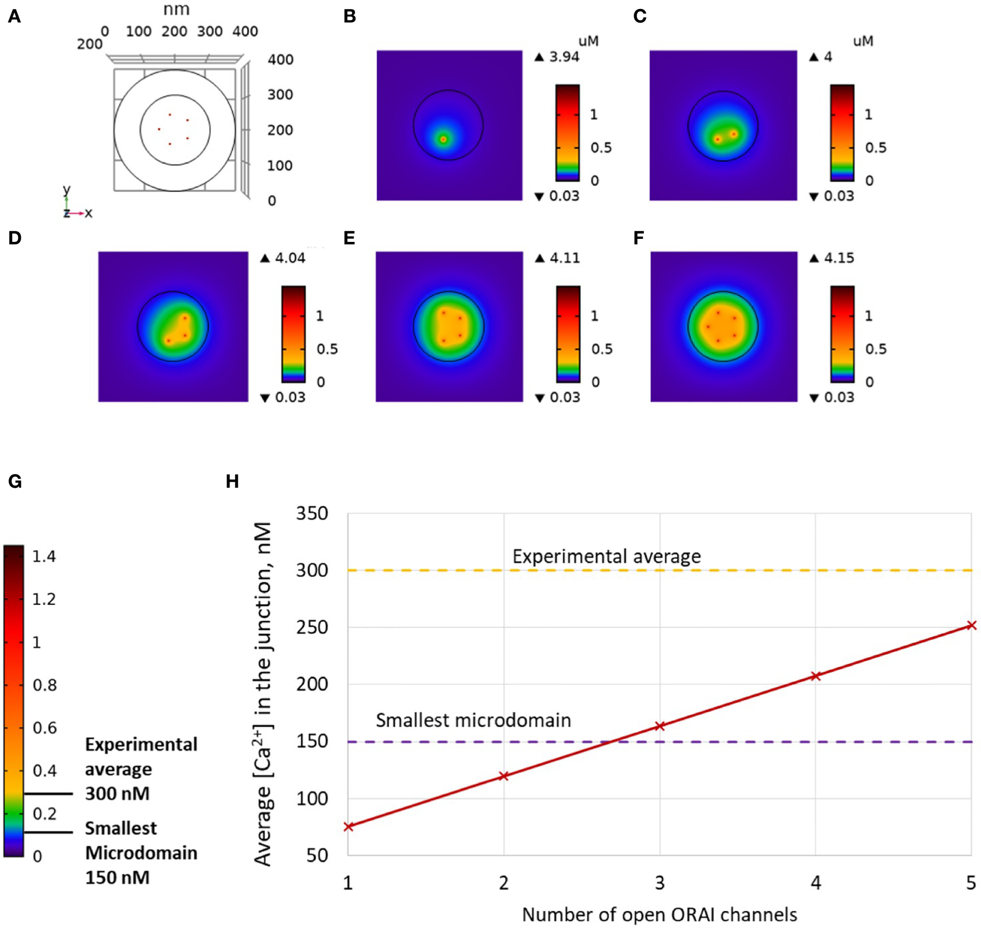

FIGURE 2 | Simulated Ca^{2+} microdomains resulting from the opening of ORAI1 channels under the conditions of a full ER. **(A)** Upper view of the arrangement of the ORAI1 channels on the PM of the junction using COMSOL. **(B–F)** Steady-state Ca^{2+} profiles in the junction when opening 1 **(B)** to 5 **(F)** ORAI1 channels simultaneously. Left bars indicate the color codes, together with the minimal and maximal concentrations reached in the related panels. Shown are the profiles 22ms after opening of the ORAI1s, but these stabilize very rapidly, after a few ms. **(G)** Extended color code with marking of the smallest amplitude experimentally considered to correspond to a microdomain and of the average amplitude of microdomain in unstimulated T cells (4). **(H)** Evolution of the amplitude of the simulated Ca^{2+} microdomains with the number of simultaneously open ORAI1 in the junction, showing that experimentally observed microdomains cannot result from the sole opening of the ORAI1 in conditions of a full ER that only allows for a partial opening of these channels (see text).

recently (15). In this scenario, microdomains would result in part from Ca^{2+} flowing through the IP_3Rs located near the junction and in another part from the ORAI1-mediated Ca^{2+} entry that follows the local, IP_3-induced decrease in ER Ca^{2+}.

We tested this hypothesis computationally by including IP_3Rs in the model, as schematized in **Figure 1**. In **Figure 3** increasing numbers of IP_3Rs are opened during 44 ms, to simulate the stochastic opening of these receptors in the presence of a basal concentration of IP_3. ORAI1 channels then open according to the ER Ca^{2+} concentration around the closest IP_3Rs. In this situation, Ca^{2+} microdomains with realistic amplitudes and invading the whole junction are created when 2 to 5 IP_3Rs are assumed to open simultaneously (Anim. S2a). Clearly, two sources of Ca^{2+} contribute to this Ca^{2+} event: first, Ca^{2+} released by nearby IP_3Rs can diffuse in the junction as discussed below. Second, the local depletion at the luminal extremity of the IP_3R activates ORAI1 opening and Ca^{2+} influx from the extracellular medium. Because in the luminal region surrounding an open IP_3R, ER Ca^{2+} drops to 330 µM, closest ORAI1 channels open half-maximally (**Figure S1**), generating a Ca^{2+} flux through ORAI1 that is more than twice the one occurring in the absence of IP_3R. The combination between the Ca^{2+} fluxes through the IP_3R and ORAI1 allow the formation of a Ca^{2+} microdomain in the junction that agrees with observations in T cells. **Figure 6A** shows that the Ca^{2+} concentration at the cytosolic side of the IP_3R reaches ~16 µM (Anim. S3a, S4a, S5a & S6a). However, IP_3Rs are not in the junction itself and the contribution of ER Ca^{2+} in Ca^{2+} microdomains is rather limited, as attested by simulations that do not consider Ca^{2+} entry (**Figure 4**). The local depletion created by the $InsP_3$-induced Ca^{2+} release however plays a crucial role in allowing ORAI1 to open to a larger extent than with a full ER. As visible in **Figure 3**, when more than 6 IP_3Rs open simultaneously, the Ca^{2+} increase in the domain much exceeds those observed experimentally. This is in agreement with the fact

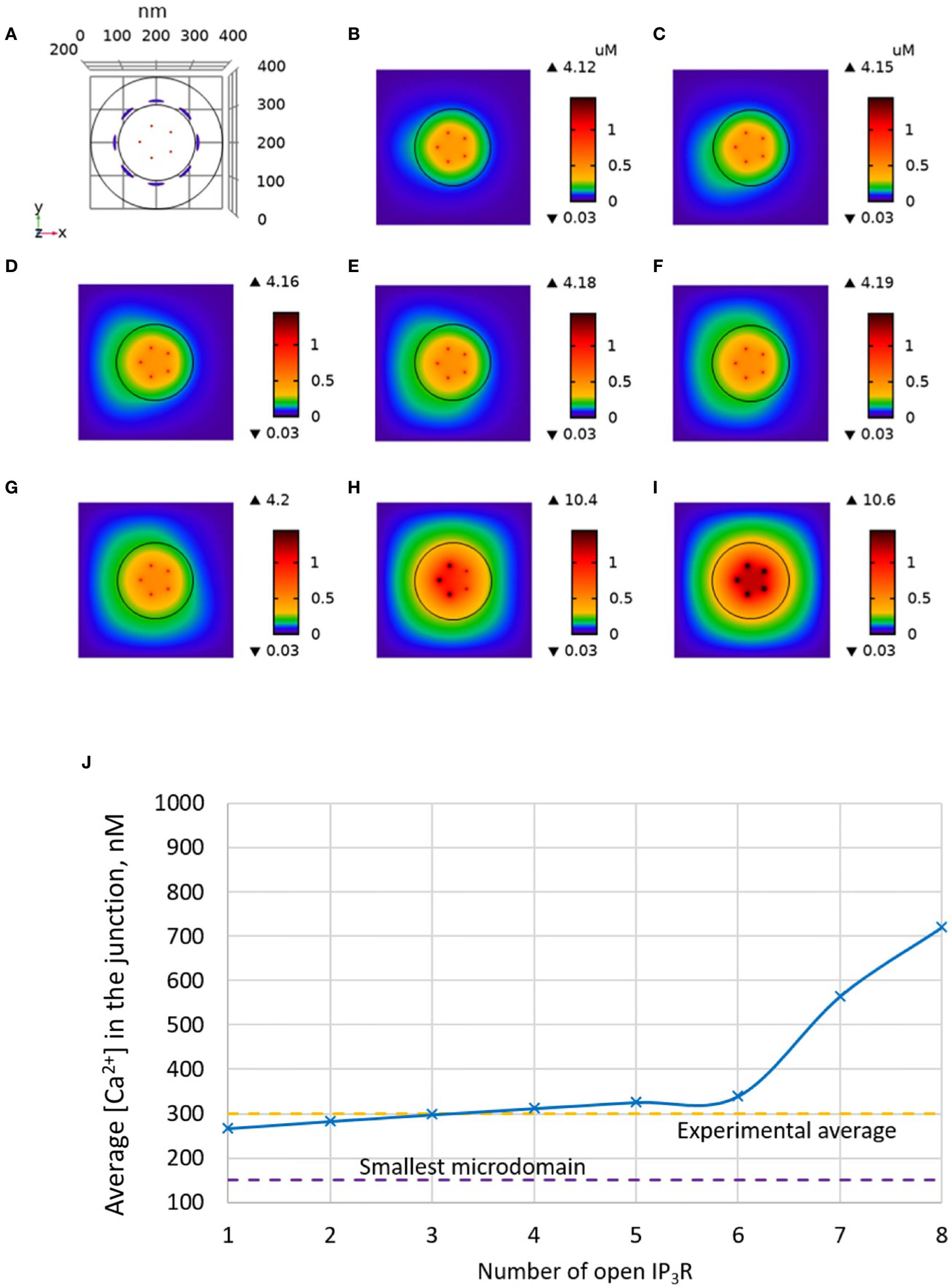

FIGURE 3 | Simulated Ca^{2+} microdomains resulting from the opening of the IP_3Rs adjacent to the junctions, which in turn induces the opening of ORAI1 channels in the junctions as a result of local depletion of ER Ca^{2+}. **(A)** Upper view of the arrangement of the ORAI1 channels on the PM of the junction (red dots) and of the adjacent IP_3Rs (blue lines) using COMSOL. **(B–I)** Steady-state Ca^{2+} profiles in the junction when opening 1 **(B)** to 8 **(I)** IP_3Rs simultaneously. Left bars indicate the color codes, together with the minimal and maximal concentrations reached in the related panel. Shown are the profiles 22ms after opening of the IP_3Rs. Upon depletion of local Ca^{2+} in the ER, which is quasi-instantaneous, ORAI1 channels open to an extent that depends on this local concentration, as defined by the function *f* (see **Supplementary Information**). ORAI1 opening is assumed to occur immediately after depletion because ORAI1-STIM2 aggregates are pre-formed (4). **(J)** Evolution of the amplitude of the simulated Ca^{2+} microdomains with the number of simultaneously open IP_3Rs in the junction, showing that experimentally observed microdomains can in principle result from the opening of ORAI1 channels induced by the spontaneous opening of a few IP_3Rs near the junction, in conditions of a full ER.

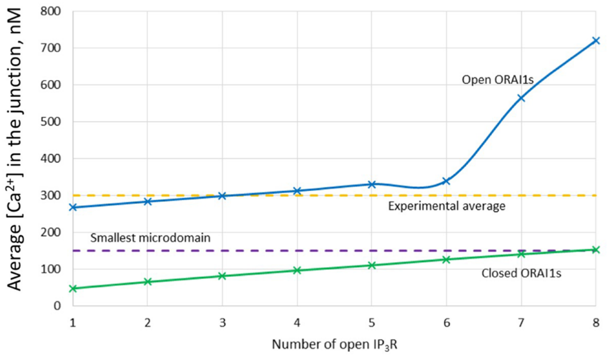

FIGURE 4 | Evolution of the amplitude of the simulated Ca^{2+} microdomains with the number of simultaneously open IP_3Rs in the junction in the presence and in the absence of ORAI1s in the junction. The blue curve (with ORAI1) corresponds to the situation considered in **Figure 3**. The theoretical situation of a junction that does not contain ORAI1 channels (green curve) allows to appreciate that the contribution of Ca^{2+} released through the IP_3Rs to the Ca^{2+} microdomain is rather limited.

that only a fraction of IP_3Rs can spontaneously open at basal IP_3 concentration. Thus, non-TCR/CD3-dependent Ca^{2+} microdomains such as those observed in T cells can be reproduced with the model when considering both the ORAI1 channels located in the junction and the adjacent IP_3Rs.

The Diffusion Coefficient of Ca^{2+} in the ER Dramatically Affects the Amplitude of Non-TCR/CD3-Dependent Ca^{2+} Microdomains

Much uncertainty remains as to the exact value of the diffusion coefficient of Ca^{2+} in the ER (21, 32, 43, 44). We thus took profit of the possibility offered by computational modelling to analyze the effect of changing the value of this key parameter. Increasing D_S from 10 (43, 44) to 110 (21) has a drastic effect on the dynamics of junctional Ca^{2+}. Such a change could be related to a decrease in the buffering capacity of the ER, or to a change in the tortuosity that characterizes this organelle. As seen in **Figure 5**, opening of one IP_3R with a high value of D_S suffices to create an extended microdomain whose amplitude exceeds the experimental average junctional amplitude. Interestingly, simulations show that in this case, ORAI1 channels never open in a more than minimal conductance state because the Ca^{2+} concentration in a region surrounding an open IP_3R does not drop below 360 µM, which is larger than the 330 µM reached in the same volume when D_S=10 $\mu m^2/s$ (Anim. S2b). Changes in the value of the diffusion coefficient much affects the Ca^{2+} profile near the mouth of the channel (**Figure 6A**). When the diffusion coefficient increases, Ca^{2+} is replenished faster. This does not only affect the state of ORAI1, but also the flux through the IP_3R. The concentration difference between the luminal and cytosolic extremities of the channel is indeed larger than in the slow diffusion situation, which increases the Ca^{2+} flux (**Figure 6B**). Such effect is also visible in **Figure 7** where the Ca^{2+} profiles in the presence of ORAI1 channels can be compared for the two values of the diffusion coefficient (Anim. S3b, S4b, S5b & S6b). Simulations thus predict that if Ca^{2+} diffusion inside the ER is fast (D_S = 110 $\mu m^2/s$), non-TCR/CD3-dependent Ca^{2+} microdomains could occur in the absence of extracellular Ca^{2+} or in T cells that do not express ORAI1, which does not agree with experimental observations (4).

ORAI1 Channel Clustering Without Major Effect On Non-TCR/CD3-Dependent Ca^{2+} Microdomains

Another factor that may have an influence on the amplitude of the Ca^{2+} microdomain is the distance between ORAI1 channels in the ER-PM junction. This was investigated in our simulations by decreasing the distance between ORAI1 channels from 47 to 37.7 nm. As shown in **Figure 8**, channel clustering has a very limited effect on the characteristics of the Ca^{2+} microdomains, resulting in a slight increase in the amplitude of the Ca^{2+} signal in the junction. This conclusion does not depend on the value of the diffusion coefficient in the ER (not shown). Actually, clustering of the ORAI1 channels could increase the amplitude of the microdomain if either Ca^{2+} diffusion in the junction or Ca^{2+} pumping was affected by the inter-channel distance. Since Ca^{2+} increases near ORAI1 channels always remain highly localized in both situations, diffusion is not much affected. SERCA pump activity associated with an active microdomain based on clustered or non-clustered ORAI1 channels are shown in **Figure 9**. Steady-state Ca^{2+} fluxes through SERCA pumps when IP_3Rs and ORAI1 channels are open are clearly not much sensitive to the conditions, whatever the value of the Ca^{2+} diffusion coefficient in the ER. Interestingly, pumps are not saturated in contrast to the situation encountered with a highly depleted ER (32).

DISCUSSION

Ca^{2+} signaling is fundamental for activation of T cells, where it largely relies on SOCE. Although SOCE controls physiological functions at the cellular level, it creates highly heterogeneous local Ca^{2+} signals. Given that Ca^{2+} channels, pumps and downstream signaling molecules are controlled locally, cellular Ca^{2+} dynamics results from the detailed regulation of SOCE in an ensemble of compartmentalized microdomains.

In the present modeling study, we have investigated Ca^{2+} dynamics in a confined configuration corresponding to a junctional cytosolic space and the adjacent sub-PM ER, taking into account Ca^{2+} influx through ORAI1 and IP_3R, Ca^{2+} pumping into the ER through SERCA, and diffusion within the cytosolic and ER compartments. Our main aim was to gain insight into the mechanistic origin of the Ca^{2+} microdomains observed in non TCR/CD3 stimulated T cells that have been reported in Diercks et al. (4). These are short-lived (<50 ms), low amplitude (~300 nM) Ca^{2+} increases located just below the PM. Their spatial spread is most probably below the spatial resolution of the optical imaging system, i.e. 368 nm. Importantly, they do not involve Ca^{2+} release through RYR1, but we obtained initial evidence for a signaling pathway evoked by weak cell adhesion to

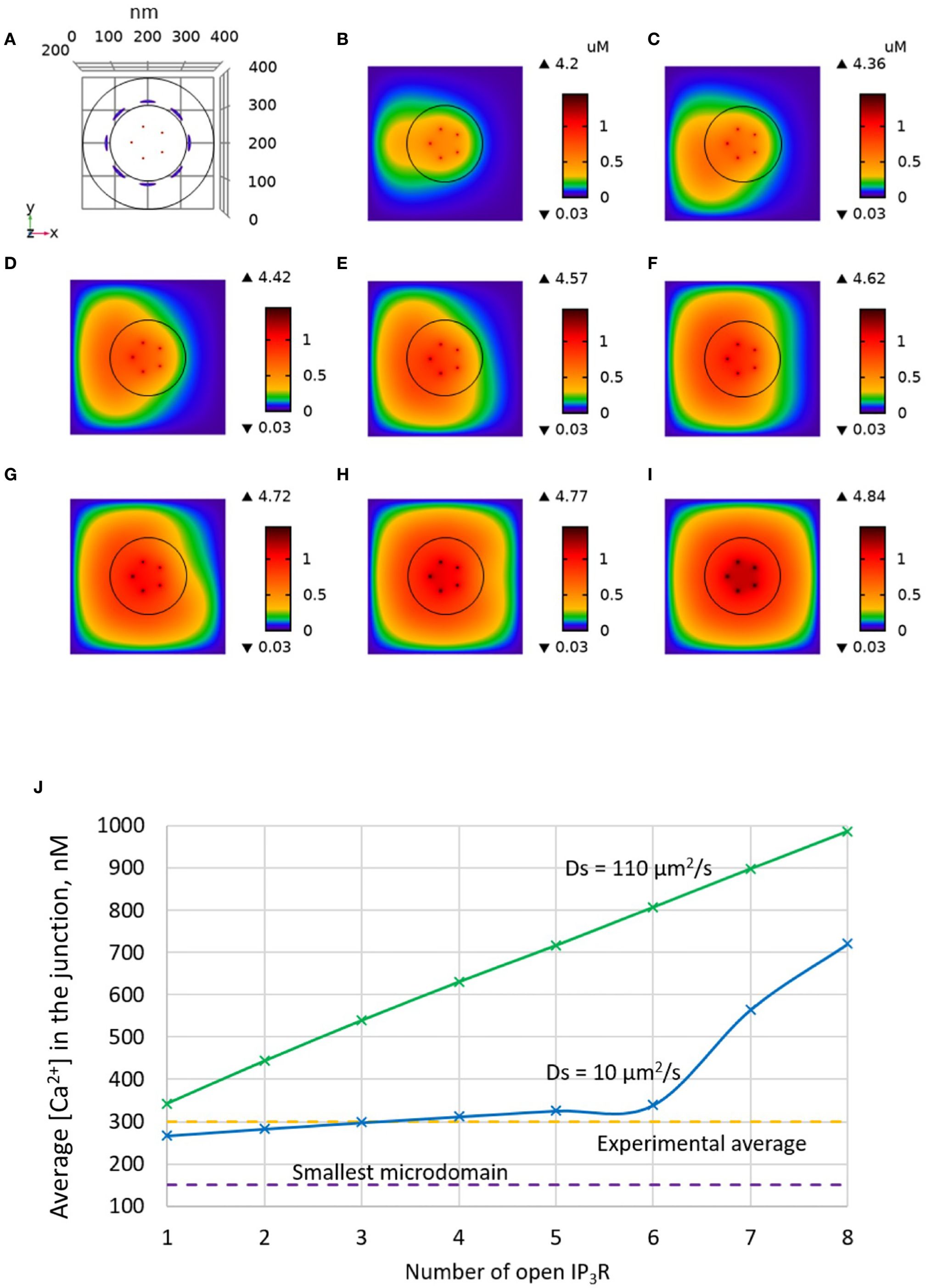

FIGURE 5 | Influence of the value of the Ca^{2+} diffusion coefficient in the ER (D$_S$) on the Ca^{2+} microdomains in the ER-PM junction. **(A)** Upper view of the arrangement of the ORAI1 channels on the PM of the junction (red dots) and of the adjacent IP$_3$Rs (blue lines) using COMSOL. **(B–I)** Steady-state Ca^{2+} profiles in the junction when opening 1 **(B)** to 8 **(I)** IP$_3$Rs simultaneously with D$_S$ = 110 µm^2/s. Left bars indicate the color codes, together with the minimal and maximal concentrations reached in the related panels. Shown are the profiles 22ms after opening of the IP$_3$Rs. Upon depletion of local Ca^{2+} in the ER, which is quasi-instantaneous, ORAI1 channels open to an extent that depends on this local concentration, as defined by the function *f* (see **Supplementary Information**). ORAI1 opening is assumed to occur immediately after depletion because ORAI1-STIM2 aggregates are pre-formed (4). **(J)** Evolution of the amplitude of the simulated Ca^{2+} microdomains with the number of simultaneously open IP$_3$Rs in the junction. Results obtained with the default value for D$_S$ (10 µm^2/s) corresponding to the results shown in **Figure 3** are also indicated for comparison.

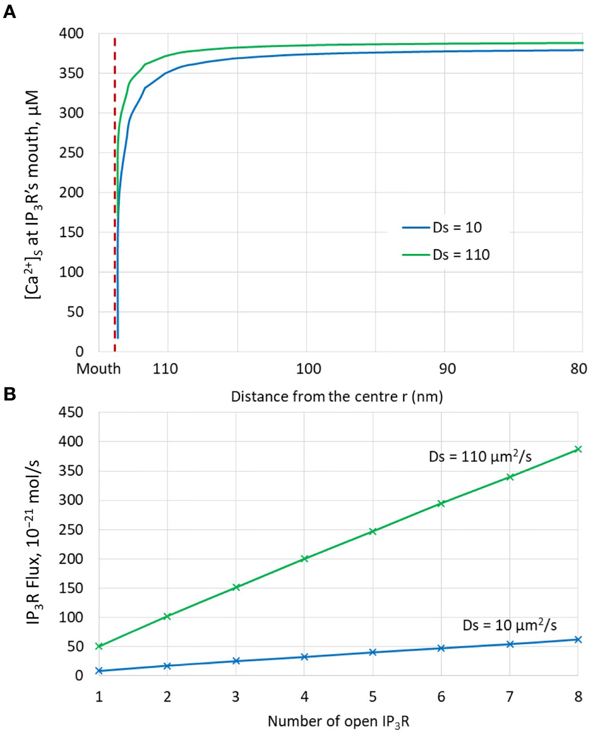

FIGURE 6 | Analysis of the influence of the presence of IP_3Rs and of the value of the Ca^{2+} diffusion coefficient in the ER, D_S. **(A)** Ca^{2+} concentration around the luminal mouth of an IP_3R for the two values of D_S considered in the simulations. The largest this value, the fastest the replenishment around an open channel. **(B)** Fluxes through open IP_3Rs for the two values of D_S considered in the simulations. Because of faster replenishment around an open channel when D_S is larger, the concentration gradient around the two extremities of the channel pore is larger, and hence the flux.

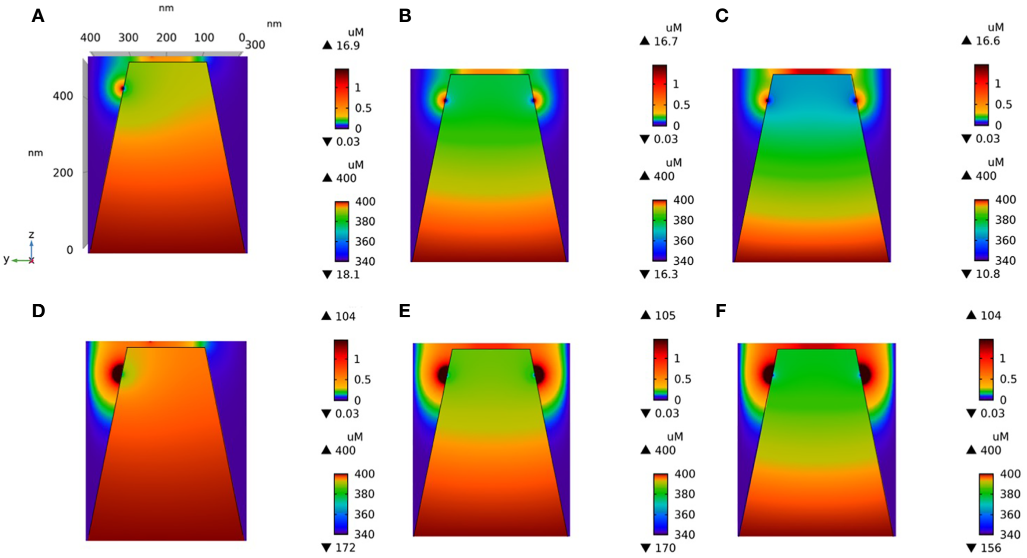

FIGURE 7 | Cross-section of the Ca^{2+} profiles in the junction, in the cytosol adjacent to the junction and in the sub-PM ER during microdomain for two values of the Ca^{2+} diffusion coefficient in the ER, D_S. **(A–C)**: microdomains created by the opening of 2, 5 and 7 IP_3Rs, respectively, for D_S = 10 µm^2/s. Local depletion of ER Ca^{2+} provokes the opening of the nearby ORAI1s. This situation corresponds to the one shown in **Figure 3**. **(D–F)**: microdomains created by the opening of 2, 5 and 7 IP_3Rs, respectively, for D_S = 110 µm^2/s. Local depletion of ER Ca^{2+} provokes the opening of the nearby ORAI1s. This situation corresponds to the one shown in **Figure 5**. For all panels, the upper right bar indicates the color code of Ca^{2+} concentration in the cytosol while the lower right bar indicates the color code of Ca^{2+} concentration in the ER.

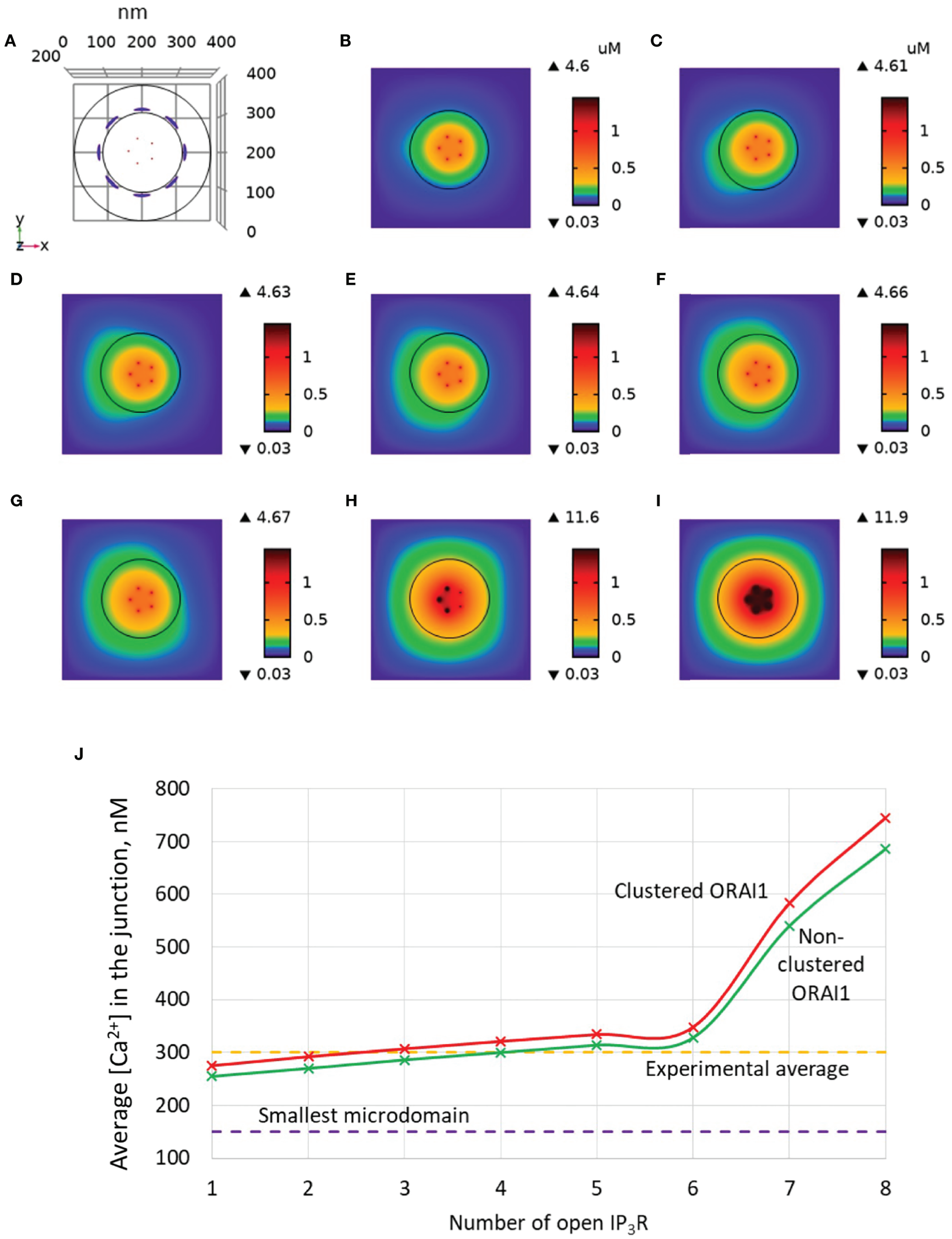

FIGURE 8 | Influence of the distance between ORAI1 channels on the Ca^{2+} microdomains in the ER-PM junction. The situation is similar to the default situation shown in **Figure 3**, except for the distance between ORAI1 channels that is here equal to 37.7 nm (clustered) instead of 47 nm (non-clustered). **(A)** Upper view of the arrangement of the ORAI1 channels on the PM of the junction (red dots) and of the adjacent IP$_3$Rs (blue lines) using COMSOL. **(B–I)** Steady-state Ca^{2+} profiles in the junction when opening 1 **(B)** to 8 **(I)** IP$_3$Rs simultaneously. Left bars indicate the color codes, together with the minimal and maximal concentrations reached in the related panel. Shown are the profiles 22ms after opening of the IP$_3$Rs. Upon depletion of local Ca^{2+} in the ER, which is quasi-instantaneous, ORAI1 channels open to an extent that depends on this local concentration, as defined by the function *f* (see **Supplementary Information**). ORAI1 opening is assumed to occur immediately after depletion because ORAI1-STIM2 aggregates are pre-formed (4). **(J)** Evolution of the amplitude of the simulated Ca^{2+} microdomains with the number of simultaneously open IP$_3$Rs in the junction. Results obtained with the default value of the inter-ORAI1 channels distance (47 nm, non-clustered) corresponding to the results shown in **Figure 3** are also indicated for comparison.

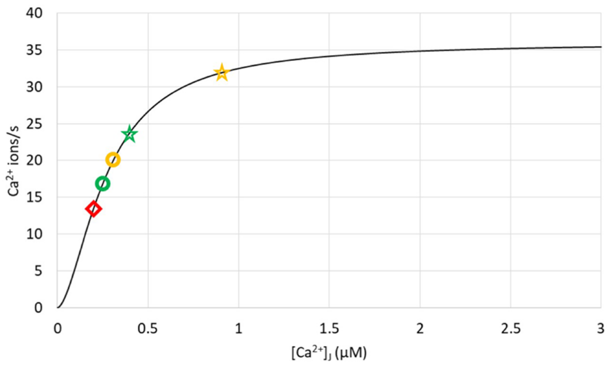

FIGURE 9 | Ca^{2+} fluxes through SERCA pumps in different simulation conditions showing that pumps are not saturated during Ca^{2+} microdomains. The curve represents the rate of pumping as a function of cytosolic Ca^{2+}, as given by Eq. S19, with C_S = 400 µM. Yellow symbols correspond to the opening of the 4 IP_3Rs nearest to the SERCA, with the circle corresponding to D_S = 10 $\mu m^2/s$ and the star to D_S = 110 $\mu m^2/s$. Green symbols correspond to the opening of the 4 IP_3Rs furthest from the SERCA, with the circle corresponding to D_S = 10 $\mu m^2/s$ and the star to D_S = 110 $\mu m^2/s$. The red diamond refers to a situation with closed IP_3Rs, 5 ORAI1 channels of the junction being open as in **Figure 2**.

β1-integrins, IP_3 signaling, and ORAI activation *via* pre-formed complexes with STIM1 and STIM2 (15). Weak adhesion of T cells migrating to inflamed tissue occurs during leukocyte rolling in venules, during diapedesis and migration through basement membrane and interstitium. Thus, such weak adhesion processes during the T cell's journey into the inflamed area may lift the activation status from a non-activated, quiescent cell to a pre-activated T cell. This shift in activation state would then facilitate full activation through the TCR/CD3 complex by local antigen-presenting cells.

For that purpose, we modified several aspects of the spatial model of SOCE previously proposed by McIvor et al. (32). First, we considered the situation of a full ER with C_S = 400 µM, while the former study focused on a massively depleted ER, i.e. C_S = 150 µM. This change affects initial and boundary conditions, but also led us to consider the sub-maximal conductance states of ORAI1 corresponding to not fully STIM-bound ORAI channels (37, 45, 46). We indeed hypothesized that a larger C_S results in a reduced availability of Ca^{2+}-unbound STIM that are susceptible to bind to and open ORAI1. This assumption agrees with the observed relationship between the SOC current and C_S reported at the whole cell level (7, 10). Second, we took into account the presence of IP_3Rs in regions of the ER membrane close to the junctional space, following a spatial arrangement suggested by Thillaiappan et al. (34). As a consequence, we also considered a slightly larger portion of the cell than McIvor et al. (32). From a technical point of view, we resorted to COMSOL Multiphysics, which allowed us extra flexibility and considerably reduced the computing time. This software not only allows to simulate realistic geometries but is also very well adapted to the computational study of Ca^{2+} dynamics in confined domains in which steep concentrations gradients arise, as for example in

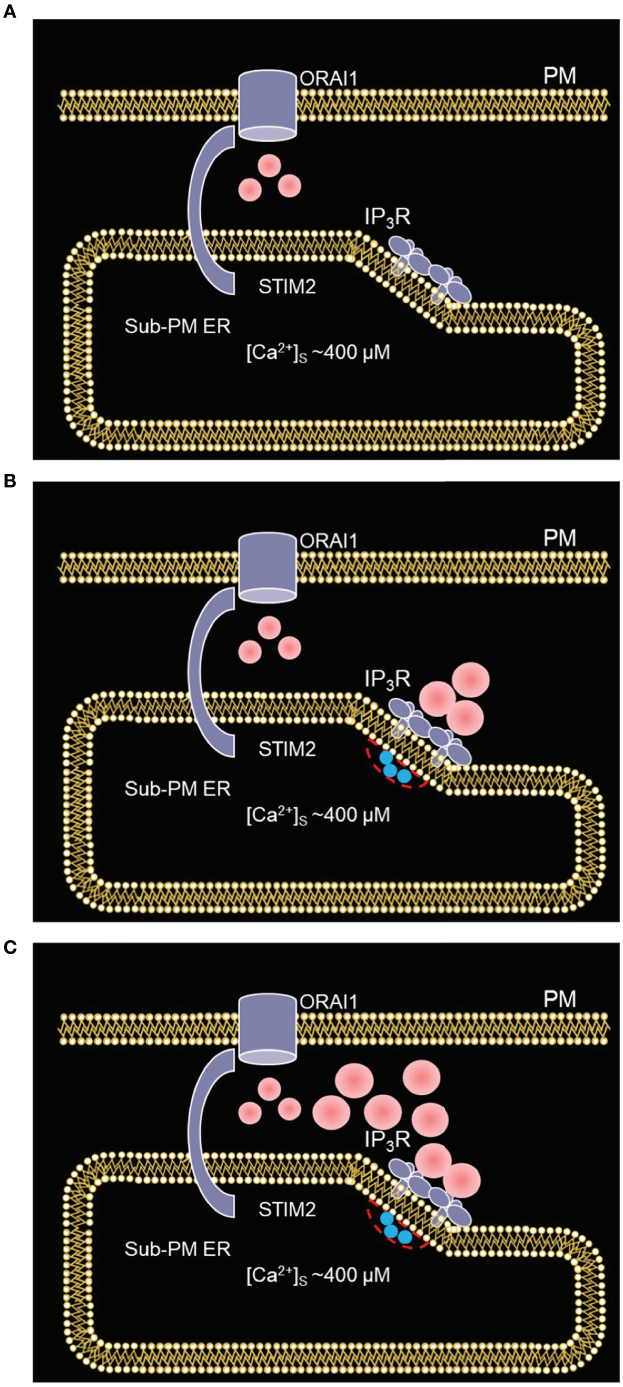

FIGURE 10 | Schematized representation of the proposed mechanism underlying the spontaneous formation of Ca^{2+} microdomains in T cells. **(A)** The smallest microdomains arise from nano-scale $[Ca^{2+}]$ fluctuations in the sub-PM ER leading to the opening of ORAI1 channels STIM2 inherently co-localized with STIM2. **(B)** Following a short, spontaneous activation of one or a few IP_3Rs close to the junction, Ca^{2+} is released from the sub-PM ER into the cytosol. **(C)** The resulting local Ca^{2+} depletion close to the IP_3R's mouth provokes the unbinding of Ca^{2+} from STIM2, which further activates ORAI1 channels. This results in larger Ca^{2+} signals in the microdomains. Red spots represent Ca^{2+} ions.

dendritic spines (47). Additionally, it allows to easily include, remove or spatially rearrange the model's components (like pumps, channels or Ca^{2+} stores) in order to match experimental conditions, as it was done by Maccari et al. (48) to show the role of mitochondria relocation and PMCA pumps accumulation at the immunological synapse in global Ca^{2+} increase during T cell polarization.

Based on our simulations, we concluded that the concerted activity of IP_3R and ORAI1 channels is responsible for non-TCR/CD3 dependent Ca^{2+} microdomains in T cells *via* the mechanism schematized in **Figure 10**, where two different states are described. In a first state (**Figure 10A**), nano-scale $[Ca^{2+}]$ fluctuations in the sub-PM ER (25) are sensed by STIM2 inherently co-localized with ORAI1 (7, 15). The latter ORAI1 channels are then activated shortly and partially (37) and form small microdomains. Although it is likely that these ORAI1-based microdomains correspond to some of the events observed in the absence of TCR/CD3 stimulation, they cannot account on their own for all the events reported since even 5 simulated ORAI1 channels simultaneously open in the junction do not increase $[Ca^{2+}]$ up to a level that corresponds to the experimental average $[Ca^{2+}]$. In a second state (**Figure 10B**), following a short activation of one or a few immobile IP_3Rs close to the junction (34), Ca^{2+} is released through IP_3Rs from the sub-PM ER into the cytosol. The resulting local Ca^{2+} depletion close to the IP_3R's mouth provokes the unbinding of Ca^{2+} from STIM2, which further activates ORAI1 channels (**Figure 10C**) increasing Ca^{2+} in the junction and thus forming larger non-TCR/CD3-dependent Ca^{2+} signals in the microdomains. Although it is important that the IP_3Rs are located close to the junction to create local depletions that can be sensed by SOC channels, simulations suggest that these receptors are not located inside the junction (34). Indeed, if this would be the case, their opening would generate an increase in junctional Ca^{2+} concentration that would much exceed the observed amplitude of a microdomain. Such a computational observation is expected given the respective values of the currents through ORAI1 and IP_3Rs.

We also used the model to investigate the impact of the distance between ORAI1 channels in the junction. In agreement with the results of McIvor et al. (32), we found that ORAI1 clustering has a limited effect on the characteristics of the Ca^{2+} microdomain, both in the presence and in the absence of IP_3Rs. Clustered ORAI1 channels lead to higher local $[Ca^{2+}]$, an effect that is compensated by the reduced extent of the Ca^{2+} increase. In contrast, the value of the Ca^{2+} diffusion coefficient in the ER (D_s) has a drastic effect on the Ca^{2+} microdomain in the junction. Agreement with observations could only be reached when considering $D_s = 10\ \mu m^2/s$, i.e. a value that is ~20 times smaller than the value reported for the cytoplasm. This smaller value could result from molecular crowding in the lumen (43) and from the tortuosity of the tubular network of the ER (49). The latter effect is expected to be particularly strong in the sub-PM regions of the ER adjacent to the junctions.

At this stage, the contribution of IP_3Rs has been included in a simple way. It is well established that the opening of these channels is stochastic and regulated by cytosolic Ca^{2+} (17, 50), two factors that need to be considered in a refined version of the model. In particular, we have shown here that local depletion of C_S following the opening of an IP_3R favors the opening of ORAI1. However, resting STIMs negatively regulate IP_3R's activity (51). Moreover, the entry of Ca^{2+} through ORAI1 could further activate Ca^{2+} release through the IP_3R. These two feed-forward loops are expected to be particularly significant when IP_3 is produced, as it is the case upon the intermediate phase of TCR/CD3 stimulation, e.g. after the initial phase of NAADP/RYR1 signaling in the first 15 s (3, 4, 52).

Next, a quantitative model describing Ca^{2+} microdomains elicited by NAADP/RYR1 signaling, e.g. NAADP/RYR1-dependent increased number of microdomains and transition of Ca^{2+} microdomains into global Ca^{2+} signaling in the first 15 s of directed TCR/CD3 signaling, should be established. Such an extended model including a detailed description of the interplay between SOCE dynamics, NAADP signaling, RYR1s and IP_3Rs should improve our detailed understanding of the first steps of T cell activation.

DATA AVAILABILITY STATEMENT

The original contributions presented in the study are included in the article/**Supplementary Material**. Further inquiries can be directed to the corresponding author.

AUTHOR CONTRIBUTIONS

DG, AG and GD contributed to the conceptualization and design of the study. DG, AG and GD contributed to the development and analysis of the model. DG performed all numerical simulations. All authors contributed to the article and approved the submitted version.

FUNDING

This work was supported by the Deutsche Forschungsgemeinschaft (DFG) (project number 335447717; SFB1328, project A01 to AG), by the Joachim-Herz-Stiftung (Hamburg), Infectophysics Consortium (project 4; to AG), by NCL-Stiftung Hamburg (to AG), the Hamburg Ministry of Science, Research and Equality (LFF- FV75/0070-134, to AG), and by University Medical Center Hamburg-Eppendorf (M3I consortium, to AG). Research in the AG labs is also supported by EU project INTEGRATA - DLV-813284. GD is Research Director at the FNRS.

SUPPLEMENTARY MATERIAL

The Supplementary Material for this article can be found online at: https://www.frontiersin.org/articles/10.3389/fimmu.2021.659790/full#supplementary-material

REFERENCES

1. Trebak M, Kinet JP. Calcium Signalling in T Cells. *Nat Rev Immunol* (2019) 19:154–69. doi: 10.1038/s41577-018-0110-7
2. Streb H, Irvine RF, Berridge MJ, Schulz I. Release of Ca^{2+} From a Nonmitochondrial Intracellular Store in Pancreatic Acinar Cells by Inositol-1,4,5-Trisphosphate. *Nature* (1983) 306:67–9. doi: 10.1038/306067a0
3. Wolf IM, Diercks BP, Gattkowski E, Czarniak F, Kempski J, Werner R, et al. Frontrunners of T Cell Activation: Initial, Localized Ca^{2+} Signals Mediated by NAADP and the Type 1 Ryanodine Receptor. *Sci Signaling* (2015) 8:ra102. doi: 10.1126/scisignal.aab0863
4. Diercks BP, Werner R, Weidemüller P, Czarniak F, Hernandez L, Lehmann C, et al. Orai1, STIM1/2, and RYR1 Shape Subsecond Ca^{2+} Microdomains Upon T Cell Activation. *Sci Signaling* (2018) 11:eaat0358. doi: 10.1126/scisignal.aat0358
5. Putney JW. Capacitative Calcium Entry: From Concept to Molecules. *Immunol Rev* (2009) 231:10–22. doi: 10.1111/j.1600-065X.2009.00810.x
6. Brandman O, Liou J, Park WS, Meyer T. STIM2 is a Feedback Regulator That Stabilizes Basal Cytosolic and Endoplasmic Reticulum Ca2+ Levels. *Cell* (2007) 131:1327–39. doi: 10.1016/j.cell.2007.11.039
7. Subedi KP, Ong HL, Son GY, Liu X, Ambudkar IS. Stim2 Induces Activated Conformation of STIM1 to Control Orai1 Function in ER-PM Junctions. *Cell Rep* (2018) 23:522–34. doi: 10.1016/j.celrep.2018.03.065
8. Wu MM, Buchanan J, Luik RM, Lewis RS. Ca^{2+} Store Depletion Causes STIM1 to Accumulate in ER Regions Closely Associated With the Plasma Membrane. *J Cell Biol* (2006) 174:803–13. doi: 10.1083/jcb.200604014
9. Feske S, Wulff H, Skolnik EY. Ion Channels in Innate and Adaptive Immunity. *Annu Rev Immunol* (2015) 33:291–353. doi: 10.1146/annurev-immunol-032414-112212
10. Luik RM, Wang B, Prakriya M, Wu MM, Lewis RS. Oligomerization of STIM1 Couples ER Calcium Depletion to CRAC Channel Activation. *Nature* (2008) 454:538–42. doi: 10.1038/nature07065
11. Stathopulos PB, Li GY, Plevin MJ, Ames JB, Ikura M. Stored Ca^{2+} Depletion-Induced Oligomerization of Stromal Interaction Molecule 1 (STIM1) Via the EF-SAM Region: An Initiation Mechanism for Capacitive Ca^{2+} Entry. *J Biol Chem* (2006) 281:35855–62. doi: 10.1074/jbc.M608247200
12. Chatton JY, Liu H, Stucki JW. Simultaneous Measurements of Ca^{2+} in the Intracellular Stores and the Cytosol of Hepatocytes During Hormone-Induced Ca^{2+} Oscillations. *FEBS Lett* (1995) 368(1):165–8. doi: 10.1016/0014-5793(95)00632-J
13. Bootman MD, Lipp P, Berridge MJ. The Organisation and Functions of Local Ca^{2+} Signals. *J Cell Sci* (2001) 114:2213–22. doi: 10.1242/jcs.114.12.2213
14. Quintana A, Pasche M, Junker C, Al-Ansary D, Rieger H, Kummerow C, et al. Calcium Microdomains At the Immunological Synapse: How ORAI Channels, Mitochondria and Calcium Pumps Generate Local Calcium Signals for Efficient T-cell Activation. *EMBO J* (2011) 30:3895–912. doi: 10.1038/emboj.2011.289
15. Hernandez L, Gil D, Löhndorf A, Krüger A, Nawrocki M, Huber S, et al. In Preparation.
16. Dupont G, Falcke M, Kirk V, Sneyd J. Models of Calcium Signalling. *Springer* (2016). doi: 10.1007/978-3-319-29647-0
17. Swillens S, Dupont G, Combettes L, Champeil P. From Calcium Blips to Calcium Puffs: Theoretical Analysis of the Requirements for Interchannel Communication. *Proc Natl Acad Sci USA* (1999) 96:13750–5. doi: 10.1073/pnas.96.24.13750
18. DeRemigio H, Groff JR, Smith GD. Calcium Release Site Ultrastructure and the Dynamics of Puffs and Sparks. *Math Med Biol* (2008) 25:65–85. doi: 10.1093/imammb/dqn004
19. Solovey G, Fraiman D, Pando B, Ponce Dawson S. Simplified Model of Cytosolic Ca^{2+} Dynamics in the Presence of One or Several Clusters of Ca^{2+}-release Channels. *Phys Rev E Statistical nonlinear soft matter Phys* (2008) 78:041915. doi: 10.1103/PhysRevE.78.041915
20. Swaminathan D, Ullah G, Jung P. A Simple Sequential-Binding Model for Calcium Puffs. *Chaos* (2009) 19:037109. doi: 10.1063/1.3152227
21. Thul R, Falcke M. Release Currents of IP(3) Receptor Channel Clusters and Concentration Profiles. *Biophys J* (2004) 86:2660–73. doi: 10.1016/S0006-3495(04)74322-2
22. Rückl M, Rüdiger S. Calcium Waves in a Grid of Clustered Channels With Synchronous IP_3 Binding and Unbinding. *Eur Phys J E Soft matter* (2016) 39:108. doi: 10.1140/epje/i2016-16108-4
23. Walker MA, Gurev V, Rice JJ, Greenstein JL, Winslow RL. Estimating the Probabilities of Rare Arrhythmic Events in Multiscale Computational Models of Cardiac Cells and Tissue. *PloS Comput Biol* (2017) 13:e1005783. doi: 10.1371/journal.pcbi.1005783
24. Cosi FG, Giese W, Neubert W, Luther S, Chamakuri N, Parlitz U, et al. Multiscale Modeling of Dyadic Structure-Function Relation in Ventricular Cardiac Myocytes. *Biophys J* (2019) 117:2409–19. doi: 10.1016/j.bpj.2019.09.023
25. Ong HL, Liu X, Tsaneva-Atanasova K, Singh BB, Bandyopadhyay BC, Swaim WD, et al. Relocalization of STIM1 for Activation of Store-Operated Ca^{2+} Entry is Determined by the Depletion of Subplasma Membrane Endoplasmic Reticulum Ca^{2+} Store. *J Biol Chem* (2007) 282:12176–85. doi: 10.1074/jbc.M609435200
26. Liu W, Tang F, Chen J. Designing Dynamical Output Feedback Controllers for Store-Operated Ca^2+ Entry. *Math Biosci* (2010) 228:110–8. doi: 10.1016/j.mbs.2010.08.013
27. Croisier H, Tan X, Perez-Zoghbi JF, Sanderson MJ, Sneyd J, Brook BS. Activation of Store-Operated Calcium Entry in Airway Smooth Muscle Cells: Insight From a Mathematical Model. *PloS One* (2013) 8:e69598. doi: 10.1371/journal.pone.0069598
28. Yang PC, Jafri MS. Ca^{2+} Signaling in T Lymphocytes: The Interplay of the Endoplasmic Reticulum, Mitochondria, Membrane Potential, and CRAC Channels on Transcription Factor Activation. *Heliyon* (2020) 6:e03526. doi: 10.1016/j.heliyon.2020.e03526
29. Yoast RE, Emrich SM, Zhang X, Xin P, Johnson MT, Fike AJ, et al. The Native ORAI Channel Trio Underlies the Diversity of Ca^{2+} Signaling Events. *Nat Commun* (2020) 11:2444. doi: 10.1038/s41467-020-16232-6
30. Hogan PG. The STIM1-ORAI1 Microdomain. *Cell calcium* (2015) 58:357–67. doi: 10.1016/j.ceca.2015.07.001
31. Samanta K, Kar P, Mirams GR, Parekh AB. Ca^{2+} Channel Re-Localization to Plasma-Membrane Microdomains Strengthens Activation of Ca^{2+}-Dependent Nuclear Gene Expression. *Cell Rep* (2015) 12:203–16. doi: 10.1016/j.celrep.2015.06.018
32. McIvor E, Coombes S, Thul R. Three-dimensional Spatio-Temporal Modelling of Store Operated Ca^{2+} Entry: Insights Into ER Refilling and the Spatial Signature of Ca^{2+} Signals. *Cell calcium* (2018) 73:11–24. doi: 10.1016/j.ceca.2018.03.006
33. Alonso MT, Manjarrés IM, García-Sancho J. Privileged Coupling Between Ca^{2+} Entry Through Plasma Membrane Store-Operated Ca^{2+} Channels and the Endoplasmic Reticulum Ca^{2+} Pump. *Mol Cell Endocrinol* (2012) 353:37–44. doi: 10.1016/j.mce.2011.08.021
34. Thillaiappan NB, Chavda AP, Tovey SC, Prole DL, Taylor CW. Ca^{2+} Signals Initiate At Immobile IP_3 Receptors Adjacent to ER-plasma Membrane Junctions. *Nat Commun* (2017) 8:1505. doi: 10.1038/s41467-017-01644-8
35. Diambra L, Marchant JS. Inositol (1,4,5)-Trisphosphate Receptor Microarchitecture Shapes Ca^{2+} Puff Kinetics. *Biophys J* (2011) 100:822–31. doi: 10.1016/j.bpj.2011.01.003
36. Rüdiger S, Nagaiah CH, Warnecke G, Shuai JW. Calcium Domains Around Single and Clustered IP_3 Receptors and Their Modulation by Buffers. *Biophys J* (2010) 99:3–12. doi: 10.1016/j.bpj.2010.02.059
37. Li Z, Liu L, Deng Y, Ji W, Du W, Xu P, et al. Graded Activation of CRAC Channel by Binding of Different Numbers of STIM1 to Orai1 Subunits. *Cell Res* (2011) 21:305–15. doi: 10.1038/cr.2010.131
38. Schmidt B, Alansary D, Bogeski I, Niemeyer BA, Rieger H. Reaction-diffusion Model for STIM-ORAI Interaction: The Role of ROS and Mutations. *J Theor Biol* (2019) 470:64–75. doi: 10.1016/j.jtbi.2019.02.010
39. Emrich S, Yoast R, Xin P, Zhang X, Pathak T, Nwokonko R. Crosstalk Between N-terminal and C-terminal Domains in Stromal Interaction Molecule 2 (STIM2) Determines Enhanced STIM2 Sensitivity. *J Biol Chem* (2019) 294:6318–32. doi: 10.1074/jbc.RA118.006801
40. Mazel T, Raymond R, Raymond-Stintz M, Jett S, Wilson B. Stochastic Modelling of Calcium in 3D Geometry. *Biophys J* (2009) 96:1691–706. doi: 10.1016/j.bpj.2008.10.066
41. Means S, Smith AJ, Shepherd J, Shadid J, Fowler J, Wojcikiewicz RJ, et al. Reaction Diffusion Modeling of Calcium Dynamics With Realistic ER Geometry. *Biophys J* (2006) 91:537–57. doi: 10.1529/biophysj.105.075036

42. Lock JT, Smith IF, Parker I. Spatial-temporal Patterning of Ca^{2+} Signals by the Subcellular Distribution of IP_3 and IP_3 Receptors. *Semin Cell Dev Biol* (2019) 94:3–10. doi: 10.1016/j.semcdb.2019.01.012
43. Dayel MJ, Hom EF, Verkman AS. Diffusion of Green Fluorescent Protein in the Aqueous-Phase Lumen of Endoplasmic Reticulum. *Biophys J* (1999) 76:2843–51. doi: 10.1016/S0006-3495(99)77438-2
44. Swietach P, Spitzer KW, Vaughan-Jones RD. Ca^{2+}-mobility in the Sarcoplasmic Reticulum of Ventricular Myocytes is Low. *Biophys J* (2008) 95:1412–27. doi: 10.1529/biophysj.108.130385
45. Hoover P, Lewis R. Stoechiometric Requirements for Trapping and Gating of Ca^{2+} Release-Activated Ca^{2+} (CRAC) Channels by Stromal Interaction Molecule 1 (STIM1) Proc. *Natl Acad Sci USA* (2011) 108:13299–304. doi: 10.1073/pnas.1101664108
46. Dynes J, Amcheslavsky A, Cahalan M. Genetically Targeted Single-Channel Optical Recording Reveals Multiple Orai1 Gating States and Oscillations in Calcium Influx. *Proc Natl Acad Sci USA* (2016) 113:440–5. doi: 10.1073/pnas.1523410113
47. Cugno A, Bartol TM, Sejnowski TJ, Iyengar R, Rangamani P. Geometric Principles of Second Messenger Dynamics in Dendritic Spines. *Sci Rep* (2019) 9:11676. doi: 10.1038/s41598-019-48028-0
48. Maccari I, Zhao R, Peglow M, Schwarz K, Hornak I, Pasche M, et al. Cytoskeleton Rotation Relocates Mitochondria to the Immunological Synapse and Increases Calcium Signals. *Cell calcium* (2016) 60:309–21. doi: 10.1016/j.ceca.2016.06.007
49. Ölveczky B, Verkman A. Monte Carlo Analysis of Obstructed Diffusion in Three Dimensions: Application to Molecular Diffusion in Organelles. *Biophys J* (1998) 74:2722–30. doi: 10.1016/S0006-3495(98)77978-0
50. Thul R, Thurley K, Falcke M. Toward a Predictive Model of Ca^{2+} Puffs. *Chaos* (2009) 19:037108. doi: 10.1063/1.3183809
51. Emrich S, Yoast R, Xin P, Arige V, Wagner L, Hempel N, et al. Omnitemporal Choreographies of All Five STIM/Orai and IP_3Rs Underlie the Complexity of Mammalian Ca^{2+} Signaling. *Cell Rep* (2021) 34:108760. doi: 10.1016/j.celrep.2021.108760
52. Wolf I, Guse AH. Ca^{2+} Microdomains in T-Lymphocytes. *Front Oncol* (2017) 7:73. doi: 10.3389/fonc.2017.00073

Conflict of Interest: The authors declare that the research was conducted in the absence of any commercial or financial relationships that could be construed as a potential conflict of interest.

frontiers
in Immunology

REVIEW
published: 04 August 2021
doi: 10.3389/fimmu.2021.704779

The Extracellular NADome Modulates Immune Responses

Valentina Audrito†, *Vincenzo Gianluca Messana*, *Lorenzo Brandimarte* and *Silvia Deaglio**

Laboratory of Cancer Immunogenetics, Department of Medical Sciences, University of Turin, Turin, Italy

The term NADome refers to the intricate network of intracellular and extracellular enzymes that regulate the synthesis or degradation of nicotinamide adenine dinucleotide (NAD) and to the receptors that engage it. Traditionally, NAD was linked to intracellular energy production through shuffling electrons between oxidized and reduced forms. However, recent data indicate that NAD, along with its biosynthetic and degrading enzymes, has a life outside of cells, possibly linked to immuno-modulating non-enzymatic activities. Extracellular NAD can engage puriginergic receptors triggering an inflammatory response, similar - to a certain extent – to what described for adenosine triphosphate (ATP). Likewise, NAD biosynthetic and degrading enzymes have been amply reported in the extracellular space, where they possess both enzymatic and non-enzymatic functions. Modulation of these enzymes has been described in several acute and chronic conditions, including obesity, cancer, inflammatory bowel diseases and sepsis. In this review, the role of the extracellular NADome will be discussed, focusing on its proposed role in immunomodulation, together with the different strategies for its targeting and their potential therapeutic impact.

Keywords: nucleotides, NAD, signaling, DAMPs, immune cell regulation, immunometabolism, tumor microenvironment

Edited by:
Björn Rissiek,
University Medical Center
Hamburg-Eppendorf, Germany

Reviewed by:
Friedrich Haag,
University Medical Center
Hamburg-Eppendorf, Germany
Barbara Molon,
University of Padua, Italy

***Correspondence:**
Silvia Deaglio
silvia.deaglio@unito.it

†Present address:
Valentina Audrito,
Department of Molecular
Biotechnology and Health
Sciences, University of Turin,
Turin, Italy

Specialty section:
This article was submitted to
Cytokines and Soluble
Mediators in Immunity,
a section of the journal
Frontiers in Immunology

Received: *03 May 2021*
Accepted: *21 July 2021*
Published: *04 August 2021*

Citation:
Audrito V, Messana VG,
Brandimarte L and Deaglio S (2021)
The Extracellular NADome
Modulates Immune Responses.
Front. Immunol. 12:704779.
doi: 10.3389/fimmu.2021.704779

INTRODUCTION: THE MANY FACES OF NAD, FROM ENERGETIC FACTOR TO DANGER SIGNAL

NAD is an essential intracellular metabolite with key roles in energy metabolism and electron transfer (1–7). In addition, NAD is a cofactor for different families of enzymes, including sirtuins and poly-ADP-ribosyl polymerases (PARPs). NAD can be present outside of cells, with levels fluctuating widely in response to extracellular signals (8–11). A firm observation is that under steady state extracellular (e)NAD levels are thousands of times lower (nM) compared to the intracellular ones (μM-mM) (7, 12–16).

However, during conditions of cellular stress, such as those observed in an inflamed microenvironment, or during hypoxia, or in conditions of shear stress due to physical distortion, plasma membrane damage, stress elicited by cytotoxic agents, NAD concentrations may rapidly spike. This observation, together with the finding that some purinergic receptors are activated by NAD suggested that eNAD serves as a "danger signal" that alerts the immune system to tissue damage (8–10, 12, 17–20). According to this view, eNAD could be considered as damage-associated molecular pattern molecule (DAMP), able to activate the innate immune system, like what has been shown for pathogen-associated molecular patterns (PAMPs) (18, 21–24). For example, released eNAD from active neuronal cells can serve as neurotransmitter and neuromodulator (25–27); or in a mouse model of inflammation, induced by injection of polyacrylamide beads, eNAD reached a concentration of 10mM acting as danger signal (28).

NAD release may occur by several mechanisms involving active exocytosis, or diffusion through transmembrane transporters (e.g., pannexin, connexin) in living cells, or passive leakage across the membrane from necrotic or injured cells (15, 29–32).

Homeostasis is rapidly restored through a scavenging circuit operated by nucleotide-catabolizing enzymes that produce the immunosuppressant adenosine (ADO) and inosine, which can re-enter the cell, reconstituting the nucleotide pool (5, 33–36). All these mechanisms of nucleotide/nucleoside release to alert or switch off the immune system, respectively, are enhanced during acute and chronic inflammation, including cancer (29, 37, 38). Even though very unlikely, eNAD synthesis has not been conclusively ruled out, also in consideration of the presence of several key NAD biosynthetic enzymes (NBEs) (16, 39).

INTRACELLULAR AND EXTRACELLULAR NAD-METABOLIZING MACHINERY

The biosynthesis of NAD takes place in different locations in the cell, through one *de novo* pathway starting from the catabolism of tryptophan, and *via* degradation of vitamin B3 precursors. The latter is considered a salvage pathway that occurs through the metabolism of three precursors [i.e. nicotinic acid (Na), nicotinamide (Nam) and nicotinamide riboside (NR)]. In the majority of tissues, intracellular NAD is generated mostly from Nam, which is the degradation product of all NAD-consuming signaling reactions (6, 40–42). Under normal conditions >70% of the cellular NAD content is stored and is utilized in the mitochondria primarily for metabolic purposes (16, 43). The cytosolic and nuclear NAD pools serve primarily to sustain activity of PARPs and sirtuins, which are NAD-dependent enzymes with key roles in regulating DNA repair and epigenetic controlling of gene transcription, respectively (**Figure 1**) (7, 44, 45). NAD levels can therefore restrict the activity of these two classes of NAD-metabolizing enzymes. Intriguingly, NAD can rapidly shuttle between different cellular

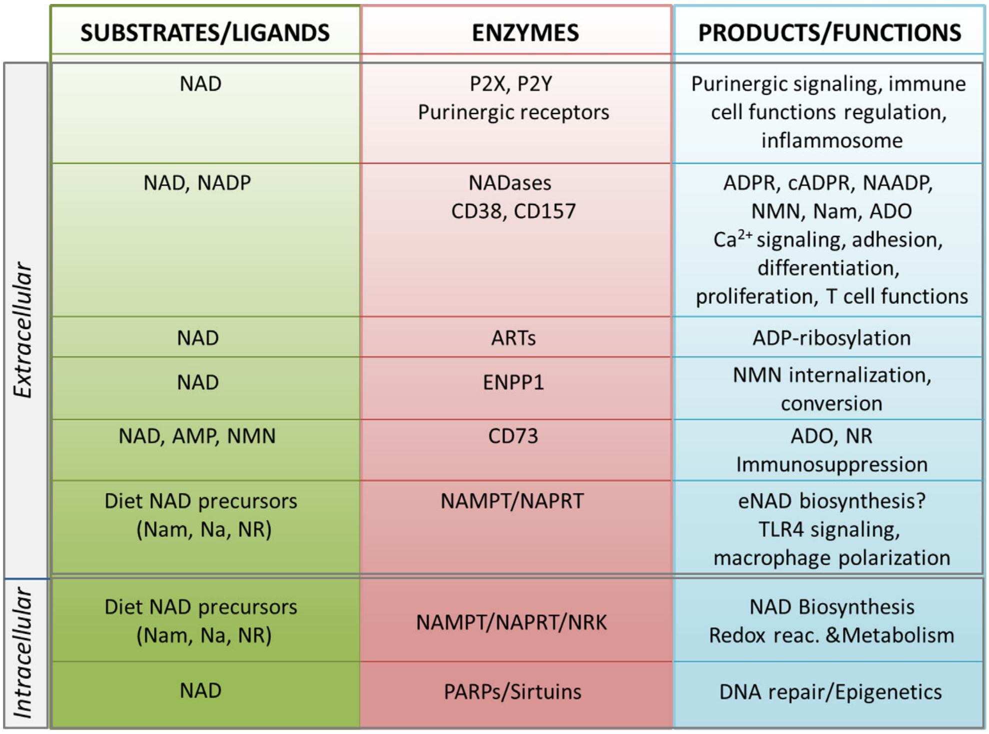

	SUBSTRATES/LIGANDS	ENZYMES	PRODUCTS/FUNCTIONS
Extracellular	NAD	P2X, P2Y Purinergic receptors	Purinergic signaling, immune cell functions regulation, inflammosome
	NAD, NADP	NADases CD38, CD157	ADPR, cADPR, NAADP, NMN, Nam, ADO Ca^{2+} signaling, adhesion, differentiation, proliferation, T cell functions
	NAD	ARTs	ADP-ribosylation
	NAD	ENPP1	NMN internalization, conversion
	NAD, AMP, NMN	CD73	ADO, NR Immunosuppression
	Diet NAD precursors (Nam, Na, NR)	NAMPT/NAPRT	eNAD biosynthesis? TLR4 signaling, macrophage polarization
Intracellular	Diet NAD precursors (Nam, Na, NR)	NAMPT/NAPRT/NRK	NAD Biosynthesis Redox reac. &Metabolism
	NAD	PARPs/Sirtuins	DNA repair/Epigenetics

FIGURE 1 | Schematic representation of the NADome. Schematic representation of the network of substrates/ligands, NAD-metabolizing cell surface and intracellular enzymes and their products in the extracellular and intracellular space. Biological functions regulated by NAD-related enzymes and products are listed. NAD, nicotinamide adenine dinucleotide; NADP, NAD phosphate; eNAD, extracellular NAD; Nam, nicotinamide; NR, nicotinamide riboside; Na, nicotinic acid; NAMPT, nicotinamide phosphoribosyltransferase; NAPRT, nicotinate phosphoribosyltransferase; NRK, nicotinamide riboside kinase; ARTs, mono adenosine diphosphate (ADP)-ribose transferases; PARPs, poly ADP-ribose polymerases; ADPR, ADP ribose; cADPR, cyclic ADP ribose; NAADP, nicotinic acid adenine dinucleotide phosphate; Ca^{2+}, calcium; NMN, nicotinamide mononucleotide; ADO, adenosine; AMP, adenosine monophosphate; ENPP1; ectonucleotide pyrophosphatase/phosphodiesterases; TLR4, toll-like receptor 4.

compartments to reconstitute the pool that allows enzyme activation, as has recently been shown (46). When in the extracellular space, eNAD functions are linked to the modulation of cell surface P2X and P2Y purinergic receptor families, thereby acting in an apparently enzyme-independent way and eliciting pro-inflammatory immune responses (**Figure 1**). In addition, within the extracellular space, a complete network of different ectonucleotidases can rapidly hydrolyze eNAD generating intermediates that modulate signaling, cell metabolism, adhesion, migration and activate immunoregulatory circuits (14, 39, 47), as summarized in **Figure 1**. eNAD is degraded by different classes of ectoenzymes: the NADases CD38 and CD157 (48–50), the ADP-ribosyltransferases (ARTs) (51), the Ectonucleotide Pyrophosphatase/Phosphodiesterase 1 (ENPP1) and the ecto-5′-nucleotidase CD73 (34, 52, 53). NADase, ENPP1 and CD73 can lead to the formation of ADO, a potent natural immunosuppressive factor mediating the activation of the inhibitory P1 purinergic receptors (34, 54, 55). In addition, eNAD can be cleaved to nicotinamide mononucleotide (NMN) and subsequently dephosphorylated to NR by CD38 and CD73 (53, 56, 57). All these intermediates can enter the cell as NAD precursors and can be used by NBEs, reconstituting the intracellular pool (57, 58) (**Figure 1**).

In the next sections of this review, we will summarize the role of eNAD, its derived-metabolites and a set of NAD-dependent enzymes, giving examples of their role in the regulation of specific immune responses.

eNAD AND PURINERGIC RECEPTORS

The idea of purinergic signaling, i.e., of nucleotides acting as extracellular signaling molecules, was initially put forward by the seminal work of Geoff Burnstock in 1972 (59, 60).

Since then, this complex network of receptors has progressively been unveiled to reveal seven evolutionarily conserved subtypes of the P2X ion channel receptors and eight subtypes of the P2Y G protein-coupled receptor, all with roles in immune cell activation (5, 24, 61). On the contrary, four subtypes of the ADO P1 receptors on effector T cells have immunosuppressive effects. Shifting the balance from pro-inflammatory P2R signaling to anti-inflammatory P1R signaling or vice versa, the purinergic signaling system fine-tunes immune cell functions (5). eNAD can bind different subtypes of purinergic P2 receptors as summarized in **Figure 2**.

For example, eNAD activates human granulocytes by binding P2Y11 and triggering: (i) overproduction of cyclic (c)AMP, (ii) activation of protein kinase A, (iii) stimulation of ADP-ribosyl cyclase and overproduction of cyclic ADP-ribose (cADPR), a universal calcium (Ca^{2+}) mobilizer, and (iv) influx of extracellular Ca^{2+}, ultimately causing increased proliferation and migration (62). eNAD can bind P2Y1 and P2Y11 in human monocytes activated with lipopolysaccharide (LPS), triggering a transient rise in intracellular Ca^{2+}, which is caused by a release of Ca^{2+} from IP (3)-responsive intracellular stores and an influx of extracellular Ca^{2+} (63). eNAD has also been identified as an agonist at P2Y1 receptors in human embryonic kidney (HEK) cells and mouse colonic muscle (27, 64). Moreover, binding to postsynaptic P2Y1 receptors, like ATP, eNAD also acts as a neurotransmitter, released by stimulated terminals of mammalian central nervous system and peripheral nervous system neurons (65). In addition, it has been shown that purinoceptors, including P2X1, P2X4, and P2X7, are engaged in eNAD-mediated signaling (27, 63, 66). However, more experimental data should be published to confirm this direct binding of NAD *per se*.

eNAD may also engage P2X7R receptors, the main eATP receptor, extensively studied in the context of inflammation and immunity (24). P2X7R signaling is a major regulator of the intensity and duration of inflammatory responses (24, 67, 68). The receptor/channel is prominently expressed on all cells of innate and adaptive immunity and aberrant signaling has been linked to diverse inflammatory and autoimmune diseases, as recently reviewed in (5, 24). P2X7R signaling mediates NLR family pyrin domain containing 3 (NLRP3) inflammasome activation, cytokine, and chemokine release [i.e., interleukin (IL)-1β, tumor necrosis factor (TNF), IL-6, monocyte chemoattractant protein-1 (MCP-1/CCL2)], T lymphocyte survival and differentiation, transcription factor activation, and cell death (24, 69, 70). At inflammatory sites, P2X7R could also be bound directly by alternative ligands, including eNAD that accumulates at sites of inflammation and tissue damage (28). In murine T lymphocytes, eNAD serves as an ADP-ribose donor to ADP-ribosylate the P2X7R at arginine 125, close to the ATP-binding pocket (71). This reaction, catalyzed by the plasma membrane enzyme ART2.2, causes long-lasting activation of mouse P2X7R, negatively affecting T-regulatory (Treg) and natural killer T (NKT) cell survival and arguing in favor of a direct role of eNAD in the pathophysiological mechanism of P2X7R activation. The reduction of Treg function *via* NAD-induced gating of P2X7 can be employed *in vivo* as a strategy to promote the antitumor response of effector T cells. Systemic injection of NAD results in the selective depletion of Tregs *via* NAD-mediated activation of P2X7, which enhances anticancer immune responses in several mouse tumor models (20, 72). While highly interesting and potentially relevant for human immune responses, this mechanism of P2X7R activation *via* eNAD is demonstrated only in mouse models: additional research is needed to determine whether it is relevant for human immune responses too.

eNAD DEGRADATION-SIGNALING SYSTEM IN REGULATING IMMUNE RESPONSES

One of the reasons why eNAD levels are generally low is that there are several extracellular enzymes that rapidly transform it, guaranteeing recycling of a high energy molecule through the generation of products that can be easily up-taken by cells. The intermediates, however, have a life of their own as signaling molecules, thereby modulating activity of immune cells.

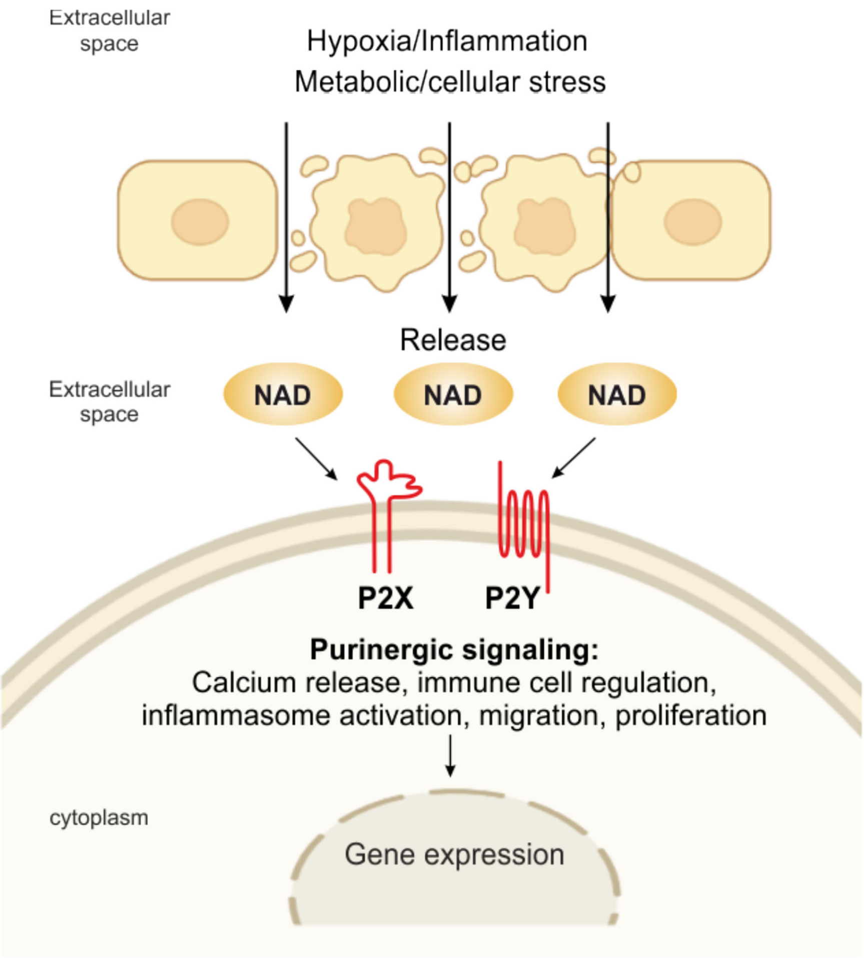

FIGURE 2 | eNAD and purinergic signaling. Pathological or physiological stimuli, including hypoxic and inflammatory conditions, metabolic and cellular stress, promote the release of NAD from the cell. NAD can then bind to P2X (isoforms P2X1, P2X4, P2X7) and P2Y (isoforms P2Y1, P2Y11), activating several intracellular signaling and modulating immune responses.

The best-known NAD-degrading/signaling systems rely on the activity of CD38, an immunomodulatory enzyme (**Figure 3**).

Human CD38, the main member of the NADase/ADPR cyclase family that includes also CD157/*BST-1*, is a surface glycoprotein characterized by a relatively large extracellular domain that contains the catalytic site, a single transmembrane pass, and a short cytoplasmic tail (73, 74). CD38 is a multifunctional ectoenzyme, involved in the catabolism and degradation of eNAD (under normal pH) and NAD phosphate (NADP, under acidic pH), producing ADP ribose (ADPR) together with signaling metabolites involved in intracellular Ca^{2+} mobilization. The main catalytic activity is the NAD glycohydrolase that generates Nam and ADPR. CD38 can also act as NAD cyclase, producing cADPR, which is then hydrolyzed to ADPR. Lastly, in the presence of NADP and Na, under acidic pH levels, CD38 can generate nicotinic acid adenine dinucleotide phosphate (NAADP) (49). The finding of an extracellular enzymatic activity of CD38 leading to the generation of messengers that enter cells to induce intracellular Ca^{2+} fluxes remains an unsolved "topological paradox" (49, 75). More recent data have enriched the picture by showing that CD38 can also be found in the nucleus and mitochondrial membrane and that a soluble form of CD38 is most likely present in the cytoplasm, leading to the hypothesis of a compartmentalized generation of NAD-derived signaling metabolites (49, 76–78). ADPR, cADPR and NAADP share the ability to mobilize Ca^{2+} ions from intracellular stores: cADPR binds to ryanodine receptors (RyR) expressed on the endoplasmic reticulum, ADPR binds to membrane melastatin related transient receptor potential cation channels TRPM2 (49, 79) and NAADP binds to receptors expressed by acidic organelles, such as lysosomes, suggesting a role as Ca^{2+} messenger in the endocytic pathway (80). It is therefore likely that during an immune response, NAD, released outside of cells due to local conditions of inflammation and cellular damage is converted into Ca^{2+}-active metabolites through the action of CD38 expressed by activated lymphocytes,

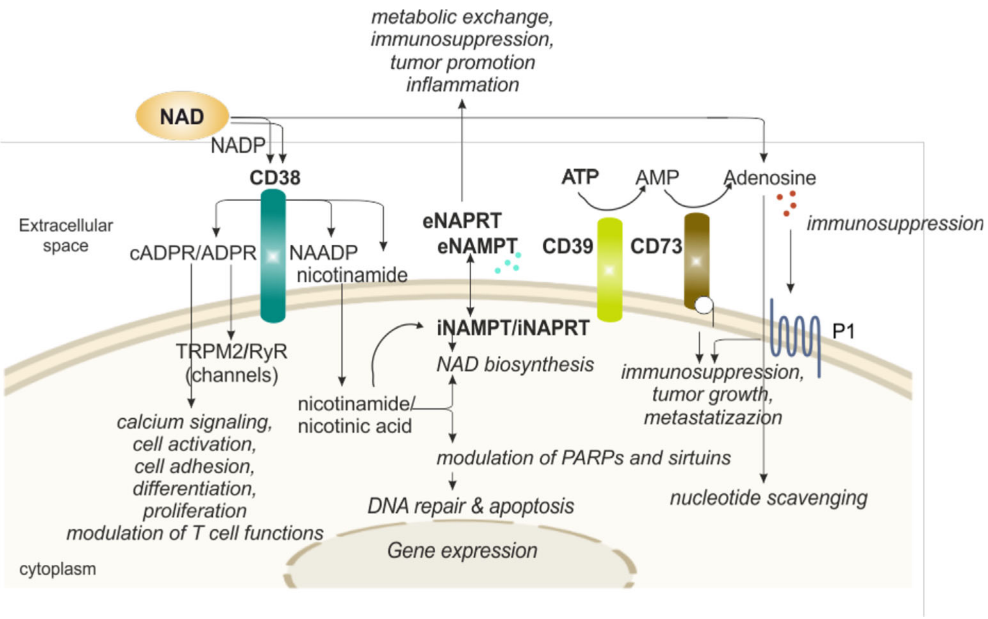

FIGURE 3 | eNAD and enzymatic/functional extracellular machinery in regulating immune responses. Extracellular NAD can also be metabolized by a series of enzymes of the cell surface that are involved in scavenging of nucleotides. The end product of the reaction, adenosine, can then be internalized and reconverted to related nucleosides (e.g., ATP or NAD). In particular, CD38 hydrolyzes NAD to generate intermediates (cADPR and ADPR), potent intracellular Ca^{2+}-mobilizing agents, through binding RyR or TRPM2 receptors. CD38 activation induces migration, proliferation, and modulation of immune responses, specifically T cell functions, as detailed in the text. In addition, CD38 activity releases nicotinamide (the main NAD precursor) that can be internalized into the cell and, together with a second precursor nicotinic acid, converted in NAD by NAMPT and NAPRT activities, respectively, increasing intracellular NAD levels and affecting sirtuins and PARPs (NAD-consuming enzymes) functions. NAMPT and NAPRT can be secreted/released in the extracellular space acting as cytokine-like proteins. Finally, NAD and ATP can be converted in adenosine. ATP is metabolized by CD39 to AMP that is further hydrolyzed by ecto-5'-nucleotidase/CD73 which promotes the formation of adenosine. Adenosine then activates adenosine receptors (purinergic receptor P1). The final outcome depends on the relative concentrations of substrates and products and on the expression of nucleotide-metabolizing ecto-enzymes and NAD-biosynthetic enzymes. NAD, nicotinamide adenine dinucleotide; NADP, NAD phosphate; NAMPT, nicotinamide phosphoribosyltransferase; NAPRT, nicotinate phosphoribosyltransferase; PARPs, poly ADP-ribose polymerases; ADPR, ADP ribose; cADPR, cyclic ADP ribose; NAADP, nicotinic acid adenine dinucleotide phosphate; ATP, adenosine triphosphate; AMP, adenosine monophosphate; P1, adenosine purinergic receptor; RYR, ryanodine receptors; TRPM2, transient receptor potential melastatin-related 2; i, intracellular; e, extracellular.

which in turn contribute to lymphocyte activation through Ca^{2+} signaling (80–82).

There is a second alternative possibility that is gaining momentum in the context of tumor immunosuppression. According to this hypothesis, ADPR could also be short-circuited to ADO *via* the action of CD203, which generates AMP from ADPR and CD73 (53, 83, 84), which cleaves the last phosphate, generating ADO (49). In this way, CD38 could contribute to the generation of a tumor-favorable environment, as recently demonstrated in tumors characterized by a large T cell infiltrate (85). Therefore, it seems that according to the environment, CD38 can generate both immune-boosting and immune-suppressive metabolites, thereby activating or suppressing immune responses.

These at times opposing roles of CD38 in defining immune responses are in part confirmed by studies on *CD38*-deficient mice. Interestingly, when the animals are kept in clean facilities without infectious challenges, they grow and develop normally, without major defects (86). On the other hand, during infections they show impaired lymphocyte activation and homing and are ultimately more susceptible to death due to sepsis (87, 88). *CD38*-deficient animals also show reduced tumor formation, attributed to the lack CD38-mediated immunosuppression.

In the human system, CD38 is widely expressed on the surface of immune cells, particularly in conditions of cellular activation. On the cell surface, CD38 is part of the immunological synapse, forming lateral associations with critical receptors on T, B, and myeloid cells, thereby positioning itself at the center of action (48, 49). In fact, it was reported that CD38 localizes in close contact with T cell receptor (TCR), the B cell receptor (BCR), and key chemokine receptors, among other molecules (89). Perhaps the best understood function of CD38 is in the regulation of T lymphocyte functions, where the enzyme works again different ways (90–93).

First, CD38-dependent-Ca^{2+} signaling directly contributes to T cell activation, likely providing an essential second signal that drives gene expression and consequently differentiation, development, and cytotoxicity (93–95).

As a second level of T cell regulation, the NAD/CD38 axis was proposed to control T cell metabolic reprogramming needed for full T lymphocyte activation through the modulation of sirtuin activity (90, 96). Several studies are shedding light on this molecular circuit as an important metabolic checkpoint contributing to several aspects of cellular energy metabolisms, including glycolysis, oxidative phosphorylation (OXPHOS), glutaminolysis, which are strictly associated with T cell functional fate (90, 93, 97, 98). According to the models proposed, expression of CD38 on the cell surface would limit intracellular NAD levels, negatively impacting on the activities of the NAD-dependent enzymes SIRT1 and SIRT3, which are deacetylases with fundamental roles in epigenetic regulation (93). Lastly, recent data indicate that CD38 is highly expressed by specific subsets of immunosuppressive tumor infiltrating lymphocytes, including regulatory T cells and T helper 17 cells (90, 99–101). Expression of the molecule occurs often in association with exhaustion markers, such as programmed cell death protein 1 (PD-1), pointing to an active role of CD38 in modulating T cell fate toward the generation of an immune tolerant landscape in tumors, likely through the generation of ADO (90) (**Figure 3**).

What remains unclear so far is what are the factors that tip the balance in favor of Ca^{2+}-active metabolites and hence immune activation or in favor of ADO and hence immunosuppression (93, 94, 102–104). Therefore, inhibition of CD38 is a valid therapeutic strategy to reestablish a functional immune surveillance (105), open the way to combination therapies with immune checkpoint inhibitors, as discussed in a separate paragraph.

eNAD BIOSYNTHETIC-SIGNALING SYSTEM IN REGULATING IMMUNE RESPONSES

Beside NAD-consuming, also NBEs were reported in the extracellular compartment. The best known and characterized among them is nicotidamide phosphoribosyltransferase (NAMPT), which catalyzes the conversion of Nam to NMN in the presence of phosphoribosyl pyrophosphate (PRPP) and ATP (7, 44).

The presence of NAMPT in biological fluids is now well established: however, several years were needed before realizing that a cytokine promoting B cell differentiation and originally described in mid-nineties (106), and an extracellular adipokine called visfatin were in fact the same protein as NAMPT (11, 107, 108). Of note, different cell types, including neutrophils, monocytes, macrophages, and cancer cells secrete eNAMPT in the extracellular space in response to inflammation, cellular stress, infections, and hypoxic conditions, among others. In human plasma eNAMPT normal levels are in the low nanomolar range (2-4 ng/ml), but it is over-expressed in several inflammatory and metabolic disorders, including cancer, where concentrations can increase 10-20 times (11, 108).

The second NBE dosed in biological fluids is nicotinic acid phosphoribosyltransferase (NAPRT), which controls the NAD generation pathway starting from Na. While the NAMPT pathway is probably the predominant one in most cells and tissues, considering that all NAD-consuming enzymes generate Nam, the activity of NAPRT is believed to boost NAD levels in stress conditions (44, 109–111). Information on eNAPRT is far more limited, even though concentration data indicate again a physiological level in low nanomolar range (1-2 ng/ml), raising sometimes dramatically, particularly during sepsis (112).

Whether these enzymes are active in the extracellular compartment remains uncertain, mainly because of the absence of detectable PRPP levels, an essential co-factor to produce NMN and nicotinic acid mononucleotide (NaMN). In addition, the rest of the enzymatic cascade producing NAD has never been reported in the extracellular space (109). From data present in the literature, we can exclude a direct eNAD synthesis in physiological conditions, but we cannot exclude a site-specific and transient eNAD synthesis in inflammatory conditions, due to release of intracellular molecules (ATP, PRPP) and enzymes. In favor of a compartment-specific function, the active forms of these enzymes are in a dimeric conformation, but within the extracellular compartment they should be in a monomeric, and hence inactive, form (113). Lastly, functional studies have shown that eNAMPT and eNAPRT, genetically modified to be enzymatically inactive, retain their pro-inflammatory properties (112) (**Figure 3**).

A second area of investigation concerns the mechanisms of trafficking of these enzymes from the intracellular to the extracellular space, which appear "non-classical", as secretion is unaffected by monensin and brefeldin A, two inhibitors of the classical endoplasmatic reticulum (ER)–Golgi secretory pathway (114–117). An interesting finding indicates that NAMPT secretion could be regulated through SIRT1- and SIRT6-deacetylation, thereby linking NAD-biosynthetic and -consuming enzymes, and potentially suggesting eNAMPT secretion as regulatory mechanism to decrease its intracellular concentrations (118, 119). Recent evidence showed that eNAMPT is carried in extracellular vesicles (EVs) through systemic circulation in mice and humans. EV-contained-eNAMPT is internalized into cells, enhancing NMN and hence NAD synthesis (120). eNAMPT is actively secreted *via* exosomes also from microglia during neuroinflammation due to ischemic injury (121). These findings support the possibility of metabolic exchange between tumor/inflammatory and immune cells and vice versa within the site of inflammation or the tumor microenvironment (TME), as previously described for other cytokines and metabolic molecules (122, 123).

The conclusion from these data is that outside of cells it is unlikely that NAMPT and NAPRT function as NAD-producing enzymes, raising the alternative possibility that they possess different functions. In fact, eNAMPT can directly bind Toll-like receptor 4 (TLR4) (112, 124) and C–C chemokine receptor type 5 (CCR5) (125), which might explain how the protein is involved in the activation of an inflammatory signature. The binding with TLR4 was demonstrated in different cellular models, leading to activation of specific intracellular signaling pathways (e.g., STAT3, NF-κB, Akt, P38) within minutes, and activation of inflammasome in few hours (112, 124).

Less recently, it was reported that eNAMPT can selectively inhibit infection of monocytes by human immunodeficiency virus (HIV) and this activity was linked to a direct interaction with CCR5, shown using surface plasmon resonance (SPR) (126). More recently, Torretta et al. suggested that eNAMPT acts as a natural antagonist of CCR5 in cancer cells (125). Within the cancer microenvironment, eNAMPT seems to contribute to shape an immunotolerant environment, mostly acting on the myeloid component. We described a role for eNAMPT in the differentiation of circulating monocytes from chronic lymphocytic leukemia (CLL) patients toward tumor-supporting M2 macrophages (127). Recently, it was demonstrated that iNAMPT acts also on myeloid-derived suppressor cells (MDSCs) *via* a SIRT1/hypoxia-inducible factor (HIF)-1α axis, promoting their mobilization (128). The activation of these circuits creates an immunosuppressive and tumor-promoting microenvironment (**Figure 3**).

Much less is known on eNAPRT, even though from early information it seems to possess properties similar to NAMPT when in extracellular fluids. Managò et al. demonstrated that eNAPRT binds TLR4 on macrophages triggering NF-kB activation and pro-inflammatory cytokines secretion (112). Moreover, eNAPRT shares with eNAMPT the activation of a transcriptional program, maybe mediated by the induction of macrophage colony-stimulating factor (M-CFS), to force monocyte differentiation into macrophages. In turn, macrophages are a source of eNAMPT and eNAPRT *in vivo* (112). Even if several issues remain to be investigated, a functional role of these enzymes in primary innate immunity responses is clearly emerging, opening the way to target these enzymes to modulate inflammation.

IS THE NADome A THERAPEUTIC TARGET?

Alterations in the NADome have been described in several human diseases, including inflammatory conditions (gastric and intestinal inflammatory diseases, graft-versus-host disease, sepsis and multiple organ failure, allergies particularly in the lungs, atherosclerosis, age-associated insulin resistance, neuroinflammation/degeneration), autoimmune diseases (multiple sclerosis, psoriasis, systemic lupus erithematosous), cardiovascular diseases and cancer (7, 55, 129).

In addition to their role in shaping the immune system and in creating immunosuppressive conditions, in some instances NAD-metabolizing enzymes are considered biological prognostic markers and therapeutic targets. Among them, the most promising are CD38, CD73 and NAMPT and the disease setting is cancer (**Figure 4**).

CD38 is expressed in hematological malignancies, including acute B lymphoblastic leukemia (B-ALL), acute myeloid leukemia (AML), mantle cell lymphoma (MCL), CLL, multiple myeloma (MM) and NK/T cell leukemia (T-ALL) (55, 94, 102, 105, 130–132). The role of CD38 has been widely explored and defined in CLL and in MM. On CLL B lymphocytes, CD38 associates with the BCR complex [BCR/CD81/CD19/CD21] and cooperates to amplify the signal transduction driving cell proliferation (55, 133, 134).

Patients with CLL with a higher proportion of leukemic cells expressing CD38 ≥30% experience a shorter time to first treatment and a more aggressive clinical course with inferior overall survival compared to patients who have <30% of CD38$^+$ CLL cells, thus establishing surface CD38 as a marker of poor prognosis (135–137).

MM is a plasma cell neoplastic aggressive disease with a median overall survival of 4.4–7.1 years (138). CD38 is highly and ubiquitously expressed on MM cells and at low levels on normal lymphoid and myeloid cells (49, 139). Daratumumab is a first-in-class anti-CD38 therapeutic monoclonal antibody (mAb) approved in 2015 for the treatment of relapsed/refractory MM (140).

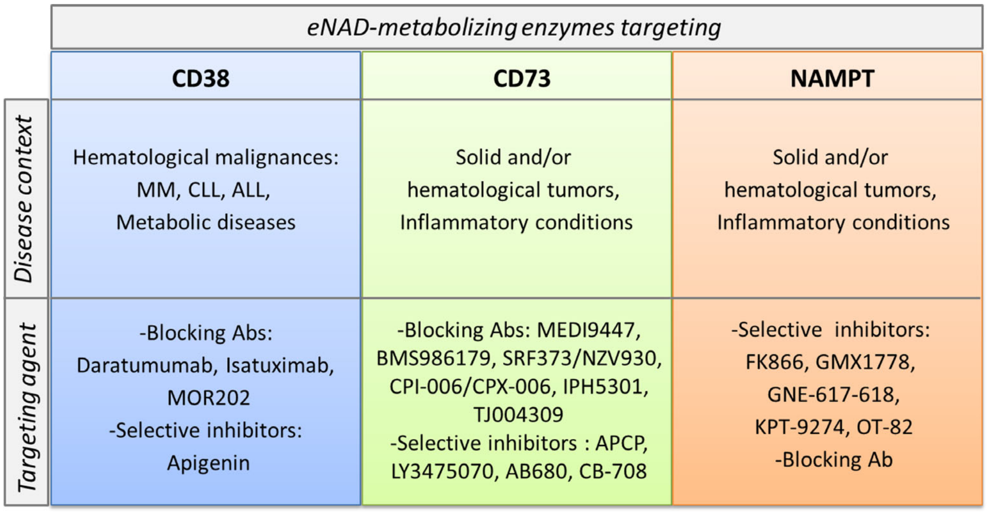

eNAD-metabolizing enzymes targeting

	CD38	CD73	NAMPT
Disease context	Hematological malignancies: MM, CLL, ALL, Metabolic diseases	Solid and/or hematological tumors, Inflammatory conditions	Solid and/or hematological tumors, Inflammatory conditions
Targeting agent	-Blocking Abs: Daratumumab, Isatuximab, MOR202 -Selective inhibitors: Apigenin	-Blocking Abs: MEDI9447, BMS986179, SRF373/NZV930, CPI-006/CPX-006, IPH5301, TJ004309 -Selective inhibitors : APCP, LY3475070, AB680, CB-708	-Selective inhibitors: FK866, GMX1778, GNE-617-618, KPT-9274, OT-82 -Blocking Ab

FIGURE 4 | CD38, CD73 and NAMPT as markers and therapeutic targets in pathological conditions. CD38, CD73 and NAMPT expression levels increase in several pathological conditions. These molecules become markers of aggressive disease. In the lower part of the cartoon specific pharmacological inhibitors and/or blocking antibodies, currently in preclinical or clinical trials for each target are listed.

The documented mechanisms of action include antibody-dependent cell cytotoxicity (ADCC), complement dependent cytotoxicity (CDC), antibody-dependent cellular phagocytosis (ADCP), and inhibition of CD38 enzymatic activities and induction of apoptosis in a caspase-dependent manner (132, 141, 142). This Ab is now used in combination with other drugs; however, the density of CD38 molecules on MM cells is a predictive factor to the efficacy and durability of daratumumab treatment (143). In CLL, CD38 engagement by daratumumab modulates BCR signaling and enhances the anti-CLL activity of ibrutinib, an inhibitor of BCR signaling (144). In addition, CD38 is highly expressed in different solid tumors (i.e., gliomas, pancreatic cancer, non-small cell lung cancer, melanoma, hepatocellular carcinoma), generally associated to increased aggressiveness and creating a tumor-supporting microenvironment (145), providing a rationale for the expansion of daratumumab's field of action.

Targeting CD73 to interfere with the degradation of AMP into ADO, reducing the generation of an immunosuppressed and pro-angiogenic niche that promotes the onset and progression of cancer, is an attractive therapeutic option (146). CD73 expression is higher in the majority of human solid tumors. Its expression and activity are closely associated with tumor invasiveness and metastasis (147, 148).

Inhibition of CD73 using either mAb or small molecule inhibitors such as a,b-methylene-ADP (APCP) have demonstrated antitumor activities in preclinical tumor mouse models (148, 149). Furthermore, a number of anti-CD73 mAbs (MEDI9447, BMS986179, SRF373/NZV930, CPI-006/CPX-006, IPH5301, TJ004309) and selective inhibitors (LY3475070, AB680, CB-708) are being tested in early phase clinical trials, as recently reviewed in (147, 150).

Therefore, combination therapies with CD73 blocking Abs or small molecule inhibitors and other therapeutic strategies including immune checkpoint blockade, adoptive T cell therapy, agonistic immunotherapy, chemotherapy, and radiation therapy, could have synergic effects in various cancers boosting immune response to keep the tumor cells in control, as emerged by recent studies (148, 151).

The first NAMPT inhibitor FK866 (also known as APO866) was described in 2003 by Hasmann et al. (152) Since that, several specific NAMPT inhibitors were developed as recently reviewed in in (7, 153, 154). The rationale was mainly supported by the over-expression of NAMPT in cancer cells, as extensively described by us and by several research groups (11, 108, 117, 127, 155–158).

This led to a first wave of molecules that entered clinical trials for cancer therapy; however, no molecules reported to have progressed to later stages [www.clinicaltrials.gov (7, 153)].

Toxicity of old inhibitors and rescue mechanisms by the activation of other NBEs following NAMPT block, have limited the use of NAMPT inhibitors as single agents. However, increasing evidence suggests that a better selection of tumor subtype rely exclusively on NAMPT activity to generate NAD, as well as novel drugs less toxic, could open a second life for NAMPT inhibition strategy. Moreover, a combination between NAMPT inhibitors and selective inhibitors of oncogenic signaling driving cancer progression could be therapeutically exploited as suggested (11, 117, 159).

An unknown notion is whether these inhibitors could also affect eNAMPT activity, even if, as mentioned before, the enzymatic activity of eNAMPT is controversial. Travelli et al. developed novel inhibitors that can't cross the plasma membrane and have more activity to block eNAMPT form, demonstrating reduced growth of triple negative mammary carcinoma in mice (160). On the other hand, there is also intense research to develop a blocking antibody to neutralize eNAMPT and reduce its "cytokine-like activity" within the TME. The group of Garcia firstly has devised a polyclonal eNAMPT neutralizing antibody (pAb) (161). They used this Ab in different models of inflammation and cancer, including lung injury and prostate cancer. Recently, in acute respiratory distress syndrome (ARDS) they demonstrated the highly significant contribution of endothelial cell (EC)-derived NAMPT to the severity of inflammatory lung injury in preclinical ARDS models. Intravenous delivery of either eNAMPT-neutralizing pAb/mAb significantly attenuated inflammatory lung injury in mouse model. *In vitro* studies on EC demonstrated that eNAMPT-neutralizing antibodies strongly abrogate eNAMPT-induced TLR4 pathway activation (162). In invasive prostate cancer (PCa) Sun et al. proved the activity of eNAMPT in supporting the invasive features of PCa, and the tumor blocking activity of the anti-eNAMPT neutralizing antibody in a pre-clinical *in vivo* model of PCa invasion (163). In parallel, the group of Prof. Genazzani in Italy is developing a novel monoclonal antibody (C269) that neutralizes *in vitro* the cytokine-like action of eNAMPT and that reduces its serum levels in rodents. This Ab is able to significantly reduce acute and chronic colitis in two models of induced-colitis (164), suggesting a role of eNAMPT in the pathogenesis of inflammatory bowel disease (IBD) and the therapeutic potential of its neutralization in this pathology. The general idea of targeting eNAMPT in tumors and in inflammatory diseases is increasing to counteract the extracellular functions of this protein, mainly linked to the activation of TLR4 and modulation of immune responses. The best option could be to combine i/eNAMPT targeting with immunomodulatory agents to obtain a tumor growth regression and a concomitant reversion of immunosuppressive conditions, acting on the immune system. In support of this, two papers demonstrated that NAMPT inhibitors enhance the anti-tumor efficacy of immune checkpoint inhibitors, i.e. antibody against PD-1 (128, 165).

CONCLUSIONS AND FUTURE PERSPECTIVES

Since the discovery of the presence of extracellular nucleotides such as ATP and NAD released from intracellular stores in conditions of cell stress or inflammation, they are considered "danger signals" to alert the immune system, participating in the recruitment, activation, and differentiation of immune cells, and promoting the production and release of pro-inflammatory cytokines. Within the TME, extracellular nucleotides create pro-tumor conditions acting directly on tumor aggressive features but also on immune cells promoting a general immunosuppression.

The extracellular machinery that regulates eNAD functions is complex, as we summarized in this review several eNAD-metabolizing enzymes rapidly degrade it into metabolites that in turn can function as signaling messengers or can be internalized and used to reconstitute the intracellular NAD pool. Directly, eNAD can bind purinergic receptors and activate signaling. The effects of eNAD are therefore dependent on the presence of receptors, metabolizing enzymes and cellular stress conditions within the microenvironment. Understanding this intricate machinery remains the most important challenge to develop therapeutic strategies to modulate expression of these extracellular nucleotides, relative enzymes, and receptors to re-educate the immune system in different diseases, including cancer.

AUTHOR CONTRIBUTIONS

SD designed and reviewed the work, which was assembled by VA, with contribution of VM and LB. All authors contributed to the article and approved the submitted version.

FUNDING

This work was supported by the Ministry of Education University and Research-MIUR, PRIN Project 2017CBNCYT and Progetto strategico di Eccellenza Dipartimentale #D15D18000410001 (the latter awarded to the Dept. of Medical Sciences, University of Turin) and ITN INTEGRATA program (grant agreement 813284), and by Associazione Italiana Ricerca sul Cancro (AIRC), Investigator Grant –IG 2019 #23095.

REFERENCES

1. Vander Heiden MG, Cantley LC, Thompson CB. Understanding the Warburg Effect: The Metabolic Requirements of Cell Proliferation. *Science* (2009) 324(5930):1029–33. doi: 10.1126/science.1160809
2. Bonora M, Patergnani S, Rimessi A, De Marchi E, Suski JM, Bononi A, et al. ATP Synthesis and Storage. *Purinergic Signal* (2012) 8(3):343–57. doi: 10.1007/s11302-012-9305-8
3. Xiao W, Wang RS, Handy DE, Loscalzo J. NAD(H) and NADP(H) Redox Couples and Cellular Energy Metabolism. *Antioxid Redox Signal* (2018) 28 (3):251–72. doi: 10.1089/ars.2017.7216
4. Yaku K, Okabe K, Nakagawa T. NAD Metabolism: Implications in Aging and Longevity. *Ageing Res Rev* (2018) 47:1–17. doi: 10.1016/j.arr.2018.05.006
5. Linden J, Koch-Nolte F, Dahl G. Purine Release, Metabolism, and Signaling in the Inflammatory Response. *Annu Rev Immunol* (2019) 37:325–47. doi: 10.1146/annurev-immunol-051116-052406
6. Amjad S, Nisar S, Bhat AA, Shah AR, Frenneaux MP, Fakhro K, et al. Role of NAD(+) in Regulating Cellular and Metabolic Signaling Pathways. *Mol Metab* (2021) 49:101195. doi: 10.1016/j.molmet.2021.101195
7. Xie N, Zhang L, Gao W, Huang C, Huber PE, Zhou X, et al. NAD(+) Metabolism: Pathophysiologic Mechanisms and Therapeutic Potential. *Signal Transduct Target Ther* (2020) 5(1):227. doi: 10.1038/s41392-020-00311-7
8. Di Virgilio F, Sarti AC, Falzoni S, De Marchi E, Adinolfi E. Extracellular ATP and P2 Purinergic Signalling in the Tumour Microenvironment. *Nat Rev Cancer* (2018) 18(10):601–18. doi: 10.1038/s41568-018-0037-0
9. Haag F, Adriouch S, Brass A, Jung C, Moller S, Scheuplein F, et al. Extracellular NAD and ATP: Partners in Immune Cell Modulation. *Purinergic Signal* (2007) 3(1-2):71–81. doi: 10.1007/s11302-006-9038-7
10. Scheuplein F, Schwarz N, Adriouch S, Krebs C, Bannas P, Rissiek B, et al. NAD+ and ATP Released From Injured Cells Induce P2X7-Dependent Shedding of CD62L and Externalization of Phosphatidylserine by Murine T Cells. *J Immunol* (2009) 182(5):2898–908. doi: 10.4049/jimmunol.0801711
11. Audrito V, Messana VG, Deaglio S. NAMPT and NAPRT: Two Metabolic Enzymes With Key Roles in Inflammation. *Front Oncol* (2020) 10:358. doi: 10.3389/fonc.2020.00358
12. Pellegatti P, Raffaghello L, Bianchi G, Piccardi F, Pistoia V, Di Virgilio F. Increased Level of Extracellular ATP at Tumor Sites: *In Vivo* Imaging With Plasma Membrane Luciferase. *PloS One* (2008) 3(7):e2599. doi: 10.1371/journal.pone.0002599
13. Wilhelm K, Ganesan J, Muller T, Durr C, Grimm M, Beilhack A, et al. Graft-Versus-Host Disease Is Enhanced by Extracellular ATP Activating P2X7R. *Nat Med* (2010) 16(12):1434–8. doi: 10.1038/nm.2242
14. O'Reilly T, Niven DF. Levels of Nicotinamide Adenine Dinucleotide in Extracellular Body Fluids of Pigs may be Growth-Limiting for Actinobacillus Pleuropneumoniae and Haemophilus Parasuis. *Can J Vet Res* (2003) 67 (3):229–31.
15. Billington RA, Bruzzone S, De Flora A, Genazzani AA, Koch-Nolte F, Ziegler M, et al. Emerging Functions of Extracellular Pyridine Nucleotides. *Mol Med* (2006) 12(11-12):324–7. doi: 10.2119/2006-00075.Billington
16. Di Stefano M, Conforti L. Diversification of NAD Biological Role: The Importance of Location. *FEBS J* (2013) 280(19):4711–28. doi: 10.1111/febs.12433
17. Trautmann A. Extracellular ATP in the Immune System: More Than Just a "Danger Signal". *Sci Signal* (2009) 2(56):pe6. doi: 10.1126/scisignal.256pe6
18. Corriden R, Insel PA. Basal Release of ATP: An Autocrine-Paracrine Mechanism for Cell Regulation. *Sci Signal* (2010) 3(104):re1. doi: 10.1126/scisignal.3104re1
19. Schilling E, Hauschildt S. Extracellular ATP Induces P2X7-Dependent Nicotinamide Phosphoribosyltransferase Release in LPS-Activated Human Monocytes. *Innate Immun* (2012) 18(5):738–44. doi: 10.1177/1753425912439614
20. Adriouch S, Haag F, Boyer O, Seman M, Koch-Nolte F. Extracellular NAD (+): A Danger Signal Hindering Regulatory T Cells. *Microbes Infect* (2012) 14(14):1284–92. doi: 10.1016/j.micinf.2012.05.011
21. Bianchi ME. DAMPs, PAMPs and Alarmins: All We Need to Know About Danger. *J Leukoc Biol* (2007) 81(1):1–5. doi: 10.1189/jlb.0306164
22. Venereau E, Ceriotti C, Bianchi ME. DAMPs From Cell Death to New Life. *Front Immunol* (2015) 6:422. doi: 10.3389/fimmu.2015.00422
23. Tanaka K, Choi J, Cao Y, Stacey G. Extracellular ATP Acts as a Damage-Associated Molecular Pattern (DAMP) Signal in Plants. *Front Plant Sci* (2014) 5:446. doi: 10.3389/fpls.2014.00446
24. Di Virgilio F, Dal Ben D, Sarti AC, Giuliani AL, Falzoni S. The P2X7 Receptor in Infection and Inflammation. *Immunity* (2017) 47(1):15–31. doi: 10.1016/j.immuni.2017.06.020
25. Smyth LM, Bobalova J, Mendoza MG, Lew C, Mutafova-Yambolieva VN. Release of Beta-Nicotinamide Adenine Dinucleotide Upon Stimulation of Postganglionic Nerve Terminals in Blood Vessels and Urinary Bladder. *J Biol Chem* (2004) 279(47):48893–903. doi: 10.1074/jbc.M407266200M407266200[pii
26. Breen LT, Smyth LM, Yamboliev IA, Mutafova-Yambolieva VN. Beta-NAD Is a Novel Nucleotide Released on Stimulation of Nerve Terminals in Human Urinary Bladder Detrusor Muscle. *Am J Physiol Renal Physiol* (2006) 290(2):F486–95. doi: 10.1152/ajprenal.00314.2005
27. Mutafova-Yambolieva VN, Hwang SJ, Hao X, Chen H, Zhu MX, Wood JD, et al. Beta-Nicotinamide Adenine Dinucleotide Is an Inhibitory Neurotransmitter in Visceral Smooth Muscle. *Proc Natl Acad Sci USA* (2007) 104(41):16359–64. doi: 10.1073/pnas.0705510104
28. Adriouch S, Hubert S, Pechberty S, Koch-Nolte F, Haag F, Seman M. NAD(+) Released During Inflammation Participates in T Cell Homeostasis

by Inducing ART2-Mediated Death of Naive T Cells *In Vivo*. *J Immunol* (2007) 179(1):186–94. doi: 10.4049/jimmunol.179.1.186

29. Cekic C, Linden J. Purinergic Regulation of the Immune System. *Nat Rev Immunol* (2016) 16(3):177–92. doi: 10.1038/nri.2016.4
30. Bruzzone S, Guida L, Zocchi E, Franco L, De Flora A. Connexin 43 Hemi Channels Mediate Ca2+-Regulated Transmembrane NAD+ Fluxes in Intact Cells. *FASEB J* (2001) 15(1):10–2. doi: 10.1096/fj.00-0566fje
31. Hwang SJ, Durnin L, Dwyer L, Rhee PL, Ward SM, Koh SD, et al. Beta-Nicotinamide Adenine Dinucleotide Is an Enteric Inhibitory Neurotransmitter in Human and Nonhuman Primate Colons. *Gastroenterology* (2011) 140 (2):608–17 e6. doi: 10.1053/j.gastro.2010.09.039
32. Mottahedeh J, Haffner MC, Grogan TR, Hashimoto T, Crowell PD, Beltran H, et al. CD38 is Methylated in Prostate Cancer and Regulates Extracellular NAD(). *Cancer Metab* (2018) 6:13. doi: 10.1186/s40170-018-0186-3
33. Sitkovsky MV, Ohta A. The 'Danger' Sensors That STOP the Immune Response: The A2 Adenosine Receptors? *Trends Immunol* (2005) 26(6):299–304. doi: 10.1016/j.it.2005.04.004
34. Deaglio S, Robson SC. Ectonucleotidases as Regulators of Purinergic Signaling in Thrombosis, Inflammation, and Immunity. *Adv Pharmacol* (2011) 61:301–32. doi: 10.1016/B978-0-12-385526-8.00010-2
35. Vaisitti T, Audrito V, Serra S, Bologna C, Brusa D, Malavasi F, et al. NAD+-Metabolizing Ecto-Enzymes Shape Tumor-Host Interactions: The Chronic Lymphocytic Leukemia Model. *FEBS Lett* (2011) 585(11):1514–20. doi: 10.1016/j.febslet.2011.04.036
36. Kazemi MH, Raoofi Mohseni S, Hojjat-Farsangi M, Anvari E, Ghalamfarsa G, Mohammadi H, et al. Adenosine and Adenosine Receptors in the Immunopathogenesis and Treatment of Cancer. *J Cell Physiol* (2018) 233 (3):2032–57. doi: 10.1002/jcp.25873
37. Di Virgilio F. Purines, Purinergic Receptors, and Cancer. *Cancer Res* (2012) 72(21):5441–7. doi: 10.1158/0008-5472.CAN-12-16000008-5472.CAN-12-1600[pii
38. Di Virgilio F, Sarti AC, Coutinho-Silva R. Purinergic Signaling, DAMPs, and Inflammation. *Am J Physiol Cell Physiol* (2020) 318(5):C832–C5. doi: 10.1152/ajpcell.00053.2020
39. Gasparrini M, Sorci L, Raffaelli N. Enzymology of Extracellular NAD Metabolism. *Cell Mol Life Sci* (2021) 78(7):3317–31. doi: 10.1007/s00018-020-03742-1
40. Audrito V, Messana VG, Moiso E, Vitale N, Arruga F, Brandimarte L, et al. NAMPT Over-Expression Recapitulates the BRAF Inhibitor Resistant Phenotype Plasticity in Melanoma. *Cancers (Basel)* (2020) 12(12):3855–77. doi: 10.3390/cancers12123855
41. Houtkooper RH, Canto C, Wanders RJ, Auwerx J. The Secret Life of NAD+: An Old Metabolite Controlling New Metabolic Signaling Pathways. *Endocr Rev* (2010) 31(2):194–223. doi: 10.1210/er.2009-0026
42. Hassinen IE. Signaling and Regulation Through the NAD(+) and NADP(+) Networks. *Antioxid Redox Signal* (2019) 30(6):857–74. doi: 10.1089/ars.2017.7479
43. Nikiforov A, Dolle C, Niere M, Ziegler M. Pathways and Subcellular Compartmentation of NAD Biosynthesis in Human Cells: From Entry of Extracellular Precursors to Mitochondrial NAD Generation. *J Biol Chem* (2011) 286(24):21767–78. doi: 10.1074/jbc.M110.213298M110.213298[pii
44. Ruggieri S, Orsomando G, Sorci L, Raffaelli N. Regulation of NAD Biosynthetic Enzymes Modulates NAD-Sensing Processes to Shape Mammalian Cell Physiology Under Varying Biological Cues. *Biochim Biophys Acta* (2015) 1854(9):1138–49. doi: 10.1016/j.bbapap.2015.02.021
45. Canto C, Menzies KJ, Auwerx J. NAD(+) Metabolism and the Control of Energy Homeostasis: A Balancing Act Between Mitochondria and the Nucleus. *Cell Metab* (2015) 22(1):31–53. doi: 10.1016/j.cmet.2015.05.023
46. Grolla AA, Miggiano R, Di Marino D, Bianchi M, Gori A, Orsomando G, et al. A Nicotinamide Phosphoribosyltransferase-GAPDH Interaction Sustains the Stress-Induced NMN/NAD(+) Salvage Pathway in the Nucleus. *J Biol Chem* (2020) 295(11):3635–51. doi: 10.1074/jbc.RA119.010571
47. Nikiforov A, Kulikova V, Ziegler M. The Human NAD Metabolome: Functions, Metabolism and Compartmentalization. *Crit Rev Biochem Mol Biol* (2015) 50(4):284–97. doi: 10.3109/10409238.2015.1028612
48. Chini EN. CD38 as a Regulator of Cellular NAD: A Novel Potential Pharmacological Target for Metabolic Conditions. *Curr Pharm Des* (2009) 15(1):57–63. doi: 10.2174/138161209787185788
49. Malavasi F, Deaglio S, Funaro A, Ferrero E, Horenstein AL, Ortolan E, et al. Evolution and Function of the ADP Ribosyl Cyclase/CD38 Gene Family in Physiology and Pathology. *Physiol Rev* (2008) 88(3):841–86. doi: 10.1152/physrev.00035.2007
50. Deaglio S, Malavasi F. The CD38/CD157 Mammalian Gene Family: An Evolutionary Paradigm for Other Leukocyte Surface Enzymes. *Purinergic Signaling* (2006) 2:431–41. doi: 10.1007/s11302-006-9002-6
51. Seman M, Adriouch S, Haag F, Koch-Nolte F. Ecto-ADP-Ribosyltransferases (ARTs): Emerging Actors in Cell Communication and Signaling. *Curr Med Chem* (2004) 11(7):857–72. doi: 10.2174/0929867043455611
52. Katada T, Kontani K, Wada T, Hosoda N, Hoshino S, Nishina H. Enzymic and Signal Transduction Properties of CD38/NADase and PC-1/Phosphodiesterase. *Chem Immunol* (2000) 75:60–78. doi: 10.1159/000058762
53. Garavaglia S, Bruzzone S, Cassani C, Canella L, Allegrone G, Sturla L, et al. The High-Resolution Crystal Structure of Periplasmic Haemophilus Influenzae NAD Nucleotidase Reveals a Novel Enzymatic Function of Human CD73 Related to NAD Metabolism. *Biochem J* (2012) 441(1):131–41. doi: 10.1042/BJ20111263
54. Horenstein AL, Chillemi A, Zaccarello G, Bruzzone S, Quarona V, Zito A, et al. A CD38/CD203a/CD73 Ectoenzymatic Pathway Independent of CD39 Drives a Novel Adenosinergic Loop in Human T Lymphocytes. *Oncoimmunology* (2013) 2(9):e26246. doi: 10.4161/onci.26246
55. Vaisitti T, Arruga F, Guerra G, Deaglio S. Ectonucleotidases in Blood Malignancies: A Tale of Surface Markers and Therapeutic Targets. *Front Immunol* (2019) 10:2301. doi: 10.3389/fimmu.2019.02301
56. Kemmer G, Reilly TJ, Schmidt-Brauns J, Zlotnik GW, Green BA, Fiske MJ, et al. NadN and E (P4) are Essential for Utilization of NAD and Nicotinamide Mononucleotide But Not Nicotinamide Riboside in Haemophilus Influenzae. *J Bacteriol* (2001) 183(13):3974–81. doi: 10.1128/JB.183.13.3974-3981.2001
57. Grozio A, Sociali G, Sturla L, Caffa I, Soncini D, Salis A, et al. CD73 Protein as a Source of Extracellular Precursors for Sustained NAD+ Biosynthesis in FK866-Treated Tumor Cells. *J Biol Chem* (2013) 288(36):25938–49. doi: 10.1074/jbc.M113.470435M113.470435
58. Sociali G, Raffaghello L, Magnone M, Zamporlini F, Emionite L, Sturla L, et al. Antitumor Effect of Combined NAMPT and CD73 Inhibition in an Ovarian Cancer Model. *Oncotarget* (2015) 7(3):2968–84. doi: 10.18632/oncotarget.65026502
59. Burnstock G. Purinergic Nerves. *Pharmacol Rev* (1972) 24(3):509–81.
60. Burnstock G, Verkhratsky A. Evolutionary Origins of the Purinergic Signalling System. *Acta Physiol (Oxf)* (2009) 195(4):415–47. doi: 10.1111/j.1748-1716.2009.01957.x
61. Burnstock G. Purine and Purinergic Receptors. *Brain Neurosci Adv* (2018) 2:2398212818817494. doi: 10.1177/2398212818817494
62. Moreschi I, Bruzzone S, Nicholas RA, Fruscione F, Sturla L, Benvenuto F, et al. Extracellular NAD+ Is an Agonist of the Human P2Y11 Purinergic Receptor in Human Granulocytes. *J Biol Chem* (2006) 281(42):31419–29. doi: 10.1074/jbc.M606625200
63. Klein C, Grahnert A, Abdelrahman A, Muller CE, Hauschildt S. Extracellular NAD(+) Induces a Rise in [Ca(2+)](i) in Activated Human Monocytes *via* Engagement of P2Y(1) and P2Y(11) Receptors. *Cell Calcium* (2009) 46 (4):263–72. doi: 10.1016/j.ceca.2009.08.004
64. Alefishat E, Alexander SP, Ralevic V. Effects of NAD at Purine Receptors in Isolated Blood Vessels. *Purinergic Signal* (2015) 11(1):47–57. doi: 10.1007/s11302-014-9428-1
65. Durnin L, Hwang SJ, Ward SM, Sanders KM, Mutafova-Yambolieva VN. Adenosine 5-Diphosphate-Ribose Is a Neural Regulator in Primate and Murine Large Intestine Along With Beta-NAD(+). *J Physiol* (2012) 590(Pt 8):1921–41. doi: 10.1113/jphysiol.2011.222414
66. Grahnert A, Klein C, Hauschildt S. Involvement of P2X Receptors in the NAD(+)-Induced Rise in [Ca (2+)] (I) in Human Monocytes. *Purinergic Signal* (2009) 5(3):309–19. doi: 10.1007/s11302-009-9144-4
67. Khakh BS, North RA. P2X Receptors as Cell-Surface ATP Sensors in Health and Disease. *Nature* (2006) 442(7102):527–32. doi: 10.1038/nature04886
68. Dubyak GR. P2X7 Receptor Regulation of Non-Classical Secretion From Immune Effector Cells. *Cell Microbiol* (2012) 14(11):1697–706. doi: 10.1111/cmi.12001

69. Adinolfi E, Giuliani AL, De Marchi E, Pegoraro A, Orioli E, Di Virgilio F. The P2X7 Receptor: A Main Player in Inflammation. *Biochem Pharmacol* (2018) 151:234–44. doi: 10.1016/j.bcp.2017.12.021
70. Giuliani AL, Sarti AC, Falzoni S, Di Virgilio F. The P2X7 Receptor-Interleukin-1 Liaison. *Front Pharmacol* (2017) 8:123. doi: 10.3389/fphar.2017.00123
71. Seman M, Adriouch S, Scheuplein F, Krebs C, Freese D, Glowacki G, et al. NAD-Induced T Cell Death: ADP-Ribosylation of Cell Surface Proteins by ART2 Activates the Cytolytic P2X7 Purinoceptor. *Immunity* (2003) 19 (4):571–82. doi: 10.1016/S1074-7613(03)00266-8
72. Hubert S, Rissiek B, Klages K, Huehn J, Sparwasser T, Haag F, et al. Extracellular NAD+ Shapes the Foxp3+ Regulatory T Cell Compartment Through the ART2-P2X7 Pathway. *J Exp Med* (2010) 207(12):2561–8. doi: 10.1084/jem.20091154
73. Alessio M, Roggero S, Funaro A, De Monte LB, Peruzzi L, Geuna M, et al. CD38 Molecule: Structural and Biochemical Analysis on Human T Lymphocytes, Thymocytes, and Plasma Cells. *J Immunol* (1990) 145 (3):878–84.
74. Malavasi F, Deaglio S, Ferrero E, Funaro A, Sancho J, Ausiello CM, et al. CD38 and CD157 as Receptors of the Immune System: A Bridge Between Innate and Adaptive Immunity. *Mol Med* (2006) 12(11-12):334–41. doi: 10.2119/2006–00094.Malavasi
75. De Flora A, Guida L, Franco L, Zocchi E. The CD38/cyclic ADP-Ribose System: A Topological Paradox. *Int J Biochem Cell Biol* (1997) 29(10):1149–66. doi: 10.1016/s1357-2725(97)00062-9
76. Zhao YJ, Lam CM, Lee HC. The Membrane-Bound Enzyme CD38 Exists in Two Opposing Orientations. *Sci Signal* (2012) 5(241):ra67. doi: 10.1126/scisignal.2002700
77. Shrimp JH, Hu J, Dong M, Wang BS, MacDonald R, Jiang H, et al. Revealing CD38 Cellular Localization Using a Cell Permeable, Mechanism-Based Fluorescent Small-Molecule Probe. *J Am Chem Soc* (2014) 136(15):5656–63. doi: 10.1021/ja411046j
78. Liu J, Zhao YJ, Li WH, Hou YN, Li T, Zhao ZY, et al. Cytosolic Interaction of Type III Human CD38 With CIB1 Modulates Cellular Cyclic ADP-Ribose Levels. *Proc Natl Acad Sci U.S.A.* (2017) 114(31):8283–8. doi: 10.1073/pnas.1703718114
79. Sumoza-Toledo A, Penner R. TRPM2: A Multifunctional Ion Channel for Calcium Signalling. *J Physiol* (2011) 589(Pt 7):1515–25. doi: 10.1113/jphysiol.2010.201855
80. Lee HC. Structure and Enzymatic Functions of Human CD38. *Mol Med* (2006) 12(11-12):317–23. doi: 10.2119/2006-00086.Lee
81. Adebanjo OA, Anandatheerthavarada HK, Koval AP, Moonga BS, Biswas G, Sun L, et al. A New Function for CD38/ADP-Ribosyl Cyclase in Nuclear Ca2+ Homeostasis. *Nat Cell Biol* (1999) 1(7):409–14. doi: 10.1038/15640
82. Guse AH. Cyclic ADP-Ribose: A Novel Ca2+-Mobilising Second Messenger. *Cell Signal* (1999) 11(5):309–16. doi: 10.1016/S0898-6568(99)00004-2
83. Colgan SP, Eltzschig HK, Eckle T, Thompson LF. Physiological Roles for Ecto-5'-Nucleotidase (CD73). *Purinergic Signal* (2006) 2(2):351–60. doi: 10.1007/s11302-005-5302-5
84. Allard D, Allard B, Gaudreau PO, Chrobak P, Stagg J. CD73-Adenosine: A Next-Generation Target in Immuno-Oncology. *Immunotherapy* (2016) 8 (2):145–63. doi: 10.2217/imt.15.106
85. Chen Z, Han ZC. STAT3: A Critical Transcription Activator in Angiogenesis. *Med Res Rev* (2008) 28(2):185–200. doi: 10.1002/med.20101
86. Fukushi Y, Kato I, Takasawa S, Sasaki T, Ong BH, Sato M, et al. Identification of Cyclic ADP-Ribose-Dependent Mechanisms in Pancreatic Muscarinic Ca2+ Signaling Using CD38 Knockout Mice. *J Biol Chem* (2001) 276(1):649–55. doi: 10.1074/jbc.M004469200
87. Partida-Sanchez S, Cockayne DA, Monard S, Jacobson EL, Oppenheimer N, Garvy B, et al. Cyclic ADP-Ribose Production by CD38 Regulates Intracellular Calcium Release, Extracellular Calcium Influx and Chemotaxis in Neutrophils and Is Required for Bacterial Clearance *In Vivo*. *Nat Med* (2001) 7(11):1209–16. doi: 10.1038/nm1101-1209
88. Partida-Sanchez S, Goodrich S, Kusser K, Oppenheimer N, Randall TD, Lund FE. Regulation of Dendritic Cell Trafficking by the ADP-Ribosyl Cyclase CD38: Impact on the Development of Humoral Immunity. *Immunity* (2004) 20(3):279–91. doi: 10.1016/S1074-7613(04)00048-2
89. Munoz P, Mittelbrunn M, de la Fuente H, Perez-Martinez M, Garcia-Perez A, Ariza-Veguillas A, et al. Antigen-Induced Clustering of Surface CD38 and Recruitment of Intracellular CD38 to the Immunologic Synapse. *Blood* (2008) 111(7):3653–64. doi: 10.1182/blood-2007-07-101600
90. Chatterjee S, Daenthanasanmak A, Chakraborty P, Wyatt MW, Dhar P, Selvam SP, et al. CD38-NAD(+)Axis Regulates Immunotherapeutic Anti-Tumor T Cell Response. *Cell Metab* (2018) 27(1):85–100.e8. doi: 10.1016/j.cmet.2017.10.006
91. Krejcik J, Casneuf T, Nijhof IS, Verbist B, Bald J, Plesner T, et al. Daratumumab Depletes CD38+ Immune Regulatory Cells, Promotes T-Cell Expansion, and Skews T-Cell Repertoire in Multiple Myeloma. *Blood* (2016) 128(3):384–94. doi: 10.1182/blood-2015-12-687749
92. Sharif T, Martell E, Dai C, Ghassemi-Rad MS, Kennedy BE, Lee PWK, et al. Regulation of Cancer and Cancer-Related Genes *via* NAD. *Antioxid Redox Signal* (2018) 30(6):906–23. doi: 10.1089/ars.2017.7478
93. Kar A, Mehrotra S, Chatterjee S. CD38: T Cell Immuno-Metabolic Modulator. *Cells* (2020) 9(7):1716–36. doi: 10.3390/cells9071716
94. Hogan KA, Chini CCS, Chini EN. The Multi-Faceted Ecto-Enzyme CD38: Roles in Immunomodulation, Cancer, Aging, and Metabolic Diseases. *Front Immunol* (2019) 10:1187. doi: 10.3389/fimmu.2019.01187
95. Feske S. Calcium Signalling in Lymphocyte Activation and Disease. *Nat Rev Immunol* (2007) 7(9):690–702. doi: 10.1038/nri2152
96. Jeng MY, Hull PA, Fei M, Kwon HS, Tsou CL, Kasler H, et al. Metabolic Reprogramming of Human CD8(+) Memory T Cells Through Loss of SIRT1. *J Exp Med* (2018) 215(1):51–62. doi: 10.1084/jem.20161066
97. Geltink RIK, Kyle RL, Pearce EL. Unraveling the Complex Interplay Between T Cell Metabolism and Function. *Annu Rev Immunol* (2018) 36:461–88. doi: 10.1146/annurev-immunol-042617-053019
98. Chang HC, Guarente L. SIRT1 and Other Sirtuins in Metabolism. *Trends Endocrinol Metab* (2014) 25(3):138–45. doi: 10.1016/j.tem.2013.12.001S1043-2760(13)00206-3
99. Feng X, Zhang L, Acharya C, An G, Wen K, Qiu L, et al. Targeting CD38 Suppresses Induction and Function of T Regulatory Cells to Mitigate Immunosuppression in Multiple Myeloma. *Clin Cancer Res* (2017) 23 (15):4290–300. doi: 10.1158/1078-0432.CCR-16-3192
100. Newton R, Priyadharshini B, Turka LA. Immunometabolism of Regulatory T Cells. *Nat Immunol* (2016) 17(6):618–25. doi: 10.1038/ni.3466
101. Huang L, Xu H, Peng G. TLR-Mediated Metabolic Reprogramming in the Tumor Microenvironment: Potential Novel Strategies for Cancer Immunotherapy. *Cell Mol Immunol* (2018) 15(5):428–37. doi: 10.1038/cmi.2018.4
102. Morandi F, Airoldi I, Marimpietri D, Bracci C, Faini AC, Gramignoli R. CD38, A Receptor With Multifunctional Activities: From Modulatory Functions on Regulatory Cell Subsets and Extracellular Vesicles, to a Target for Therapeutic Strategies. *Cells* (2019) 8(12):1527–44. doi: 10.3390/cells8121527
103. Hartman WR, Pelleymounter LL, Moon I, Kalari K, Liu M, Wu TY, et al. CD38 Expression, Function, and Gene Resequencing in a Human Lymphoblastoid Cell Line-Based Model System. *Leuk Lymphoma* (2010) 51(7):1315–25. doi: 10.3109/10428194.2010.483299
104. Glaria E, Valledor AF. Roles of CD38 in the Immune Response to Infection. *Cells* (2020) 9(1):228–44. doi: 10.3390/cells9010228
105. Chini EN, Chini CCS, Espindola Netto JM, de Oliveira GC, van Schooten W. The Pharmacology of CD38/NADase: An Emerging Target in Cancer and Diseases of Aging. *Trends Pharmacol Sci* (2018) 39(4):424–36. doi: 10.1016/j.tips.2018.02.001
106. Samal B, Sun Y, Stearns G, Xie C, Suggs S, McNiece I. Cloning and Characterization of the cDNA Encoding a Novel Human Pre-B-Cell Colony-Enhancing Factor. *Mol Cell Biol* (1994) 14(2):1431–7. doi: 10.1128/mcb.14.2.1431-1437.1994
107. Rongvaux A, Shea RJ, Mulks MH, Gigot D, Urbain J, Leo O, et al. Pre-B-Cell Colony-Enhancing Factor, Whose Expression Is Up-Regulated in Activated Lymphocytes, is a Nicotinamide Phosphoribosyltransferase, a Cytosolic Enzyme Involved in NAD Biosynthesis. *Eur J Immunol* (2002) 32(11):3225–34. doi: 10.1002/1521-4141(200211)32:11<3225::AID-IMMU3225>3.0.CO;2-L
108. Heske CM. Beyond Energy Metabolism: Exploiting the Additional Roles of NAMPT for Cancer Therapy. *Front Oncol* (2019) 9:1514. doi: 10.3389/fonc.2019.01514

109. Hara N, Yamada K, Shibata T, Osago H, Tsuchiya M. Nicotinamide Phosphoribosyltransferase/Visfatin Does Not Catalyze Nicotinamide Mononucleotide Formation in Blood Plasma. *PloS One* (2011) 6(8):e22781. doi: 10.1371/journal.pone.0022781
110. Galassi L, Di Stefano M, Brunetti L, Orsomando G, Amici A, Ruggieri S, et al. Characterization of Human Nicotinate Phosphoribosyltransferase: Kinetic Studies, Structure Prediction and Functional Analysis by Site-Directed Mutagenesis. *Biochimie* (2012) 94(2):300–9. doi: 10.1016/j.biochi.2011.06.033
111. Duarte-Pereira S, Pereira-Castro I, Silva SS, Correia MG, Neto C, da Costa LT, et al. Extensive Regulation of Nicotinate Phosphoribosyltransferase (NAPRT) Expression in Human Tissues and Tumors. *Oncotarget* (2016) 7 (2):1973–83. doi: 10.18632/oncotarget.6538
112. Manago A, Audrito V, Mazzola F, Sorci L, Gaudino F, Gizzi K, et al. Extracellular Nicotinate Phosphoribosyltransferase Binds Toll Like Receptor 4 and Mediates Inflammation. *Nat Commun* (2019) 10(1):4116. doi: 10.1038/s41467-019-12055-2
113. Sayers SR, Beavil RL, Fine NHF, Huang GC, Choudhary P, Pacholarz KJ, et al. Structure-Functional Changes in eNAMPT at High Concentrations Mediate Mouse and Human Beta Cell Dysfunction in Type 2 Diabetes. *Diabetologia* (2020) 63(2):313–23. doi: 10.1007/s00125-019-05029-y
114. Revollo JR, Korner A, Mills KF, Satoh A, Wang T, Garten A, et al. Nampt/PBEF/Visfatin Regulates Insulin Secretion in Beta Cells as a Systemic NAD Biosynthetic Enzyme. *Cell Metab* (2007) 6(5):363–75. doi: 10.1016/j.cmet.2007.09.003
115. Tanaka M, Nozaki M, Fukuhara A, Segawa K, Aoki N, Matsuda M, et al. Visfatin is Released From 3T3-L1 Adipocytes *via* a Non-Classical Pathway. *Biochem Biophys Res Commun* (2007) 359(2):194–201. doi: 10.1016/j.bbrc.2007.05.096
116. Grolla AA, Torretta S, Gnemmi I, Amoruso A, Orsomando G, Gatti M, et al. Nicotinamide Phosphoribosyltransferase (NAMPT/PBEF/visfatin) is a Tumoural Cytokine Released From Melanoma. *Pigment Cell Melanoma Res* (2015) 28(6):718–29. doi: 10.1111/pcmr.12420
117. Audrito V, Manago A, La Vecchia S, Zamporlini F, Vitale N, Baroni G, et al. Nicotinamide Phosphoribosyltransferase (NAMPT) as a Therapeutic Target in BRAF-Mutated Metastatic Melanoma. *J Natl Cancer Inst* (2018) 110 (3):290–303. doi: 10.1093/jnci/djx198
118. Yoon MJ, Yoshida M, Johnson S, Takikawa A, Usui I, Tobe K, et al. SIRT1-Mediated eNAMPT Secretion From Adipose Tissue Regulates Hypothalamic NAD+ and Function in Mice. *Cell Metab* (2015) 21(5):706–17. doi: 10.1016/j.cmet.2015.04.002
119. Sociali G, Grozio A, Caffa I, Schuster S, Becherini P, Damonte P, et al. SIRT6 Deacetylase Activity Regulates NAMPT Activity and NAD(P)(H) Pools in Cancer Cells. *FASEB J* (2019) 33(3):3704–17. doi: 10.1096/fj.201800321R
120. Yoshida M, Satoh A, Lin JB, Mills KF, Sasaki Y, Rensing N, et al. Extracellular Vesicle-Contained eNAMPT Delays Aging and Extends Lifespan in Mice. *Cell Metab* (2019) 30(2):329–42 e5. doi: 10.1016/j.cmet.2019.05.015
121. Lu YB, Chen CX, Huang J, Tian YX, Xie X, Yang P, et al. Nicotinamide Phosphoribosyltransferase Secreted From Microglia *via* exosome during ischemic injury. *J Neurochem* (2019) 150(6):723–37. doi: 10.1111/jnc.14811
122. Chiarugi P, Cirri P. Metabolic Exchanges Within Tumor Microenvironment. *Cancer Lett* (2015) 380(1):272–80. doi: 10.1016/j.canlet.2015.10.027
123. Kaymak I, Williams KS, Cantor JR, Jones RG. Immunometabolic Interplay in the Tumor Microenvironment. *Cancer Cell* (2021) 39(1):28–37. doi: 10.1016/j.ccell.2020.09.004
124. Camp SM, Ceco E, Evenoski CL, Danilov SM, Zhou T, Chiang ET, et al. Unique Toll-Like Receptor 4 Activation by NAMPT/PBEF Induces NFkappaB Signaling and Inflammatory Lung Injury. *Sci Rep* (2015) 5:13135. doi: 10.1038/srep13135srep13135[pii
125. Torretta S, Colombo G, Travelli C, Boumya S, Lim D, Genazzani AA, et al. The Cytokine Nicotinamide Phosphoribosyltransferase (eNAMPT; PBEF; Visfatin) Acts as a Natural Antagonist of C-C Chemokine Receptor Type 5 (CCR5). *Cells* (2020) 9(2):495–509. doi: 10.3390/cells9020496
126. Van den Bergh R, Morin S, Sass HJ, Grzesiek S, Vekemans M, Florence E, et al. Monocytes Contribute to Differential Immune Pressure on R5 Versus X4 HIV Through the Adipocytokine Visfatin/NAMPT. *PloS One* (2012) 7 (4):e35074. doi: 10.1371/journal.pone.0035074
127. Audrito V, Serra S, Brusa D, Mazzola F, Arruga F, Vaisitti T, et al. Extracellular Nicotinamide Phosphoribosyltransferase (NAMPT) Promotes M2 Macrophage Polarization in Chronic Lymphocytic Leukemia. *Blood* (2015) 125(1):111–23. doi: 10.1182/blood-2014-07-589069blood-2014-07-589069[pii
128. Travelli C, Consonni FM, Sangaletti S, Storto M, Morlacchi S, Grolla AA, et al. Nicotinamide Phosphoribosyltransferase (NAMPT) Acts as a Metabolic Gate for Mobilization of Myeloid-Derived Suppressor Cells. *Cancer Res* (2019) 79(8):1938–51. doi: 10.1158/0008-5472.CAN-18-1544
129. Audrito V, Manago A, Gaudino F, Sorci L, Messana VG, Raffaelli N, et al. NAD-Biosynthetic and Consuming Enzymes as Central Players of Metabolic Regulation of Innate and Adaptive Immune Responses in Cancer. *Front Immunol* (2019) 10:1720. doi: 10.3389/fimmu.2019.01720
130. Naik J, Themeli M, de Jong-Korlaar R, Ruiter RWJ, Poddighe PJ, Yuan H, et al. CD38 as a Therapeutic Target for Adult Acute Myeloid Leukemia and T-Cell Acute Lymphoblastic Leukemia. *Haematologica* (2019) 104(3):e100–e3. doi: 10.3324/haematol.2018.192757
131. Zeijlemaker W, Grob T, Meijer R, Hanekamp D, Kelder A, Carbaat-Ham JC, et al. CD34(+)CD38(-) Leukemic Stem Cell Frequency to Predict Outcome in Acute Myeloid Leukemia. *Leukemia* (2019) 33(5):1102–12. doi: 10.1038/s41375-018-0326-3
132. van de Donk N, Richardson PG, Malavasi F. CD38 Antibodies in Multiple Myeloma: Back to the Future. *Blood* (2018) 131(1):13–29. doi: 10.1182/blood-2017-06-740944
133. Damle RN, Temburni S, Calissano C, Yancopoulos S, Banapour T, Sison C, et al. CD38 Expression Labels an Activated Subset Within Chronic Lymphocytic Leukemia Clones Enriched in Proliferating B Cells. *Blood* (2007) 110(9):3352–9. doi: 10.1182/blood-2007-04-083832
134. Malavasi F, Deaglio S, Damle R, Cutrona G, Ferrarini M, Chiorazzi N. CD38 and Chronic Lymphocytic Leukemia: A Decade Later. *Blood* (2011) 118 (13):3470–8. doi: 10.1182/blood-2011-06-275610
135. Damle RN, Wasil T, Fais F, Ghiotto F, Valetto A, Allen SL, et al. Ig V Gene Mutation Status and CD38 Expression as Novel Prognostic Indicators in Chronic Lymphocytic Leukemia. *Blood* (1999) 94(6):1840–7. doi: 10.1182/blood.V94.6.1840
136. Durig J, Naschar M, Schmucker U, Renzing-Kohler K, Holter T, Huttmann A, et al. CD38 Expression Is an Important Prognostic Marker in Chronic Lymphocytic Leukaemia. *Leukemia: Off J Leukemia Soc America Leukemia Res Fund UK* (2002) 16(1):30–5. doi: 10.1038/sj.leu.2402339
137. Deaglio S, Vaisitti T, Zucchetto A, Gattei V, Malavasi F. CD38 as a Molecular Compass Guiding Topographical Decisions of Chronic Lymphocytic Leukemia Cells. *Semin Cancer Biol* (2010) 20(6):416–23. doi: 10.1016/j.semcancer.2010.08.003
138. Kumar SK, Rajkumar SV, Dispenzieri A, Lacy MQ, Hayman SR, Buadi FK, et al. Improved Survival in Multiple Myeloma and the Impact of Novel Therapies. *Blood* (2008) 111(5):2516–20. doi: 10.1182/blood-2007-10-116129
139. Kawano Y, Moschetta M, Manier S, Glavey S, Gorgun GT, Roccaro AM, et al. Targeting the Bone Marrow Microenvironment in Multiple Myeloma. *Immunol Rev* (2015) 263(1):160–72. doi: 10.1111/imr.12233
140. Lonial S, Weiss BM, Usmani SZ, Singhal S, Chari A, Bahlis NJ, et al. Daratumumab Monotherapy in Patients With Treatment-Refractory Multiple Myeloma (SIRIUS): An Open-Label, Randomised, Phase 2 Trial. *Lancet* (2016) 387(10027):1551–60. doi: 10.1016/S0140-6736(15)01120-4
141. van der Veer MS, de Weers M, van Kessel B, Bakker JM, Wittebol S, Parren PW, et al. The Therapeutic Human CD38 Antibody Daratumumab Improves the Anti-Myeloma Effect of Newly Emerging Multi-Drug Therapies. *Blood Cancer J* (2011) 1(10):e41. doi: 10.1038/bcj.2011.42
142. Khagi Y, Mark TM. Potential Role of Daratumumab in the Treatment of Multiple Myeloma. *Onco Targets Ther* (2014) 7:1095–100. doi: 10.2147/OTT.S49480
143. Garcia-Guerrero E, Gotz R, Doose S, Sauer M, Rodriguez-Gil A, Nerreter T, et al. Upregulation of CD38 Expression on Multiple Myeloma Cells by Novel HDAC6 Inhibitors Is a Class Effect and Augments the Efficacy of Daratumumab. *Leukemia* (2021) 35(1):201–14. doi: 10.1038/s41375-020-0840-y
144. Manna A, Aulakh S, Jani P, Ahmed S, Akhtar S, Coignet M, et al. Targeting CD38 Enhances the Antileukemic Activity of Ibrutinib in Chronic Lymphocytic Leukemia. *Clin Cancer Res* (2019) 25(13):3974–85. doi: 10.1158/1078-0432.CCR-18-3412

145. Wo YJ, Gan ASP, Lim X, Tay ISY, Lim S, Lim JCT, et al. The Roles of CD38 and CD157 in the Solid Tumor Microenvironment and Cancer Immunotherapy. *Cells* (2019) 9(1):26–44. doi: 10.3390/cells9010026
146. Antonioli L, Yegutkin GG, Pacher P, Blandizzi C, Hasko G. Anti-CD73 in Cancer Immunotherapy: Awakening New Opportunities. *Trends Cancer* (2016) 2(2):95–109. doi: 10.1016/j.trecan.2016.01.003
147. Roh M, Wainwright DA, Wu JD, Wan Y, Zhang B. Targeting CD73 to Augment Cancer Immunotherapy. *Curr Opin Pharmacol* (2020) 53:66–76. doi: 10.1016/j.coph.2020.07.001
148. Chen S, Wainwright DA, Wu JD, Wan Y, Matei DE, Zhang Y, et al. CD73: An Emerging Checkpoint for Cancer Immunotherapy. *Immunotherapy* (2019) 11(11):983–97. doi: 10.2217/imt-2018-0200
149. Allard D, Chrobak P, Allard B, Messaoudi N, Stagg J. Targeting the CD73-Adenosine Axis in Immuno-Oncology. *Immunol Lett* (2019) 205:31–9. doi: 10.1016/j.imlet.2018.05.001
150. Perrot I, Michaud HA, Giraudon-Paoli M, Augier S, Docquier A, Gros L, et al. Blocking Antibodies Targeting the CD39/CD73 Immunosuppressive Pathway Unleash Immune Responses in Combination Cancer Therapies. *Cell Rep* (2019) 27(8):2411. doi: 10.1016/j.celrep.2019.04.091
151. Allard B, Allard D, Buisseret L, Stagg J. The Adenosine Pathway in Immuno-Oncology. *Nat Rev Clin Oncol* (2020) 17(10):611–29. doi: 10.1038/s41571-020-0382-2
152. Hasmann M, Schemainda I. FK866, a Highly Specific Noncompetitive Inhibitor of Nicotinamide Phosphoribosyltransferase, Represents a Novel Mechanism for Induction of Tumor Cell Apoptosis. *Cancer Res* (2003) 63 (21):7436–42.
153. Galli U, Colombo G, Travelli C, Tron GC, Genazzani AA, Grolla AA. Recent Advances in NAMPT Inhibitors: A Novel Immunotherapic Strategy. *Front Pharmacol* (2020) 11:656. doi: 10.3389/fphar.2020.00656
154. Dalamaga M, Christodoulatos GS, Mantzoros CS. The Role of Extracellular and Intracellular Nicotinamide Phosphoribosyl-Transferase in Cancer: Diagnostic and Therapeutic Perspectives and Challenges. *Metabolism* (2018) 82:72–87. doi: 10.1016/j.metabol.2018.01.001
155. Sampath D, Zabka TS, Misner DL, O'Brien T, Dragovich PS. Inhibition of Nicotinamide Phosphoribosyltransferase (NAMPT) as a Therapeutic Strategy in Cancer. *Pharmacol Ther* (2015) 151:16–31. doi: 10.1016/j.pharmthera.2015.02.004
156. Lucena-Cacace A, Otero-Albiol D, Jimenez-Garcia MP, Peinado-Serrano J, Carnero A. NAMPT Overexpression Induces Cancer Stemness and Defines a Novel Tumor Signature for Glioma Prognosis. *Oncotarget* (2017) 8 (59):99514–30. doi: 10.18632/oncotarget.20577
157. Zhu Y, Liu J, Park J, Rai P, Zhai RG. Subcellular Compartmentalization of NAD(+) and Its Role in Cancer: A sereNADe of Metabolic Melodies. *Pharmacol Ther* (2019) 200:27–41. doi: 10.1016/j.pharmthera.2019.04.002
158. Chowdhry S, Zanca C, Rajkumar U, Koga T, Diao Y, Raviram R, et al. NAD Metabolic Dependency in Cancer is Shaped by Gene Amplification and Enhancer Remodelling. *Nature* (2019) 569(7757):570–5. doi: 10.1038/s41586-019-1150-2
159. Tateishi K, Wakimoto H, Iafrate AJ, Tanaka S, Loebel F, Lelic N, et al. Extreme Vulnerability of IDH1 Mutant Cancers to NAD+ Depletion. *Cancer Cell* (2015) 28(6):773–84. doi: 10.1016/j.ccell.2015.11.006
160. Travelli C, Aprile S, Mattoteia D, Colombo G, Clemente N, Scanziani E, et al. Identification of Potent Triazolylpyridine Nicotinamide Phosphoribosyltransferase (NAMPT) Inhibitors Bearing a 1,2,3-Triazole Tail Group. *Eur J Med Chem* (2019) 181:111576. doi: 10.1016/j.ejmech.2019.111576
161. Oita RC, Camp SM, Ma W, Ceco E, Harbeck M, Singleton P, et al. Novel Mechanism for Nicotinamide Phosphoribosyltransferase Inhibition of TNF-Alpha-Mediated Apoptosis in Human Lung Endothelial Cells. *Am J Respir Cell Mol Biol* (2018) 59(1):36–44. doi: 10.1165/rcmb.2017-0155OC
162. Quijada H, Bermudez T, Kempf CL, Valera DG, Garcia AN, Camp SM, et al. Endothelial eNAMPT Amplifies Preclinical Acute Lung Injury: Efficacy of an eNAMPT-Neutralising mAb. *Eur Respir J* (2021) 57(5):2002536. doi: 10.1183/13993003.02536-2020
163. Sun X, Sun BL, Babicheva A, Vanderpool R, Oita RC, Casanova N, et al. Direct Extracellular NAMPT Involvement in Pulmonary Hypertension and Vascular Remodeling. Transcriptional Regulation by SOX and HIF-2alpha. *Am J Respir Cell Mol Biol* (2020) 63(1):92–103. doi: 10.1165/rcmb.2019-0164OC
164. Colombo G, Clemente N, Zito A, Bracci C, Colombo FS, Sangaletti S, et al. Neutralization of Extracellular NAMPT (Nicotinamide Phosphoribosyltransferase) Ameliorates Experimental Murine Colitis. *J Mol Med (Berl)* (2020) 98(4):595–612. doi: 10.1007/s00109-020-01892-0
165. Soncini D, Caffa I, Zoppoli G, Cea M, Cagnetta A, Passalacqua M, et al. Nicotinamide Phosphoribosyltransferase Promotes Epithelial-to-Mesenchymal Transition as a Soluble Factor Independent of Its Enzymatic Activity. *J Biol Chem* (2014) 289(49):34189–204. doi: 10.1074/jbc.M114.594721

Conflict of Interest: The authors declare that the research was conducted in the absence of any commercial or financial relationships that could be construed as a potential conflict of interest.

frontiers in Immunology

ORIGINAL RESEARCH
published: 19 August 2021
doi: 10.3389/fimmu.2021.704408

A Methodological Approach Using rAAV Vectors Encoding Nanobody-Based Biologics to Evaluate ARTC2.2 and P2X7 *In Vivo*

Henri Gondé*[1,2], *Mélanie Demeules*[1], *Romain Hardet*[1], *Allan Scarpitta*[1], *Marten Junge*[3], *Carolina Pinto-Espinoza*[3], *Rémi Varin*[1,2], *Friedrich Koch-Nolte*[3], *Olivier Boyer*[1,4] and *Sahil Adriouch*[1]*

[1] Normandie University, UNIROUEN, INSERM U1234, Pathophysiology, Autoimmunity, Neuromuscular Diseases and Regenerative THERapies, Rouen, France, [2] Rouen University Hospital, Department of Pharmacy, Rouen, France, [3] Institute of Immunology, University Medical Center Hamburg-Eppendorf, Hamburg, Germany, [4] Rouen University Hospital, Department of Immunology and Biotherapy, Rouen, France

OPEN ACCESS

Edited by:
Serge Muyldermans,
Vrije University Brussel, Belgium

Reviewed by:
Luciana D'Apice,
National Research Council (CNR), Italy
Arantzazu Alfranca,
Hospital de la Princesa, Spain

***Correspondence:**
Sahil Adriouch
sahil.adriouch@univ-rouen.fr

Specialty section:
This article was submitted to Cytokines and Soluble Mediators in Immunity, a section of the journal Frontiers in Immunology

Received: 02 May 2021
Accepted: 03 August 2021
Published: 19 August 2021

Citation:
Gondé H, Demeules M, Hardet R, Scarpitta A, Junge M, Pinto-Espinoza C, Varin R, Koch-Nolte F, Boyer O and Adriouch S (2021) A Methodological Approach Using rAAV Vectors Encoding Nanobody-Based Biologics to Evaluate ARTC2.2 and P2X7 In Vivo. Front. Immunol. 12:704408. doi: 10.3389/fimmu.2021.704408

On murine T cells, mono-ADP ribosyltransferase ARTC2.2 catalyzes ADP-ribosylation of various surface proteins when nicotinamide adenine dinucleotide (NAD^+) is released into the extracellular compartment. Covalent ADP-ribosylation of the P2X7 receptor by ARTC2.2 thereby represents an additional mechanism of activation, complementary to its triggering by extracellular ATP. P2X7 is a multifaceted receptor that may represents a potential target in inflammatory, and neurodegenerative diseases, as well as in cancer. We present herein an experimental approach using intramuscular injection of recombinant AAV vectors (rAAV) encoding nanobody-based biologics targeting ARTC2.2 or P2X7. We demonstrate the ability of these *in vivo* generated biologics to potently and durably block P2X7 or ARTC2.2 activities *in vivo*, or in contrast, to potentiate NAD^+- or ATP-induced activation of P2X7. We additionally demonstrate the ability of rAAV-encoded functional heavy chain antibodies to elicit long-term depletion of T cells expressing high levels of ARTC2.2 or P2X7. Our approach of using rAAV to generate functional nanobody-based biologics *in vivo* appears promising to evaluate the role of ARTC2.2 and P2X7 in murine acute as well as chronic disease models.

Keywords: P2X7 (purino) receptor, AAV vectors, nanobodies (V_{HH}), animal models, extracellular ATP (eATP), extracellular NAD^+, methodological approach

INTRODUCTION

Nicotinamide adenine dinucleotide (NAD^+) is a key molecule in cellular metabolism and acts as an intermediate in several essential enzymatic reactions (1). In addition, in response to cellular stress, intracellular NAD^+ is released into the extracellular compartment and serves as a substrate for various ectoenzymes (2, 3). Mono-ADP ribosyl transferases (ART) represent a family of ectoenzymes that use extracellular NAD^+ to catalyze posttranslational modification of cell surface proteins by the transfer of ADP-ribose to specific amino-acid residues (4, 5). In mice, the ART family comprises six members: ARTC1-5, including two isoforms of ARTC2, termed ARTC2.1 and ARTC2.2 (6). While ARTC2.1 is enzymatically inactive in the absence of reducing agents, ARTC2.2 is active in standard conditions and is able to ADP-ribosylate multiple cell-surface protein-targets when NAD^+ is present in the extracellular space (7, 8). ARTC2.2 is localized predominantly on the surface of murine T cells as a 35 kDa GPI-anchored ectoenzyme. Although its levels of expression varies depending on mouse strain and cell-activation status, membrane expression of ARTC2 remains overall higher on $CD8^+$ T cells as compared to $CD4^+$ T cells (9). When murine T cells are exposed to micromolar levels of extracellular NAD^+, ARTC2.2 catalyzes the ADP-ribosylation of exposed arginines in several cell surface protein targets, including the purinergic P2X7, a well described protein expressed by immune cells and involved in immune regulation (10, 11).

P2X7 assembles at the cell surface as a homo-trimeric receptor that forms a nonselective ion channel upon gating with high extracellular ATP concentrations (*i.e.*, in the hundreds micromolar range). Depending on ATP concentration and on the extent of cell exposition, activation of P2X7 receptor can lead to multiple cellular events starting by the rapid activation of surface metalloproteases (leading to shedding for instance of CD62L and CD27) and by the externalization of phosphatidylserine (11). Prolonged P2X7 receptor activation induces the formation of nonselective pores and to massive membrane depolarization, ultimately leading to cell death (3). Interestingly, prolonged P2X7 activation can also be triggered by brief exposition to extracellular NAD^+. Indeed, in the presence of extracellular NAD^+, ARTC2.2 catalyzes covalent ADP-ribosylation of P2X7 at the arginine residue 125, located in the vicinity of the ATP-binding site, and thereby triggers the activation of P2X7 receptor (10). Remarkably, much lower concentrations of extracellular NAD^+ (*i.e.*, in the micromolar range) are sufficient to activate P2X7 receptor and to induce cell death (12, 13). This process was termed NAD-induced cell death (NICD) and demonstrated to play a major role *in vivo* in the fate and regulation of immune cells that express high levels of ARTC2.2 and P2X7, including regulatory T cells (Treg), invariant NKT cells, follicular helper T cells (Tfh), and tissue-resident memory T cells (T_{RM}) (12, 14–18).

Nanobodies are derived from unconventional natural antibodies devoid of light chains that are found in llamas and other camelids (19–21). The single-chain variable fragment of the so-called heavy-chain antibodies is termed V_{HH} or nanobody. Nanobodies exhibit similar specificities and affinities than conventional antibodies but are smaller in size (15 kDa) and present a complementary determining region 3 (CDR3) that is usually longer, with the remarkable propensity to reach protein cavities that are otherwise difficult to target with conventional antibodies, offering opportunities to engineer these molecules into original biologics (22). Such cavities often correspond to functional regions and allosteric sites, conferring to nanobodies the ability to act as modulators of enzyme and receptor activities (*e.g.*, potentiating or blocking). Anti-ARTC2.2 nanobodies have been isolated by phage display from llamas immunized with cDNA expression vectors encoding full-length ARTC2.2 (23). Nanobodies s-14, s+16a, s+16b and l-17 are able to bind with high specificity cell line stably transfected to express ARTC2.2. In addition, T cells can be protected from NICD by ARTC2.2-blocking nanobodies s+16a, s+16b and l-17, but not s-14 (23). In additional studies, intravenous (i.v.) injection of the ARTC2.2-blocking nanobody s+16a prevented NICD in cells co-expressing ARTC2.2 and P2X7 *ex vivo* as well as *in vivo*. ARTC2.2 antagonism has hence been recognized as a crucial step for the functional studies of Treg, NKT and T_{RM} subsets (14–16, 24). Anti-P2X7 nanobodies were generated in a similar manner (25, 26). Taking advantage of the single-chain structure of nanobodies, we derived highly specific P2X7-potentiating nanobody 14D5 and P2X7-blocking nanobody 13A7 either as homodimers fused to the Alb8 albumin-binding nanobody (*i.e.*, to provide improved half-life *in vivo*) or fused to the Fc-region of mouse conventional antibody to reconstitute the bivalent heavy chain antibody (hcAb) format of camelids (25, 27). Nanobody-based hcAb therefore offer the possibility not only to increase their half-life *in vivo* but also to provide effector functions related to the Fc-region that can bind to Fc-receptors (FcR) at the surface of immune cells or activate the classical complement cascade (26). Depending on the isotype, it is then possible to promote antibody-dependent cell cytotoxicity (ADCC), complement-dependent cell cytotoxicity (CDC) and antibody-dependent phagocytosis (ADCP). Interestingly, hinge and/or Fc-region engineering can further enhance Fc-fused nanobody half-life or fine tune effector properties by enhancing or abolishing FcγR and/or complement related effector functions (28).

In this study, we report two different strategies for manipulating the ARTC2.2/P2X7 pathway *in vivo*, with the aim of better addressing the versatile role of NAD^+ and ATP in immune cells. For that, we developed a methodology that rely on nanobody-based biologics expressed directly *in vivo* upon a single intramuscular (i.m.) administration of recombinant AAV vectors (rAAV) encoding the biological constructs. We demonstrated here the ability to durably block the activity of ARTC2.2 enzyme or of the P2X7 ion channel *in vivo* upon a single i.m. injection of the rAAV encoding a construct containing the ARTC2.2-blocking nanobody s+16a, or a construct containing the P2X7-blocking nanobody 13A7. In addition, we provide evidence that P2X7 can be potentiated *in vivo* using an rAAV encoding a construct containing the P2X7-potentiating nanobody 14D5. In another strategy, based on the fusion of specific nanobodies to mouse IgG2a, to generate a heavy chain antibody (hcAb) format, we demonstrate durable depletion of cells expressing high levels of ARTC2.2 *in vivo*. These methodologies represent valuable tools that might be used in future studies to better delineate the role of the NAD^+/ARTC2.2/P2X7 pathway *in vivo* in various pathophysiological situations including inflammatory diseases, and immune responses to infectious pathogens or to tumor cells.

Abbreviations: NAD^+, nicotinamide adenine dinucleotide; ART, ADPribosyltransferase; hcAb, heavy chain antibody; dimHLE, dimer half-life extended; rAAV, recombinant adeno-associated virus used as a vector; AAVnano, methodological approach based on the injection of rAAV encoding for nanobody-based biologics.

MATERIAL AND METHODS

Mice, Reagents, Antibodies

C57BL/6 wild-type mice obtained from Janvier Labs were used for all experiments. Mice were housed in a specific pathogen-free facility and were aged of 8 weeks at the beginning of experiments. All animal experiments were approved by the local institutional ethic committee.

Adenosine 5'-tri-phosphate disodium salt (A2383) and β-nicotinamide adenine dinucleotide hydrate (N7004) were purchased from Sigma Aldrich. Red blood cell (RBC) lysis/fixation Solution, True-Nuclear transcription factor buffer set, fluorochrome-conjugated streptavidin, and antibodies to CD45 (clone 30-F11), CD4 (RM4-5), CD8 (53-6.7), CD25 (PC-61), CD19 (1D3/CD19), B220 (RA3-6B2), FoxP3 (MF-14), CD27 (LG.3A10), CD62L (MEL-14), CD69 (H1.2F3) or P2X7R (1F11), and purified CD16/CD32 (TruStain FcX) were obtained from Biolegend or Sony Biotechnology. Rabbit polyclonal antibody K1G, specific to mouse P2X7, was described in our previous studies (12, 13). K1G was used to stain P2X7 at the surface of blood myeloid cells as illustrated in **Supplemental Figure 3**, using a secondary donkey anti-rabbit IgG from Jackson ImmunoResearch. Biotinylated polyclonal antibody specific to mouse IgGa was obtained from Jackson ImmunoResearch and monoclonal antibody to ARTC2.2 (Nika102) from Novus Biologicals.

Flow Cytometry Analyses

For evaluation of P2X7 and ARTC2.2 expression on T cells, splenocytes were collected and single-cell suspensions were prepared and washed using standard procedures. Cells were stained with fluorochrome-conjugated antibodies, including anti-P2X7 and anti-ARTC2.2 or related isotype controls before fixation and red blood cell lysis using the RBC lysis/fixation Solution (Sony biotechnology).

For evaluation of P2X7-dependent shedding of CD27 and CD62L upon *ex vivo* exposition to NAD^+ or ATP, blood samples were collected, washed, resuspended into PBS (without Ca^{2+} and Mg^{2+}), and divided into 4 tubes. Cells were then treated with 30 μM ATP, 150 μM ATP, or 30 μM NAD^+, or left untreated. After incubation for 15 min at 37°C, cells were washed in cold D-PBS containing 10% FBS, and stained on ice with fluorochrome-conjugated antibodies before fixation and RBC lysis. The percentages of cells co-expressing CD27 and CD62L were then evaluated by flow cytometry.

For evaluation of the binding of the dimHLE constructs on liver NKT cells and liver T_{RM}, single cells suspension were prepared and stained with a mouse IgG1 mAb that specifically recognizes the Alb8 nanobody (kindly provided by Dr. Catelijne Stortelers, Ablynx nv, Zwijnarde, Belgium), followed by a secondary mouse IgG1-specific mAb. To evaluate the levels of occupation of the target protein, cells were incubated *in vitro* with a saturating concentration of the same recombinant nanobody construct as the one produced *in vivo*, followed by the same secondary detection reagents. This allowed estimation of signal saturation that correlates with target occupation by bounded biologics. Similar MFI were obtained with or without addition *in vitro* of the corresponding recombinant nanobody construct, confirming that target occupancy reached saturation *in vivo* (data not shown). To distinguish vascular T cells from liver parenchyma cells, a fluorochrome-conjugated CD45-specific mAb has been injected i.v. (CD45iv) 3 min before sacrifice and preparation of liver lymphocytes. This procedure allowed the staining of vascular T cells *in vivo* (CD45iv^{high}) while liver resident T cells remained mostly unstained (CD45iv^{low}). Untransduced mice additionally received 50 μg of recombinant s+16a-dim construct (i.e., a dimer of s+16a that does not contain the Alb8 nanobody, and that cannot be detected by the anti-Alb8 mAb77 detection system) 30 min before organ collection to prevent NICD and cell loss *ex vivo* during cell preparation, as described earlier (15, 18). All cells were counterstained with mAbs directed against CD45 (coupled to a different fluorochrome than CD45iv), CD4, and CD69 (marker of tissue resident lymphocytes). To distinguish the NKT subset, cells were stained with PE-conjugated CD1d-tetramer loaded with, an analogue of α-galatosylceramide (αGal/Cer), kindly provided by the NIH tetramer core facility.

For evaluation of the binding capacity of the nanobody-based hcAb on T cells surface, samples were collected, washed, resuspended into FACS buffer and stained with isotype specific secondary antibodies, i.e. Ab directed against mouse IgG1 (to detect 13A7-IgG1^{LSF} hcAb), or Ab directed against mouse IgG2a (for detection of 7E2-IgG2a or s-14-IgG2a hcAb). Cells were washed and counterstained with fluorochrome-conjugated antibodies directed against the indicated cell surface markers.

Flow cytometry measurements were performed using a LSRFortessa or a FACSCanto-I (BD Biosciences) apparatus and subsequent analyses were performed using FlowJo software (Tree Star, Ashland, OR).

Nanobody Constructs

Some of the constructs used in this study were based on nanobody dimers ("dim" format) fused to the Alb8 anti-albumin nanobody (half-life extended "HLE" format) (25, 29). 14D5-dimHLE and s+16a-dimHLE were constructed by fusing the coding sequences of two 14D5 nanobodies or two s+16a nanobodies using a 35-GS linker $(GGGGS)_7$. These homodimeric bivalent constructs were then fused to the anti-albumin nanobody Alb8 *via* a 9-GS linker (GGGGSGGGS) (25). The P2X7-blocking 13A7-IgG1^{LSF} hcAb was constructed by fusing the nanobody 13A7 to the hinge region and Fc region of a mutated mouse IgG1 antibody carrying the "LSF" mutations (T252L, T254S, T256F) (30). For the design of the depleting hcAb constructs 7E2-IgG2a and s-14-IgG2a, anti-P2X7 nanobody 7E2 or anti-ARTC2.2 nanobody s-14, were fused to the hinge and Fc-region of a mouse IgG2a using 5-GS linker (GGGGS).

Production of rAAV and Muscle Transduction

For the production of rAAV, all constructs were cloned into a pFB plasmid under the control of either a CBA promoter (for rAAV1 constructs encoding 14D5-dimHLE, 13A7-IgG1^{LSF} and s+16a-dimHLE) or under the related CASI promoter (for rAAV8 constructs encoding 7E2-IgG2a and s-14-IgG2a) (31, 32). Production, purification, and titration of rAAV1 and rAAV8 were performed by Virovek (Hayward, California, USA) using the baculovirus expression system in Sf9 insect cells (31). For muscle transduction, mice hind legs were shaved under anesthesia and 100 µL diluted rAAV were injected into 4 gastrocnemius muscle sites to reach a total dose of 10^{11} viral genomes (vg) per mouse.

NAD$^+$ Treatment *In Vivo*

Injections of rAAV encoding either 13A7-IgG1^{LSF} hcAb or 14D5-dimHLE were performed i.m. on day 0 and followed 28 days later by the i.v. injection of 30 mg NAD$^+$ diluted in 200 µL PBS (pH adjusted to 7.4) as described earlier (24). Splenocytes were collected 24 h later and single-cell suspensions were prepared on ice and stained with fluorochrome-coupled antibodies. After fixation, RBC lysis, permeabilization and intracellular staining, single cell suspensions were analyzed by flow cytometry. Absolute cell numbers collected for each spleen was evaluated by direct enumeration using an automated cell counter (ADAM-MC apparatus). Percentages of CD4$^+$ and CD8$^+$ T cells were determined by flow cytometry and compared to CD19$^+$ B cells taken as an NAD$^+$-insensitive reference population.

Statistical Analysis

All data are shown as mean values and error bars represent standard error of the mean (SEM). Statistical comparison between experimental groups was performed using one-way analysis of variance (ANOVA). Differences were considered statistically significant when p values were less than 0.05 (*), 0.01 (**), or 0.001 (***). All calculations were performed using the Prism software (Graphpad, La Jolla, CA).

RESULTS

Nanobody Constructs and rAAV Used to Study the Role of ARTC2.2 and P2X7 *In Vivo*

The ARTC2.2/P2X7 axis regulates murine T cell function, differentiation and cell fate. Both proteins are expressed on T cell subsets but at different cell surface levels. Consistent with previous studies (12, 13, 24), P2X7 and ARTC2.2 were detected on CD4$^+$CD25$^+$ Treg, CD4$^+$CD25$^-$ conventional CD4$^+$ T cells (Tconv), and on CD8$^+$ T cells. P2X7 is expressed at higher level on the surface of Treg and to a lesser extent on CD4$^+$ Tconv and on CD8$^+$ T cells (**Figure 1A**, upper panels). ARTC2.2 is expressed at higher levels on CD8$^+$ T cells as compared to CD4$^+$ T cell subsets (**Figure 1A**, lower panels). To explore the role of P2X7 and ARTC2.2 *in vivo*, we developed a methodological approach based on rAAV encoding various formats of P2X7-specific or ARTC2.2-specific nanobody-based constructs. To increase their half-life and avidity, we developed bivalent nanobodies fused to the albumin-specific nanobody Alb8 (dimer Half-Life Extended format, termed “dimHLE”) (**Figure 1B**). In a second approach, we fused nanobodies to the hinge and Fc region of conventional IgG antibodies (heavy-chain antibodies format, “hcAb”) (**Figure 1B**). Mouse IgG1 Fc subclass is known to only mediate low, if any, effector functions as it binds to the inhibitory FcγRIIB and to only one member of the activating receptors, the low affinity FcγRIII (33). IgG1 also binds to the neonatal FcRn involved in antibody recycling and persistence *in vivo*. To further increase the half-life of our constructs, we took advantage of the described “LSF” point mutations (*i.e.*, T252L, T254S, T256F), known to further ameliorate *in vivo* persistence by increasing the binding to FcRn (30), to generate the mIgG1^{LSF} hcAb construct (**Figure 1B**). In contrast to mouse IgG1, mIgG2a subclass binds all mouse activating FcγR and triggers Fc-related effector functions (**Figure 1B**) (33).

In our methodological approach to target ARTC2.2 and P2X7 on T cells *in vivo*, implemented and evaluated here, we injected rAAV1 or rAAV8 encoding nanobody-based constructs instead of the corresponding purified recombinant proteins. Both rAAV1 and rAAV8 serotypes are known to efficiently transduced muscle cells upon i.m. injection. We aimed at eliciting directly *in situ* the long-term and stable production of the selected construct following a single administration of the corresponding rAAV. This approach was termed AAVnano (**Figure 1C**).

We explored here two complementary strategies for manipulating *in vivo* the NAD$^+$ pathway dependent on ARTC2.2 and P2X7. (**Figure 2**). The first strategy relies on the propensity of nanobodies to bind to functional sites and thereby modulate their enzymatic activity or receptor functions. We used constructs based on nanobodies selected for their remarkable ability to block ARTC2.2 enzymatic activity (nanobody s+16a, used here as a dimHLE format), to inhibit gating of the P2X7 ion channel (nanobody 13A7, used as IgG1^{LSF} hcAb format), or to potentiate P2X7 activity (nanobody 14D5, used as dimHLE format) (**Figure 2A**). The choice of the format for each biological construct (*i.e.*, dimHLE, or IgG1^{LSF} hcAb formats) was based on preliminary experiments comparing the efficacy of each formats (data not shown). The second strategy relies on the possibility to deplete target cells expressing high levels of ARTC2.2 or P2X7. For that, we used hcAb engineered to contain the mIg2a Fc-region, known to promote binding to FcR on immune cells and to promote ADCC by NK cells, ADCP by macrophages, and to facilitate CDC upon engagement on the classical complement pathway (**Figure 2B**). To facilitate the interpretation of their effect *in vivo*, these latter constructs were based on other nanobodies that do not modulate the functional activity of their target (*i.e.*, ARTC2.2-specifc nanobody s-14 (23) and P2X7-specifc nanobody 7E2 (25)) that were fused to the hinge and Fc-region of mouse IgG2a (**Figures 1B, C**).

Functional Modulation of ARTC2.2 or P2X7 Using rAAV Coding for Biologics With Blocking or Potentiating Properties

To evaluate our AAVnano approach and the ability of our constructs to modulate their target proteins, we first indirectly studied the activity of P2X7 and ARTC2.2 on T cells harvested

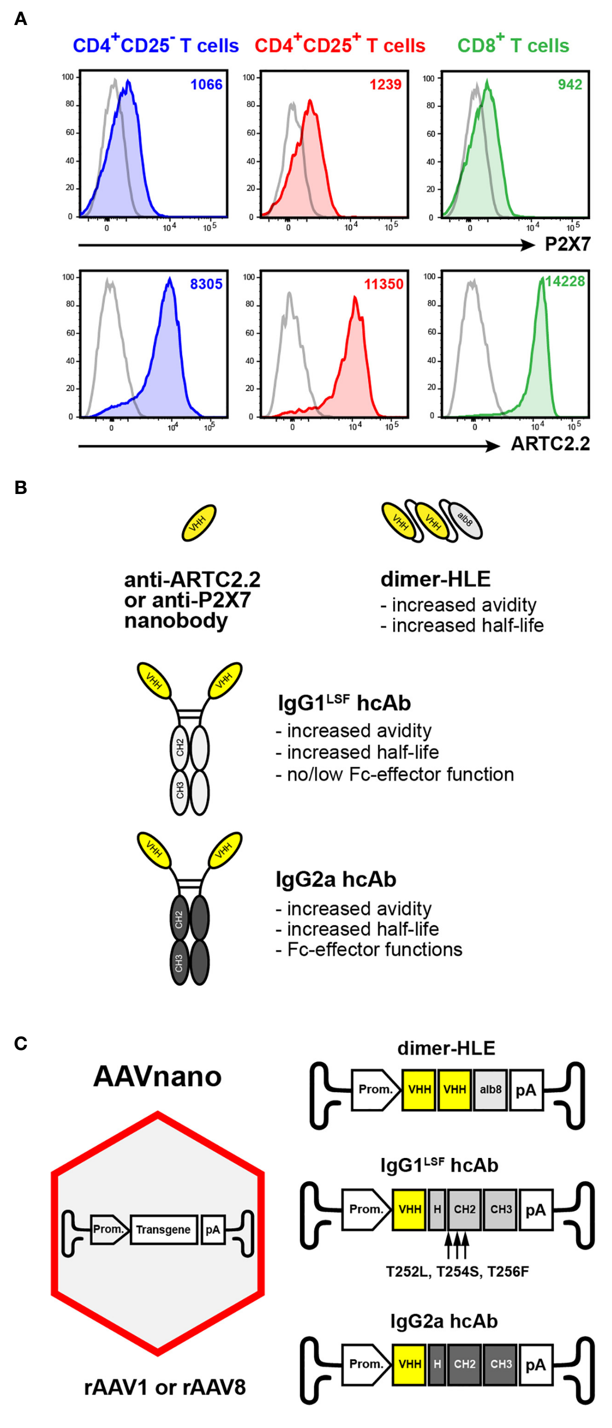

FIGURE 1 | Continued

FIGURE 1 | AAVnano methodological approach to study the role of P2X7 or ARTC2.2 *in vivo*. **(A)** Expression of ARTC2.2 and P2X7 T cell subsets. Splenocytes from C57BL/6 mice were stained with fluorochrome-conjugated monoclonal antibodies directed against P2X7 (clone 1F11), or ARTC2.2 (clone Nika102), or with the corresponding isotype controls (grey), and were analyzed by flow cytometry. Cells were gated on $CD4^+CD25^-$ T cells (Tconv, depicted in blue), on $CD4^+CD25^+$ (Treg, depicted in red), or on $CD8^+$ T cells (depicted in green) to evaluate the cell surface levels of P2X7 or ARTC2.2 on each subset. The numbers in the upper right quadrants indicate the mean fluorescence intensity (MFI). Staining was performed using fluorochrome conjugated antibodies specific to CD45 (coupled to BV510), CD4 (BV786), CD8 (BV605), CD25 (PE-Cy7), P2X7 (BV421) and ARTC2.2 (AF647). **(B)** Schematic representation of nanobody-based constructs. ARTC2.2-specific and P2X7-specific nanobodies (V_{HH}) are engineered either as bivalent dimers fused to the albumin-specific nanobody Alb8 (dimer half-life extended, termed “dimHLE”), or as heavy-chain antibodies (termed hcAb) when fused to the hinge and Fc-region of conventional mouse IgG antibodies. For the latter, nanobodies were fused to either a mouse IgG1 hinge/Fc-region bearing the LSF mutations (*i.e.*, T252L, T254S, T256F) to produce hcAb with no/low Fc-effector functions, or to the hinge/Fc-region of mouse IgG2a to generate cell-depleting hcAb. **(C)** Schematic representation of the AAVnano methodological approach and the structure of the transgenes incorporated in the rAAV (of serotype 1 or 8). The illustrated transgenes encode the nanobody-based constructs depicted in **(B)** Upon a single i.m. injection of the rAAV, the nanobody-based biologics are produced *in vivo* by the transduced muscle cells under the control of a CBA (rAAV1) or a CASI (rAAV8) promoter (Prom.).

from AAVnano injected mice. Exposure of T cells to ATP or NAD^+ induces the shedding of CD27 and CD62L by metalloproteases and this can be used as a sensitive assay to monitor P2X7 receptor activation (13, 24). For that, we injected rAAV1 encoding 13A7-IgG1^{LSF} hcAb (*i.e.*, to inhibit P2X7), 14D5-dimHLE (*i.e.*, to potentiate P2X7), or s+16a-dimHLE (*i.e.*, to inhibit ARTC2.2). Blood cells were collected 17-120 days after rAAV injection, incubated at 37°C in the absence or in the presence of NAD^+ (30 µM) or ATP (30 µM or 150 µM) to assay *ex vivo* P2X7-dependent shedding of CD27 and CD62L. Representative data obtained 30 days after AAVnano injection are shown in **Figure 3**. Comparable results were obtained from the earliest studied time point at day 17 to the last time point of the study at day 120. The results show that T cells from untransduced mice displayed P2X7-dependent shedding of CD27 and CD62L within 15 min after incubation with ATP or NAD^+ (**Figures 3A, B**). This was noticeably more pronounced on $CD4^+CD25^+$ Treg that express higher levels of P2X7 as compared to Tconv and to $CD8^+$ T cells (**Figure 3B**). Injection of AAVnano coding for 14D5-dimHLE sensitized T cells to P2X7-dependent shedding, notably also on the T cell subsets that express the lowest levels of P2X7 (*i.e.*, Tconv and $CD8^+$ T cells) as compared to untransduced control mice. In contrast, mice injected with the AAVnano coding for 13A7-IgG1^{LSF} hcAb were almost completely protected from NAD^+- and ATP-induced P2X7 activation, and only Treg cells displayed limited CD27 and CD62L shedding when incubated with the highest dose of ATP (**Figure 3B**). T cells from mice injected with the AAVnano coding for s+16a-dimHLE were protected from NAD^+-induced, but not from ATP-induced shedding of CD27 and CD62L, as expected from a nanobody construct that inhibits ARTC2.2 activity (**Figure 3B**). For comparison, we also evaluated the effects mediated by recombinant nanobody-based biologics added directly *in vitro* on cells from untreated animals (**Supplemental Figure 1**). We observed in dose-response experiments that each recombinant construct used at

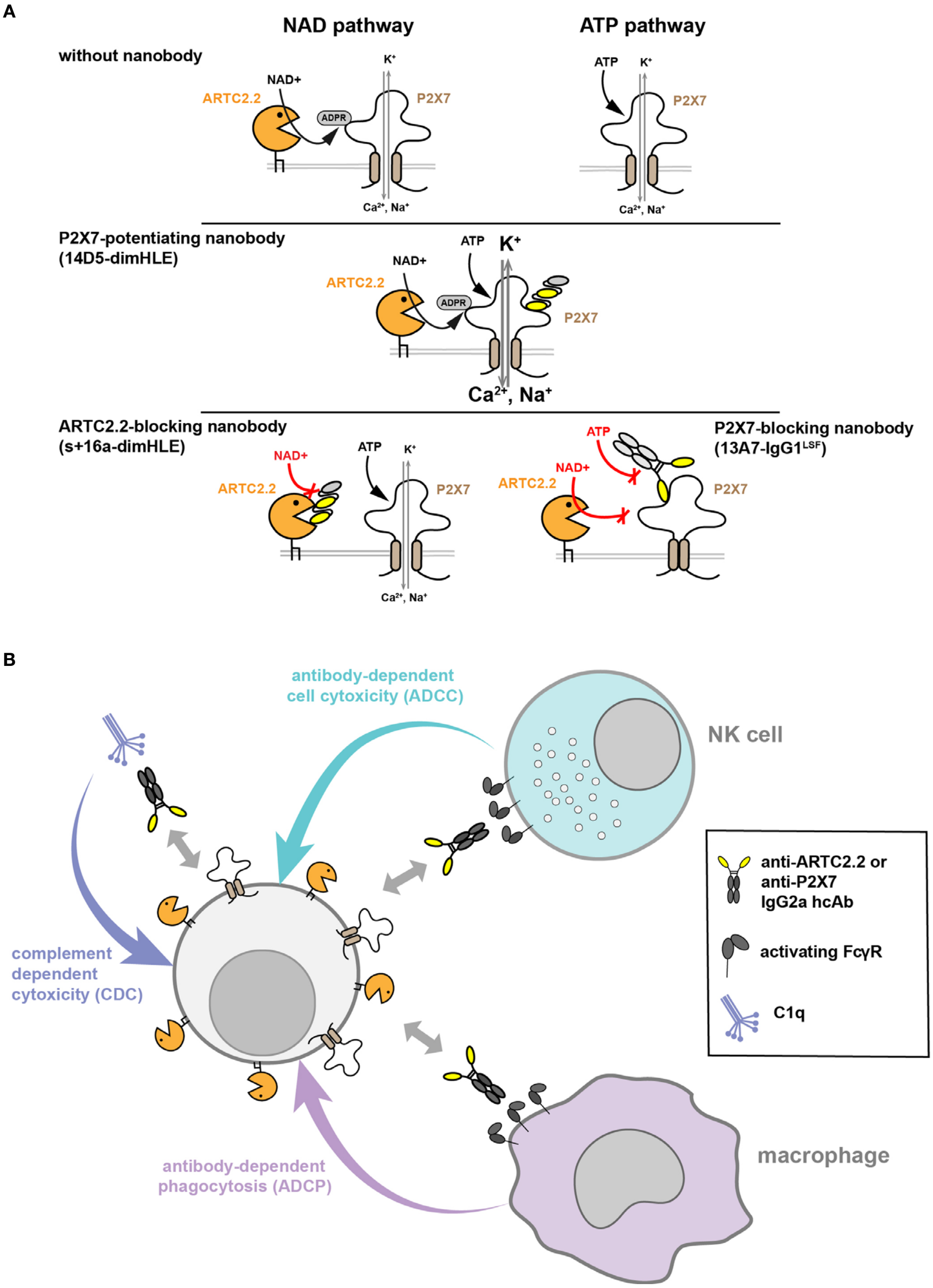

FIGURE 2 | Strategies used to manipulate ARTC2.2 or P2X7 functions *in vivo* or to deplete T cells expressing these proteins. **(A)** Modulation of ARTC2.2 and P2X7 activity using nanobody-based constructs. Two pathways can lead to the activation of P2X7 at the surface of mouse T cells. The ATP pathway involves direct gating of P2X7 ion channel by extracellular ATP. The NAD$^+$ pathway involves a post-translational modification of P2X7 catalyzed by the ectoenzyme ARTC2.2 resulting in its covalent ADP-ribosylation. The 14D5-dimHLE construct probably binds to an allosteric site on P2X7 and potentiates gating of the ion channel triggered by either ATP or NAD$^+$. The s+16a-dimHLE construct was designed to block ARTC2.2 enzymatic activity *in vivo* and thereby to inhibit activation of P2X7 by the NAD$^+$ pathway (but not the ATP pathway). The 13A7-IgG1^{LSF} hcAb construct inhibits P2X7 gating and can be used to inhibit both ATP and NAD$^+$ pathways. **(B)** Other nanobody-based constructs were designed to favor depletion of their target cells *in vivo*. For that, nanobodies s-14 and 7E2, that bind respectively to ARTC2.2 and P2X7 but do not modulate their functions, were fused to the hinge and Fc-region of mIgG2a. The resulting mIgG2a hcAb could mediate cell depletion through different mechanisms such as complement-dependent cytotoxicity (CDC), antibody-dependent cell cytotoxicity (ADCC) that rely on NK cells, and antibody-dependent cell phagocytosis (ADCP) involving macrophages.

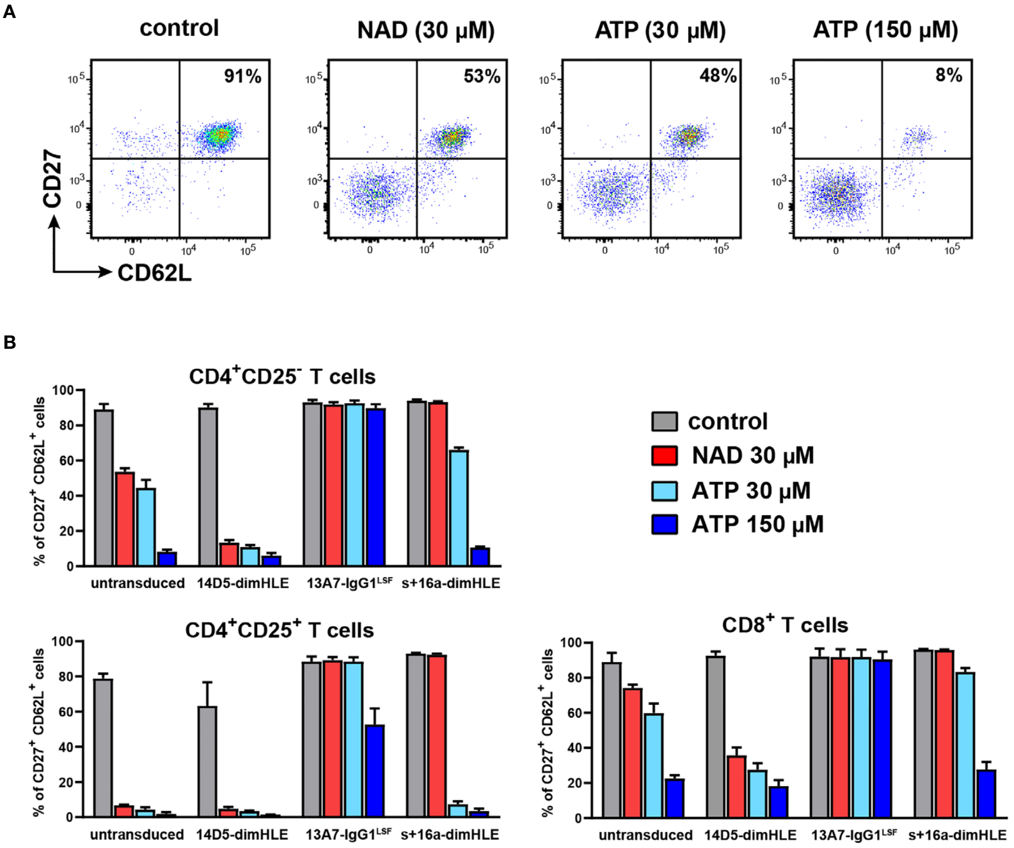

FIGURE 3 | AAVnano modulate P2X7-dependent shedding of CD27 and CD62L *ex vivo.* C57BL/6 mice were injected i.m. with PBS (control) or with rAAV1 encoding P2X7-potentiating 14D5-dimHLE, P2X7-blocking 13A7-IgG1^{LSF} hcAb or ARTC2.2-blocking s+16a-dimHLE. Blood samples were collected at different time points ranging from day 17 to day 120 after rAAV injections. Cells were then incubated for 15 min at 37°C with PBS, 30 µM ATP, 150 µM ATP or 30 µM NAD$^+$ to induce P2X7-dependent shedding of CD27 and CD62L on T cells. Representative results obtained 30 days after rAAV injection are shown. **(A)** Representative flow cytometry plots illustrating shedding of CD27 and CD62L on gated CD4$^+$CD25$^-$ T cells harvested from control mice. Numbers indicate percentages of CD27$^+$CD62L$^+$ cells. **(B)** Mean percentages of CD27$^+$CD62L$^+$ cells among gated CD4$^+$CD25$^+$, CD4$^+$CD25$^-$ and CD8$^+$ T cells after incubation with PBS (grey), 30 µM NAD$^+$ (red), 30 µM ATP (cyan) or 150 µM ATP (blue). Staining was performed using fluorochrome conjugated antibodies specific to CD45 (coupled to APC-Cy7), CD4 (FITC), CD8 (PE-Cy7), CD25 (PE), CD27 (PerCP-Cy5.5) and CD62L (APC). Errors bars represent the SEM, n=3.

saturating doses *in vitro* induced a comparable effect that the one observed *ex vivo* on cells collected from AAVnano transduced mice. These data hence suggest that i.m. injection of AAVnano induce *in vivo* production of each encoded construct in sufficient quantity to substantially inhibit or potentiate the functional activity of their target, at a level that appears to be similar to the one obtained *in vitro* with saturating doses of each given recombinant nanobody construct.

Evaluation of Tissue Resident T Cells *In Vivo* Following Administration of rAAV Coding for Biologics

To determine whether our methodological approach could be used to reach ARTC2.2 and P2X7 on tissue resident T cells, we next sought to detect the presence of the biologics on resident liver T cells 120 days after rAAV injection. For that, we focused at the end of the experiment (*i.e.*, upon sacrifice of animals) on liver tissue-resident memory T cells (T_{RM}) and for comparison on liver vascular T cells as well. Liver T_{RM} co-express higher levels of ARTC2.2 and P2X7 than conventional T cells (18) (**Figure 4**). In order to discriminate tissue resident from vascular lymphocytes, we intravenously injected a fluorochrome-conjugated CD45-specific mAb 3 min before sacrifice. In this short period of time, the injected antibody stains vascular, but not tissue resident lymphocytes (34). In order to detect the rAAV-encoded s+16a-dimHLE or 14D5-dimHLE, we used a monoclonal antibody (mAb77) that specifically recognizes the Alb8 nanobody, and for detection of 13A7-IgG1^{LSF}, we used a mouse IgG1-specific secondary antibody. We further stained cells with a CD4-specific mAb and an αGal/Cer-loaded CD1d tetramer to distinguish NKT cells from other CD4$^+$ T cells. NKT cells are also known to co-express high levels of ARTC2.2 and P2X7 and to be highly sensitive to NAD$^+$ induced cell death (NICD) (18). Cells were counterstained with a fluorochrome-

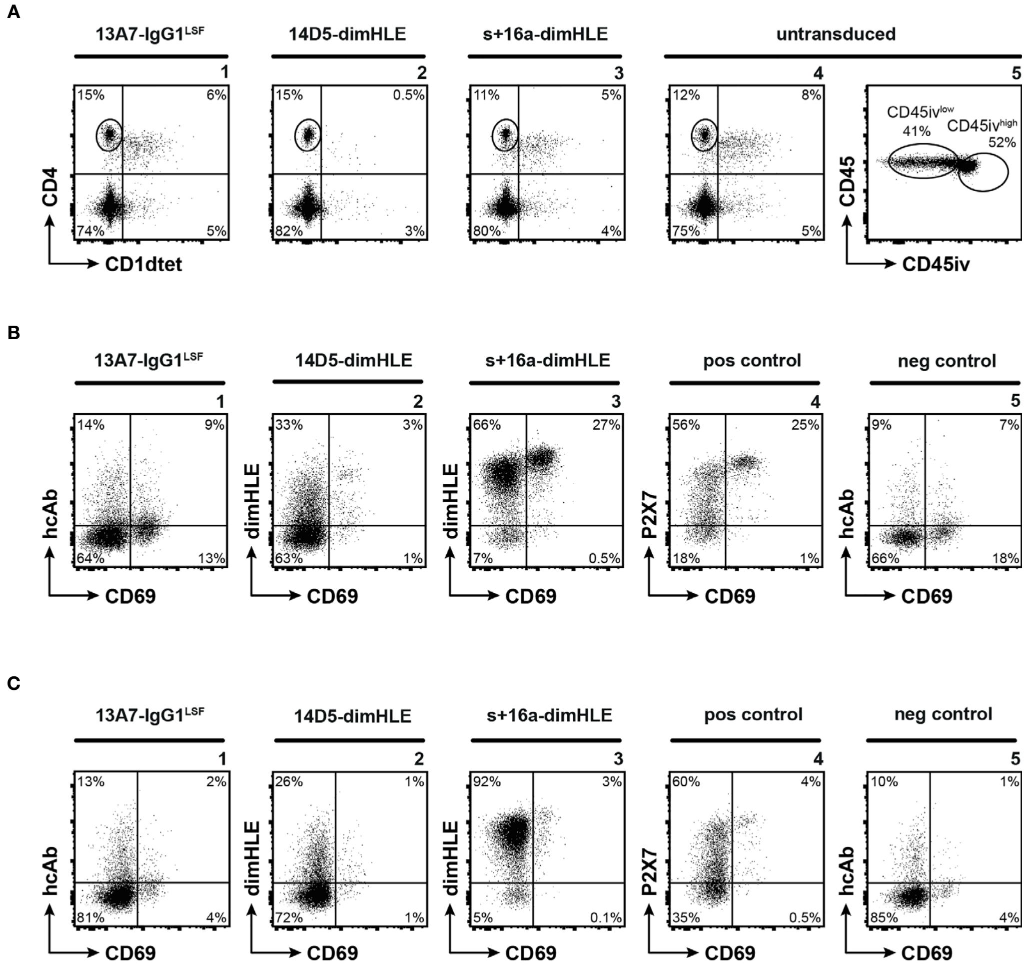

FIGURE 4 | Nanobody-based biologics produced *in vivo* following rAAV injection reach ARTC2.2 and P2X7 expressed at high levels by T_{RM} located in the liver parenchyma. C57BL/6 mice were injected i.m. with rAAV1 encoding P2X7-blocking 13A7-IgG1^{LSF} hcAb, P2X7-potentiating 14D5-dimHLE, or ARTC2.2-blocking s+16a-dimHLE, or with PBS (untransduced). 120 days after rAAV injection mice received an intravenous injection of fluorochrome-conjugated CD45-specific mAb (CD45iv) 3 min before sacrifice. Untransduced mice additionally received 50 µg of recombinant s+16a-dim construct 30 min before organ collection to prevent NICD and cell loss *ex vivo* during cell preparation, as described earlier (15, 18). Cells extracted from the liver were then counterstained with mAbs directed against CD45, CD4, and CD69 (i.e., a marker of tissue resident lymphocytes) and with a CD1d-tetramer (CD1dtet) loaded with αGal/Cer (specifically labels the invariant T cell receptor of NKT cells). **(A)** Representative flow cytometry plots illustrating liver CD4$^+$ T cells and CD4$^+$CD1dtet$^+$ NKT cells (panels 1-4), and the gating of parenchymal (CD45iv^{low}) and vascular (CD45iv^{high}) CD4$^+$CD1dtet$^-$ lymphocytes (panel 5). **(B, C)** Representative flow cytometry plots illustrating the detection of the nanobody-based constructs on the cell surface of tissue resident CD45iv^{low} **(B)** and vascular CD45iv^{high} **(C)** CD4$^+$CD1dtet$^-$ T cells. To detect cell surface bound dimHLE constructs, cells were stained with Alb8-specific mAb77 (mouse IgG1) followed by an mIgG1-specific secondary mAb. To detect cell surface bound 13A7-IgG1^{LSF}, cells were stained directly with the secondary mIgG1-specific mAb. Positive (pos) control staining was performed with liver cells from untransduced mice using the P2X7-specific 13A7-dimHLE, mAb77, and the mIgG1-specific secondary mAb. Negative (neg) control staining was performed with the secondary detection reagents alone. Numbers indicate the percentages of cells in the respective quadrants or gates (**A**, panel 5). Staining was performed using fluorochrome conjugated antibodies specific to CD45 (coupled to PerCP-Cy5.5 for the one injected i.v. and to AF700 for the one added *in vitro*), CD4 (APC), CD69 (FITC), mouse IgG1 (BV421) and CD1dtet (coupled to PE).

conjugated mAb against CD69, a marker that is highly expressed by many tissue resident T cells but by only few if any vascular T cells (35, 36). Untransduced mice were used as control and were given recombinant s+16a-dim 30 min before sacrifice to prevent NICD and cell loss during preparation as described before (15, 18). The results confirmed the higher level of ARTC2.2-specific s+16a-dimHLE bound at the surface of CD69$^+$ T_{RM} as compared to tissue resident CD69$^-$ CD4$^+$ T cells and to vascular CD4$^+$ T cells (**Figures 4B, C**, panels 3). Also, higher expression of P2X7 was detected at the surface of CD69$^+$ T_{RM} compared to other CD4$^+$ subsets (**Figures 4B, C** panels 4). In mice injected with rAAV1 encoding the ARTC2.2-specific s+16a-dimHLE, we observed high proportions of NKT cells and CD69$^+$ T_{RM} as expected from an ARTC2.2-blocking biologics that protect from NICD that occurs during cells preparation (**Figures 4A, B**, panels 3). In contrast, liver lymphocytes obtained from mice injected with rAAV1 encoding the P2X7-potentiating 14D5-dimHLE show markedly reduced percentages of tetramer-stained NKT cells and of CD69$^+$ T$_{RM}$ (**Figures 4A, B**, panels 2), *i.e.* a cell populations that display high cell surface level of P2X7 (**Figure 4B**, panel 4). This likely reflects 14D5-dimHLE enhanced cell death of these subsets due to NAD$^+$ released during liver collection and cell preparation (34). Liver lymphocytes recovered from mice injected 120 days earlier with rAAV1 encoding the P2X7-blocking 13A7-IgG1^{LSF}, contained high proportion of NKT cells (**Figure 4A**, panel 1) and of CD69$^+$ T$_{RM}$ (**Figure 4B**, panel 1), indicating that binding of 13A7-IgG1^{LSF} rendered these subpopulations resistant to NICD during cell preparation. However, the low level of staining with the IgG1-specific secondary antibody (**Figure 4B**, panel 1) suggests that this hcAb induced down modulation of cell surface P2X7, possibly by hcAb-induced endocytosis. This was not due to low binding of 13A7-IgG1^{LSF} at the surface of these cells as incubation of the cells *ex vivo* with a saturating dose of recombinant 13A7-IgG1^{LSF} followed by IgG1-specific secondary antibody did not increased the staining (data not shown). Similarly, in mice injected with rAAV1 encoding 14D5-dimHLE or s+16a-dimHLE, incubation of cells *ex vivo* with a saturating dose of the corresponding recombinant protein, followed by the appropriate secondary detection reagent, did not increased the staining intensity (not shown). This data indicate that each of these nanobody-based constructs produced *in vivo* achieved full occupancy of their respective target proteins expressed on vascular and tissue resident CD4$^+$ T cells, as expected from their continuous endogenous production mediated by rAAV1 injection 120 days earlier.

Functional *In Vivo* Modulation of ARTC2.2 or P2X7 by rAAV Encoded Biologics

We next evaluated the effect of these biological constructs *in vivo*. First, we confirmed the absence of cell depletion using these AAVnano by evaluating the percentages of CD4$^+$CD25$^+$ Treg, CD4$^+$CD25$^-$ Tconv, and CD8$^+$ T cells, throughout the study (data not shown). We then injected NAD$^+$ i.v. and evaluated *in vivo* the modulating effect of the P2X7-specific constructs. As we previously demonstrated that the injection of 60 mg NAD$^+$ provokes the depletion of 80% of Treg (24), we injected here a limited dose of 30 mg of NAD$^+$ in order to evaluate the potentiating effect of 14D5-dimHLE. For that, mice were injected again with each AAVnano, followed 28 days after by the i.v. injection of 30 mg NAD$^+$. Depletion of cell subsets was evaluated by collection and analyses of splenocytes one day after. As expected, untransduced mice showed a limited yet significant depletion of splenic Treg (**Figures 5A, B**), but not of other T cell subsets that express lower levels of P2X7. In contrast, mice injected with the AAVnano encoding 13A7-IgG1^{LSF} hcAb were protected from NAD$^+$-induced Treg depletion. Remarkably, mice injected with the vector encoding the P2X7-potentiating construct 14D5-dimHLE showed significantly enhanced cell depletion, not only for Treg but also for the less sensitive Tconv and CD8$^+$ T cell subsets, confirming the potentiating effect observed *ex vivo* (**Figures 3B**, **5B**). These data provide evidence that P2X7 activity at the surface of T cell subsets can be modulated *in vivo* following a single injection of a rAAV1 encoding blocking or potentiating anti-P2X7 nanobody-based biologics.

Depletion *In Vivo* of Cells Expressing ARTC2.2 or P2X7 Using rAAV Coding for Nanobody-Based hcAb

Upon binding, conventional antibodies can promote target cell depletion through their Fc-related effector functions. We aimed here at evaluating P2X7-specifc and ARTC2.2-specific hcAb that contain a neutral nanobody (*i.e.*, a nanobody that bind to its target but does not modulate its function) fused to the mouse IgG2a Fc-region, for their capacity to promote cell depletion *in vivo*. For that, we used again rAAV coding for these constructs that we termed 7E2-IgG2a hcAb for the one targeting P2X7, and s-14-IgG2a hcAb for the one directed against ARTC2.2. First, we evaluated the binding of each of these constructs to the surface of mouse T cell subsets. For that, serum from mice injected 63 days earlier with hcAb-encoding rAAV8 were collected and used as a source of hcAb. These sera were then incubated with splenocytes harvested from untreated naive mice and bound hcAb were detected by a IgG2a-specific secondary antibody (**Figure 6A**). Results confirmed higher binding of s-14-IgG2a hcAb on the surface of the CD8$^+$ T cell subsets in agreement with the higher expression of its ARTC2.2 target on this subset (**Figure 1A**). 7E2-IgG2a hcAb was found to bind at lower levels than s-14-IgG2a hcAb at the surface of each studied T cell subsets, in agreement with the lower expression of P2X7 as compared to ARTC2.2 on these cell populations. Yet, 7E2-IgG2a hcAb was found to bind better on Treg than on Tconv and CD8$^+$ T cells (**Figure 6A**), in agreement with the higher expression of P2X7 on Treg (**Figure 1A**). Titration analyses indicated that around 1 µl of serum contained saturating amounts of hcAb (**Figure 6B**). These results indicate that 7E2-IgG2a and s-14-IgG2a hcAb are produced in saturating amounts *in vivo* at least 63 days following a single i.m. injection of rAAV.

For comparison, and to evaluate the kinetic and relative abundance of hcAb production *in vivo*, we also used sera (or plasma) collected at different time points from another experiment to stain HEK293-ARTC2.2 or HEK293-P2X7 cell lines expressing high and stable levels of surface ARTC2.2 or P2X7, obtained by retroviral transduction of the parental HEK-293 cell line (**Supplemental Figure 2**). The data confirm that 7E2-IgG2a hcAb and s-14-IgG2a hcAb are detectable in the circulation at the earlier time point studied (i.e., at day 13 post rAAV8 i.m. injection), are produced in all animals that were studied at a rather similar level, and slowly accumulate to reach a maximum concentration between 45 and 66 days post rAAV8 injection and remains stable thereafter (**Supplemental Figure 2**).

We next analyzed the level of target cell depletion overtime induced by the production of ARTC2.2-specific or P2X7-specific hcAb *in vivo*. Results obtained with the P2X7-specific 7E2-IgG2a hcAb showed a modest depletion of Treg, reaching 18 ± 4% at day 25 post rAAV injection. The proportions of CD4$^+$CD25$^-$ Tconv and CD8$^+$ T cells were only slightly decreased in mice producing 7E2-IgG2a hcAb, consistent with lower levels of P2X7 on these subsets (**Figures 6A–C**). In contrast, in mice producing

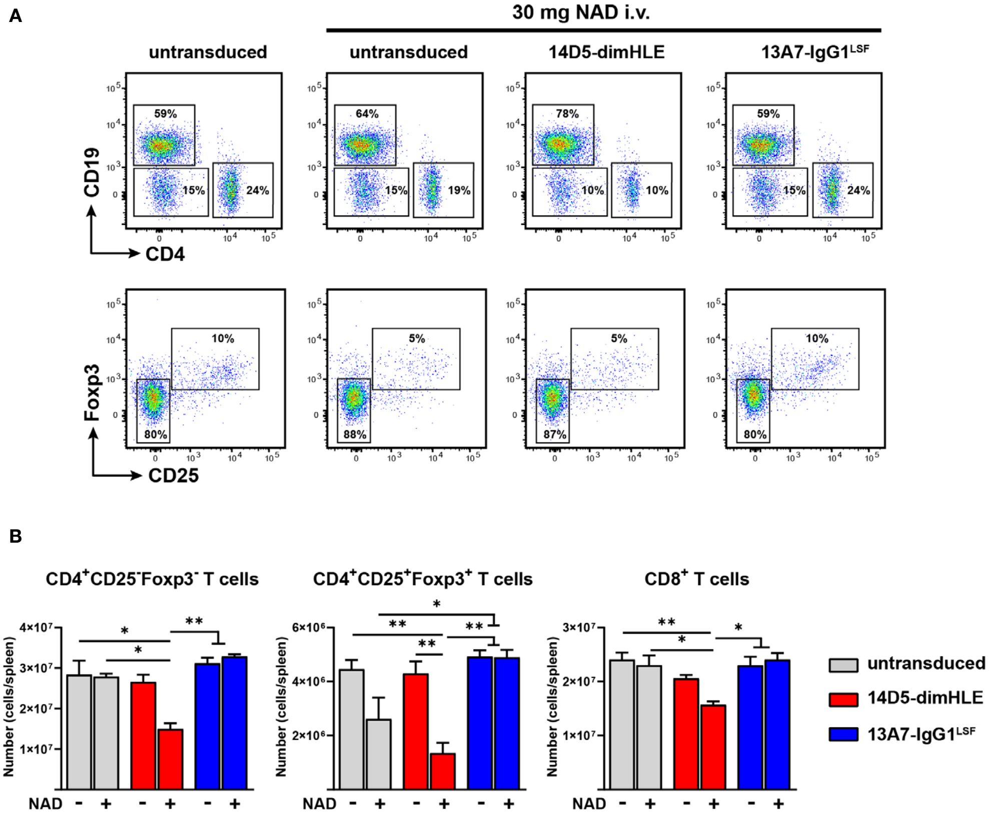

FIGURE 5 | AAVnano modulate *in vivo* the sensitivity to NAD$^+$-induced cell death. C57BL/6 mice were injected i.m. with PBS (control) or with rAAV1 encoding the P2X7-potentiating 14D5-dimHLE construct or the P2X7-blocking 13A7-IgG1^{LSF} hcAb construct. 28 days later mice were injected i.v. with PBS or 30 mg NAD$^+$. Splenocytes were collected one day after and analyzed by flow cytometry to evaluate the levels of P2X7-dependent T cell depletion induced by NAD$^+$ injection. **(A)** Representative flow cytometry plots showing the relative percentages of cells in each group. In the upper panels, CD4$^+$, CD8$^+$ and CD19$^+$ lymphocytes were concatenated in the same subpopulation and analyzed together to visualize the level of depletion of CD4$^+$ and CD8$^+$ (CD4$^-$/CD19$^-$) T cells as compared to NAD$^+$-insensitive CD19$^+$ B cells. In the lower panels, the gated CD4$^+$ cells were analyzed for both, expression of Foxp3 and CD25 to evaluate the percentages of Treg depletion in each group. Numbers indicate the percentage of cells in each indicated gate. **(B)** Absolute numbers of cells collected from spleen of untransduced control mice (grey) or from mice injected with rAAV encoding 14D5-dimHLE (red) or for 13A7-IgG1^{LSF} hcAb (blue). Each group was injected i.v. either with PBS (-) or with 30 mg of NAD$^+$ (+). Error bars represent the SEM. The statistical analysis was performed using one-way ANOVA (n=3 in each group, *$p < 0.05$, **$p < 0.01$). Staining was performed using fluorochrome conjugated antibodies specific to CD45 (coupled to BV510), CD4 (APC-Cy7), CD8 (BV605), CD19 (PerCP-Cy5.5), CD25 (PE) and FoxP3 (BV421).

ARTC2.2-specific s-14-IgG2a hcAb, we found a substantial depletion of the three T cell subsets analyzed. Depletion was most pronounced for CD8$^+$ that express the highest level of ARTC2.2. This construct was indeed found to deplete 85 ± 3% of CD8$^+$ T cells, 65 ± 6% of Tconv, and 66 ± 5% of Treg 25 days post rAAV8 injection. The level of depletion was slightly higher at day 82 post rAAV8 injection (**Figure 6C**). For comparison, CD19$^+$ B cells (that do not express P2X7 nor ARTC2.2) and myeloid non-granulocytic CD11b$^+$ cells (that do express very little, if any, ARTC2.2 and low level of P2X7) were also enumerated in the blood at the same time point. Data demonstrated the absence of depletion of these subsets in agreement with their absence of expression or low expression of ARTC2.2 and/or P2X7 (**Supplemental Figure 3**). These findings illustrate the long-term and stable depleting effects of the target T cells elicited by these IgG2a hcAb upon a single i.m. injection of the corresponding hcAb-encoding rAAV8.

DISCUSSION

Surface expression of the ectoenzyme ARTC2.2 is restricted to T cells and is found at higher levels on murine CD8$^+$ T cells as compared to CD4$^+$CD25$^+$ Treg or CD4$^+$CD25$^-$ Tconv (**Figure 1A**) (9). P2X7 is expressed by multiple cells, including immune cells of the myeloid and lymphoid compartments. On murine T cells, P2X7 is differentially expressed on T cell subsets, and was found to be expressed at higher levels on NKT cells, Treg, Tfh, and T_{RM} (12, 14–18). The homotrimeric P2X7 receptor is known to form an ATP-gated ion-channel connected to multiple signaling pathways that regulate cell phenotype, functions, differentiation and survival (11). For murine T cells, P2X7 activation can be triggered by two complementary pathways. As in myeloid and non-immune cells, the P2X7 receptor can be gated by the presence of relatively high concentrations of extracellular ATP (*i.e.*, 30 to

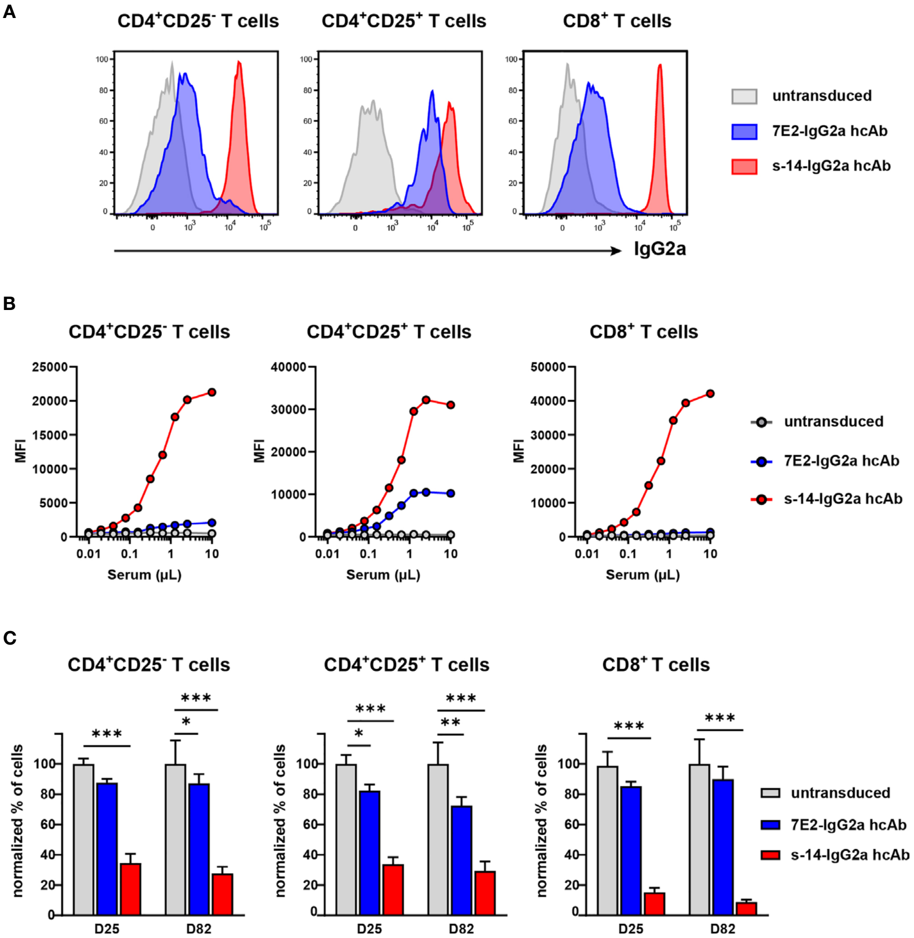

FIGURE 6 | AAVnano encoding nanobody-based IgG2a hcAb mediate depletion of cells expressing high levels of P2X7 or ARTC2.2. C57BL/6 mice were injected with PBS (untransduced, grey) or with rAAV8 encoding 7E2-IgG2a (blue) or s-14-IgG2a (red) hcAb. **(A, B)** Sera were collected 63 days post rAAV8 i.m. injection. To monitor the levels of hcAb in serum, splenocytes from an untreated naive C57BL/6 mouse were incubated with diluted serum, washed and bound hcAb were detected with an IgG2a-specific secondary antibody. **(A)** Flow cytometry analyses illustrating the binding of each nanobody-based IgG2a hcAb on the indicated subset of splenic cells from an untreated mouse when using 10 µl of pooled sera collected from rAAV injected mice. **(B)** Splenocytes from an untreated mouse were incubated with serial dilutions of sera to titrate the relative abundance of the two hcAb. For both hcAb, serum volumes between 1-10 µL were enough to saturate the signal. **(C)** To evaluate depletion of T cell subsets *in vivo*, blood samples were collected 25 days and 82 days after i.m. injection of rAAV encoding the indicated IgG2a hcAb. Cells were stained with fluorochrome-conjugated antibodies and analyzed by flow cytometry. Normalized percentage of $CD4^+CD25^-$, $CD4^+CD25^+$ and $CD8^+$ T cells are shown, as compared to the percentages of cells found in the control group taken as 100%. Staining was performed using fluorochrome conjugated antibodies specific to CD45 (coupled to PerCP-Cy5.5), CD4 (APC-Cy7), CD8 (PE-Cy7), CD25 (PE) and biotinylated antibody to mouse IgGa and streptavidin-APC. Errors bars represent the SEM and statistical analyses were performed using one-way ANOVA (n=7 in each group, $^*p < 0.05$, $^{**}p < 0.01$, $^{***}p < 0.001$).

300 µM range) that can be released from dying or stressed cells. In addition, in murine T cells, extracellular NAD^+ was found to trigger activation of the P2X7 receptor at low micromolar concentrations (12, 24). The mechanism involves the ARTC2.2 catalyzed covalent ADP-ribosylation of P2X7 on R125 in the vicinity of the ATP-binding site (23). Although much was learnt during the last years on the multifaceted P2X7 receptor, the relative contribution of the ATP and NAD^+ pathways their activation *in vivo*, their precise immunoregulatory roles, and their contribution in pathophysiological conditions, remain to be better addressed and studied. The AAVnano approach described here uses rAAV for durable production of nanobody-containing biologics *in vivo*. This could be used in future studies to better delineate ARTC2.2 and/or P2X7 functions in animal models of acute as well as chronic diseases.

Our results show that a single injection of rAAV1 or rAAV8 encoding P2X7-specific or ARTC2.2-specific nanobody-based constructs (**Figure 1**) can inhibit or in contrast potentiate ATP- or NAD^+-induced activation of P2X7 *ex vivo* on splenic T cells harvested from these mice. As one hallmark associated with P2X7 receptor activation, we used a sensitive *ex vivo* assay based on metalloprotease-dependent shedding of CD27 and CD62L from the T cell surface. Our data demonstrate that a single injection of a rAAV encoding the P2X7-blocking 13A7-

IgG1^{LSF} hcAb protects T cells from NAD$^+$- as well as ATP-induced CD27 and CD62L shedding (**Figure 3B**). Similarly, injection of a rAAV encoding the ARTC2.2-blocking s+16a-dimHLE completely inhibits NAD$^+$- but not ATP-induced shedding of CD27 and CD62L (**Figure 3B**). Remarkably, the P2X7-potentiating 14D5-dimHLE sensitized T cells to NAD$^+$- as well as ATP-induced shedding of CD27 and CD62L. This is noticeable also for Tconv and CD8$^+$ T cells that express low levels of P2X7 and are therefore less sensitive to activation of P2X7 than Treg (**Figure 3B**).

Analysis of vascular and tissue resident liver T cells from mice sacrificed 120 days after injection of AAVnano revealed full occupancy of ARTC2.2 by s+16a-dimHLE on CD4$^+$ T cells in the vasculature and liver parenchyma (**Figures 4B, C** and data not shown). Moreover, the high recovery of CD69$^+$ T$_{RM}$ indicates that this cell population is fully protected from NAD-induced cell death (NICD) during cell preparation in these mice (**Figure 4B**). Much lower numbers of NKT cells and CD69$^+$ T$_{RM}$ (*i.e.*, the cell populations with the highest cell surface levels of P2X7) were recovered from mice injected with the rAAV1 encoding 14D5-dimHLE, consistent with its P2X7-potentiating activity that might enhance cell death *in vivo* and/or during cell preparation. High numbers of liver T$_{RM}$ were recovered from mice expressing *in vivo* the P2X7-blocking 13A7-IgG1^{LSF} hcAb, consistent with its protective role on NICD. The low staining of these cells with the IgG1-specific secondary Ab, possibly reflects hcAb induced endocytosis of P2X7 by these cells.

We next evaluated directly *in vivo* the potential of these endogenously produced constructs to modulate P2X7 receptor activation. We previously reported that a single i.v. injection of 60 mg NAD$^+$ depletes about 80% of CD4$^+$CD25$^+$Foxp3$^+$ Treg following ARTC2.2-dependent activation of P2X7 (24). We injected here a lower dose of 30 mg NAD$^+$ to better evaluate the potentiating effect of 14D5-dimHLE. The results indeed demonstrate that this dose depletes 41 ± 18% of the Treg cells in untransduced control mice, while 68 ± 9% Treg cells are depleted by the same treatment in animals whose muscle cells had been transduced with rAAV1 coding for 14D5-dimHLE (**Figure 5B**). Even the less sensitive Tconv and CD8$^+$ T cells, which were not affected by 30 mg NAD$^+$ in untransduced mice, were significantly depleted in animals expressing 14D5-dimHLE (although to a lesser degree than Treg). These results are consistent with the data obtained *ex vivo*, that 14D5-dimHLE potentiates P2X7 function also in T cell subsets that display lower P2X7 surface expression. Taken together, these data demonstrate that the AAVnano approach described here is a feasible approach to reproducibly modulate ARTC2.2 or P2X7 functional activities *in vivo*.

Several small molecules P2X7 blockers have been developed by pharmaceutical and biotechnology companies in the past years since P2X7 is a potential target in inflammatory diseases and in cancer (37–41). Several studies have indeed evidenced that pharmacological blockade of P2X7 is associated with therapeutic benefits in pre-clinical animal models of inflammation, pain, autoimmune and neurodegenerative diseases, and cancer. Given that many cancer cells express high levels of P2X7 receptors (notably mutated, truncated, or splice variants that are not able to trigger P2X7-dependent cell death), and that its tonic activation in the tumor microenvironment is associated with tumor proliferation and invasiveness, P2X7-blockade was envisioned as a possible cancer therapy. This was demonstrated in several animal studies (42, 43). Using our AAVnano approach, coding for the P2X7-blocking 13A7-IgG1^{LSF} hcAb, we recently reported a similar finding (44). This suggests that the AAVnano methodological approach, in addition to knock-out models and small molecule inhibitors, represents an alternative and complementary possibility to validate *in vivo* the importance of P2X7 target in various animal models.

In addition to P2X7-blockers, some compounds were recently identified as positive allosteric modulators of P2X7 activation (45–47). As for the 14D5-dimHLE biologics described here, these molecules offer the interesting perspective to potentiate P2X7 only in the microenvironment *in vivo* where NAD$^+$ and/or ATP are present in the extracellular space in sufficient quantities to trigger P2X7-gating, as for instance in the tumor microenvironment (48). One such small-molecule positive allosteric modulator of P2X7, named HEI3090, has recently shown promising results in mouse models of non-small cell lung cancer and melanoma (49). Interestingly, the mechanism involves the stimulation of immune cells (*i.e.*, dendritic cells, NK cells, and CD4$^+$ effector T cells), and production of IL-18. This finding underscores the notion that P2X7 stimulation may indeed be beneficial in certain circumstances. Since both, blocking or potentiating P2X7 seems to be beneficial in some cancer models, the AAVnano approach described here, allowing both modalities to be studied using the same approach, might be used in future studies as a tool to extend our knowledge on the positive and negative functions of P2X7 in different disease models.

Another potential application that we explored here is the development and use of nanobody-based hcAb to promote cell depletion *in vivo*. We exploited the natural ability of Fc-region to bind to FcR on immune cells and to mediate Fc-related effector functions and/or to induce the activation of the classical complement pathway. For that, we fused P2X7-specific or ARTC2.2-specific nanobodies to the hinge and Fc region of mouse IgG2a to generate nanobody-based hcAb. We then evaluated the capacity of these biologics to mediate the depletion of target-expressing cells *in vivo* following i.m. injection of rAAV8 that encode these constructs. In line with the cell surface levels of ARTC2.2 and P2X7 on T cell subsets, our results revealed that the ARTC2.2-specific s-14-IgG2a hcAb mediated considerably higher cell depletion than the P2X7-specific 7E2-IgG2a hcAb (**Figure 6C**). Also, when considering each construct individually, the relative level of cell depletion of each T cell subset was found to correlate with the relative abundance of the target protein at the cell surface. Thus, the ARTC2.2-specific s-14-IgG2a hcAb depleted the CD8$^+$ subset more efficiently than the other two subsets (**Figures 6A, B**). Similarly, although at lower levels, the P2X7-specific 7E2-IgG2a hcAb depleted Treg more efficiently than the other two subsets (**Figures 6A–C**). Hence, cell depletion appeared in our models to depend on the level of the target antigen at the surface of each T cell subset. Higher target antigen levels might indeed promote higher FcγR cross-linking on the surface of effector cells, as well as a higher propensity to bind C1q and to activate the complement cascade. However, we cannot exclude that other factors may contribute to the differences observed in the level of depletion with these two hcAb. Factors such as the location of the epitope recognized by the nanobody, the lateral mobility of the target protein at the cell surface (*i.e.*, ARTC2.2 is GPI-anchored protein while P2X7 is a two-transmembrane domain protein), its degree of oligomerization (ARTC2.2 is a monomer while P2X7 forms a homotrimeric ion channel), may also influence the level of cell depletion. Nonetheless, high levels of cell depletion that reached up to 85% of $CD8^+$ cells were reproducibly obtained *in vivo* using the rAAV coding the ARTC2.2-specific s-14-IgG2a hcAb and this level of depletion was remarkably maintained throughout the study until the latest time point studied (**Figure 6C**). We propose that this strategy may be used to deplete cells that express the highest levels of ARTC2.2 *in vivo* and provides a tool for studying the NAD^+/ARTC2.2 signaling pathways. In parallel, increasing the depleting efficiency of P2X7-specific hcAb may also be of interest for translational preclinical cancer studies. As mentioned earlier, P2X7 is expressed at the surface of many cancer cells. Depleting P2X7-specific hcAb may thus be used directly to eliminate tumor cells and additionally to deplete Treg (*i.e.*, T cells expressing higher levels of P2X7) potentially resulting in the induction of two synergistic anti-tumor mechanisms.

In this proof-of-principle study, we illustrated the potential of two methodological approaches to study ARTC2.2 and P2X7 function in animal model using rAAV. The aim of AAVnano is to bypass the need to produce and characterize recombinant proteins *in vitro*, to avoid protein injections every 1-2 days, and to favor a stable concentration and bioavailability. We demonstrate that a single i.m. injection of a rAAV encoding a nanobody-based biologic was sufficient to elicit long-term modulation of ARTC2.2 or P2X7 activity, or depletion of the cells expressing these proteins at high cell density. We propose that the AAVnano methodology may be used in future studies for further evaluating the role of ARTC2.2 and/or P2X7 in animal models of various diseases where these proteins have been implicated.

Although this methodological approach have many advantages, including the possibility to explore in parallel potential long-term side effects *in vivo* (i.e, on-target long-term effects as well as off-target effects), AAVnano have also some limitations. Considering the potential long-term side effects, animals remained healthy in our studies during the entire observation period (until day 120) and we did not observed any conspicuous signs of disease or side effects. We cannot however ruled-out that the biologics that were evaluated here induce other effects that we did not fully explored. The P2X7-specific hcAb that we evaluated here may for instance deplete or influence other cells than the studied T cells as for instance myeloid cells or microglial cells known to also express P2X7. Even if we did not notice any significant depletion of $CD11b^+$ myeloid cells in blood during our analyses (**Supplemental Figure 3**), more detailed investigations will be required in future studies to evaluate this possibility, notably in tissue-resident cells as well as in diseased animal models. Apart from unanticipated side effects, one obvious limitation of our AAVnano approach is the difficulty to evaluate the candidate nanobody-based biologics in therapeutic schemes. Indeed, AAV-based transgenic expression *in vivo* usually require 10 to 14 days before the biologics can be significantly produced and detected in the circulation. This period can however be reduced to 2 to 4 days using a "self-complementary" (sc) transgene instead of the "single-stranded" (ss) transgene packaged in classical rAAV vectors. Production and use of scAAV may represent therefore an interesting alternative to the ssAAV used in this study when rapid production of the biologics is required (as in therapeutic protocols or for treating tumors). Hence, AAVnano represents at least a method of choice in chronic situations and as a first *in vivo* approach to evaluate efficacy and absence of long-term side effects before evaluation of the corresponding selected recombinant biologics in therapeutic and translational models.

Interestingly, the rAAV encoding P2X7-specific constructs described here represent to our knowledge the first tools that can be used *in vivo* to either inhibit or potentiate the P2X7 receptor durably, offering the possibility of evaluating the role of P2X7 in various pathophysiological animal models. This methodical approach may be particularly promising for the reevaluation of the role of P2X7 in cancer as well as in inflammatory and neurodegenerative diseases where conflicting results have been obtained so far using knock-out models and/or repetitive administration of small-molecule inhibitors.

DATA AVAILABILITY STATEMENT

The raw data supporting the conclusions of this article will be made available by the authors, without undue reservation.

ETHICS STATEMENT

The animal study was reviewed and approved by Comité d'Ethique NOrmandie en Matière d'EXpérimentation Animale (CENOMEXA).

AUTHOR CONTRIBUTIONS

FK-N and SA, conceptualization. HG, MD, RH, AS, MJ, CP-E, FK-N, and SA, methodology. HG, MD, RH, AS, MJ, CP-E, and SA, investigation. HG, FK-N, and SA, writing – original draft. HG, MD, RH, AS, FK-N, OB, and SA, writing – review and editing. FK-N and SA, funding acquisition. RV, OB, FK-N, and SA, resources. FK-N and SA, supervision. All authors contributed to the article and approved the submitted version.

FUNDING

This work was supported by a grant from the Deutsche Forschungsgemeinschaft (DFG) to FK-N (No310/13, No310/14, and SFB1192-B5), by a stipend from the Werner-Otto Foundation to MJ, and by a grant from the Agence Nationale de la Recherche (ANR) to SA (ANR-18-CE92-0046).

SUPPLEMENTARY MATERIAL

The Supplementary Material for this article can be found online at: https://www.frontiersin.org/articles/10.3389/fimmu.2021.704408/full#supplementary-material

REFERENCES

1. Koch-Nolte F, Haag F, Guse AH, Lund F, Ziegler M. Emerging Roles of NAD+ and its Metabolites in Cell Signaling. *Sci Signal* (2009) 2:mr1. doi: 10.1126/scisignal.257mr1
2. Linden J, Koch-Nolte F, Dahl G. Purine Release, Metabolism, and Signaling in the Inflammatory Response. *Annu Rev Immunol* (2019) 37:325–47. doi: 10.1146/annurev-immunol-051116-052406
3. Adriouch S, Haag F, Boyer O, Seman M, Koch-Nolte F. Extracellular NAD+: A Danger Signal Hindering Regulatory T Cells. *Microbes Infect* (2012) 14:1284–92. doi: 10.1016/j.micinf.2012.05.011
4. Koch-Nolte F, Kernstock S, Mueller-Dieckmann C, Weiss MS, Haag F. Mammalian ADP-Ribosyltransferases and ADP-Ribosylhydrolases. *Front Biosci* (2008) 13:6716–29. doi: 10.2741/3184
5. Bazan JF, Koch-Nolte F. Sequence and Structural Links Between Distant ADP-Ribosyltransferase Families. *Adv Exp Med Biol* (1997) 419:99–107. doi: 10.1007/978-1-4419-8632-0_12
6. Glowacki G, Braren R, Firner K, Nissen M, Kühl M, Reche P, et al. The Family of Toxin-Related Ecto-ADP-Ribosyltransferases in Humans and the Mouse. *Protein Sci* (2009) 11:1657–70. doi: 10.1110/ps.0200602
7. Koch-Nolte F, Petersen D, Balasubramanian S, Haag F, Kahlke D, Willer T, et al. Mouse T Cell Membrane Proteins Rt6-1 and Rt6-2 are Arginine/Protein Mono(ADPribosyl)transferases and Share Secondary Structure Motifs With ADP-Ribosylating Bacterial Toxins. *J Biol Chem* (1996) 271:7686–93. doi: 10.1074/jbc.271.13.7686
8. Hong S, Brass A, Seman M, Haag F, Koch-Nolte F, Dubyak GR. Basal and Inducible Expression of the Thiol-Sensitive ART2.1 Ecto-ADP-Ribosyltransferase in Myeloid and Lymphoid Leukocytes. *Purinergic Signal* (2009) 5:369–83. doi: 10.1007/s11302-009-9162-2
9. Koch-Nolte F, Duffy T, Nissen M, Kahl S, Killeen N, Ablamunits V, et al. A New Monoclonal Antibody Detects a Developmentally Regulated Mouse Ecto-ADP-Ribosyltransferase on T Cells: Subset Distribution, Inbred Strain Variation, and Modulation Upon T Cell Activation. *J Immunol* (1999) 163:6014–22.
10. Adriouch S, Bannas P, Schwarz N, Fliegert R, Guse AH, Seman M, et al. ADP-Ribosylation at R125 Gates the P2X7 Ion Channel by Presenting a Covalent Ligand to its Nucleotide Binding Site. *FASEB J* (2008) 22:861–9. doi: 10.1096/fj.07-9294com
11. Rissiek B, Haag F, Boyer O, Koch-Nolte F, Adriouch S. P2X7 on Mouse T Cells: One Channel, Many Functions. *Front Immunol* (2015) 6:204. doi: 10.3389/fimmu.2015.00204
12. Seman M, Adriouch S, Scheuplein F, Krebs C, Freese D, Glowacki G, et al. NAD-Induced T Cell Death: ADP-Ribosylation of Cell Surface Proteins by ART2 Activates the Cytolytic P2X7 Purinoceptor. *Immunity* (2003) 19:571–82. doi: 10.1016/s1074-7613(03)00266-8
13. Scheuplein F, Schwarz N, Adriouch S, Krebs C, Bannas P, Rissiek B, et al. NAD+ and ATP Released From Injured Cells Induce P2X7-Dependent Shedding of CD62L and Externalization of Phosphatidylserine by Murine T Cells. *J Immunol* (2009) 182:2898–908. doi: 10.4049/jimmunol.0801711
14. Rissiek B, Danquah W, Haag F, Koch-Nolte F. Technical Advance: A New Cell Preparation Strategy That Greatly Improves the Yield of Vital and Functional Tregs and NKT Cells. *J Leukocyte Biol* (2014) 95:543–9. doi: 10.1189/jlb.0713407
15. Stark R, Wesselink TH, Behr FM, Kragten NAM, Arens R, Koch-Nolte F, et al. TRM Maintenance is Regulated by Tissue Damage *via* P2RX7. *Sci Immunol* (2018) 3. doi: 10.1126/sciimmunol.aau1022
16. Borges da Silva H, Wang H, Qian LJ, Hogquist KA, Jameson SC. ARTC2.2/P2RX7 Signaling During Cell Isolation Distorts Function and Quantification of Tissue-Resident CD8$^+$ T Cell and Invariant NKT Subsets. *JI* (2019) 202:2153–63. doi: 10.4049/jimmunol.1801613
17. Georgiev H, Ravens I, Papadogianni G, Malissen B, Förster R, Bernhardt G. Blocking the ART2.2/P2X7-System Is Essential to Avoid a Detrimental Bias in Functional CD4 T Cell Studies. *Eur J Immunol* (2018) 48:1078–81. doi: 10.1002/eji.201747420
18. Rissiek B, Lukowiak M, Raczkowski F, Magnus T, Mittrücker H-W, Koch-Nolte F. *In Vivo* Blockade of Murine ARTC2.2 During Cell Preparation Preserves the Vitality and Function of Liver Tissue-Resident Memory T Cells. *Front Immunol* (2018) 9:1580. doi: 10.3389/fimmu.2018.01580
19. Muyldermans S. Nanobodies: Natural Single-Domain Antibodies. *Annu Rev Biochem* (2013) 82:775–97. doi: 10.1146/annurev-biochem-063011-092449
20. Wesolowski J, Alzogaray V, Reyelt J, Unger M, Juarez K, Urrutia M, et al. Single Domain Antibodies: Promising Experimental and Therapeutic Tools in Infection and Immunity. *Med Microbiol Immunol* (2009) 198:157–74. doi: 10.1007/s00430-009-0116-7
21. Ingram JR, Schmidt FI, Ploegh HL. Exploiting Nanobodies' Singular Traits. *Annu Rev Immunol* (2018) 36:695–715. doi: 10.1146/annurev-immunol-042617-053327
22. De Genst E, Silence K, Decanniere K, Conrath K, Loris R, Kinne J, et al. Molecular Basis for the Preferential Cleft Recognition by Dromedary Heavy-Chain Antibodies. *Proc Natl Acad Sci* (2006) 103:4586–91. doi: 10.1073/pnas.0505379103
23. Koch-Nolte F, Reyelt J, Schößow B, Schwarz N, Scheuplein F, Rothenburg S, et al. Single Domain Antibodies From Llama Effectively and Specifically Block T Cell Ecto-ADP-Ribosyltransferase ART2.2 *In Vivo*. *FASEB J* (2007) 21:3490–8. doi: 10.1096/fj.07-8661com
24. Hubert S, Rissiek B, Klages K, Huehn J, Sparwasser T, Haag F, et al. Extracellular NAD+ Shapes the Foxp3+ Regulatory T Cell Compartment Through the ART2–P2X7 Pathway. *J Exp Med* (2010) 207:2561–8. doi: 10.1084/jem.20091154
25. Danquah W, Meyer-Schwesinger C, Rissiek B, Pinto C, Serracant-Prat A, Amadi M, et al. Nanobodies That Block Gating of the P2X7 Ion Channel Ameliorate Inflammation. *Sci Trans Med* (2016) 8:366ra162. doi: 10.1126/scitranslmed.aaf8463
26. Koch-Nolte F, Eichhoff A, Pinto-Espinoza C, Schwarz N, Schäfer T, Menzel S, et al. Novel Biologics Targeting the P2X7 Ion Channel. *Curr Opin Pharmacol* (2019) 47:110–8. doi: 10.1016/j.coph.2019.03.001
27. Kaczmarek-Hajek K, Zhang J, Kopp R, Grosche A, Rissiek B, Saul A, et al. Re-Evaluation of Neuronal P2X7 Expression Using Novel Mouse Models and a P2X7-Specific Nanobody. *eLife* (2018) 7:e36217. doi: 10.7554/eLife.36217
28. Saunders KO. Conceptual Approaches to Modulating Antibody Effector Functions and Circulation Half-Life. *Front Immunol* (2019) 10:1296. doi: 10.3389/fimmu.2019.01296
29. Tijink BM, Laeremans T, Budde M, Stigter-van Walsum M, Dreier T, de Haard HJ, et al. Improved Tumor Targeting of Anti-Epidermal Growth Factor Receptor Nanobodies Through Albumin Binding: Taking Advantage of Modular Nanobody Technology. *Mol Cancer Ther* (2008) 7:2288–97. doi: 10.1158/1535-7163.MCT-07-2384

30. Ghetie V, Popov S, Borvak J, Radu C, Matesoi D, Medesan C, et al. Increasing the Serum Persistence of an IgG Fragment by Random Mutagenesis. *Nat Biotechnol* (1997) 15:637–40. doi: 10.1038/nbt0797-637
31. Chen H. Manufacturing of Adeno-Associated Viruses, for Example: AAV2. *Methods Mol Biol* (2011) 737:235–46. doi: 10.1007/978-1-61779-095-9_10
32. Balazs AB, Chen J, Hong CM, Rao DS, Yang L, Baltimore D. Antibody-Based Protection Against HIV Infection by Vectored Immunoprophylaxis. *Nature* (2011) 481:81–4. doi: 10.1038/nature10660
33. Nimmerjahn F, Ravetch JV. Divergent Immunoglobulin G Subclass Activity Through Selective Fc Receptor Binding. *Science* (2005) 310:1510–2. doi: 10.1126/science.1118948
34. Anderson KG, Mayer-Barber K, Sung H, Beura L, James BR, Taylor JJ, et al. Intravascular Staining for Discrimination of Vascular and Tissue Leukocytes. *Nat Protoc* (2014) 9:209–22. doi: 10.1038/nprot.2014.005
35. Schenkel JM, Masopust D. Tissue-Resident Memory T Cells. *Immunity* (2014) 41:886–97. doi: 10.1016/j.immuni.2014.12.007
36. Mueller SN, Mackay LK. Tissue-Resident Memory T Cells: Local Specialists in Immune Defence. *Nat Rev Immunol* (2016) 16:79–89. doi: 10.1038/nri.2015.3
37. Jacobson KA, Müller CE. Medicinal Chemistry of Adenosine, P2Y and P2X Receptors. *Neuropharmacology* (2016) 104:31–49. doi: 10.1016/j.neuropharm.2015.12.001
38. Burnstock G, Knight GE. The Potential of P2X7 Receptors as a Therapeutic Target, Including Inflammation and Tumour Progression. *Purinergic Signal* (2018) 14:1–18. doi: 10.1007/s11302-017-9593-0
39. Sluyter R. The P2X7 Receptor. *Adv Exp Med Biol* (2017) 1051:17–53. doi: 10.1007/5584_2017_59
40. De Marchi E, Orioli E, Dal Ben D, Adinolfi E. P2X7 Receptor as a Therapeutic Target. *Adv Protein Chem Struct Biol* (2016) 104:39–79. doi: 10.1016/bs.apcsb.2015.11.004
41. Di Virgilio F, Sarti AC, Falzoni S, De Marchi E, Adinolfi E. Extracellular ATP and P2 Purinergic Signalling in the Tumour Microenvironment. *Nat Rev Cancer* (2018) 18:601–18. doi: 10.1038/s41568-018-0037-0
42. De Marchi E, Orioli E, Pegoraro A, Sangaletti S, Portararo P, Curti A, et al. The P2X7 Receptor Modulates Immune Cells Infiltration, Ectonucleotidases Expression and Extracellular ATP Levels in the Tumor Microenvironment. *Oncogene* (2019) 38:3636–50. doi: 10.1038/s41388-019-0684-y
43. Adinolfi E, Raffaghello L, Giuliani AL, Cavazzini L, Capece M, Chiozzi P, et al. Expression of P2X7 Receptor Increases *In Vivo* Tumor Growth. *Cancer Res* (2012) 72:2957–69. doi: 10.1158/0008-5472.CAN-11-1947
44. Demeules M, Scarpitta A, Abad C, Gondé H, Hardet R, Pinto-Espinoza C, et al. Evaluation of P2X7 Receptor Function in Tumor Contexts Using rAAV Vector and Nanobodies (AAVnano). *Front Oncol* (2020) 10:1699. doi: 10.3389/fonc.2020.01699
45. Bartlett R, Stokes L, Sluyter R. The P2X7 Receptor Channel: Recent Developments and the Use of P2X7 Antagonists in Models of Disease. *Pharmacol Rev* (2014) 66:638–75. doi: 10.1124/pr.113.008003
46. Di Virgilio F, Giuliani AL, Vultaggio-Poma V, Falzoni S, Sarti AC. Non-Nucleotide Agonists Triggering P2X7 Receptor Activation and Pore Formation. *Front Pharmacol* (2018) 9:39. doi: 10.3389/fphar.2018.00039
47. Stokes L, Bidula S, Bibič L, Allum E. To Inhibit or Enhance? Is There a Benefit to Positive Allosteric Modulation of P2X Receptors? *Front Pharmacol* (2020) 11:627. doi: 10.3389/fphar.2020.00627
48. Di Virgilio F, Dal Ben D, Sarti AC, Giuliani AL, Falzoni S. The P2X7 Receptor in Infection and Inflammation. *Immunity* (2017) 47:15–31. doi: 10.1016/j.immuni.2017.06.020
49. Douguet L, Janho Dit Hreich S, Benzaquen J, Seguin L, Juhel T, Dezitter X, et al. A Small-Molecule P2RX7 Activator Promotes Anti-Tumor Immune Responses and Sensitizes Lung Tumor to Immunotherapy. *Nat Commun* (2021) 12:653. doi: 10.1038/s41467-021-20912-2

Conflict of Interest: The authors declare that the research was conducted in the absence of any commercial or financial relationships that could be construed as a potential conflict of interest.

ORIGINAL RESEARCH
published: 24 August 2021
doi: 10.3389/fimmu.2021.703719

Identification of the Mouse T Cell ADP-Ribosylome Uncovers ARTC2.2 Mediated Regulation of CD73 by ADP-Ribosylation

Mario Leutert[1,2]*, *Yinghui Duan*[3], *Riekje Winzer*[4], *Stephan Menzel*[4,5], *Eva Tolosa*[4], *Tim Magnus*[3], *Michael O. Hottiger*[1], *Friedrich Koch-Nolte*[4] *and Björn Rissiek*[3]*

[1] Department of Molecular Mechanisms of Disease, University of Zurich, Zurich, Switzerland, [2] Department of Genome Sciences, University of Washington, Seattle, WA, United States, [3] Department of Neurology, University Medical Centre Hamburg-Eppendorf, Hamburg, Germany, [4] Institute of Immunology, University Medical Centre Hamburg-Eppendorf, Hamburg, Germany, [5] Mildred Scheel Cancer Career Center HaTriCS4, University Medical Center Hamburg-Eppendorf, Hamburg, Germany

Edited by:
Jose Carlos Alves-Filho,
University of São Paulo, Brazil

Reviewed by:
Akio Ohta,
Foundation for Biomedical Research and Innovation, Japan
Daniele Carvalho Nascimento,
University of São Paulo, Brazil

***Correspondence:**
Björn Rissiek
b.rissiek@uke.de
Mario Leutert
mleutert@uw.edu

Specialty section:
This article was submitted to Cytokines and Soluble Mediators in Immunity, a section of the journal Frontiers in Immunology

Received: *30 April 2021*
Accepted: *02 August 2021*
Published: *24 August 2021*

Citation:
Leutert M, Duan Y, Winzer R, Menzel S, Tolosa E, Magnus T, Hottiger MO, Koch-Nolte F and Rissiek B (2021) Identification of the Mouse T Cell ADP-Ribosylome Uncovers ARTC2.2 Mediated Regulation of CD73 by ADP-Ribosylation. Front. Immunol. 12:703719. doi: 10.3389/fimmu.2021.703719

Mouse T cells express the ecto-ADP-ribosyltransferase ARTC2.2, which can transfer the ADP-ribose group of extracellular nicotinamide adenine dinucleotide (NAD^+) to arginine residues of various cell surface proteins thereby influencing their function. Several targets of ARTC2.2, such as P2X7, CD8a and CD25 have been identified, however a comprehensive mouse T cell surface ADP-ribosylome analysis is currently missing. Using the Af1521 macrodomain-based enrichment of ADP-ribosylated peptides and mass spectrometry, we identified 93 ADP-ribsoylated peptides corresponding to 67 distinct T cell proteins, including known targets such as CD8a and CD25 but also previously unknown targets such as CD73. We evaluated the impact of ADP-ribosylation on the capability of CD73 to generate adenosine from adenosine monophosphate. Our results show that extracellular NAD^+ reduces the enzymatic activity of CD73 HEK cells co-transfected with CD73/ARTC2.2. Importantly, NAD^+ significantly reduced CD73 activity on WT CD8 T cells compared to ARTC2ko CD8 T cells or WT CD8 T cells treated with an ARTC2.2-blocking nanobody. Our study provides a comprehensive list of T cell membrane proteins that serve as targets for ADP-ribosylation by ARTC2.2 and whose function may be therefore affected by ADP-ribosylation.

Keywords: NAD, CD73, ADP-ribosylation, T cells, ARTC2.2

INTRODUCTION

Ecto-ADP-ribosyltransferases (ARTCs) are cell surface enzymes that utilize extracellular nicotinamide adenine dinuleotide (NAD^+) to covalently attach the ADP-ribose group of NAD^+ to arginine residues of various cell surface proteins under the release of nicotinamide (1, 2). The mouse ARTC family consist of six members: GPI-anchored ARTC1, ARTC2.1 and ARTC2.2, ARTC3, ARTC4 and the soluble ARTC5 (3). ARTC2.1 and ARTC2.2 are the ARTCs predominantly expressed by cells of the murine immune system (4). ARTC2.1 is highly expressed on the cell surface of innate immune cells such as macrophages and microglia (5) and to some extent on T cells (6). In contrast, ARTC2.2 is highly expressed on most T cell populations. Further, it is worth noting that the ARTC2.1 encoding gene, *Art2a*, is inactivated by a premature stop codon in the C57BL/6 (B6) mouse strain, whereas other strains such as Balb/c carry an intact *Art2a* gene (7). Therefore, in B6 mice, ecto-ARTC activity in the immune system is limited to the T cell compartment.

Results from ADP-ribosylation assays using ^{32}P-NAD$^+$ or etheno-NAD$^+$ as substrate, revealed that ARTC2.2 ADP-ribosylates a broad spectrum of membrane proteins (8–11). So far, a limited number of ARTC2.2 targets have been characterized. Among them are cell surface receptors such as the interleukin 2 (IL-2) receptor alpha subunit (CD25) (12) and the alpha chain of CD8 (CD8a) (13) molecule, both chains of the integrin LFA1 (11) and the ATP-gated ion channel P2X7 (14).

The functional impact of ADP-ribosylation on the target protein has been extensively studied in case of P2X7. ADP-ribosylation of P2X7 mediates NAD$^+$-induced cell death of T cells co-expressing ARTC2.2 and high levels of P2X7, such as regulatory T cells (Tregs), natural killer T cells, T follicular helper cells and tissue-resident memory T cells (14–19). Consistently, injection of NAD$^+$ induces temporary depletion of Tregs, thereby favoring anti-tumor responses (15). Cells expressing both ARTC2.2 and P2X7 are particularly affected by NAD$^+$ released during cell preparation procedures, i.e. isolation of T cells from spleen, resulting in extensive cell death in subsequent *in vitro* assays or upon adoptive cell transfer (20). Further, it has been shown that ADP-ribosylation of CD25 dampens IL-2 signalling by regulatory T cells, as the presence of NAD$^+$ reduced STAT1 phosphorylation in response to IL-2 stimulation (12). ADP-ribosylation of CD8a inhibits binding to MHCI and ADP-ribosylation of LFA-1 inhibits homotypic binding to LFA1 on other cells (13, 21)

Apart from interference with target protein function, ADP-ribosylation can also affect the binding of monoclonal antibodies. For example, binding of clone 53-5.8 to CD8a is inhibited by ADP-ribosylation whereas clone H35-17.2 is unaffected (13). Similarly, ADP-ribosylation of P2X7 affects binding of clone Hano43, whereas clone Hano44 is unaffected (22).

The functional and technical consequences of ADP-ribosylation of cell surface proteins warrant proteomic investigation of the tissue- or cell-specific ADP-ribosylome. A comprehensive list of ADP-ribosylted target proteins opens the perspective to investigate the potential impact of this post-translational modification on the target protein function. For this, we recently developed a method combining Af1521 macrodomain-based enrichment of ADP-ribosylated peptides with mass spectrometry analyses to identify ADP-ribosylation sites across the proteome (23). Using this approach we previously generated ADP-ribosylomes of HeLa cells and mouse liver (23), mouse skeletal muscle and heart (24), mouse embryonic fibroblasts (25) and mouse microglia (26). The goal of this study was to subject mouse spleen T cells to a comprehensive ADP-ribsylome analyses in order to identify new targets of ARTC2.2-mediated cell surface protein ADP-ribosylation. From T cells incubated with NAD$^+$, we identified 67 ADP-ribosylated target proteins, including 48 plasma membrane and 16 Golgi/ER proteins.

MATERIAL AND METHODS

Mice

C57BL/6 mice were used for all experiments. ARTC2ko mice (Art2b^{tm1Fkn}, MGI#2388827) (27) were backcrossed onto the C57BL/6J background for at least 12 generations. All mice were bred at the animal facility of the University Medical Center (UKE). All experiments involving tissue derived from animals were performed with approval of the responsible regulatory committee (Hamburger Behörde für Gesundheit und Verbraucherschutz, Veterinärwesen/Lebensmittelsicherheit, ORG722, N18/006). All methods were performed in accordance with the relevant guidelines and regulations.

Preparation of Immune Cells

Spleen and liver tissue were mashed through a cell strainer (50 mL falcon strainer, 70 µm, GBO) using a syringe piston. Additionally, liver leukocytes were purified by running a percoll gradient. Cells were resuspended in 5 mL 33% percoll/PBS in a 15 mL Falcon tube, and centrifuged at 1600 rpm, 12°C, for 20 min. The pellet was washed once in PBS (ThermoFisher). Single cell suspensions were kept in FACS buffer containing 1 mM EDTA (Sigma) and 0.1% bovine serum albumin (Sigma). Erythrocytes were lyzed using an ACK lysis buffer (155 mM NH_4Cl, 10 mM $KHCO_3$, 0.1 mM EDTA, pH 7.2). Peritoneal macrophages were harvested from the peritoneal cavity by lavage with 5 mL cold PBS + 1 mM EDTA. In order to prevent T cell surface ADP-ribosylation during cell preparation, some mice were i.v. injected with 30 µg of the ARTC2.2-blocking nanobody s+16a (28) 30 min prior to sacrificing.

Antibodies and Flow Cytometry

The following monoclonal antibodies were used for flow cytometric analyses: anti-CD3e-PE (clone 17A2, Biolegend), anti-ARTC2.2-AF647 [clone A109, Prof. Koch-Nolte (29)], anti-CD73-PE (clone TY/11.8, Biolegend), anti-CD8a-FITC (clone 53-6.7, Biolegend), anti-CD11b-FITC (clone M1/70, Biolegend). For protein harvesting, CD3$^+$ T cells from spleen and liver were isolated by fluorescence activated cell sorting (FACS) on a BD FACS Aria III.

T Cell Protein Harvesting

FACS-sorted spleen T cells where subjected to *ex vivo* treatment with 50 µM NAD$^+$ (Sigma) whereas a second preparation of spleen T cells and the liver T cells were left untreated in order to identify targets that were ADP-ribosylated during cell preparation (30). NAD$^+$ was washed away after 15 min of incubation at 4°C and cells were subsequently treated with ARTC2.2-blocking nanobody s+16a for 15 min to avoid ADP-ribosylation of cell surface proteins by intracellular ADP-ribosyltransferases during lysis with denaturing RIPA buffer (Sigma).

Proteomic Sample Preparation and ADP-Ribosylated Peptide Enrichment

For buffer exchange, protein reduction, alkylation, poly to mono-ADP-ribose reduction by PARG (Poly(ADP-Ribose) Glycohydrolase) and tryptic digestion a modified FASP (filter-aided sample preparation) protocol (31) was applied. For each sample 100-200 µg protein extracts were reduced in 1 mM DTT for 30 min and subsequently transferred to a 0.5 mL molecular weight cut off centrifugal filter unit (Microcon-30kDa Milipore, Sigma) and centrifuged until all buffer was passed through the filter. Samples were alkylated for 15 min using urea buffer containing 20 mM chloroacetamide and washed once with 100 µL urea buffer (8 M Urea, 0.1 M Tris-HCl pH 8) and once with 100 µL PARG buffer (50 mM Tris-HCL pH 8, 10 mM $MgCl_2$, 250 µM DTT, 50 mM NaCl). 0.5 µg recombinant PARG enzyme (in-house) in 100 µL PARG buffer was added on to the filter and incubated for 1 h. Filter was subsequently washed with 100 µL 50 mM ammonium bicarbonate buffer. On filter digestion was performed in 100 µL 50 mM ammonium bicarbonate using 5 µg sequencing grade modified trypsin (Promega) at room temperature overnight.

ADP-ribosylated peptide enrichment was performed as previously described (23). The peptide mixture was diluted in PARG buffer (50 mM Tris–HCl, pH 8, 10 mM $MgCl_2$, 250 µM DTT and 50 mM NaCl) and binding was carried out for 2 h at 4°C using the Af1521 macrodomain GST-fusion protein coupled to glutathione-Sepharose beads. Beads were washed three times with PARG buffer and bound peptides were eluted three times with 0.15% TFA. The resulting mixture was desalted using stage tips packed with C18 filters.

Mass Spectrometry Data Acquisition

Samples were analyzed using an Orbitrap Q Exactive HF mass spectrometer (Thermo Fisher Scientific) coupled to a nano EasyLC 1000 (Thermo Fisher Scientific). Peptides were loaded onto a reverse-phase C18 (ReproSil-Pur 120 C18-AQ, 1.9 µm, Dr. Maisch GmbH) packed self-made column (75 µm × 150 mm) that was connected to an empty Picotip emitter (New Objective, Woburn, MA). Solvent compositions in buffers A and B were 0.1% formic acid in H2O and 0.1% formic acid in acetonitrile, respectively. Peptides were injected into the mass spectrometer at a flow rate of 300 nL/min and were separated using a 90 min gradient of 2% to 25% buffer B. The mass spectrometer was operated in data-dependent acquisition mode and was set to acquire full MS scans from 300–1700 m/z at 60,000 resolution with an automated gain control (AGC) target value of 3×10^6 or a maximum injection time of 110 ms. Charge state screening was enabled, and unassigned charge states and single charged precursors were excluded. The 12 most abundant ions on the full scan were selected for fragmentation using 2 m/z precursor isolation window and beam-type collisional-activation dissociation (HCD) with 28% normalized collision energy. MS/MS spectra were collected with AGC target value of 1×10^6 or a maximum injection time of 240 ms. Fragmented precursors were dynamically excluded from selection for 20 s.

Mass Spectrometry Data Analysis

MS and MS/MS spectra were converted to Mascot generic format (MGF) by use of Proteome Discoverer, v2.1 (Thermo Fisher Scientific). The MGFs were searched against the UniProtKB mouse database (taxonomy 10090, version 20160902), which included 24'905 Swiss-Prot, 34'616 TrEMBL entries, 59'783 reverse sequences, and 262 common contaminants. Mascot 2.5.1.3 (Matrix Science) was used for peptide sequence identification with previously described search settings (32). Enzyme specificity was set to trypsin, allowing up to four missed cleavages. The ADP-ribose variable modification was set to a mass shift of 541.0611, with scoring of the neutral losses equal to 347.0631 and 249.0862. The marker ions at m/z 428.0372, 348.0709, 250.0940, 136.0623 were ignored for scoring. S, R, T, K, E, D and Y residues were set as variable ADP-ribose acceptor sites. Carbamidomethylation was set as a fixed modification on C and oxidation as a variable modification on M. Peptides are considered correctly identified when a mascot score > 20 and an expectation value < 0.05 are obtained. ADP-ribosylation sites were considered correctly localized with a localization probability of > 70%.

Bioinformatic Analyses

For protein network visualization and GO enrichment analyses cytoscape (33), STRING database (v. 11) (34) and the cytoscape string app (35) were used. For the network visualization only highest confidence interactions are shown (≥0.9) and proteins were clustered using the cytoscape string app.

HEK Cell Transfection

Human embryonic kidney (HEK) 293T cells were transfected with a pCMVSport6.1 plasmid encoding mouse *Nt5e* (CD73) using jetPEI transfection reagent (Polysciences Europe). Transfected cells were FACS-isolated every 3 - 4 days for high CD73 expression in order to generate stably transfected HEK cells. The stably transfected $CD73^+$ HEK cells were then co-transfected with pME plasmid encoding for *Art2b* (ARTC2.2) in order to evaluate the impact of ADP-ribosylation on CD73 enzymatic activity.

AMP Degradation Assay

1×10^4 HEK 293 T cells were incubated with 50 µM NAD^+ on ice for 30 min. Cells were washed with FACS buffer twice (1410 rpm, 5 min, 4°C). Cells were resuspended in 100 µL FACS buffer, subsequently 100 µL AMP were added to a final concentration of 10 µM and incubated at room temperature for 40 min. Cells were spin down (1410 rpm, 5 min, 4°C) and 25 µL supernatant was transferred to a solid white plate. 25 µL AMP-Glo Reagent I were added per well, mixed and incubated at room temperature for 30 min. This was followed by addition of 50 µL AMP-Glo Detection Solution per well and incubation for 60 min at room temperature. Plate was read with a plate-reading luminometer.

HPLC CD73 Enzymatic Activity Assay

To determine the AMPase activity by high performance liquid chromatography (HPLC), 0.2×10^6 $CD8^+$ T cells or peritoneal macrophages were incubated with 1 µM 1,N^6-etheno-AMP (eAMP, Biolog) for 30 min at 37°C. After the incubation, cells were removed (450 × g, 5 min, 4°C) and all samples were passed through 10 kDa size exclusion filters (10,000 × g, 10 min, 4°C, Pall Corporation) and stored at -20°C until analyses. The analyses was performed on reversed-phase HPLC system (Agilent Technologies) with a 250 mm × 4.6 mm C8 Luna column (5 µm particle size, Phenomenex) as stationary phase. The mobile phase consisted of different compositions of HPLC buffer A (20 mM KH_2PO_4, pH 6.0) and B (50% buffer A, 50% methanol), and elution of the nucleotides from the column resulted from an increasing methanol content in the mobile phase [0.0 min (0.0% buffer B), 5.0 min (0.0% buffer B), 27.5 min (100.0% buffer B), 30.0 min (100.0% buffer B), 32.0 min (0.0% buffer B), 43.0 min (0.0% buffer B)]. The signals in both systems were detected by fluorescence detection (230 nm excitation wavelength, 410 nm emission wavelength). Different amounts of etheno-nucleotides (Biolog) were measured to quantify eAMP and the degradation product etheno-adenosine (eADO).

Statistics and Software

For statistical analyses, GraphPad Prism 8 was used. Two groups were compared using the student's t test. Multiple groups were compared using oneway ANOVA in combination with Dunnett's multiple comparison test. Analysis of flow cytometric data was performed using FlowJo (Treestar). The structure model of mouse CD73 (Q61503) was analyzed using Pymol software.

RESULTS

Identification of Potential ARTC2.2 ADP-Ribosylation Targets on T Cells

The aim of this study was to reveal potential ARTC2.2 ADP-ribosylation targets of mouse T cells. These proteins are most likely ADP-ribosylated on arginine residues facing the extracellular environment. Based on our previous studies (24, 26) we hypothesized that it is possible to detect ARTC2.2 mediated ADP-ribosylation by mass spectrometry even on proteins extracted from relatively small numbers of FACS-sorted T cells. We aimed to map ADP-ribosylated proteins of T cells isolated from mice under basal conditions [i.e. after encounter with endogenous extracellular NAD$^+$ *in vivo* or during cell preparation (30)] and after *ex vivo* treatment with exogenous NAD$^+$. For this we applied our established mass spectrometry-based strategy with modifications to make it applicable to low sample input (23, 26).

CD3$^+$ T cells were FACS sorted from seven spleens and livers of C57BL/6 mice. Aliquots of cells were incubated for 15min in the absence or presence of exogenous NAD$^+$. To prevent ADP-ribosylation of intracellular proteins after cell lysis, cells were incubated with the ARTC2.2-blocking nanobody s+16a for 15 min before lysis with RIPA buffer. Proteins were subjected to filter-aided digestion and ADP-ribosylated peptides were enriched using the Af5121 macrodomain (**Figure 1A**). Samples were subsequently analyzed by mass spectrometry to identify peptides and to localize ADP-ribosyl modification sites. Importantly, we used higher-energy collisional dissociation (HCD) for peptide fragmentation, since this allows efficient identification of arginine ADP-ribosylated peptides due to the stability of ADP-ribosyl-arginine but is less effective in localizing serine and other O-linked ADP-ribosylations due to the lability of this modification type in HCD (24, 32, 36).

We identified 93 unique ADP-ribosylated peptides corresponding to 67 proteins (**Supplementary Table 1**). 49 ADP-ribosylated proteins were exclusively identified in T cells treated with NAD$^+$ (**Figures 1B, C**), 12 ADP-ribosylated proteins were found in both untreated and NAD$^+$ treated cells, 6 ADP-ribosylated proteins were only identified in the untreated conditions. We obtained confident ADP-ribose site localizations (localization probability >70%, considering R, S, T, Y, E, D, K as variable ADP-ribose amino acid acceptor sites) for 35 unique R- and 1 S-ADP-ribosylation sites (**Figure 1C**).

Taken together, our approach allowed us to identify a considerable number of ADP-ribosylated proteins from a low number of T cells. We observed induction of R-ADP-

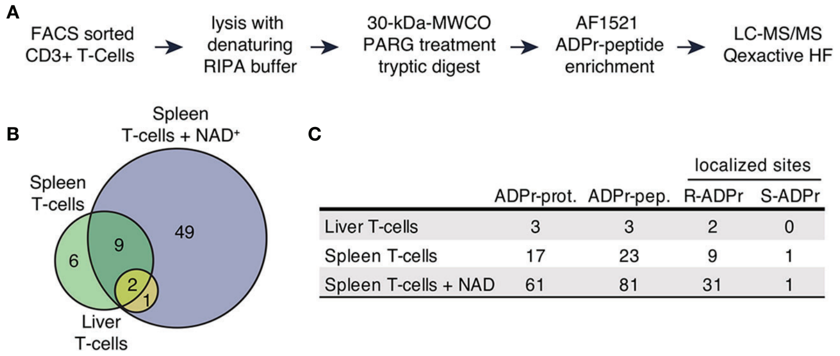

			localized sites	
	ADPr-prot.	ADPr-pep.	R-ADPr	S-ADPr
Liver T-cells	3	3	2	0
Spleen T-cells	17	23	9	1
Spleen T-cells + NAD	61	81	31	1

FIGURE 1 | The ADP-ribosylated proteome identified in T cells. **(A)** Schematic workflow of proteomic sample processing, digestion and ADPr-peptide enrichment tailored to the low input protein amount obtained from FACS sorted T cells. **(B)** ADP-ribosylated proteins identified in the three different sample types depicted in a Venn diagram. **(C)** Numbers of uniquely identified ADP-ribosylated proteins, unique ADP-ribosylated peptides and modified amino acids that were confidently localized (localization probability > 70%). Modified arginine and serine sites were found.

ribosylation upon treatment with exogenous NAD^+ indicating active ARTC2.2 on these cells.

Exogenous NAD^+ Induces Extracellular ADP-Ribosylation of Proteins Relevant for the Immune Response

To functionally cathegorize the identified ADP-ribosylation T cell target proteins, we performed gene-ontology (GO) term enrichment analysis, protein-protein interaction network visualization and literature comparisons. GO cellular component (GOCC) term enrichment analyses revealed strong enrichment for ADP-ribosylated proteins to be localized on the cell surface and plasma membrane (**Figure 2A**), providing further evidence that these proteins are most likely targets of ARTC2.2. Other significantly enriched cellular components were the endoplasmic reticulum and Golgi apparatus. GO biological processes (GOBP) were enriched in immune system processes, cell surface receptor signaling, cell adhesion and regulation of T cell activity (**Figure 2A**). Reactome pathway enrichment analysis provided additional separation of ADP-ribosylated proteins into more specific functional terms such as antigen presentation, signaling by interleukins, T cell receptor (TCR) signaling, and integrin cell surface interactions (**Figure 2A**).

Next, we performed protein level visualization of all identified ADP-ribosylated proteins by their association to Reactome pathway terms, relevant protein features, and protein-protein interactions. For this, we plotted the ADP-ribosylated proteins in form of a STRING network (**Figure 2B**) (34). ADP-ribosylated proteins with strong evidence for interactions among each other are connected with a grey line and proteins that had no interaction partners were preserved and shown as unconnected nodes. ADP-ribosylated proteins are color coded based on their affiliation to Reactome pathway terms identified in **Figure 2A**. ADP-ribosylated proteins are additionally marked if they are associated with the plasma membrane or cell surface (GOCC), are an ADP-ribosyltransferase or were already identified under basal conditions. The major hub of interacting proteins targeted by ADP-ribosylation was identified to have a role in TCR signaling, antigen presentation and cell surface integrin interactions. Connected to this cluster was *Nt5*e (5-prime-nucleotidase, CD73), a protein that hydrolyzes extracellular AMP to adenosine (37). An additional hub of interacting proteins consisted of the heteromeric IL-2 receptor complex, including IL2Rα, IL2Rβ and IL2Rγ that were all found to be ADP-ribosylated after addition of NAD^+. We have previously identified IL2Rα as a target of ARTC2.2 and shown that its ADP-ribosylation functionally diminishes IL2 signaling (12). Most ADP-ribosylated proteins present at basal conditions were disconnected from these interaction hubs and less likely localized to the cell surface (**Figure 2B**). Two ADP-ribosyltransferases, ARTC2.2 (*Art2b*) and ARTD8/PARP14 (*Parp14*), were identified to be ADP-ribosylated, potentially by auto modification. Both were found to be ADP-ribosylated under basal and NAD^+ treated conditions. Proteomic identification of ADP-ribosylation sites on ARTCs have previously been observed in mouse liver on ARTC2.2 (23), in mouse microglia cells on ARTC2.1 (26) and on ARTC1 in mouse heart and skeletal muscle tissues (24). ARTC (auto-)ADP-ribosylation can thus serve as a marker for ARTC activity. ADP-ribosylation by ARTD8/PARP14 has previously been associated with immune cell functions (38).

Next, we compared ADP-ribosylation levels of a few selected sites among the different conditions and with our previously published data on mouse liver (23) and microglia cells (26) (**Figure 2C**). ADP-ribosylation of CD73 at R149 was found exclusively on T cells treated with NAD^+. Proteins that were identified in multiple different sample types showed modification on the same site (Pdia3, Slc44a2, Ptprc, Itgb2, Il2rg, H2-K1), or on additional sites (Ptprc, Itgb2, H2-K1) (**Figure 2C**). As exemplified by Pdia3 (a cytosolic protein exclusively modified on R62) and Slc44a2 (a multispan transmembrane protein exclusively modified on extracellular R130), R-ADP-ribosylation showed high site specificity on some proteins. In most of the analyzed cases, the R-ADP-ribosylation sites are located on the extracellular domain of the protein. An exception is the intracellular ARTD8/PARP14, which we found to be modified on S842 under basal and NAD^+ treated conditions, consistent with our recent observation that ARTD8/PARP14 is modified by O-linked ADP-ribosylation (24). In summary, we identified numerous T cell surface proteins with immune system relevant functions that are R-ADP-ribosylated, likely by ARTC2.2, in the presence of exogenous NAD^+.

ADP-Ribosylation of CD73 Reduces the Capability of CD8 T Cells to Generate Adenosine

The majority of the identified T cell surface ADP-ribosylation targets are membrane proteins that act as receptors in cell signalling, antigen presentation or cell-cell adhesion. Apart from ARTC2.2 itself, CD73 was the only identified cell surface enzyme to be ADP-ribosylated. CD73 is expressed on several cell populations of the immune system, including regulatory T cells, $CD8^+$ T cells and macrophages. It converts extracellular adenosine monophosphate (AMP) to adenosine (ADO) (**Figure 3A**), which acts as an immunosuppressant e.g. by inhibiting T cell proliferation (39). While ADP-ribosylation has been shown to impact the function of several cell surface receptors, little is known about the impact of ADP-ribosylation on the enzymatic activity of cell surface enzymes. Therefore, we investigated the impact of ADP-ribosylation on the catalytic activity of CD73. Analyses of the 3D structure model of mouse CD73 (Q61503) revealed that the identified ADP-ribosylation site R149 (red) is distant to the active site (yellow) of CD73 (**Figure 3B**).

We first tested the impact of CD73 ADP-ribosylation in HEK cells stably transfected with mouse CD73 upon transient co-transfection with an expression vector for ARTC2.2. We pretreated these cells with NAD^+ 24 h after transfection, and FACS-sorted equal amounts of $CD73^+ARTC2.2^-$ and $CD73^+ARTC2.2^+$ HEK cells (**Figure 3C**). The gates during cell collections were adjusted for equivalent cell surface levels of CD73 on $ARTC2.2^-$ and $ARTC2.2^+$ HEK cells. We then performed a comparative AMP degradation assay with the

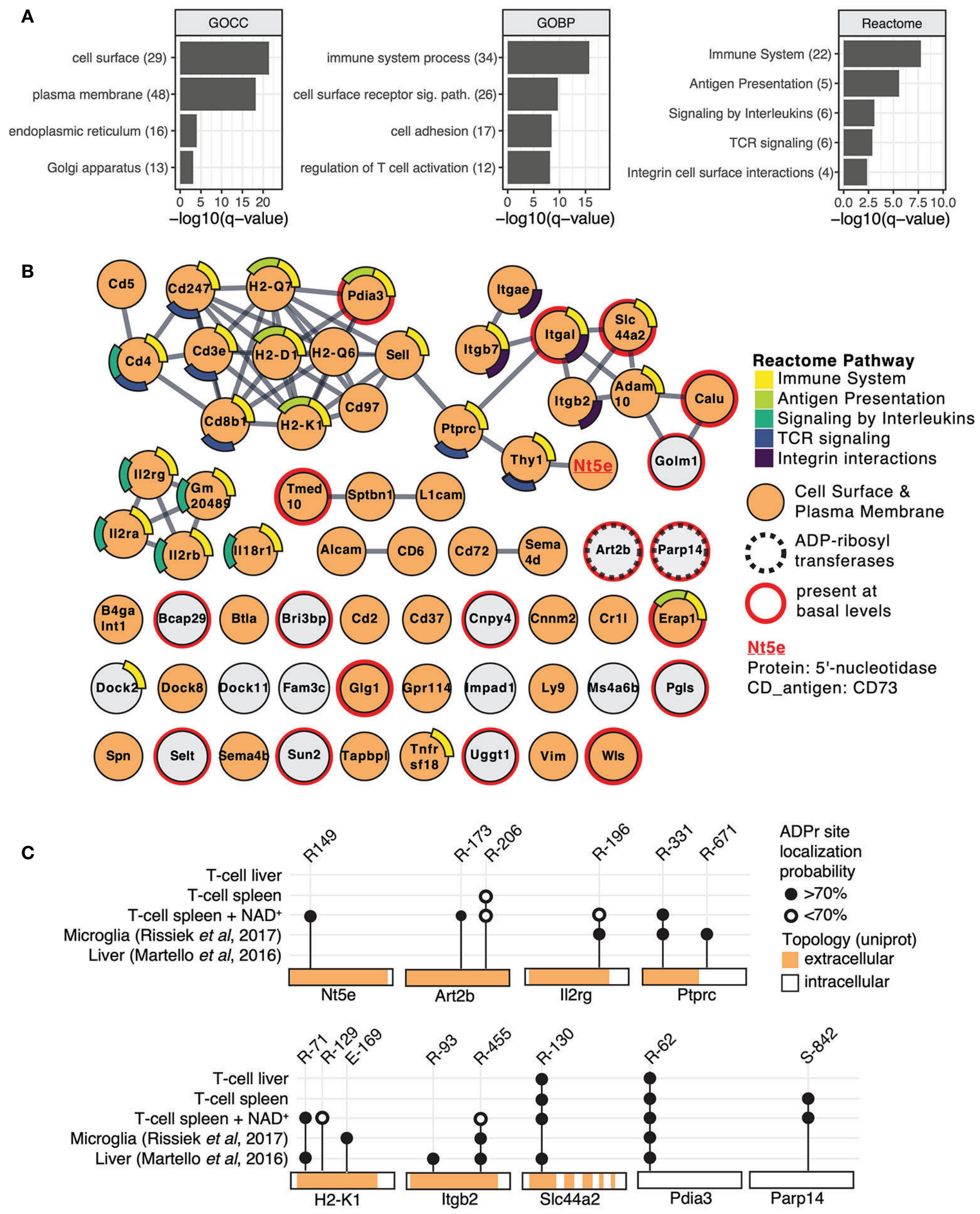

FIGURE 2 | Mouse T cell surface ADP-ribosylome analyses. **(A)** Gene ontology term enrichment was performed for ADP-ribosylated proteins identified in all conditions against the whole mouse genome. Gene ontology biological processes (GOBP), gene ontology cellular components (GOCC) and Reactome pathways were included. The q-values of selected and significantly enriched terms are plotted. Numbers of ADP-ribosylated proteins included in the specific terms are indicated in brackets. **(B)** STRING protein-protein interaction network of ADP-ribosylated proteins identified in all conditions. Gene names of ADP-ribosylated proteins are shown and high confidence protein-protein interactions (STRING interaction score ≥0.9) are indicated with grey lines. Protein nodes are color coded by their affiliation to the Reactome pathways shown in **(A)** Proteins associated with the plasma membrane or cell surface are marked in orange. Proteins that were already identified under untreated conditions are marked with a red line and the two identified ADP-ribosyltransferases with a dashed line. CD73 that was chosen for follow up studies is highlighted. **(C)** ADP-ribosylation sites on selected proteins are plotted and compared to ADP-ribosylation sites identified in (23, 26).

collected CD73$^+$ARTC2.2$^-$ and CD73$^+$ARTC2.2$^+$ HEK cells. We found that NAD$^+$-treated CD73$^+$ARTC2.2$^+$ cells were slightly but significantly less potent in degrading AMP than NAD$^+$-treated CD73$^+$ARTC2.2$^-$ HEK cells (**Figure 3C**), consistent with an inhibitory effect of ADP-ribosylation on CD73 activity.

We next analyzed the impact of NAD$^+$ on the enzymatic activity of CD73 on primary T cells. For this we chose CD8$^+$ T cells, which co-express ARTC2.2 and CD73, but are much less sensitive to NAD$^+$-mediated cell death along the ARTC2.2/P2X7 axis when compared to Tregs (15). We isolated CD8$^+$ T cells from untreated B6 WT mice, B6 WT mice treated with the ARTC2.2 blocking nanobody s+16a in order to block ARTC2.2 already *in vivo*, or from B6 ARTC2ko mice. Of note, cell surface levels of CD73 were comparable among WT and ARTC2.2ko $CD8^+$ T cells (**Figure 3D**). Since $CD8^+$ T cells express much lower cell surface levels of CD73 than CD73-transfected HEK cells, we used an HPLC-based assay measuring the CD73-dependent generation of etheno-adenosine (eADO) from etheno-adenosine monophosphate (eAMP), as this was a more sensitive approach compared to the AMP degradation assay. We treated all three samples with NAD^+ and quantified the generation of eADO. Here, we observed that NAD^+ treated WT $CD8^+$ T cells generated less eADO compared to $CD8^+$ T cells from s+16a treated WT mice or from ARTC2.2ko mice (**Figure 3D**). Finally, we performed a similar assay with peritoneal macrophages that express high surface level of CD73 but lack ARTC2.2 expression. Here, NAD^+-treated peritoneal macrophages of WT mice generate slightly but significantly more eADO compared to ARTC2ko macrophages, consistent with the fact that a larger fraction of WT peritoneal macrophages expressed high level of CD73 when compared to ARTC2ko peritoneal macrophages (**Figure 3E**). In summary, we could demonstrate that in an NAD^+-rich environment, CD73 enzymatic activity is dampened on cells co-expressing ARTC2.2.

DISCUSSION

In this study we investigated the T cell ADP-ribosylome with a focus on ARTC2.2-mediated ADP-ribosylation of T cell surface proteins. We identified 67 ADP-ribosylated target proteins 48 of which are expressed at the cell surface and 16 of which in the ER or the Golgi apparatus. Of the identified ADP-ribosylation sites 35 were on arginine residues and 1 on a serine residue. Many of the identified target proteins are involved in immune system processes such as signalling, cell adhesion and regulation of T cell

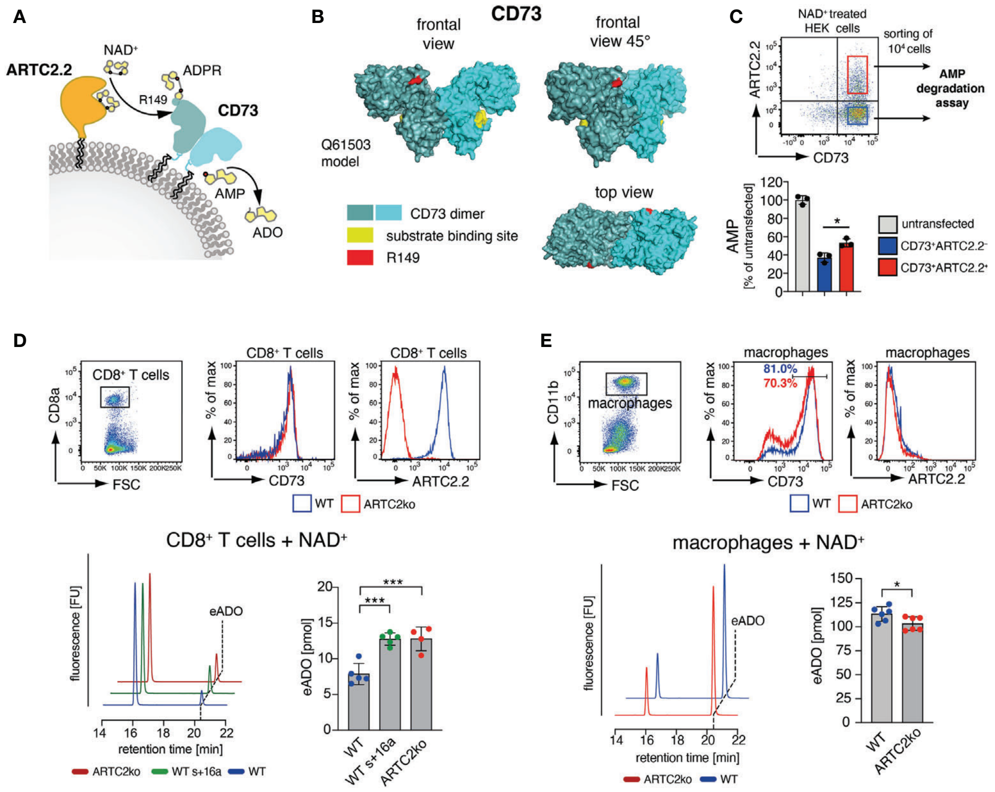

FIGURE 3 | ARTC2.2-dependent regulation of CD73 enzymatic activity. **(A)** CD73 can degrade adenosine monophosphate (AMP) to adenosine ADO. ARTC2.2 ADP-ribosylates CD73 at R149, potentially interfering with enzymatic activity. **(B)** The structure model Q61503 of a mouse CD73 dimer is shown in cyan. ADP-ribosylation site R149 (red) and substrate binding site (yellow) are indicated. **(C)** $ARTC2.2^+CD73^+$ and $ARTC2.2^-CD73^+$ HEK cells (n = 3) were incubated with NAD^+, FACS sorted and compared towards their capacity to degrade AMP in the AMPGlo assay. **(D)** Spleen $CD8^+$ T cells from B6 WT, B6 WT treated with ARTC2.2-blocking nanobody s+16a, and from ARTC2ko mice were analyzed towards CD73 and ARCT2.2 expression. After NAD^+ treatment, FACS sorted cells (n = 4-5 technical replicates) were further subjected to an HPLC-based assay to measure their capacity to generate etheno-ADO (eADO) from etheno-AMP (eAMP). **(E)** Peritoneal macrophages from B6 WT and ARTC2ko mice were analyzed towards CD73 and ARCT2.2 expression. After NAD^+ treatment, FACS sorted cells (n = 6 technical replicates) were analyzed for their capacity to generate eADO. Statistical comparison of the two groups was performed by using the Student's t test, comparison of more than two groups was performed by using oneway ANOVA analyses with Dunnett's multiple comparisons ($p < 0.05$ = */$p < 0.001$ = ***). Data represent results from two **(C, E)** or three **(D)** independent experiments.

activity. It is conceivably that ADP-ribosylation modifies the function of many of these target proteins, thereby fine tuning immune reactions (2, 20). As an example, we analyzed the impact of ADP-ribosylation on the capacity of CD73 to hydrolyze AMP into adenosine. Our results indicate that ADP-ribosylation of CD73 leads to a reduced conversion of AMP to adenosine.

In our study we analyzed the ADP-ribosylome of T cells treated with or without exogenous NAD^+. It is important to note that NAD^+ is also released during the preparation of murine T cells (30), which is sufficient to allow the ADP-ribosylation of T cell surface proteins. Therefore, we can not exclude that at least some of the observed ADP-ribosylated T cell surface proteins detected under basal conditions without addition of exogenous NAD^+, such as *Slc44a2* or *Itgal*, identified in untreated T cells from spleen or liver were modified during cell isolation. To further investigate whether the observed ADP-ribosylation of proteins occurred during the cell isolation or is catalyzed *in vivo*, systemic injection of the ARTC2.2 blocking nanobody s+16a prior to cell harvesting would prevent ADP-ribosylation during preparation (17, 28). However, this would also block ADP-ribosylation *in vivo* during the time between injection and the sacrifice of mice, but would not prevent de-ADP-ribosylation by enzymes. In order to identify further targets that are ADP-ribosylated *in vivo* it might thus be necessary to block de-ADP-ribosylation. Finally, it would also be interesting to compare the ADP-ribosylome of different T cell types such as $CD4^+$ helper T cells, $CD4^+$ regulatory T cells or cytotoxic $CD8^+$ T cells as well as the ADP-ribosylome of the same T cell population from different organs, e.g. spleen and liver. However, this would probably need large amounts of cell material to start with.

Our analyses of proteins derived from NAD^+ treated T cells identified known and new targets of ARTC2.2-mediated ADP-ribosylation. We confirmed already known ARTC2.2 targets such as CD25 (*Il2rg*), CD8β (*Cd8b*) and CD45 (*Ptprc*). For CD25 we confirmed R196 (R178 in the mature protein) as ADP-ribosylation site, as reported in a previous study (12). Similarly, CD45 was found to be ADP-ribosylated on R331 of cells analyzed in the microglia study (26). Of note, the T cells used in this study were isolated from C57BL/6 (B6) mice, whereas the microglia study used cells from Balb/c mice. B6 mice carry a premature stop codon in the gene for the ARTC2.1 (40), and B6 T cells therefore exclusively express ARTC2.2 as cell surface ADP-ribosyltransferase (41). Balbc microglia express the thiol-activated ARTC2.1, but not ARTC2.2 and Balb/c T cells co-express ARTC2.1 and ARTC2.2 (5, 6). The finding of the same ADP-ribosylated targets on microglia and T cells indicates that these two closely related ADP-ribosyltransferases may share common targets and modify common sites.

MHC class I (MHC-I) molecules are yet not well characterized regarding the potential impact of ADP-ribosylation. In this study we identified H2-D, H2-K and the MHC-Ib molecule H2-Q to be ADP-ribosylated on T cells. MHC-I molecules present endogenous peptides to $CD8^+$ T cells. Therefore, it would be interesting to test if MHC-I ADP-ribosylation affects its interaction with the T cell receptor (TCR) or loading of the peptide to form the MHC-I/peptide complex. Indeed, the identified R169 ADP-ribosylation site in H2-D1 is in close proximity to the TCR interaction surface (see PDB file 5m01). Further, a former study showed that ADP-ribosylation of the CD8β T cell coreceptor affects MHC-I/TCR interaction (13). It would thus be interesting to investigate, whether MHC-I ADP-ribosylation diminishes TCR binding in a similar fashion. Moreover, it is tempting to speculate that MHC-I ADP-ribosylation has an impact on TCR binding in an antigen-specific fashion: introduction of an ADP-ribose group at the MHC-I/TCR interaction site could lead to the activation of alternative $CD8^+$ T cell clones that recognize this modified MHC-I/peptide complex. Future studies should address this hypothesis.

The list of ADP-ribosylation targets on T cells identified here is probably underestimated. The ATP gated P2X7 ion channel for example, a prominent and well characterized ARTC2.2 target on T cells (14), was not identified as target for ADP-ribosylation by our MS approach. P2X7 is expressed on regulatory T cells, NKT cells and CD4 effector/memory T cells (15, 17, 42) – together these cells constitute only a minor fraction of the T cells analyzed here. Therefore, the amount of available P2X7 proteins might have been below the detectable threshold. Furthermore, it is possible that ADP-ribosylated peptides are lost during sample preparation or mass spectrometry analysis due to technical circumstances.

In this study, we focused on the functional impact of CD73 ADP-ribosylation. CD73 is a ecto-5´-nucleotidase that generates immunosuppressive adenosine from AMP and thus plays a critical role in balancing the course of an inflammatory reaction (43). From a technical point of view, it is worth noting that adenosine is rapidly degraded to inosine by adenosine deaminase (ADA), both *in vivo* and *in vitro*. The etheno-adenosine (eADO) used in our HPLC-based assay to monitor and quantify CD73 enzymatic activity, however, is not a substrate for ADA (44) and therefore much more stable. Further, it has been recently shown that eADO is not taken up by cells *via* adenosine transporters (45). Therefore, differential degradation or uptake resulting in an experimental bias seems unlikely to explain the impact of NAD^+ on the CD73 enzymatic activity. The identified ADP-ribosylation site at R149 is distant from the active site of CD73 and is therefore likely to act allosterically. When comparing $CD8^+$ T cells and macrophages, NAD^+ only had a dampening impact on the catalytic activity of CD73 on $CD8^+$ T cells that co-express ARTC2.2 but not on macrophages that lack ARTC2.2. Therefore, CD73 ADP-ribosylation might be a T cell-specific mechanism that modulates CD73 activity in an NAD^+ rich microenvironment, such as tumor tissue. Here, NAD^+ could be released along with ATP during tumor cell secondary necrosis. Indeed, prostate cancer cell lines have been reported to actively release intracellular NAD^+ into the culture medium (46). $CD8^+$ T cells play a critical role in anti-tumor immune responses. CD73 on CD8 T cells seems to significantly contribute to the anti-tumor immunity response, since adoptively transferred CD73-deficient ovalbumin-specific OT-I T cells were more potent in killing OVA-expressing B16 melanoma tumors compared to

WT OT-I T cells (47). This was accompanied by lower expression levels of the exhaustion markers programmed cell death protein 1 (PD-1) and CD39, strengthening the role of CD73 as an immune checkpoint and as a potential target in tumor therapy. Vice versa, it would be interesting to evaluate whether ARTC2-deficient OT-I T cells are less potent in killing OVA-expressing B16 melanoma, as CD73 activity would not be dampened by NAD$^+$ in the tumor environment.

Interestingly, both ARTC2.2 and CD73 can be shed from T cells (48, 49) and it has recently been shown that soluble ARTC2.2 can ADP-ribosylate various cytokines, including IFNγ (50). Therefore, it would be interesting to elucidate whether soluble ARTC2.2 could also ADP-ribosylate the soluble form of CD73 and thereby control the cell-independent generation of adenosine.

DATA AVAILABILITY STATEMENT

The original contributions presented in the study are included in the article/**Supplementary Material**. Further inquiries can be directed to the corresponding authors.

ETHICS STATEMENT

The animal study was reviewed and approved by Hamburger Behörde für Gesundheit und Verbraucherschutz, Veterinärwesen/Lebensmittelsicherheit.

AUTHOR CONTRIBUTIONS

BR and SM collected and prepared samples for mass spectrometry. ML performed mass spectrometry experiments, data collection and analyses. YD and RW performed CD73 functional assays. ET and TM assisted with CD73 functional assay data analyses and interpretation. FK-N and MH supervised the experiments and assisted with data interpretation and manuscript preparation. BR and ML assembled the figures and wrote the manuscript, which has been reviewed by all authors. All authors contributed to the article and approved the submitted version.

FUNDING

This work was funded by the Deutsche Forschungsgemeinschaft (DFG, German Research Foundation) - Project-ID: 335447717 - SFB 1328 to FK-N (A10, Z2), TM (A13) and ET (A13/A14), a grant from "Hermann und Lilly Schilling-Stiftung für Medizinische Forschung" to TM, ADP-ribosylation research in the laboratory of MH is funded by the Kanton of Zurich and the Swiss National Science Foundation (grant 31003A_176177). ML is supported by a postdoctoral fellowship from the Swiss National Science Foundation (grant P400PB_194379). SM is supported by a grant of the Mildred Scheel Cancer Career Center HaTriCS4.

ACKNOWLEDGMENTS

The authors would like to thank Peter Gehrig, Paolo Nanni, Christian Panse, and Jonas Grossmann (Functional Genomics Center of the University of Zurich) for help with the mass spectrometry measurements and data analysis, the lab of Andreas Guse (UKE Hamburg, Germany) for assistance with the HPLC measurements, and the HEXT FACS Core Facility (UKE Hamburg, Germany) for cell sorting.

SUPPLEMENTARY MATERIAL

The Supplementary Material for this article can be found online at: https://www.frontiersin.org/articles/10.3389/fimmu.2021.703719/full#supplementary-material

REFERENCES

1. Bazan JF, Koch-Nolte F. Sequence and Structural Links Between Distant ADP-Ribosyltransferase Families. *Adv Exp Med Biol* (1997) 419:99–107. doi: 10.1007/978-1-4419-8632-0_12
2. Koch-Nolte F, Adriouch S, Bannas P, Krebs C, Scheuplein F, Seman M, et al. ADP-Ribosylation of Membrane Proteins: Unveiling the Secrets of a Crucial Regulatory Mechanism in Mammalian Cells. *Ann Med* (2006) 38:188–99. doi: 10.1080/07853890600655499
3. Glowacki G, Braren R, Firner K, Nissen M, Kühl M, Reche P, et al. The Family of Toxin-Related Ecto-ADP-Ribosyltransferases in Humans and the Mouse. *Protein Sci* (2002) 11:1657–70. doi: 10.1110/ps.0200602
4. Koch-Nolte F, Kernstock S, Mueller-Dieckmann C, Weiss MS, Haag F. Mammalian ADP-Ribosyltransferases and ADP-Ribosylhydrolases. *Front Biosci* (2008) 13:6716. doi: 10.2741/3184
5. Hong S, Braß A, Seman M, Haag F, Koch-Nolte F, Dubyak GR. Lipopolysaccharide, IFN-Gamma, and IFN-Beta Induce Expression of the Thiol-Sensitive ART2.1 Ecto-ADP-Ribosyltransferase in Murine Macrophages. *J Immunol* (2007) 179:6215–27. doi: 10.4049/jimmunol.179.9.6215
6. Hong S, Braß A, Seman M, Haag F, Koch-Nolte F, Dubyak GR. Basal and Inducible Expression of the Thiol-Sensitive ART2.1 Ecto-ADP-Ribosyltransferase in Myeloid and Lymphoid Leukocytes. *Purinergic Signal* (2009) 5:369–83. doi: 10.1007/s11302-009-9162-2
7. Kanaitsuka T, Bortell R, Stevens LA, Moss J, Sardinha D, Rajan TV, et al. Expression in BALB/c and C57BL/6 Mice of Rt6-1 and Rt6-2 ADP-Ribosyltransferases That Differ in Enzymatic Activity: C57BL/6 Rt6-1 Is a Natural Transferase Knockout. *J Immunol* (1997) 159:2741–9.
8. Krebs C, Koestner W, Nissen M, Welge V, Parusel I, Malavasi F, et al. Flow Cytometric and Immunoblot Assays for Cell Surface ADP-Ribosylation Using a Monoclonal Antibody Specific for Ethenoadenosine. *Anal Biochem* (2003) 314:108–15. doi: 10.1016/S0003-2697(02)00640-1
9. Menzel S, Adriouch S, Bannas P, Haag F, Koch-Nolte F. Monitoring Expression and Enzyme Activity of Ecto-ARTCs. *Methods Mol Biol* (2018) 1813:167–86. doi: 10.1007/978-1-4939-8588-3_11
10. Koch-Nolte F, Petersen D, Balasubramanian S, Haag F, Kahlke D, Willer T, et al. Mouse T Cell Membrane Proteins Rt6-1 and Rt6-2 are Arginine/Protein Mono(ADPribosyl)transferases and Share Secondary Structure Motifs With ADP-Ribosylating Bacterial Toxins. *J Biol Chem* (1996) 271:7686–93. doi: 10.1074/jbc.271.13.7686
11. Okamoto S, Azhipa O, Yu Y, Russo E, Dennert G. Expression of ADP-Ribosyltransferase on Normal T Lymphocytes and Effects of Nicotinamide Adenine Dinucleotide on Their Function. *J Immunol* (1998) 160:4190–8.

12. Teege S, Hann A, Miksiewicz M, MacMillan C, Rissiek B, Buck F, et al. Tuning IL-2 Signaling by ADP-Ribosylation of CD25. *Sci Rep* (2015) 5:8959. doi: 10.1038/srep08959
13. Lischke T, Schumacher V, Wesolowski J, Hurwitz R, Haag F, Koch-Nolte F, et al. CD8-β ADP-Ribosylation Affects CD8(+) T-Cell Function. *Eur J Immunol* (2013) 43:1828–38. doi: 10.1002/eji.201243231
14. Seman M, Adriouch S, Scheuplein F, Krebs C, Freese D, Glowacki G, et al. NAD-Induced T Cell Death: ADP-Ribosylation of Cell Surface Proteins by ART2 Activates the Cytolytic P2X7 Purinoceptor. *Immunity* (2003) 19:571–82. doi: 10.1016/S1074-7613(03)00266-8
15. Hubert S, Rissiek B, Klages K, Huehn J, Sparwasser T, Haag F, et al. Extracellular NAD+ Shapes the Foxp3+ Regulatory T Cell Compartment Through the ART2-P2X7 Pathway. *J Exp Med* (2010) 207:2561–8. doi: 10.1084/jem.20091154
16. Kawamura H, Aswad F, Minagawa M, Govindarajan S, Dennert G. P2X7 Receptors Regulate NKT Cells in Autoimmune Hepatitis. *J Immunol* (2006) 176:2152–60. doi: 10.4049/jimmunol.176.4.2152
17. Rissiek B, Danquah W, Haag F, Koch-Nolte F. Technical Advance: A New Cell Preparation Strategy That Greatly Improves the Yield of Vital and Functional Tregs and NKT Cells. *J Leukoc Biol* (2014) 95:543–9. doi: 10.1189/jlb.0713407
18. Georgiev H, Ravens I, Papadogianni G, Malissen B, Förster R, Bernhardt G. Blocking the ART2.2/P2X7-System Is Essential to Avoid a Detrimental Bias in Functional CD4 T Cell Studies. *Eur J Immunol* (2018) 48:1078–81. doi: 10.1002/eji.201747420
19. Rissiek B, Lukowiak M, Raczkowski F, Magnus T, Mittrücker H-W, Koch-Nolte F. *In Vivo* Blockade of Murine ARTC2.2 During Cell Preparation Preserves the Vitality and Function of Liver Tissue-Resident Memory T Cells. *Front Immun* (2018) 9:1580. doi: 10.3389/fimmu.2018.01580
20. Rissiek B, Haag F, Boyer O, Koch-Nolte F, Adriouch S. ADP-Ribosylation of P2X7: A Matter of Life and Death for Regulatory T Cells and Natural Killer T Cells. *Curr Top Microbiol Immunol* (2015) 384:107–26. doi: 10.1007/82_2014_420
21. Nemoto E, Yu Y, Dennert G. Cell Surface ADP-Ribosyltransferase Regulates Lymphocyte Function-Associated Molecule-1 (LFA-1) Function in T Cells. *J Immunol* (1996) 157:3341–9.
22. Rissiek B, Stabernack J, Cordes M, Duan Y, Behr S, Menzel S, et al. Astrocytes and Microglia Are Resistant to NAD+-Mediated Cell Death Along the ARTC2/P2X7 Axis. *Front Mol Neurosci* (2019) 12:330. doi: 10.3389/fnmol.2019.00330
23. Martello R, Leutert M, Jungmichel S, Bilan V, Larsen SC, Young C, et al. Proteome-Wide Identification of the Endogenous ADP-Ribosylome of Mammalian Cells and Tissue. *Nat Commun* (2016) 7:12917. doi: 10.1038/ncomms12917
24. Leutert M, Menzel S, Braren R, Rissiek B, Hopp A-K, Nowak K, et al. Proteomic Characterization of the Heart and Skeletal Muscle Reveals Widespread Arginine ADP-Ribosylation by the ARTC1 Ectoenzyme. *Cell Rep* (2018) 24:1916–1929.e5. doi: 10.1016/j.celrep.2018.07.048
25. Abplanalp J, Leutert M, Frugier E, Nowak K, Feurer R, Kato J, et al. Proteomic Analyses Identify ARH3 as a Serine Mono-ADP-Ribosylhydrolase. *Nat Commun* (2017) 8:2055. doi: 10.1038/s41467-017-02253-1
26. Rissiek B, Menzel S, Leutert M, Cordes M, Behr S, Jank L, et al. Ecto-ADP-Ribosyltransferase ARTC2.1 Functionally Modulates Fcγr1 and Fcγr2b on Murine Microglia. *Sci Rep* (2017) 7:16477. doi: 10.1038/s41598-017-16613-w
27. Ohlrogge W, Haag F, Löhler J, Seman M, Littman DR, Killeen N, et al. Generation and Characterization of Ecto-ADP-Ribosyltransferase ART2.1/ART2.2-Deficient Mice. *Mol Cell Biol* (2002) 22:7535–42. doi: 10.1128/MCB.22.21.7535-7542.2002
28. Koch-Nolte F, Reyelt J, Schössow B, Schwarz N, Scheuplein F, Rothenburg S, et al. Single Domain Antibodies From Llama Effectively and Specifically Block T Cell Ecto-ADP-Ribosyltransferase ART2.2 *In Vivo*. *FASEB J* (2007) 21:3490–8. doi: 10.1096/fj.07-8661com
29. Koch-Nolte F, Duffy T, Nissen M, Kahl S, Killeen N, Ablamunits V, et al. A New Monoclonal Antibody Detects a Developmentally Regulated Mouse Ecto-ADP-Ribosyltransferase on T Cells: Subset Distribution, Inbred Strain Variation, and Modulation Upon T Cell Activation. *J Immunol* (1999) 163:6014–22.
30. Scheuplein F, Schwarz N, Adriouch S, Krebs C, Bannas P, Rissiek B, et al. NAD+ and ATP Released From Injured Cells Induce P2X7-Dependent Shedding of CD62L and Externalization of Phosphatidylserine by Murine T Cells. *J Immunol* (2009) 182:2898–908. doi: 10.4049/jimmunol.0801711
31. Wiśniewski JR, Zougman A, Nagaraj N, Mann M. Universal Sample Preparation Method for Proteome Analysis. *Nat Methods* (2009) 6:359–62. doi: 10.1038/nmeth.1322
32. Bilan V, Leutert M, Nanni P, Panse C, Hottiger MO. Combining HCD and EThcD Fragmentation in a Product Dependent-Manner Confidently Assigns Proteome-Wide ADP-Ribose Acceptor Sites. *Anal Chem* (2016) 89(3):1523–30. doi: 10.1021/acs.analchem.6b03365
33. Shannon P, Markiel A, Ozier O, Baliga NS, Wang JT, Ramage D, et al. Cytoscape: A Software Environment for Integrated Models of Biomolecular Interaction Networks. *Genome Res* (2003) 13:2498–504. doi: 10.1101/gr.1239303
34. Szklarczyk D, Gable AL, Lyon D, Junge A, Wyder S, Huerta-Cepas J, et al. STRING V11: Protein–Protein Association Networks With Increased Coverage, Supporting Functional Discovery in Genome-Wide Experimental Datasets. *Nucleic Acids Res* (2018) 47:D607–13. doi: 10.1093/nar/gky1131
35. Doncheva NT, Morris JH, Gorodkin J, Jensen LJ. Cytoscape StringApp: Network Analysis and Visualization of Proteomics Data. *J Proteome Res* (2018) 18:623–32. doi: 10.1021/acs.jproteome.8b00702
36. Gehrig PM, Nowak K, Panse C, Leutert M, Grossmann J, Schlapbach R, et al. Gas-Phase Fragmentation of ADP-Ribosylated Peptides: Arginine-Specific Side-Chain Losses and Their Implication in Database Searches. *J Am Soc Mass Spectrom* (2021) 32:157–68. doi: 10.1021/jasms.0c00040
37. Zimmermann H, Zebisch M, Sträter N. Cellular Function and Molecular Structure of Ecto-Nucleotidases. *Purinergic Signal* (2012) 8:437–502. doi: 10.1007/s11302-012-9309-4
38. Iwata H, Goettsch C, Sharma A, Ricchiuto P, Goh WWB, Halu A, et al. PARP9 and PARP14 Cross-Regulate Macrophage Activation Via STAT1 ADP-Ribosylation. *Nat Commun* (2016) 7:12849. doi: 10.1038/ncomms12849
39. Huang S, Apasov S, Koshiba M, Sitkovsky M. Role of A2a Extracellular Adenosine Receptor-Mediated Signaling in Adenosine-Mediated Inhibition of T-Cell Activation and Expansion. *Blood* (1997) 90:1600–10. doi: 10.1182/blood.V90.4.1600
40. Matthes M, Hollmann C, Bertuleit H, Kühl M, Thiele HG, Haag F, et al. "Natural" RT6-1 and RT6-2 “Knock-Out” Mice. *Adv Exp Med Biol* (1997) 419:271–4. doi: 10.1007/978-1-4419-8632-0_35
41. Koch-Nolte F, Klein J, Hollmann C, Kühl M, Haag F, Gaskins HR, et al. Defects in the Structure and Expression of the Genes for the T Cell Marker Rt6 in NZW and (NZB X NZW)F1 Mice. *Int Immunol* (1995) 7:883–90. doi: 10.1093/intimm/7.5.883
42. Er-Lukowiak M, Duan Y, Rassendren F, Ulmann L, Nicke A, Ufer F, et al. A P2rx7 Passenger Mutation Affects the Vitality and Function of T Cells in Congenic Mice. *iScience* (2020) 23:101870. doi: 10.1016/j.isci.2020.101870
43. Antonioli L, Pacher P, Vizi ES, Haskó G. CD39 and CD73 in Immunity and Inflammation. *Trends Mol Med* (2013) 19:355–67. doi: 10.1016/j.molmed.2013.03.005
44. Jamal Z, Afkham-Ebrahimi A, Saggerson ED. A Novel Assay for 5'-Nucleotidase Using 1,N6-Etheno-AMP as Substrate, and Comments on the Properties of the Reaction Product, Ethenoadenosine. *Biochem J* (1988) 250:369–73. doi: 10.1042/bj2500369
45. Jackson EK, Gillespie DG, Cheng D, Mi Z, Menshikova EV. Characterization of the N6-Etheno-Bridge Method to Assess Extracellular Metabolism of Adenine Nucleotides: Detection of a Possible Role for Purine Nucleoside Phosphorylase in Adenosine Metabolism. *Purinergic Signal* (2020) 16:187–211. doi: 10.1007/s11302-020-09699-x
46. Mottahedeh J, Haffner MC, Grogan TR, Hashimoto T, Crowell PD, Beltran H, et al. CD38 Is Methylated in Prostate Cancer and Regulates Extracellular NAD. *Cancer Metab* (2018) 6:13. doi: 10.1186/s40170-018-0186-3
47. Briceño P, Rivas-Yáñez E, Rosemblatt MV, Parra-Tello B, Farías P, Vargas L, et al. CD73 Ectonucleotidase Restrains CD8+ T Cell Metabolic Fitness and Anti-Tumoral Activity. *Front Cell Dev Biol* (2021) 9:638037. doi: 10.3389/fcell.2021.638037
48. Menzel S, Rissiek B, Bannas P, Jakoby T, Miksiewicz M, Schwarz N, et al. Nucleotide-Induced Membrane-Proximal Proteolysis Controls the Substrate Specificity of T Cell Ecto-ADP-Ribosyltransferase ARTC2.2. *J Immunol* (2015) 195(5):2057–66. doi: 10.4049/jimmunol.1401677
49. Schneider E, Rissiek A, Winzer R, Puig B, Rissiek B, Haag F, et al. Generation and Function of Non-Cell-Bound CD73 in Inflammation. *Front Immun* (2019) 10:1729. doi: 10.3389/fimmu.2019.01729
50. Menzel S, Koudelka T, Rissiek B, Haag F, Meyer-Schwesinger C, Tholey A, et al. ADP-Ribosylation Regulates the Signaling Function of IFN-γ. *Front Immun* (2021) 12:642545. doi: 10.3389/fimmu.2021.642545

Conflict of Interest: FK-N receives royalties from sales of antibodies developed in the lab *via* MediGate GmbH, a 100% subsidiary of the University Medical Center, Hamburg.

The remaining authors declare that the research was conducted in the absence of any commercial or financial relationships that could be construed as a potential conflict of interest.

frontiers
in Immunology

ORIGINAL RESEARCH
published: 24 August 2021
doi: 10.3389/fimmu.2021.713697

Edited by:
Björn Rissiek,
University Medical Center
Hamburg-Eppendorf, Germany

Reviewed by:
Tiziana Vaisitti,
University of Turin, Italy
Trine N. Jorgensen,
Case Western Reserve University,
United States

***Correspondence:**
Mercedes Zubiaur
mzubiaur@ipb.csic.es
Jaime Sancho
granada@ipb.csic.es

†These authors have contributed
equally to this work and
share first authorship

Specialty section:
This article was submitted to
Cytokines and Soluble
Mediators in Immunity,
a section of the journal
Frontiers in Immunology

Received: 23 May 2021
Accepted: 30 July 2021
Published: 24 August 2021

Citation:
Martínez-Blanco Á,
Domínguez-Pantoja M,
Botía-Sánchez M, Pérez-Cabrera S,
Bello-Iglesias N, Carrillo-Rodríguez P,
Martin-Morales N, Lario-Simón A,
Pérez-Sánchez-Cañete MM,
Montosa-Hidalgo L,
Guerrero-Fernández S,
Longobardo-Polanco VM,
Redondo-Sánchez S,
Cornet-Gomez A, Torres-Sáez M,
Fernández-Ibáñez A,
Terrón-Camero L, Andrés-León E,
O'Valle F, Merino R, Zubiaur M and
Sancho J (2021) CD38 Deficiency
Ameliorates Chronic Graft-Versus-
Host Disease Murine Lupus via a B-
Cell-Dependent Mechanism.
Front. Immunol. 12:713697.
doi: 10.3389/fimmu.2021.713697

CD38 Deficiency Ameliorates Chronic Graft-*Versus*-Host Disease Murine Lupus *via* a B-Cell-Dependent Mechanism

África Martínez-Blanco[1†], Marilú Domínguez-Pantoja[1†], María Botía-Sánchez[1†], Sonia Pérez-Cabrera[1], Nerea Bello-Iglesias[1], Paula Carrillo-Rodríguez[1], Natividad Martin-Morales[2], Antonio Lario-Simón[3], María M. Pérez-Sánchez-Cañete[4], Laura Montosa-Hidalgo[5], Salvador Guerrero-Fernández[4], Victoria M. Longobardo-Polanco[3], Sandra Redondo-Sánchez[4], Alberto Cornet-Gomez[1], María Torres-Sáez[1], Ana Fernández-Ibáñez[6], Laura Terrón-Camero[7], Eduardo Andrés-León[7], Francisco O'Valle[2], Ramón Merino[8], Mercedes Zubiaur[1] and Jaime Sancho[1*]*

[1] Department of Cellular Biology and Immunology, Institute of Parasitology and Biomedicine López-Neyra (IPBLN), Consejo Superior de Investigaciones Científicas (CSIC), Granada, Spain, [2] Department of Pathology, Faculty of Medicine, University of Granada (UGR), Granada, Spain, [3] Proteomics Unit, IPBLN, CSIC, Granada, Spain, [4] Flow Cytometry Unit, IPBLN, CSIC, Granada, Spain, [5] Microscopy Unit, IPBLN, CSIC, Granada, Spain, [6] Scientific Instrumentation Center (CIC), UGR, Granada, Spain, [7] Bioinformatics Unit, IPBLN, CSIC, Granada, Spain, [8] Department of Molecular and Cellular Signalling, Instituto de Biomedicina y de Biotecnología de Cantabria (IBBTEC), Consejo Superior de Investigaciones Científicas-Universidad de Cantabria (CSIC-UC), Santander, Spain

The absence of the mouse cell surface receptor CD38 in *Cd38*$^{-/-}$ mice suggests that this receptor acts as a positive regulator of inflammatory and autoimmune responses. Here, we report that, in the context of the chronic graft-*versus*-host disease (cGVHD) lupus inducible model, the transfer of B6.C-H2bm12/KhEg(bm12) spleen cells into co-isogenic *Cd38*$^{-/-}$ B6 mice causes milder lupus-like autoimmunity with lower levels of anti-ssDNA autoantibodies than the transfer of bm12 spleen cells into WT B6 mice. In addition, significantly lower percentages of Tfh cells, as well as GC B cells, plasma cells, and T-bet^{+}CD11c^{hi} B cells, were observed in *Cd38*$^{-/-}$ mice than in WT mice, while the expansion of Treg cells and Tfr cells was normal, suggesting that the ability of *Cd38*$^{-/-}$ B cells to respond to allogeneic help from bm12 CD4^{+} T cells is greatly diminished. The frequencies of T-bet^{+}CD11c^{hi} B cells, which are considered the precursors of the autoantibody-secreting cells, correlate with anti-ssDNA autoantibody serum levels, IL-27, and sCD40L. Proteomics profiling of the spleens from WT cGVHD mice reflects a STAT1-driven type I IFN signature, which is absent in *Cd38*$^{-/-}$ cGVHD mice. Kidney, spleen, and liver inflammation was mild and resolved faster in *Cd38*$^{-/-}$ cGVHD mice than in WT cGVHD mice. We conclude that CD38 in B cells functions as a modulator receptor that controls autoimmune responses.

Keywords: CD38, cGVHD lupus-like, T-bet^{+} B cells, anti-ssDNA antibodies, GC B cells, STAT1, type I IFN-signature, inflammation

INTRODUCTION

Systemic lupus erythematosus or SLE is an incurable systemic autoimmune disease, which occurs predominantly in women of childbearing age, characterized by the production of autoantibodies that are deposited as immunocomplexes in various organs (1). The SLE courses with periods of activity and remission, resulting in accumulated damage over time (2). It is a very heterogeneous disease from a clinical point of view and difficult to follow (3). Hence, there is a need of experimental lupus models to investigate the molecular mechanisms of the disease and to discover new biomarkers that better reflect the pathogenesis and activity of the disease and which may be of diagnostic or therapeutic interest (4).

CD38 has an enormous potential to be used as a target to inhibit the chronic inflammatory reactions linked to aging and autoimmunity and to eliminate autoreactive plasma cells that produce potentially harmful autoantibodies (5–7). Increased CD38 expression greatly affects cellular metabolism by lowering intracellular NAD^+ levels and decreasing NAD-dependent deacetylation performed by sirtuins (8). Thus, high levels of CD38 lead to decreased CD8 T-cell-mediated cytotoxicity and increased propensity to infections in patients with SLE (9). The relevance to lupus is that abnormal NAD-dependent deacetylation could be reverted pharmacologically or with anti-CD38 therapy (10–12). In lupus models, this could also be approached by analyzing the functional effect of CD38 deficiency (13–16). Using the pristane lupus model, we have demonstrated the crucial role of CD38 in promoting aberrant inflammation and lupus-like autoimmunity *via* an apoptosis-driven mechanism, which requires TRPM2 expression (13).

A chronic graft-*versus*-host reaction (cGVHD) induced in non-autoimmune C57BL6 mice (B6) by the adoptive transfer of Ia-incompatible bm12 spleen cells results in a syndrome that closely resembles SLE in the spectrum of autoantibodies and immunopathology (17). In the cGVHD lupus model, the key cellular mechanism that results in the loss of B-cell tolerance is the interaction of donor bm12 $CD4^+$ T cells with MHC class II on host B6 B-cell surface, inducing high levels of circulating anti-nuclear antibodies, concomitantly with large frequencies of T follicular helper (Tfh) cells, germinal center (GC) B cells, and plasma cells (18, 19). During T- and B-cell interactions, allogeneic donor $CD4^+$ T cells provide the abnormal T cell help to the host B cells, which act as efficient APCs, and the host B cells further augment the clonal expansion, differentiation, and survival of pathogenic T cells. Therefore, this is a suitable model to study the role of CD38 in autoreactive B cells using CD38-deficient mice *versus* B6 WT mice as recipients.

MATERIAL AND METHODS

Mice

C57BL/6J (B6) (RRID: IMSR_JAX:000664) WT female mice were from Charles River. B6(C)-H2-Ab1bm12/KhEgJ (bm12) (RRID: IMSR_JAX:001162) female mice were from the Jackson Laboratory. B6.129P2-Cd38tm1Lnd/J (*Cd38*$^{-/-}$) (RRID: IMSR_JAX:003727) female mice were backcrossed for 12 generations to the C57BL/6J (B6) background and were bred and maintained under specific pathogen-free conditions at the IPBLN-CSIC Animal Facility in Granada, Spain. The experimental procedures in animals at IPBLN-CSIC, Spain, were approved by the Institutional Animal Care and Use Committee. The procedures follow the ARRIVE guidelines (20) in accordance with the U.K. Animals (Scientific Procedures Act, 1986) and associated guidelines (EU Directive 2010/63/EU for animal experiments) and with the National Institutes of Health Guide for the Care and Use of Laboratory Animals (NIH Publications No. 8023, revised 1978).

The bm12-Inducible Model of Systemic Lupus Erythematosus in C57BL/6 Mice

We adapted the bm12 transfer model, as originally described by Morris et al. (21) and modified by Klarquist and Janssen (18). Eight- to 18-week-old B6 WT or *Cd38*$^{-/-}$ female mice were injected i.p. with 50–70 × 10^6 spleen cells from bm12 female mice. Alternatively, bm12 female mice were injected i.p. with 50–70 × 10^6 spleen cells from WT or *Cd38*$^{-/-}$ female mice.

Flow Cytometry

To block non-specific Fc binding, single-cell suspensions of spleens were incubated with anti-mouse CD16/32 (BD Biosciences Cat# 553142, RRID: AB_394657), 1:200 dilution for 30–60 min, on ice in staining media (1× PBS, w/o calcium or magnesium, 0.5% BSA, 2 mM EDTA). Cells were then separated in different panels and stained with the following anti-mouse antibodies: CD4-PercP (1:250 dilution) (BD Biosciences Cat# 561090, RRID: AB_10562560), TCR-β-FITC (1:500 dilution) (BD Biosciences Cat# 553170, RRID: AB_394682), CXCR5-biotin (1:350 dilution) (BD Biosciences Cat# 551960, RRID: AB_394301), PD1-APC (1:350) (BD Biosciences Cat# 562671, RRID: AB_2737712), CD19-PE-CF594 (1:350 dilution) (BD Biosciences Cat# 562329, RRID: AB_11154580), CD138-PE (1:350 dilution) (BD Biosciences Cat# 561070, RRID: AB_2033998), B220-PE (1:350 dilution) (BD Biosciences Cat# 553089, RRID: AB_394619), CD95-Alexa Fluor 647 (1:350 dilution) (BD Biosciences Cat# 563647, RRID: AB_2738346), GL7-FITC (1:350 dilution) (BD Biosciences Cat# 562080, RRID: AB_10894953), CD38-FITC (1:350 dilution) (BD Biosciences Cat# 558813, RRID: AB_397126), CD19-APC (1:350 dilution) (BD Biosciences Cat# 550992, RRID: AB_398483), CD183-VioBright FITC (1:50 dilution) (Miltenyi Biotec Cat# 130-111-092, RRID: AB_2655744), CD11c-PE (1:50 dilution) (Miltenyi Biotec Cat# 130-110-701, RRID: AB_2654708), and Streptavidin-PE (1:350) (BioLegend Cat# 405203). Flow cytometry analyses at IPBLN-CSIC were performed as previously described (13, 14). Ten thousand to 200,000 events per sample were acquired either in a FACS Calibur flow cytometer (BD Biosciences, RRID: SCR_000401) or FACS Symphony (BD Biosciences) and analyzed with FlowJo software v10.7.1 (BD Biosciences) (FlowJo, RRID: SCR_008520). Absolute cell numbers were calculated by multiplying the percentages of each cell type, referred to as live and singlet cells, with the total number of live spleen cells/mouse counted immediately after isolation by the Trypan blue method. Gating strategies for the different cell subsets are shown in **Figures S1–S4**.

Intracellular T-bet or FoxP3 Staining

After cell surface staining, cells were washed, fixed, and permeabilized using the FoxP3 Staining Buffer Set (Miltenyi Biotec Cat# 130-093-142) and stained with anti-mouse antibodies either T-bet-APC (1:50 dilution) (Miltenyi Biotec Cat# 130-119-783, RRID: AB_2784464) or FoxP3-Alexa Fluor 488 (BD Biosciences Cat# 560407, RRID: AB_1645193) (1:250 dilution). Cells were then washed twice in Perm/Wash buffer (Miltenyi Biotec Cat# 130-093-142), resuspended in staining media, and analyzed by flow cytometry.

Cytokine Multiplex

The Bio-Plex Pro Mouse Cytokine Th17 kit assay custom 7-Plex (BioRad Cat#LJ00000163, Standard Lot#: 64298607) and 10-Plex kit assay (BioRad Cat#12010828, Standard Lot#64298607) were used to simultaneously test cytokines IL-17F, IL-21, IL-22, IL-23, IL-31, IL-33, and MIP-3α (7-Plex) and IL-17F, IL-21, IL-22, IL-23, IL-25, IL-27, IL-31, IL-33, sCD40L, and MIP-3α (10-Plex). The assay Bio-Plex Pro$^{\text{TM}}$ Mouse Cytokine Th17 Panel A 6-Plex Cat#M6000007NY was used to simultaneously quantify cytokines IFN-γ, IL-1β, IL-6, IL-10, IL-17A, and TNF-α. Assays were performed according to the protocols of the manufacturers. Analyses of experimental data were carried out using five-parameter logistic curve fitting in a Luminex 200 (Luminex 100 or 200 Flow Cytometry Analyzer System, RRID: SCR_018025) and in a Bio-Plex (BioRad, RRID: SCR_018026).

Histopathological Study

For conventional morphology, buffered 10% formaldehyde-fixed, paraffin-embedded longitudinal mice kidney, liver, and spleen sections in sagittal plane were deparaffinized in xylol and rehydrated in ethanol of decreasing gradation. Tissue sections were stained with hematoxylin–eosin (H&E), Masson's trichrome (MT), and periodic acid-Schiff (PAS). The presence of glomerular lesions (glomerulosclerosis, mesangium increase, crescent, immunocomplexes, and cells per glomerulus) was assessed in at least 100 glomeruli. Tubulo-interstitial damage (brush border loss, tubular dilation, tubular atrophy, hyaline casts, tubular necrosis, tubular mitoses, fibrosis, and inflammatory infiltrate) was also studied. Injury was graded according to Shih et al. (22). A semiquantitative scale of 0 to 3.0 was considered: 0, normal; 0.5, small focal areas of damage; 1, involvement of less than 10% of the cortex; 2, involvement of 10% to 25% of the cortex; and 3, involvement above 25% of the cortex. A morphological study was done in a blinded fashion (FO'V and NMM) on 3-μm sections with light microscopy, using the most appropriate stain for each lesion. The presence of steatosis, hydropic degeneration, inflammatory infiltrate, cholestasis, mitosis, apoptosis, and cell binucleation was assessed in liver sections using a semiquantitative scale of 0 to 4. A millimeter scale in the eyepiece of a microscope (BH2 Olympus (LabX, RRID: SCR_020338) with 40% objective was used to count the leucocyte subset per mm^2 in the spleen.

Serological Studies

Serum levels of IgG anti-ssDNA autoantibodies were measured by ELISA, and the results were expressed in titration units (U/ml) as previously described (23, 24). Total IgG serum levels were measured by ELISA as previously described (23, 24).

Cellular Lysates

Isolated spleen cell count and viability was done on a hemocytometer with 1:1 Trypan blue solution (Sigma-Aldrich Cat# T8154). The spleen cells were washed thoroughly three times with cold 1× PBS, pH 7.6, and 2 mM EDTA and filter sterilized in 0.22 μm filter. The spleen cells were lysed 30 min on ice, as previously described (24–26): 100 μl 1× lysis buffer/10 million cells; the 1× lysis buffer composition is as follows: 150 mM NaCl, 20 mM HEPES (pH: 7.6), 50 mM sodium fluoride, 1 mM EGTA, 0.5% NP-40, and small peptide inhibitors (SPI) (stock, 50×) (25); 1 mM sodium orthovanadate, 10 mM iodoacetamide, and 1 mM PMSF, as phosphatases inhibitors; plus 0.25 μM trichostatin and 5 mM nicotinamide as acetylase inhibitors. Micro BCA Protein Assay (ThermoFisher Cat# 23235) was used for the analysis of the protein concentration of 17,000×*g*-clarified spleen cell lysates.

Mass Spectrometry Proteomics and Data Processing

Thirty to 40 μg of protein from spleen cell lysates in 1× Laemmli sample buffer was loaded on 4%–20% prestained gels (BioRad Cat# 4568095). Electrophoresis was done at 200 V, in 25 mM TrizMa OH, 192 mM glycine, and pH 8.3, 0.1% SDS buffer, until the whole sample volume was introduced into the gel matrix. The proteins in the gel were visualized by the exposure of the gel during 1 to 5 min to UV light in a GelDoc EZ Image (BioRad). In addition, gel was stained with SYPRO Ruby (BioRad Cat# 1703126) according to the protocol of the manufacturers. An EXQuest Spot Cutter (BioRad) with the PDQuest Advanced program was used to cut the protein bands of the gel.

Protein extracts were analyzed by liquid chromatography-tandem mass spectrometry (LC-MS/MS) (Amazon Speed, Bruker) at IPBLN-CSIC Proteomic Facility as described previously (26). Protein identification was done with ProteinScape 4.0 (Bruker) and MASCOT 2.4 data searching using the SwissProt database. For label-free proteomic quantification, we used the exponentially modified protein abundance index (emPAI) implemented into the MASCOT data searching platform without any additional experimental steps. In order to compare between different samples, it is required to normalize emPAI values from MASCOT search to the sum of all emPAI values. Thus, the protein content in molar fraction percentage (M%) can be calculated using the following formula: Protein content (M%) = emPAI/Σ(emPAI), where Σ(emPAI) is the summation of emPAI values for all the identified proteins (27). Two biological samples per mouse type and three technical replicates per biological sample were analyzed [The mass spectrometry proteomics data have been deposited to the ProteomeXchange Consortium *via* the PRIDE (28) partner repository with the dataset identifier PXD026947 and 10.6019/PXD026947]. We used ClueGO_v2.5.8 (29) and CluePedia_v1.5.8 (30) within the Cytoscape_v3.8.2 software environment (31) for functional enrichment analysis of the lists of identified proteins. Results are visualized as networks in which Gene Ontology (GO) terms and pathways are grouped based on their biological role. CluePedia allows to expand ClueGO terms into nested networks with associated genes.

Bioinformatics Analysis

To reduce the dimensionality of the data and to represent the samples based on the amount of variance they contain, a principal component analysis (PCA) was performed to integrate the data from all experiments. A total of 58 mice were used for this purpose: those with complete experimental data for the 11 monitored variables (see **Table S1** in the **Supplementary Material** the total number of experiments and mice used per experiment): for the first group of samples, "NT," $n = 8$ mice—4 WT and 4 KOs; for the second week, $n = 18$ mice—11 WT and 7 KOs; for the fourth week, $n = 17$—7 WT and 10 KOs. Finally, for the eighth week, $n = 15$ mice, of which 7 were WT and 8 were KO. First, for each time point, we used the turkey_mc_up function from the bigutils package to infer possible outliers (32). It should be noted that it is difficult to distinguish between a mouse with a value that classifies it as an outlier and a mouse with a high response. Therefore, to classify a mouse as an outlier in the total set of variables, it should be an outlier in several variables. As an example, we found that WT13-4 appears as a marginal outlier in the CD4$^+$ T, Tfh, and PC variables. Therefore, we decided to keep it. Besides, the vast majority of mice were not marked as outliers for any variable. Then, values were scaled, and subsequently, plots were generated using the factoextra, ggfortify, and cluster R packages (33–35).

Statistics

Statistical analyses were performed using the GraphPad Prism 9 software (GraphPad Prism, RRID: SCR_002798), using statistical tests as indicated in the text. Statistical significance was visualized as follows: ns = not significant ($P > 0.05$), * = $P < 0.05$, ** = $P < 0.01$, *** = $P < 0.001$, **** = $P < 0.0001$. All experiments have been done using three or more mice and representative images have been chosen for the figures.

RESULTS

Long-Term Decreased Frequencies and Numbers of Tfh Cells in *Cd38*$^{-/-}$ Mice After Adoptive Transfer of bm12 Spleen Cells

Selection, isotype switching, and expansion of GC B cells require critical signals from Tfh cells. The adoptive transfer of bm12 lymphocytes into WT B6 mice (WT cGVHD) leads to the expansion of donor-derived Tfh, expansion of recipient-derived GC B cells and plasma cells, and production of ANAs including anti-dsDNA, anti-ssDNA, anti-chromatin, and anti-RBC antibodies (17). We assessed whether the lack of CD38 expression on B cells impairs the expansion of Tfh cells. To this end, 2, 4, and 8 weeks after transferring bm12 CD38-suficient spleen cells into *Cd38*$^{-/-}$ mice (*Cd38*$^{-/-}$ cGVHD), the frequencies and total numbers of Tfh cells (FoxP3$^-$PD-1^{hi}CXCR5$^+$ within CD4$^+$ cells) were assessed in spleen and compared with basal levels (**Figures 1A, B**). The whole gating strategy is shown in **Figure S1**. The data showed that the frequencies and absolute numbers of Tfh cells were significantly lower in CD38-deficient mice as compared with B6 WT cGVHD mice throughout the experiment (**Figures 1C, D**). Decreased frequencies and numbers of CD4$^+$TCR-β$^+$ T cells in *Cd38*$^{-/-}$ cGVHD mice were only shown 4 weeks after the adoptive transfer experiment (**Figures 1E, F**). However, both WT and *Cd38*$^{-/-}$ recipients developed similar levels of splenomegaly as judged by a similar increase in the total number of splenocytes (**Figure 1G**). In contrast, the increase in spleen size was more modest in *Cd38*$^{-/-}$ than in WT mice, particularly at 8 weeks of the adoptive transfer of bm12 cells, where these differences reached statistical significance (**Figure 1H**). Since in this cGVHD model it is well stablished that the initial expansion of Tfh cells comes from the donor T cells, and to a very low extent from host T cells (18, 36), our results suggested that the distinct allo-response elicited by donor bm12 T cells in *Cd38*$^{-/-}$ recipient mice was dependent on the host cellular environment.

Decreased Frequencies of GC B Cells and Plasma Cells Upon Induction of cGVHD in *Cd38*$^{-/-}$ Recipients

Tfh and GC B cells are reciprocally supportive of each other: the frequency of Tfh is associated with the magnitude of the B-cell response, and GC B cells have been shown to promote Tfh expansion (36–38). In **Figures 2A, B**, the gating strategies used to detect plasma cells and GC B cells are shown, respectively. The whole gating strategy is shown in **Figure S2**. In agreement with the data on Tfh cells, the expansion of GC B cells (CD19$^+$Fas$^+$GL7$^+$) in *Cd38*$^{-/-}$ recipient mice was significantly lower than that observed in WT recipient mice (**Figures 2C, D**). Moreover, the percentages and numbers of plasma cells, as assessed by the high expression of CD138 in CD19$^{int/low}$ cells, were significantly reduced in *Cd38*$^{-/-}$ *versus* WT cGVHD mice 4 and 8 weeks after the adoptive transfer of bm12 spleen cells and not after 2 weeks (**Figures 2E, F**). Therefore, the observed reduction in B-cell responses in the *Cd38*$^{-/-}$ cGVHD mice could result from changes in reciprocal Tfh and B-cell interactions, rather than a sole effect of the CD38 deficiency on B cells. However, both WT and *Cd38*$^{-/-}$ mice were adoptively transferred with bm12 CD38-suficient spleen cells that contain the same initial numbers of allo-reactive donor bm12 CD4$^+$ T cells, which were fully functional. Moreover, WT and *Cd38*$^{-/-}$ recipient mice share the same class II I-A^b allele, and the frequencies and absolute numbers of CD19$^+$ B cells did not change significantly from 2 to 8 weeks after the adoptive transfer (**Figures 2G, H**). In summary, the lower frequency of GC B cells in *Cd38*$^{-/-}$ recipients compared with WT might be a direct consequence of a defective allogeneic cell response of the *Cd38*$^{-/-}$ B-cell counterpart, not from defective signals provided by the donor bm12 CD4$^+$ T cells.

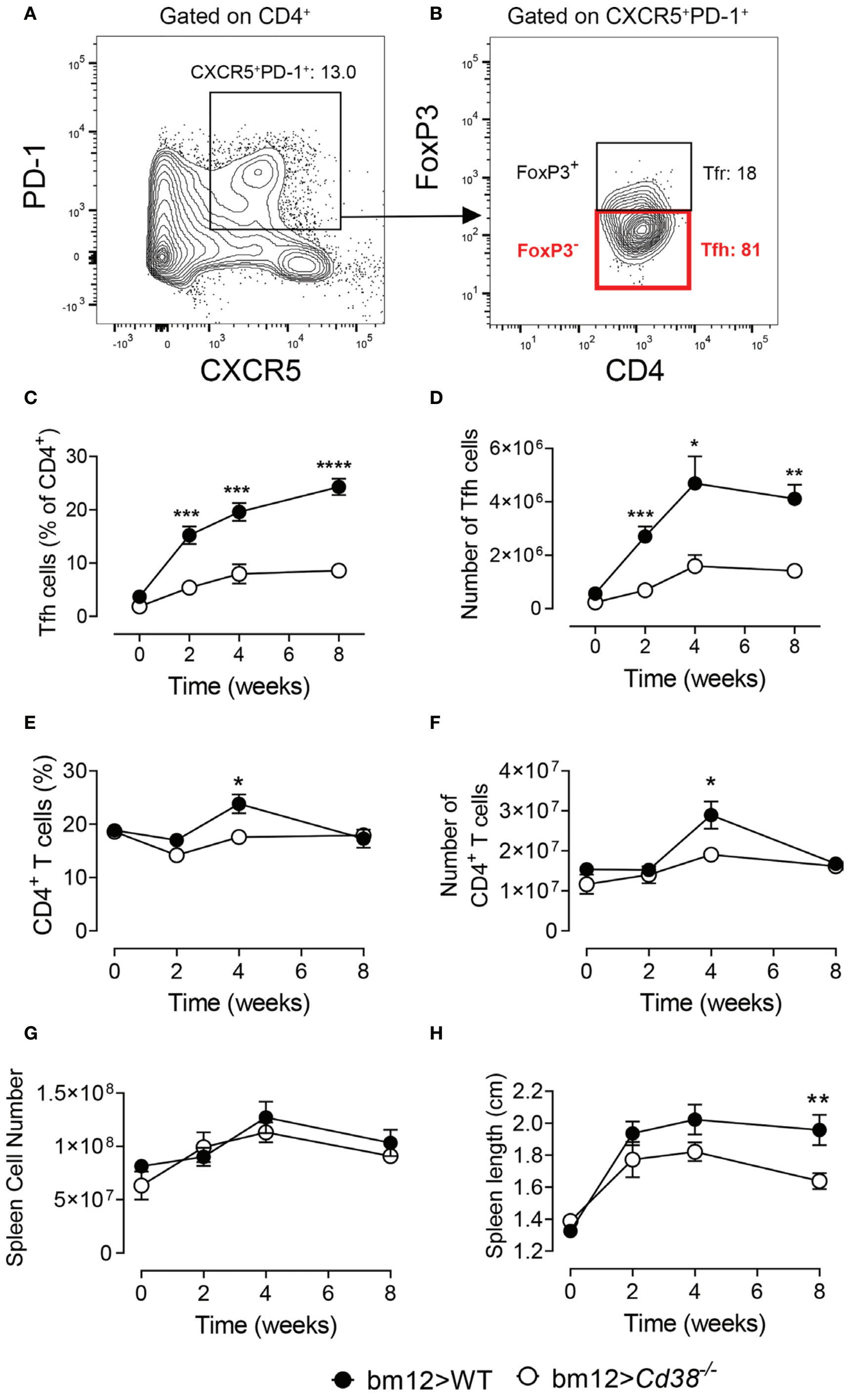

FIGURE 1 | Long-term decreased frequencies and numbers of T follicular helper (Tfh) cells in *Cd38*$^{-/-}$ mice after adoptive transfer of bm12 spleen cells. WT mice (closed circles) or *Cd38*$^{-/-}$ mice (open circles) were i.p. injected with bm12 cells and euthanized at the indicated time points and spleens were analyzed. **(A, B)** Representative flow cytometry contour plots showing gating strategy for Tfh cells. **(A)** First, gating on CD4$^+$ cells, then gating on CXCR5$^+$PD-1$^+$. **(B)** Then, gating on FoxP3$^-$ cells: CD4$^+$PD-1^{hi}CXCR5$^+$FoxP3$^-$. **(C)** Percentages of Tfh cells (of CD4$^+$ T cells) in spleen at the indicated time points. **(D)** Total number of Tfh cells (in spleen) over time. **(E)** Percentages of CD4$^+$ T cells (CD4$^+$TCR-β$^+$) in spleens. **(F)** Total number of CD4$^+$ T cells in spleen. **(G)** Total number of spleen cells over time. **(H)** Spleen length (cm) over time upon the adoptive transfer. In all panels, the symbols are the mean values and the vertical bars represent ± SEM. *P*-values are shown for Welch's *t*-test. The results are cumulative data from two to four different experiments per time point and mouse type, each with three to five mice per experiment. $^*P < 0.05$, $^{**}P < 0.01$, $^{***}P < 0.001$, $^{****}P < 0.0001$.

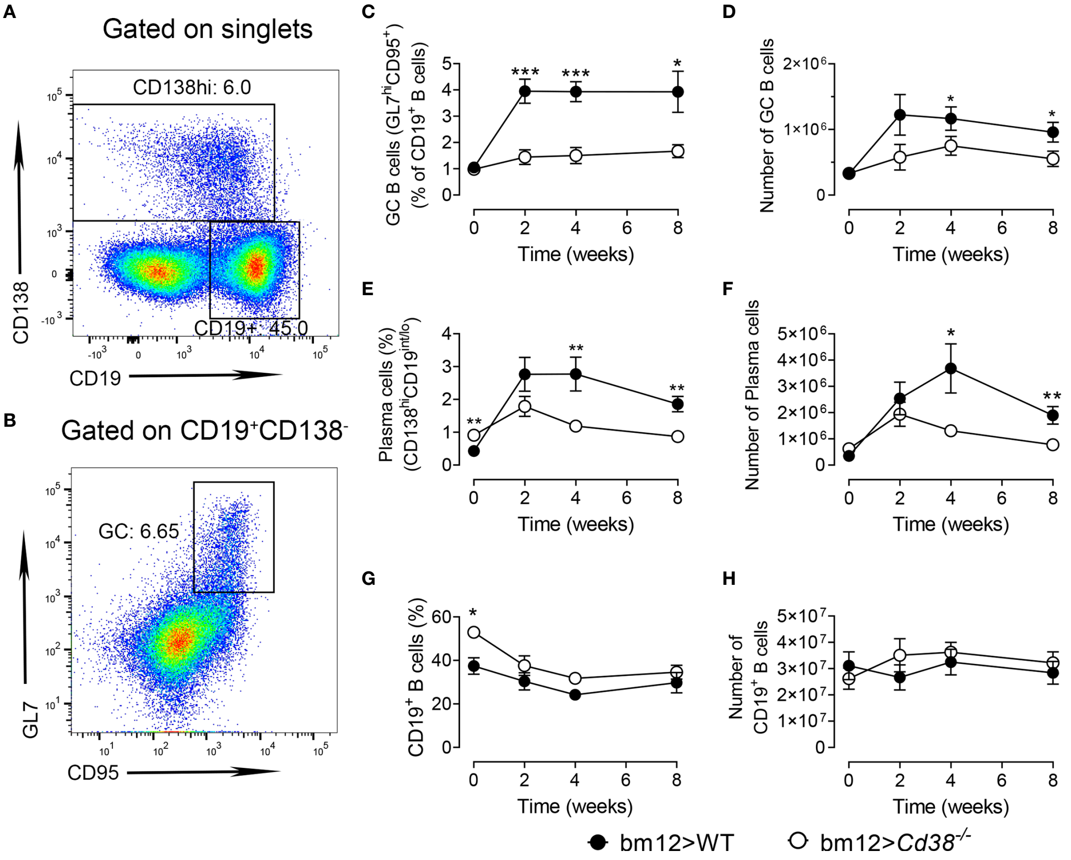

FIGURE 2 | Decreased frequencies of GC B cells and plasma cells upon induction of chronic graft-*versus*-host disease (cGVHD) in *Cd38*$^{-/-}$ recipients. WT (closed circles) and *Cd38*$^{-/-}$ (open circles). **(A)** Representative flow cytometry plot showing CD19^{lo-int}CD138^{hi} plasma cells and CD19$^+$CD138$^-$ B cells from the spleen cells gated on singlets. **(B)** Flow cytometry plot of CD95$^+$GL7^{hi} GC B cells from gated CD19$^+$CD138$^-$ cells. **(C)** Percentages of GC B cells (of CD19$^+$ B cells). **(D)** Total number GC B cells. **(E)** Percentages of plasma cells in spleen cells. **(F)** Total number of plasma cells in spleen cells. **(G)** Percentages of CD19$^+$ B cells in the spleen. **(H)** Total number of CD19$^+$ B cells over time upon the adoptive transfer of bm12 cells. In panels **(C–H)** WT mice (closed circles) and *Cd38*$^{-/-}$ mice (open circles). The symbols are the mean values and the vertical bars represent ± SEM. *P*-values are shown for Welch's *t*-test. The results are cumulative data from two to four different experiments per time point and mouse type, each with three to five mice per experiment. *$P < 0.05$, **$P < 0.01$, ***$P < 0.001$.

Decreased Frequencies and Numbers of CD11c^{hi}T-bet$^+$ B Cells in *Cd38*$^{-/-}$ cGVHD Mice

B-cell-intrinsic expression of T-bet is required for the development of autoantibody-mediated disease in lupus mouse models, including in the cGVHD model (39, 40). Therefore, it was of interest to assess whether the frequencies of CD11c^{hi}T-bet$^+$ B cells in *Cd38*$^{-/-}$ cGVHD mice were reduced as compared with WT cGVHD mice. **Figures 3A** and **S3** illustrate the gating strategy used to identify the CD11c^{hi}T-bet$^+$ cells within the CD19$^+$ B-cell subset. These cells were also positive for CD183 (CXCR3) on the cell surface, whose expression depends on the transcriptional activity of T-bet (**Figure S3**). There was a significant decrease in the frequencies and numbers of CD11c^{hi}T-bet$^+$ B cells in *Cd38*$^{-/-}$ cGVHD (**Figures 3B, C**). This decrease in CD11c^{hi}T-bet$^+$ B cells appeared to be long-lasting as the differences with WT cGVHD mice were observed up to 8 weeks after the induction of the disease. Moreover, the weak expansion of these cells in *Cd38*$^{-/-}$ cGVHD mice was even more dramatic than in GC B cells.

Decreased Anti-ssDNA Autoantibody Serum Levels in *Cd38*$^{-/-}$ cGVHD Mice

In *Cd38*$^{-/-}$ cGVHD mice, the anti-ssDNA levels were significantly lower than those in WT recipient mice along the study (**Figure 3D**). Total IgG, which reflects polyclonal B-cell activation, followed different kinetics in *Cd38*$^{-/-}$ cGVHD mice, with a peak 2 weeks after the adoptive transfer, diminishing steadily afterwards (**Figure 3E**). In contrast, in WT cGVHD mice, the IgG peak was at 4 weeks. It is worthy to note the significant correlation between anti-ssDNA serum levels and the frequencies of CD11c^{hi}T-bet$^+$ B cells (**Figure 3F**).

Normal Expansion of Tfr Cells and Treg Cells in *Cd38*$^{-/-}$ cGVHD Mice

Regulatory T cells (Treg) have been demonstrated to play vital roles in suppressing cellular and humoral immune responses, i.e., by

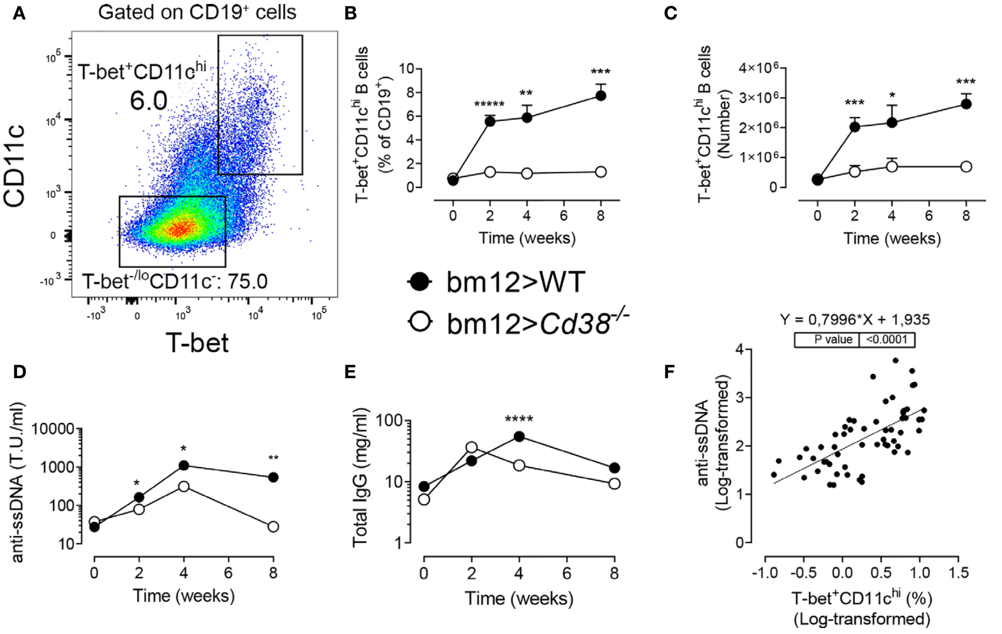

FIGURE 3 | **(A–C)** Decreased frequencies and numbers of T-bet$^+$CD11c^{hi} B cells in *Cd38$^{-/-}$* cGVHD mice. **(D–F)** Decreased anti-ssDNA autoantibody serum levels in *Cd38$^{-/-}$* cGVHD mice. Correlation with the frequencies of T-bet$^+$CD11c^{hi} B cells. **(A)** Representative flow cytometry plot showing T-bet$^+$CD11c^{hi} cells and T-bet$^{-/lo}$CD11c$^-$ on gated CD19$^+$ B cells from spleen. **(B)** Percentages of CD11c^{hi}T-bet$^+$ cells (of CD19$^+$ B cells). Mean ± SEM. *P*-values are shown for Welch's *t*-test. **(C)** Total number of CD11c^{hi}T-bet$^+$ cells. Mean ± SEM. *P*-values are shown for Welch's *t*-test. **(D)** Anti-ssDNA serum levels. Median values. *P*-values are shown for Mann–Whitney test. **(E)** Total IgG serum levels. Median values. *P*-values are shown for Mann–Whitney test. **(F)** Positive correlation between anti-ssDNA serum levels from cGVHD mice and the frequencies of CD11c^{hi}T-bet$^+$ B cells (simple linear regression). The anti-ssDNA levels and frequencies are shown in log scale. The results are cumulative data from two to four different experiments per time point and mouse type, each with three to five mice per experiment. *$P < 0.05$, **$P < 0.01$, ***$P < 0.001$, ****$P < 0.0001$, *****$P < 0.00001$.

suppressing autoreactive B-cell functions and subsequent autoantibody production (41, 42). Tfr cells are a specialized subset of effector Treg cells that gain access to the GC and suppresses B-cell responses. Like Tfh cells, Tfr cells express high levels of CXCR5 (which directs them to the GC), PD-1, and ICOS (43–45). However, Tfr cells originate from natural Treg precursors unlike Tfh cells, which originate from naive CD4$^+$ T cells. Tfr cells also differ from Tfh cells by expressing FoxP3 and Blimp-1. Importantly, Tfr cells specifically and potently suppress both Tfh and B cells in the GC reaction (45). The low frequencies and numbers of Tfh cells (**Figures 1C, D**) and GC B cells (**Figures 2C, D**) found in cGVHD *Cd38$^{-/-}$* mice suggested that Tfr cells may have increased presence in the GC of these mice. On the other hand, it is important to note that in CD38-deficient mice, Treg and iNKT cells are highly sensitive to NAD-induced cell death activated by ADP ribosyltransferase-2 (ART2)-mediated ADP ribosylation of P2X7 receptors (46, 47). The relatively low numbers of these immunoregulatory CD4$^+$ T-cell populations greatly affect the outcome of a number of autoimmune or inflammatory diseases in CD38-deficient mice (48–50). Therefore, it was of interest to test whether the Treg cells may have a role in the weak allogeneic response triggered by the i.p. injection of bm12 cells into CD38-deficient mice, at the peak of the GC formation (41, 47). Tfr cells were defined as FoxP3$^+$ within the CD4$^+$CXCR5$^+$ subset (**Figure 4A**), which also contains the Tfh cells (CD4$^+$CXCR5$^+$FoxP3$^-$), whereas Treg cells were the FoxP3$^+$ cells within the CD4$^+$CXCR5$^-$ subset (**Figure 4C**). The whole gating strategy is shown in **Figure S4**. According to Sage et al. (45), this strategy better reflects the total number of Tfr cells, independently of the expression of PD-1, and allows a better perception of the development of Tfr cells *versus* the expansion of precursor Treg cells (43, 45). Notably, the percentages of Tfr cells in *Cd38$^{-/-}$* mice were significantly higher than in WT mice under steady-state conditions (**Figure 4B**), while the opposite occurs for Tregs (**Figure 4D**). Two weeks after the adoptive transfer, both mice showed similar frequencies of Tfr cells and Treg cells, despite some changes occurred relative to basal levels (**Figures 4B, D**). Overall, these results indicate that in *Cd38$^{-/-}$* cGVHD mice, the Treg-dependent Tfr expansion was quite similar to that in WT cGVHD.

Distinct Kinetic Profiles of PD-1$^+$ and PD-1$^-$ Tfr Cells in cGVHD *Cd38$^{-/-}$ Versus* cGVHD WT Mice

Increased PD-1 expression on Tfr cells makes them less suitable to perform their suppressive function (45); therefore, it was of interest to assess whether there were differences in PD-1 expression in Tfr cells from cGVHD *Cd38$^{-/-}$* mice *versus* WT mice. In **Figures 5A** and **S1**, the gating strategy used to detect PD1$^+$ and PD-1$^-$ Tfr cells is shown. In non-treated *Cd38$^{-/-}$* mice, 90% of the Tfr cells were PD-1$^-$, with a significant decrease to

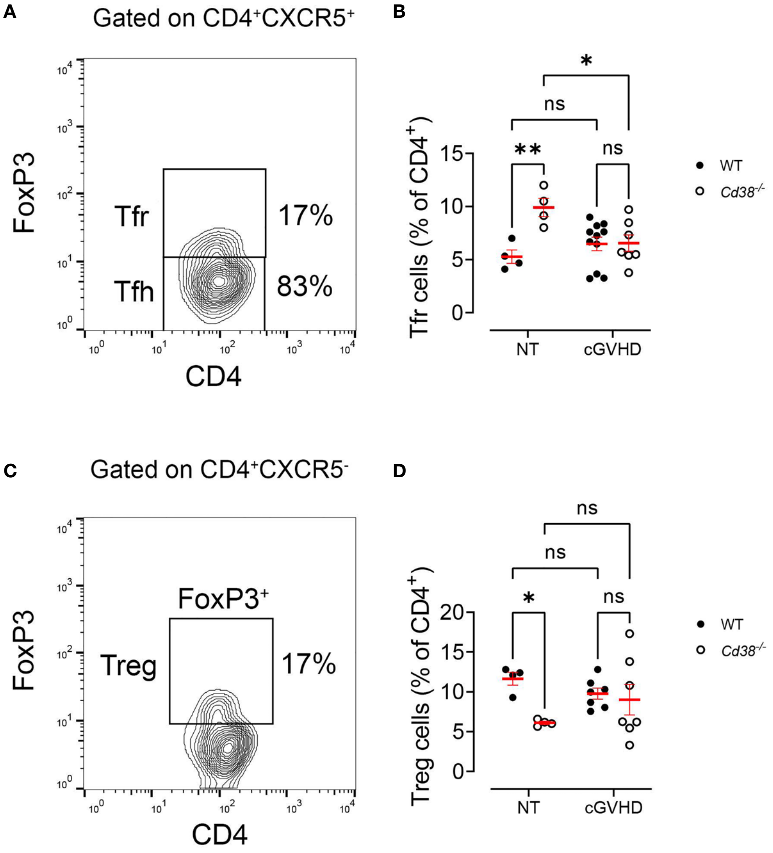

FIGURE 4 | Normal expansion of Tfr cells and Treg cells in *Cd38*$^{-/-}$ cGVHD mice. **(A, C)** Gating strategy used to detect total Tfr cells (independently of PD-1 expression) and Treg cells. **(A)** Representative flow cytometry plot showing FoxP3$^+$ Tfr cells and FoxP3$^-$ Tfh cells on gated CD4$^+$CXCR5$^+$ T cells. **(B)** Frequencies of Tfr cells (% of CD4$^+$) in non-treated (NT) mice or after 2 weeks of i.p. injection of bm12 cells (cGVHD). **(C)** Representative flow cytometry plot showing FoxP3$^+$ Treg cells on gated CD4$^+$CXCR5$^-$ T cells. **(D)** Frequencies of Treg cells (% of CD4$^+$) in NT mice or after 2 weeks of i.p. injection of bm12 cells (cGVHD). In panels **(B)** and **(D)** WT mice (closed circles) and *Cd38*$^{-/-}$ mice (open circles). Horizontal bars represent mean values and vertical bars ± SEM. The *P*-values are for two-way ANOVA test for multiple comparisons (Fisher's LSD test). ns, not significant ($P > 0.05$), *$P < 0.05$, **$P < 0.01$.

about 50% 2 weeks after the adoptive transfer of bm12 cells, remaining in that range thereafter (**Figure 5B**). In contrast, in cGVHD WT mice, about 40% of the Tfr cells were PD-1$^-$, with a significant increase at 2 weeks, dropping down to 17% at 8 weeks, where 84% Tfr cells were PD-1$^+$ (**Figure 5C**). Absolute numbers of PD-1$^+$ and PD-1$^-$ Tfr cells reflected distinct kinetic profiles in *Cd38*$^{-/-}$ mice *versus* WT mice. In cGVHD *Cd38*$^{-/-}$ mice, the number of Tfr cells reached a maximum at 4 weeks with some predominance of the PD-1$^-$ Tfr cells, while in cGVHD WT mice, there was a progressive increase in the number of PD-1$^+$ Tfr cells over the PD-1$^-$ Tfr cells that reached statistical significance only 8 weeks after the adoptive transfer of bm12 cells (**Figures 5D, E**). Therefore, there was a relatively balanced situation in terms of the number of cells of each phenotype in both cGVHD *Cd38*$^{-/-}$ mice and WT mice, which is clearly broken at 8 weeks.

Distinct Clustering of *Cd38*$^{-/-}$ cGVHD Mice

We used PCA, a multivariate statistical approach, to confirm and select the best features for distinguishing the allo-response elicited by *Cd38*$^{-/-}$ cGVHD *versus* WT cGVHD mice and to discriminate them from non-treated mice. **Figure 6** shows in four panels the score plots of the individual *Cd38*$^{-/-}$ and WT mice after the adoptive transfer of bm12 cells at different time points. Each score plot shows the distribution of mice according to the expression variance of the 11 features tested (total number of seven T-cell and B-cell subsets; anti-ssDNA, total IgG, spleen cell numbers, and spleen length). Non-treated (**Figure 6A**) and cGVHD *Cd38*$^{-/-}$ mice (**Figures 6B–D**) clustered in different areas than cGVHD WT mice with the exception at 2 weeks where 5 out of 11 WT mice overlapped with *Cd38*$^{-/-}$ mice (**Figure 6B**). This overlapping is likely due to the heterogeneity of the allo-response at that time and not to the presence of outliers (see outliers identification in the *Material and Methods*). The feature loading plot with arrows was useful to cluster each individual feature in an attempt to identify strain-specific feature expression profiles that could be used to distinguish the groups of mice analyzed (**Figure S5**). It is striking to note that most of the features seemed to be clustered to the areas where the cGVHD WT mice were located, which is in agreement

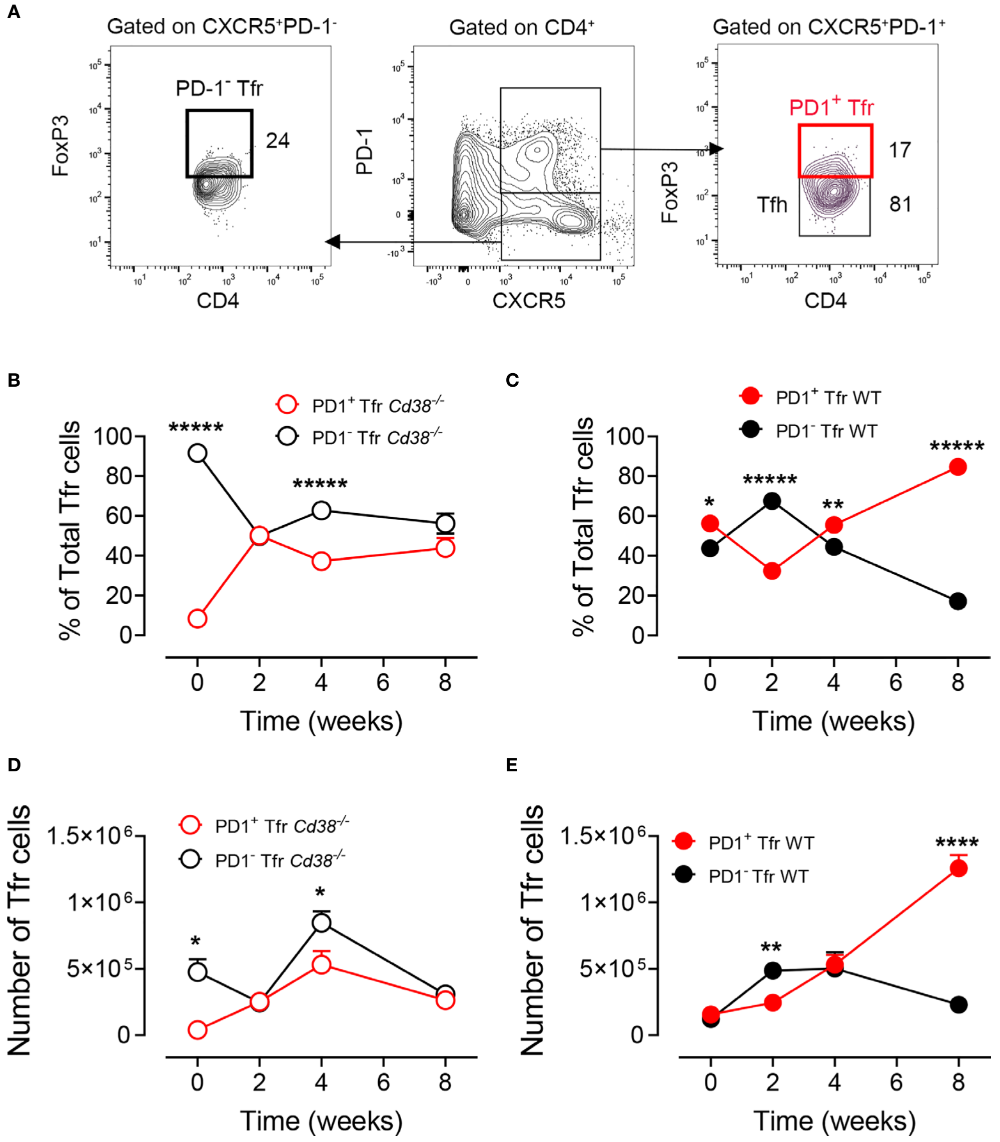

FIGURE 5 | Distinct kinetic profiles of PD-1$^+$ and PD-1$^-$ Tfr cells in cGVHD *Cd38*$^{-/-}$ *versus* cGVHD WT mice. **(A)** Gating strategy to detect PD-1^{hi}CXCR5$^+$ FoxP3$^+$ or PD1$^-$CXCR5$^+$FoxP3$^+$ Tfrs cells in spleen cells from cGVHD mice. Left panel: FoxP3 *versus* CD4 plot of gated CD4$^+$CXCR5$^+$PD-1$^-$ cells, showing the frequency of the PD-1$^-$FoxP3$^+$ Tfr cells. Middle panel: PD-1 *versus* CXCR5 plot on gated CD4$^+$ cells showing the gated CXCR5$^+$PD-1^{hi} and CXCR5$^-$PD-1$^-$ subpopulations. Right panel: FoxP3 *versus* CD4 plot showing the frequencies of PD-1$^+$FoxP3$^+$ Tfr cells and PD-1$^-$FoxP3$^-$ Tfr cells. **(B)** Kinetics of the frequencies of PD1$^+$ (open red circles) and PD-1$^-$ (open black circles) Tfr cells relative to total Tfr cells in spleen cells from cGVHD *Cd38*$^{-/-}$ mice. **(C)** Kinetics of the frequencies of PD1$^+$ (closed red circles) and PD-1$^-$ (closed black circles) Tfr cells relative to total Tfr cells in spleen cells from cGVHD WT mice. **(D)** Kinetics of total numbers of PD1$^+$ (open red circles) and PD-1$^-$ (open black circles) Tfr cells relative to total Tfr cells in spleen cells from cGVHD *Cd38*$^{-/-}$ mice. **(E)** Kinetics of total numbers of PD1$^+$ (closed red circles) and PD-1$^-$ (closed black circles) Tfr cells relative to total Tfr cells in spleen cells from cGVHD WT mice. The symbols are the mean values and the vertical bars represent ± SEM. *P*-values are shown for Welch's *t*-test. The results are cumulative data from two to three different experiments per time point and mouse type, each with three to four mice per experiment. $^*P < 0.05$, $^{**}P < 0.01$, $^{****}P < 0.0001$, $^{*****}P < 0.00001$.

with the fact that most of these features showed increased levels in these mice. In non-treated mice, the distribution of the variables was completely different, with most of them located in the upper right quadrant in an intermediate area between non-treated *Cd38*$^{-/-}$ and WT mice (**Figure S5**). Overall, these data suggest that these 11 features could be useful to discriminate the ongoing allo-immune response elicited by *Cd38*$^{-/-}$ mice *versus* WT mice. The major differences between *Cd38*$^{-/-}$ and WT mice to the bm12 challenge were observed at 4 and 8 weeks.

Abnormal Cytokine Serum Levels in *Cd38*$^{-/-}$ cGVHD Mice

Analysis of serum levels for 10 Th17-mediated cytokines indicated a distinct profile in *Cd38*$^{-/-}$ cGVHD mice, with significantly higher

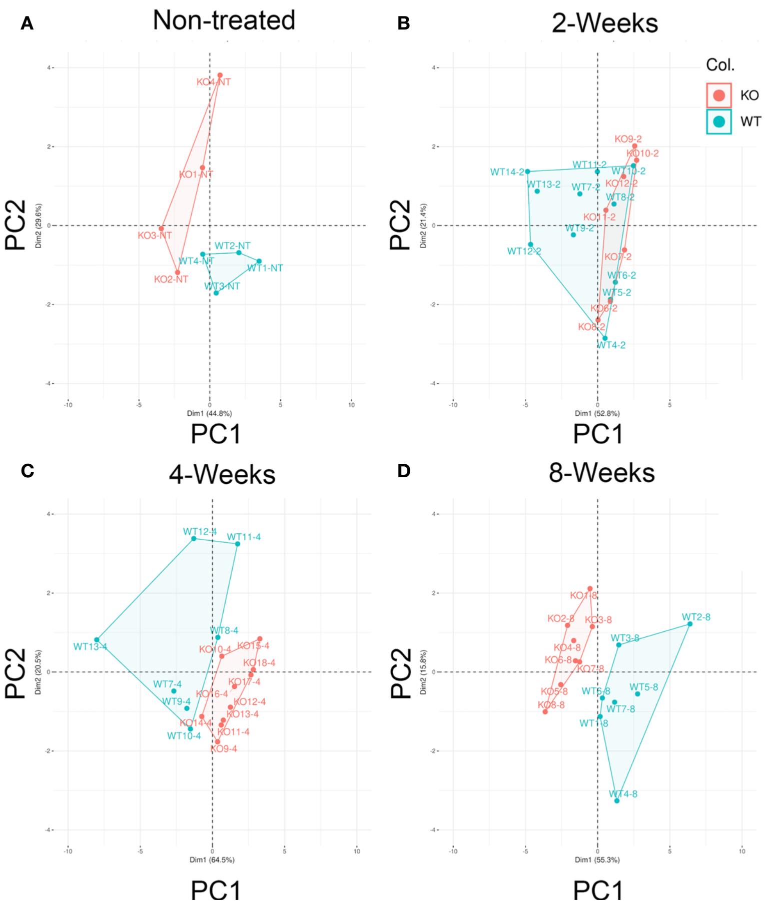

FIGURE 6 | Distinct clustering of *Cd38*$^{-/-}$ cGVHD mice. The PCA score plots show the distribution of mice according with two principal components that accumulate the greatest variance (71%–85% range) of the 11 features (variables) tested. Principal component 1 (PC1, *x*-axis) X% and principal component 2 (PC2, *y*-axis) Y%. Each panel represents one given time. **(A)** Non-treated (NT) healthy mice (*n* = 4, per mouse). **(B)** Two-weeks cGVHD (*n* = 11, WT; *n* = 7, KO). **(C)** Four-weeks cGVHD (*n* = 7; WT; *n* = 10, KO). **(D)** Eight-weeks cGVHD (*n* = 7, WT; *n* = 8, KO). Each dot represents an individual mouse, and except for NT, they are representative of two or more experiments. WT samples are represented by filled red circles. *Cd38*$^{-/-}$ samples with filled green circles.

serum levels of IL-22 and IL-23 relative to WT cGVHD mice at 4 and 2 weeks, respectively (**Figures 7A, B**). In contrast, IL-27 serum levels were significantly increased in WT *versus Cd38*$^{-/-}$ cGVHD mice 2 weeks after the adoptive transfer of bm12 cells (**Figure 7C**). Likewise, sCD40L serum levels were higher in WT cGVHD at 8 weeks (**Figure 7D**). Serum levels for IL-17F, IL-21, IL-31, IL-33, and MIP-3α were similar in both mouse types (**Figure S6** of the **Supplementary Material**). In a relatively small number of mice, we were also able to test another panel of cytokines including IL-10, IL-1β, IL-6, IL-17A, IFN-γ, and TNF-α. As shown in **Figure S7**, only IL-10 serum levels were significantly increased in bm12>WT mice as compared with bm12> *Cd38*$^{-/-}$ mice, 2 weeks after the adoptive transfer of bm12 cells. IL-10 has been related with autoantibody production in SLE patients (51). Notably, IL-27 correlated positively with the frequencies of most of the T-cell and B-cell subsets analyzed, with the exception of CXCR5^{+}PD-1^{hi} Tfr cells and CD4^{+} T cells, while it correlated negatively with the frequencies of CD19^{+} B cells (**Figure 7E**). Moreover, IL-27 levels correlated with anti-ssDNA and total IgG levels. sCD40L followed a similar path, although with a distinct and more restrictive profile than IL-27. On the other hand, IL-22 correlated negatively with Tfh cells, GC B cells, and CD4^{+} T cells. Note that many of these correlations should be analyzed collectively and not individually. Thus, IL-27 and sCD40L correlated positively with the CD11c^{hi}T-bet^{+} B-cell frequencies and IL-27, sCD40L, and IL-23 with anti-ssDNA levels (**Figure 7E**). In contrast, IL-27, IL-31, IL-21, and MIP-3α correlated negatively with the frequencies of CD19^{+} B cells (**Figure 7E**). Notable is the positive correlation found between IL-21 and the frequencies of the CXCR5^{+}PD-1^{hi} Tfr cell subset and IL-33 with CD4^{+} T cells, which may be related with similar kinetic profiles.

Proteomic Profile From Spleens of cGVHD WT Mice Reflects a STAT1-Driven Type I IFN Signature

The cytokine network type I IFN–IL-27–IL-10 is augmented in murine and human lupus (52), and IL-27 induces T-bet expression *via* STAT1 signaling and class switching in B cells (53).

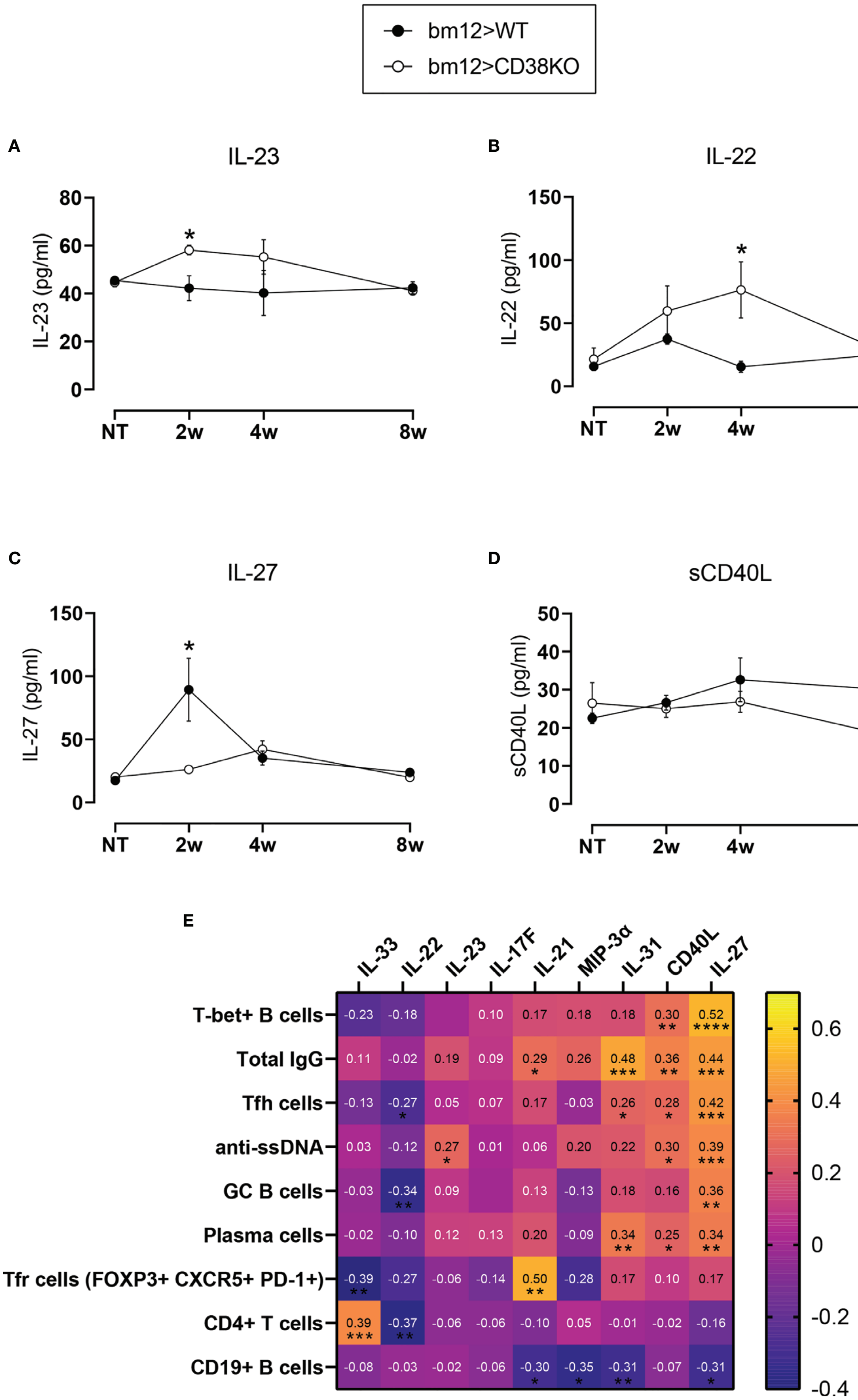

	IL-33	IL-22	IL-23	IL-17F	IL-21	MIP-3α	IL-31	CD40L	IL-27
T-bet+ B cells	-0.23	-0.18		0.10	0.17	0.18	0.18	0.30 **	0.52 ****
Total IgG	0.11	-0.02	0.19	0.09	0.29 *	0.26	0.48 ***	0.36 **	0.44 ***
Tfh cells	-0.13	-0.27 *	0.05	0.07	0.17	-0.03	0.26 *	0.28 *	0.42 ***
anti-ssDNA	0.03	-0.12	0.27 *	0.01	0.06	0.20	0.22	0.30 *	0.39 ***
GC B cells	-0.03	-0.34 **	0.09		0.13	-0.13	0.18	0.16	0.36 **
Plasma cells	-0.02	-0.10	0.12	0.13	0.20	-0.09	0.34 **	0.25 *	0.34 **
Tfr cells (FOXP3+ CXCR5+ PD-1+)	-0.39 **	-0.27	-0.06	-0.14	0.50 **	-0.28	0.17	0.10	0.17
CD4+ T cells	0.39 ***	-0.37 **	-0.06	-0.06	-0.10	0.05	-0.01	-0.02	-0.16
CD19+ B cells	-0.08	-0.03	-0.02	-0.06	-0.30 *	-0.35 *	-0.31 **	-0.07	-0.31 *

FIGURE 7 | Abnormal cytokine serum levels in *Cd38*$^{-/-}$ cGVHD mice. **(A)** IL-23. **(B)** IL-22. **(C)** IL-27. **(D)** sCD40L. In panels **(A–D)** WT mice (closed circles) and *Cd38*$^{-/-}$ mice (open circles). The symbols are the mean values and the vertical bars represent ± SEM. *P*-values are shown for Welch's *t*-test. The results are cumulative data from two to three different experiments per time point and mouse type, each with three to five mice per experiment. **(E)** Matrix showing Spearman's *r* correlation values between cytokines serum levels (horizontal) and the frequencies of the T- and B-cell subsets analyzed + anti-ssDNA and total IgG. Asterisks below *r* numbers denote statistical significance, which could be positive correlation (no sign) or negative correlation (–). $^*P < 0.05$.

Therefore, it was of interest to test whether the augmented serum levels of IL-27 and increased T-bet expression found in B cells from WT mice had a proteomic profile sustaining these findings. To this end, a semiquantitative proteomic approach was taken using the exponentially modified protein abundance index (emPAI) and molar percentages (%M) described in the *Material and Methods* section. Protein extracts from the spleens of *Cd38*$^{-/-}$ and WT cGVHD mice and non-treated mice were analyzed. Volcano plots showed significant differences in protein abundance in the spleen lysates from bm12>*Cd38*$^{-/-}$ mice *versus* bm12>WT mice, 2 weeks after the adoptive cell transfer (**Figure 8A**). Among the proteins which showed increased abundance in spleens of bm12>WT mice *versus* bm12> *Cd38*$^{-/-}$ was STAT1 (**Figure 8B**). ClueGO functional enrichment analysis showed that STAT1 was associated with a cluster of proteins in GO terms including positive regulation of type I IFN production, type I interferon production, positive regulation of interferon-alpha production, interferon-beta production, and cellular response to IL-7 (**Figure 8C**). A positive regulation of type I interferon production was investigated in a subnetwork using the CluePedia plug-in. STAT1 was clearly involved in the regulation of the type I IFN signaling pathway with other identified proteins (**Figure 8D**). STAT1 was also inserted in other ClueGO functional terms including the IL-3 signaling pathway and the TNF-α NF-κB signaling pathway, among others (data not shown).

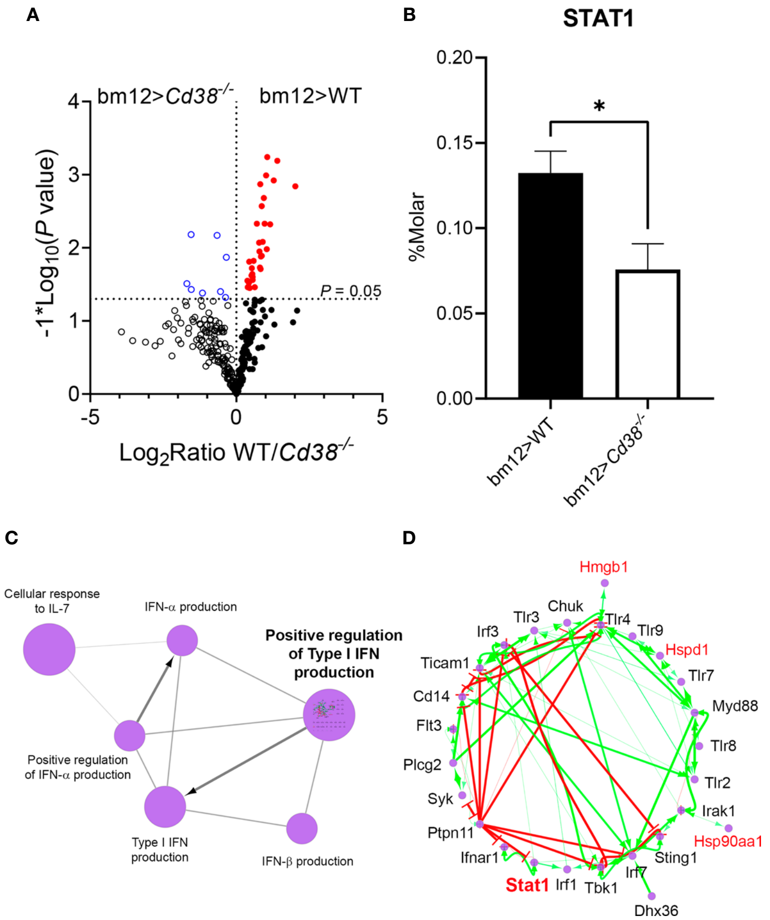

FIGURE 8 | **(A)** Volcano plots showing the differences in protein abundance in spleens of bm12>*Cd38*$^{-/-}$ mice (open blue circles, upper left quadrant) relative to bm12>WT mice (closed red circles, upper right quadrant), 2 weeks after the adoptive transfer. Each circle denotes a different protein, and those above the horizontal dotted line showed statistical significant differences in abundance between mice. $P < 0.05$. **(B)** Histogram graph showing STAT1 protein abundance in spleens from bm12>*Cd38*$^{-/-}$ *versus* bm12>WT mice at 2 weeks. Histograms represent the mean ± SEM, and the *P*-values are for unpaired *t*-test. Proteomic data shown in panels **(A, B)** are from two biological replicas per mouse type and three technical replicas per sample. **(C)** Functionally grouped network of GO terms/pathways and genes are visualized using the ClueGO/CluePedia application. Note that in this application the protein accession numbers of the identified proteins are transformed to their gene names. Terms (large purple circles) are linked based on κ score (≥0.3). Edges show the known expression. The edge thickness is scaled between the minimum and maximum scores shown. The size of the terms is related with their statistical significance. **(D)** "Positive regulation of type I interferon production'" pathway, which showed the highest statistical significance, was investigated in a subnetwork. Gene names of the identified proteins are highlighted in red. Genes not included in the initial selection are highlighted in black. Known activation [activation symbols in green (arrows)] and inhibition (inhibitory symbols in red) effects are shown. Stat1 and some of the genes of the identified proteins (highlighted in red) are acting as activators in this pathway. **P* < 0.05.

Tissue Alterations in cGVHD Mice

The comparative study of the spleen, liver, and renal tissues of bm12>WT and bm12>*Cd38*$^{-/-}$ mice at 2, 4, and 8 weeks after the adoptive transfer of bm12 cells is shown in the representative microphotographs of **Figures 9–11**. In the spleen, a stronger cellular response was observed in tissue sections from bm12>WT mice as compared with bm12>*Cd38*$^{-/-}$ mice (panels **A** and **B** in each figure), with a larger number of cells, that is reflected by a significant increase in white pulp in bm12>WT *versus* bm12>*Cd38*$^{-/-}$ (for a semiquantitative assessment, see **Table S2** in the **Supplementary Material**). In the liver, greater areas of inflammatory infiltrates were detected in bm12>WT mice relative to bm12>*Cd38*$^{-/-}$ mice, with the highest intensity at 4 and 8 weeks (panels **C** and **D** of each figure). In this sense, in bm12>WT, the increased inflammation was quite patent around the centrolobular vein in the liver (indicated by a black head arrow in **Figures 9C**, **10C**, **11C**). Another striking difference in the liver of these mice at 8 weeks was the evident signs of macrovesicular steatosis in some of the bm12>WT mice (**Figure 11C**), which were not observed in liver sections from bm12>*Cd38*$^{-/-}$ mice (**Figure 11D**). No glomerular, tubulo-interstitial, or vascular lesions were present in the renal parenchyma of bm12>WT and bm12> *Cd38*$^{-/-}$ mice (panels **E–J** in **Figures 9–11**). However, in bm12>WT mice, PAS staining showed inflammatory infiltrates that appeared earlier and lasted longer than in bm12> *Cd38*$^{-/-}$ mice (panels **E–H**, **Figures 9–11**). The foci of inflammatory infiltrates were perivascular (**Figures 10E**, **11E**), periglomerular (**Figure 11E**), and tubulo-interstitial (**Figure 11J**), with few hyaline casts (**Figure 9E**) and without the staining evidence of the presence of glomerular immune complexes (see **Table S3** in the **Supplementary Material** for a semiquantitative assessment). Renal lesions in non-treated control groups were absent (not shown). MT staining in bm12>WT mice showed an increased thickening process of the mesangium that was maximal at 4 weeks (**Figure 10I**) and still detectable at 8 weeks (**Figure 11I**). In contrast, MT staining in bm12>*Cd38*$^{-/-}$ mice showed mesangial thickening in the glomeruli at 2 weeks (**Figure 9J**), which was markedly reduced at 4 weeks (**Figure 10J**) and virtually absent at 8 weeks (**Figure 11J**). In summary, in *Cd38*$^{-/-}$ cGVHD mice, a milder inflammatory reaction was observed in all tissues analyzed as compared with WT cGVHD, and the histological evolution of these tissue alterations suggests a faster resolution of the inflammation in *Cd38*$^{-/-}$ mice.

Normal cGVHD Response in bm12 Mice After the Adoptive Transfer of *Cd38*$^{-/-}$ Spleen Cells

It has been described that TCR-activated *Cd38*$^{-/-}$ CD4^{+} T cells show a hybrid Th1/Th17 phenotype exhibiting intrinsically higher NAD^{+}, enhanced oxidative phosphorylation, higher glutaminolysis, and altered mitochondrial dynamics that vastly improved tumor control (54, 55). These functional characteristics of *Cd38*$^{-/-}$ CD4^{+} T cells may alter the cGVHD response in bm12 mice. To test this hypothesis, we took the advantage that in the cGVHD lupus model bm12 or C57BL/6 WT mice can serve as the donor or the recipient, with similar outcomes (21). Therefore, we assessed whether the

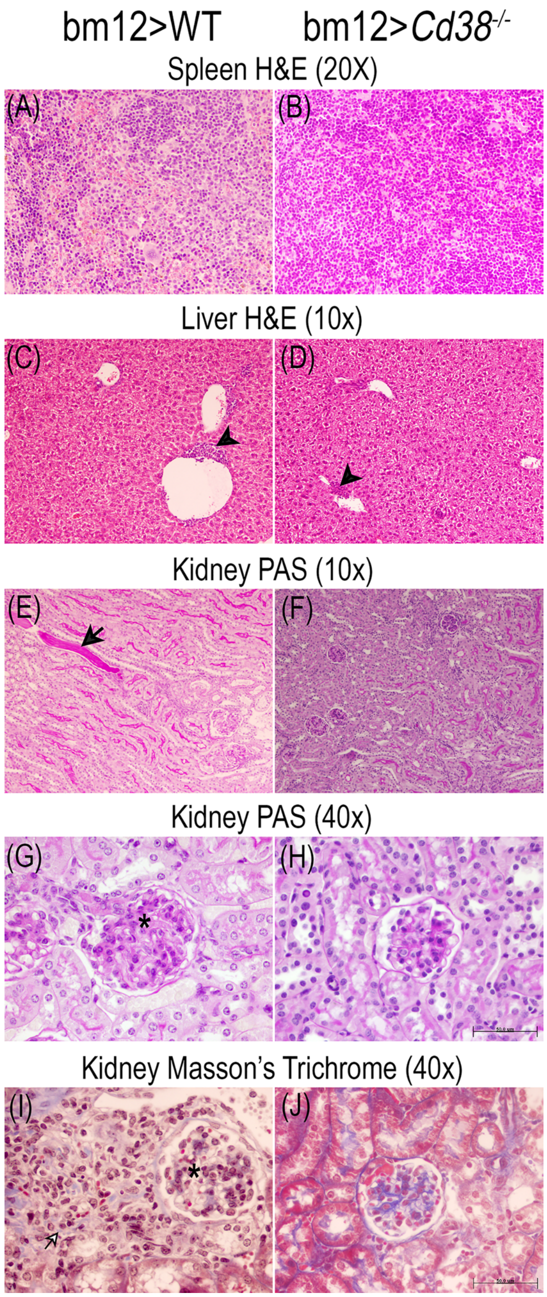

FIGURE 9 | Representative microphotographs of the histological studies performed on the spleen, liver, and kidney 3-µm sections at 2 weeks of the adoptive transfer of spleen cells from female bm12 to female WT (left panels) or to *Cd38*$^{-/-}$ (right panels) mice. **(A, B)** Spleen, **(C, D)** liver, and **(E–J)** kidney. **(A–D)** Spleen and liver tissue sections stained with H&E. **(E–H)** Kidney tissue sections stained with PAS. **(I, J)** Kidney sections stained with Masson's trichrome. Images were taken with a BH2 Olympus microscope. **(A, B)** ×20 magnification; **(C–F)** ×10 magnification; **(G–J)** 40× magnification. **(H, J)** Scale bar: 50 µm. Note in WT cGVHD mice and *Cd38*$^{-/-}$ cGVHD mice the presence of mild perivascular chronic inflammatory infiltrate in liver [black head arrow in **(C)** and **(D)**]. Note in WT cGVHD mice hyaline casts in kidney [black arrow in **(E)**], periglomerular chronic inflammatory infiltrate [black and white arrow in **(I)**], and increased glomerular size [asterisks in **(G)** and **(I)**].

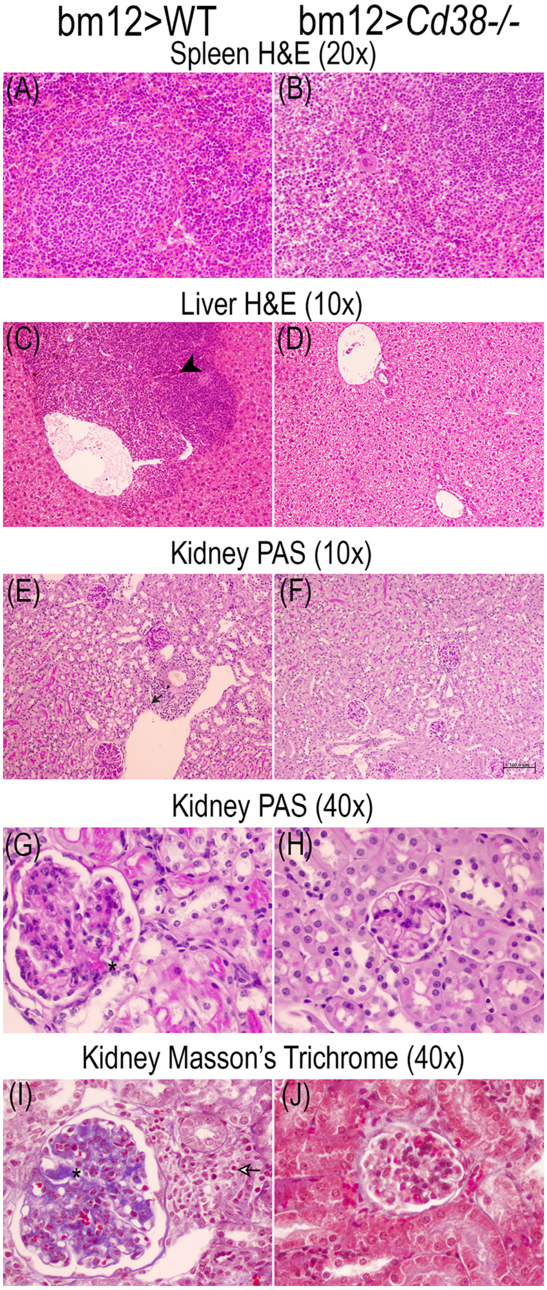

FIGURE 10 | Representative microphotographs of the histological studies performed on the spleen, liver, and kidney 3-µm sections at 4 weeks of the adoptive transfer of spleen cells from female bm12 to female WT (left panels) or *Cd38*$^{-/-}$ (right panels) mice. **(A, B)** Spleen, **(C, D)** liver, and **(E–J)** kidney. **(A–D)** Spleen and liver tissue sections were stained with H&E. (**E–H**) Kidney tissue sections were stained with PAS. **(I, J)** Kidney sections were stained with Masson's trichrome. Images were taken with a BH2 Olympus microscope. **(A, B)** ×20 magnification; **(C–F)** ×10 magnification; **(G–J)** ×40 magnification. **(F)** Scale bar: 50 µm. Note in the liver from WT cGVHD mice the presence of moderate/severe perivascular chronic inflammatory infiltrate [black head arrow in **(C)**]. Note in the kidney of WT cGVHD mice the presence of inflammatory infiltrate [small black arrow in **(E)**], periglomerular chronic inflammatory infiltrate [black and white arrow in **(I)**], and increased glomerular size with increased mesangial matrix [asterisks in **(G)** and **(I)**].

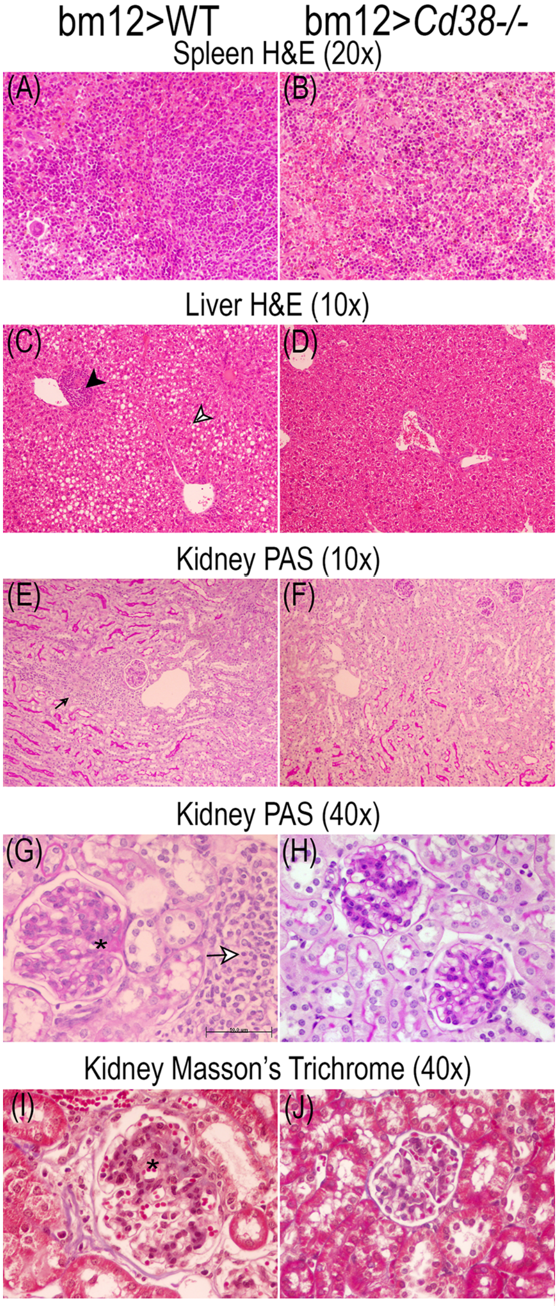

FIGURE 11 | Representative microphotographs of the histological studies performed on the spleen, liver, and kidney 3-µm sections at 8 weeks of the adoptive transfer of spleen cells from female bm12 to female WT (left panels) or *Cd38*$^{-/-}$ (right panels) mice. **(A, B)** Spleen, **(C, D)** liver, and **(E–J)** kidney. **(A–D)** Spleen and liver tissue sections were stained with H&E. **(E–H)** Kidney tissue sections were stained with PAS. **(I, J)** Kidney sections were stained with Masson's trichrome. **(A, B)** ×20 magnification; **(C–F)** ×10 magnification; **(G–J)** ×40 magnification. **(G)** Scale bar: 50 µm. Note in the liver from WT cGVHD mice the presence of mild perivascular chronic inflammatory infiltrate [black head arrow in **(C)**] and macrovesicular steatosis [black and white head arrow in **(C)**]. Note in the kidney of WT cGVHD the periglomerular chronic inflammatory infiltrate [small black arrow in **(E)**] and the increased glomerular size [asterisks in **(G)** and **(I)**].

same is true using *Cd38*$^{-/-}$ cells as donors instead of being recipients. Two weeks after the adoptive transfer of *Cd38*$^{-/-}$ or WT spleen cells, bm12 recipients showed comparable increases in frequencies and absolute numbers of Tfh, GC B cells, plasma cells, and CD11c^{hi}T-bet^{+} B cells (**Figures 12A, B**). In contrast, increased frequencies and numbers of CXCR5^{+}PD-1^{hi} Tfr cells and low frequencies and numbers of CD19^{+} B cells were shown (**Figures 12A, B**), which were statistically significant for the frequencies *versus* WT>bm12 mice. Likewise, anti-ssDNA and total IgG serum levels were similar (**Figures 12C, D**). Moreover, similar serum cytokine levels were observed in these mice, which is in marked contrast with the data when *Cd38*$^{-/-}$ mice were the recipients of bm12 cells (**Figure S8**).

DISCUSSION

In the cGVHD lupus model, the key cellular mechanism that results in the loss of B-cell tolerance is the interaction of donor CD4^{+} T cells with MHC class II on the host B-cell surface. Autoantibodies are produced almost entirely by the host B cells. The transferred donor B cells contributed neither to the autoimmune response nor to the total serum Ig, with rare exceptions (56). Therefore, in the bm12>*Cd38*$^{-/-}$ setting, the defective response of B cells is likely due to the inability of *Cd38*$^{-/-}$ B cells to respond to an allogeneic stimulus provided by donor bm12 CD4^{+} T cells. The defective B-cell response was evidenced by the low frequencies of CD11c^{hi}T-bet^{+} B cells, GC B cells, and plasma cells along the disease process. These findings correlated with low levels of anti-ssDNA autoantibodies, despite the relatively strong polyclonal activation as judged by a significant increase in total IgG serum levels above basal levels. Furthermore, CD38 deficiency in host mice results in diminished generation of Tfh cells. Given that the transferred bm12-CD4^{+} T cells were CD38 sufficient and the allo-reactive donor bm12 CD4^{+} T cells activated by host MHC II provide cognate help for host B cells to initiate lupus (36), these data support the role for Ag-presenting, B-cell-intrinsic CD38 in the induction of autoreactive immune responses. Alternatively, another antigen-presenting cell such as CD8α^{+} DCs, known for its tolerogenic phenotype, may act in the early phases of the allo-immune response (57).

Another interesting feature of this model is that when the transferred donor cells were from CD38-deficient mice, the allo-

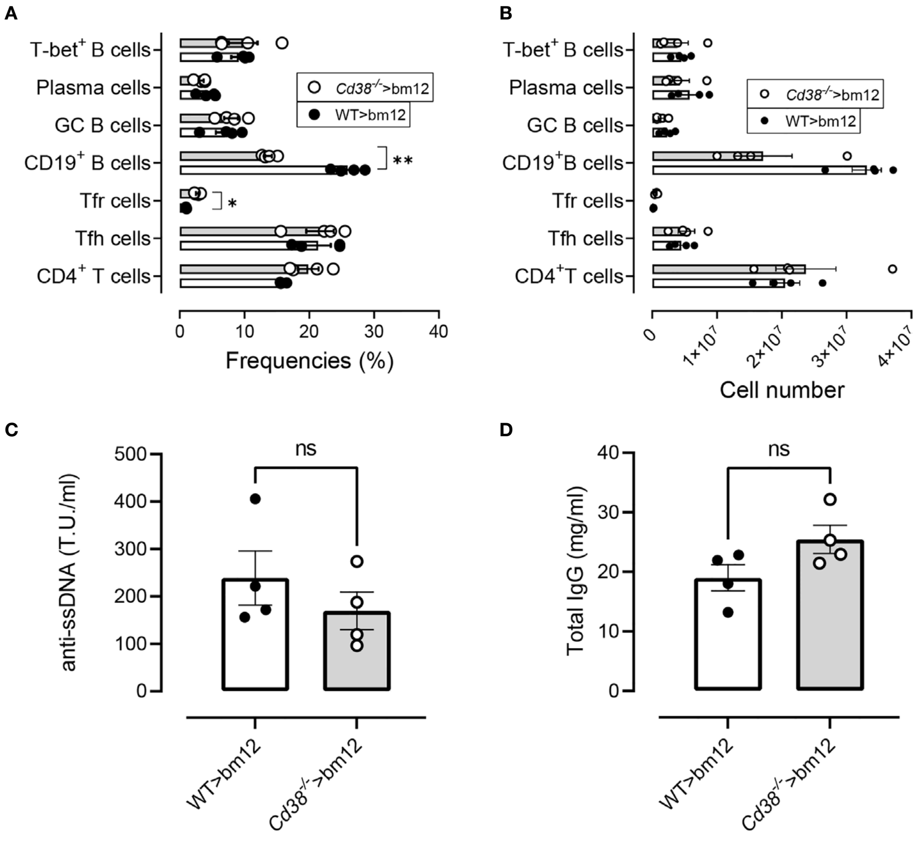

FIGURE 12 | Normal cGVHD response in bm12 mice after the adoptive transfer of *Cd38*$^{-/-}$ spleen cells. **(A)** Frequencies of the T- and B-cell subsets analyzed in WT>bm12 mice (closed circles and open bars) and *Cd38*$^{-/-}$>bm12 mice (open circles and gray bars), 2 weeks after the adoptive transfer of cells. **(B)** Total numbers of the same subsets and mice of panel **(A)**. **(C)** Anti-ssDNA serum levels. **(D)** Total IgG serum levels. Data in **(A–D)** are from one out of two independent experiments, each symbol representing one mouse. In **(A, B)**, *P*-values are for multiple *t*-tests corrected for multiple comparisons by the Holm–Šidák method. In **(C, D)**, the *P*-values are for unpaired *t*-test. ns, not significant ($P > 0.05$), $^{*}P < 0.05$, $^{**}P < 0.01$.

immune response elicited by the interaction of donor *Cd38*$^{-/-}$ T cells with the host bm12 B cells results in similar frequencies and numbers of most T-cell and B-cell subsets analyzed in comparison with the combination WT donor>bm12 recipient. Moreover, the anti-ssDNA autoantibody response and cytokine plasma levels were quite similar to those in the WT>bm12 setting. This was an important control for the experiments where *Cd38*$^{-/-}$ mice were acting as recipients. Although in the classical cGVHD model the expansion of Tfh cells comes preferentially from the donor bm12 cells, a relatively small but significant proportion of Tfh cells come from the recipient WT mice (18). Therefore, recipient T cells may also participate somewhat in the germinal center response, as some of them do develop a Tfh phenotype. Given the fact that in the *Cd38*$^{-/-}$donor>bm12 recipient setting, where *Cd38*$^{-/-}$ Tfh cells are strongly expanded, they seem to behave as WT Tfh cells, it is not expected that endogenous *Cd38*$^{-/-}$ Tfh cells make any functional difference in the bm12> *Cd38*$^{-/-}$ setting. To formally prove this hypothesis, it would require the use of donor and recipient mice on different congenic backgrounds, e.g., using CD45.1 bm12 donors and CD45.2 WT or CD45.2 *Cd38*$^{-/-}$ recipients in the adoptive transfer experiments would help to follow-up the fate of donor and recipient cells in the GCs and, eventually, to sort them out for functional studies.

It is worth noting that in the late phase of the allogeneic response in WT mice, the proportion and numbers of PD-1^{+} Tfr cells were significantly higher than PD-1^{-} Tfr cells, while in *Cd38*$^{-/-}$ mice, the two subsets were present in a more equilibrated situation with a ratio close to 1:1. This phenomenon occurred despite the fact that at steady-state conditions the proportion and absolute numbers of PD-1^{-} Tfr cells in *Cd38*$^{-/-}$ mice were abnormally high as compared with those in WT mice. One could argue that since the expansion of Tfh cells in *Cd38*$^{-/-}$ cGVHD mice was relatively low, while the initial expansion of Treg cells and total Tfr cells was normal, those levels of *Cd38*$^{-/-}$ Tfr cells would be suffice to efficiently inhibit Tfh cell function. It is interesting to note that the expansion of CXCR5^{+}PD1^{hi} Tfr cell in WT cGVHD mice and the high expression of PD-1 make them less suitable to their suppressive function as it has been highlighted by several studies in PD-1-deficient mice (45). Moreover, the high expression of CD38 in WT B cells may suppress even further the CXCR5^{+}PD1^{hi} Tfr cell function *via* adenosine-receptor signaling as it occurs in multiple myeloma tumor cells, which are highly positive for CD38 expression and where CD38 promotes tumor progression *via* the suppression of CD8^{+} T-cell function (58). In this sense, in the murine system, B-cell follicles are highly positive for CD38 expression; however, CD38 expression is low or negative in GC B cells and high in memory B cells and in other B-cell subsets (59). Therefore, during the allo-immune response in bm12>WT mice, it is feasible that the interaction of Tfr cells with CD38^{+} B cells, other than GC B cells, may occur (45).

The most striking finding of this study is the defective expansion of CD11c^{hi}T-bet^{+} B cells in *Cd38*$^{-/-}$ cGVHD mice, which seems to be more severe than any other B-cell or T-cell subset analyzed, with the exception of the CXCR5^{+}PD-1^{hi} Tfr cells that follow similar kinetics. Moreover, the frequency of CD11c^{hi}T-bet^{+} B cells correlates with anti-ssDNA autoantibodies and serum levels of IL-27 and sCD40L. Increased serum levels of IL-27 were only detected in WT cGVHD mice. sCD40L is elevated in SLE patients, correlates with disease activity and anti-dsDNA autoantibodies, and may have the capacity to activate B cells (60, 61). Aberrant expression of CD40L in T cells might be predicted to result in activation of bystander B cells, including those that have encountered self-antigens, and to contribute to autoantibody secretion. Elevated circulating sCD40L is likely to reflect the chronic and multiclonal Th cell activation that is most characteristic of SLE (61).

IL-27 is considered an inhibitory cytokine in the differentiation of Th17 cells and induces T-bet expression *via* STAT1 signaling and class switching in B cells (53). Moreover, our label-free quantitative proteomics study demonstrates increased abundance of STAT1 in WT cGVHD mice *versus* *Cd38*$^{-/-}$ cGVHD mice (**Figure 8B**). *In silico* analysis of the identified proteins showed that STAT1 is functionally associated with proteins positively involved in the production of type I IFN (**Figure 8D**). In this sense, dysregulation of the IFN-I signaling pathway occurs in the bm12 cGVHD lupus-like model (19) and in the pristane lupus model (62, 63), affecting particularly B cells and autoantibody production. Thus, in the pristane model, IRF9, STAT1, and IFNAR2 are required for IgG autoantibody production and increased B-cell expression of TLR7 and TLR9 (62, 63), while in the bm12 model, type I IFN sensing by B cells decreases their threshold for BCR signaling and increased their expression of MHC class II, CD40, and Bcl-6, requirements for optimal GC B-cell functions (19). Moreover, ablation of type I IFN sensing in B cells significantly reduces the accumulation of GC B cells, plasmablasts, and autoantibodies (19), which underscores the important contribution of direct type I IFN sensing in the B-cell response and concomitant autoantibody production.

B-cell-intrinsic expression of T-bet is required for the development of autoantibody-mediated disease in lupus mouse models, including in the cGVHD model (39, 40). Likewise, several groups have reported the presence of CD11c^{hi}T-bet^{+} B cells in several autoimmune diseases, including SLE. Thus, in SLE patients, the expansion of B cells lacking IgD and CD27 [double negative (DN)] reflects a subset of CXCR5^{-}CD11c^{+}T-bet^{+} cells (DN2), which represent the precursors of autoantibody-producing plasma cells, also termed by others as antibody-secreting cells (ASCs) (64, 65). Interestingly, in SLE patients, the differentiation of human CD11c^{+}T-bet^{+} cells occurs outside the follicular zone, and therefore, it is subjected to a distinct regulation than GC B cells, which eventually also differentiate to ASCs. In contrast, most murine T-bet^{+} B cells arise from germinal centers, since most pathogens engender T-dependent immune responses, generally skewed toward Th1 (66). Consistent with this view, the T-bet^{+} B cells that accumulate with age fail to appear in CD154-deficient mice and display somatic hypermutation (67). In addition, T-bet^{+} B cells that emerge from adoptively transferred naive B cells require cell-intrinsic MHC class II and CD40 expression (67). In this sense, the cGVHD lupus model involves the adoptive transfer of bm12 T cells into mismatched MHC class II recipients and requires extensive cognate interaction between donor T cells and recipient B cells. Together, these features implicate cognate T-cell help and participation in a germinal center reaction, all hallmarks of antigen-experienced cells.

Excessive CD11c$^+$T-bet$^+$ B cells promote aberrant Tfh differentiation and affinity-based GC selection in murine lupus models, including the bm12 cGVHD model, through their potent antigen-presenting function (68). In this sense, ablation of B-cell-intrinsic T-bet reduces Ag presentation by B cells, diminishing T-cell activation, inhibiting spontaneous GC formation, and reducing B-cell differentiation into autoantibody-producing plasma cells (39). Triggering of the B-cell antigen receptor (BCR), IFN-γ receptor (IFN-γR), and TLR7 on B cells induces high levels of T-bet expression in humans and mice (39, 65). Given the functional association of CD38 with CD81, CD19, Lyn, Galphai-2, Hsc-70, and actin in human B cells (69) and the presence of CD38 in B-cell-derived exosomes associated with the signaling molecules CD81, Hsc-70, and Lyn (69), it would be interesting to study whether any of these receptor-mediated signaling events are affected by the absence of CD38 in B cells.

In a previous study using the pristane lupus model, we demonstrated the crucial role for CD38 in promoting aberrant inflammation and lupus-like autoimmunity *via* an apoptosis-driven mechanism, which requires TRPM2 expression (13). Mild kidney inflammation, which usually takes 2 to 3 months to develop in WT cGVHD mice, developed even milder and resolved faster in *Cd38*$^{-/-}$ cGVHD mice. This weak inflammatory reaction was also observed in other organs such as the spleen and liver. An unprecedented result was the inflammatory reaction surrounding the centrolobular vein of the liver and the evident signs of macrovesicular steatosis in some of the WT cGVHD mice, which to our knowledge has not been reported before in this lupus model.

CONCLUSION

Taken together, the results of our study showed that the absence of CD38 plays a significant role in the development of the bm12 cGVHD lupus model. Although we have not identified the affected cells, all the experiments point out to a B-cell subset, with the CD11c$^+$T-bet$^+$ B cells being the most affected by the absence of CD38. Dysregulation of several cytokines and increased protein abundance of STAT1 were also affected. Collectively, these findings could enhance our knowledge of the pathophysiological molecular processes involved in SLE, providing strategies for early diagnosis of SLE and, in addition, therapeutic strategies based on antibodies against CD38 and pharmacological approaches targeting CD38 enzymatic activity and/or the JAK/STAT proteins.

DATA AVAILABILITY STATEMENT

The original contributions presented in the study are included in the article/**Supplementary Material**. Further inquiries can be directed to the corresponding authors.

ETHICS STATEMENT

This study was part of the funded project SAF2017–89801-R, where all protocols and procedures involving the use of laboratory animals have been supervised and approved by the Bioethical Committee of the Consejo Superior de Investigaciones Científicas (CSIC).

AUTHOR CONTRIBUTIONS

JS and MZ contributed to the conception and design of the study, organized the database, and performed the experimental work. JS wrote the first draft of the manuscript. MZ wrote sections of the manuscript. RM performed the autoantibody and total IgG analyses and contributed to the interpretation of the results. NM-M and FO'V performed the histological analyses. EA-L and LT-C performed the bioinformatic analyses. MP-S-C, SR-S, and SG-F performed the flow cytometry analyses. AF-I performed the cytokine analyses. AL-S and VL-P performed the proteomics. AM-B, MD-P, MB-S, SP-C, NB-I, PC-R, AC-G, and MT-S performed the experimental work and data analysis. LM-H performed the microscopy analysis. All authors contributed to the article and approved the submitted version.

FUNDING

JS and MZ received financial support through "Proyecto del Plan Estatal": SAF2017–89801-R. The IPBLN-CSIC Proteomics Unit belonged to ProteoRed-ISCIII (PRB2; PRB3) and was supported by grants PT13/0001/0011 (IPBLN-CSIC) and PT17/0019/0010 (CIB-CSIC; IPBLN-CSIC). RM: Project: SAF2017-82905-R. FO'V: Cátedra MIS IMPLANT-UGR. The stay of AC-G in Sancho's lab was supported by a fellowship-contract JAE-Intro (CSIC). The stay of MD-P in Sancho's lab was supported by a 1-year post-doctoral fellowship (Reference No. 502492) from the Consejo Nacional de Ciencia y Tecnología (CONACYT) of México. EA-L was recipient of a postdoctoral fellowship from the regional Andalusian Government.

ACKNOWLEDGMENTS

We thank Dr. Frances E. Lund (Department of Microbiology, University of Alabama at Birmingham, Birmingham, Alabama, USA) for the gift of *Cd38*$^{-/-}$ mice, Dr. Esther Zumaquero (Department of Microbiology, UAB, Alabama, USA) for helpful discussions on the role of CD11c^{hi}T-bet$^+$ B cells in SLE, and Clara Sánchez and her team for animal husbandry at the IPBLN-CSIC Animal Facility.

SUPPLEMENTARY MATERIAL

The Supplementary Material for this article can be found online at: https://www.frontiersin.org/articles/10.3389/fimmu.2021.713697/full#supplementary-material

REFERENCES

1. Tsokos GC, Lo MS, Costa Reis P, Sullivan KE. New Insights Into the Immunopathogenesis of Systemic Lupus Erythematosus. *Nat Rev Rheumatol* (2016) 12(12):716–30. doi: 10.1038/nrrheum.2016.186
2. Bradley SJ, Suarez-Fueyo A, Moss DR, Kyttaris VC, Tsokos GC. T Cell Transcriptomes Describe Patient Subtypes in Systemic Lupus Erythematosus. *PloS One* (2015) 10(11):e0141171. doi: 10.1371/journal.pone.0141171
3. Banchereau R, Hong S, Cantarel B, Baldwin N, Baisch J, Edens M, et al. Personalized Immunomonitoring Uncovers Molecular Networks That Stratify Lupus Patients. *Cell* (2016) 165(3):551–65. doi: 10.1016/j.cell.2016.03.008
4. Zhuang H, Szeto C, Han S, Yang L, Reeves WH. Animal Models of Interferon Signature Positive Lupus. *Front Immunol* (2015) 6:291. doi: 10.3389/fimmu.2015.00291
5. Manna A, Aulakh S, Jani P, Ahmed S, Akhtar S, Coignet M, et al. Targeting CD38 Enhances the Antileukemic Activity of Ibrutinib in Chronic Lymphocytic Leukemia. *Clin Cancer Res* (2019) 25(13):3974–85. doi: 10.1158/1078-0432.CCR-18-3412
6. Fumey W, Koenigsdorf J, Kunick V, Menzel S, Schutze K, Unger M, et al. Nanobodies Effectively Modulate the Enzymatic Activity of CD38 and Allow Specific Imaging of CD38(+) Tumors in Mouse Models *In Vivo*. *Sci Rep* (2017) 7(1):14289. doi: 10.1038/s41598-017-14112-6
7. Morandi F, Horenstein AL, Costa F, Giuliani N, Pistoia V, Malavasi F. CD38: A Target for Immunotherapeutic Approaches in Multiple Myeloma. *Front Immunol* (2018) 9:2722. doi: 10.3389/fimmu.2018.02722
8. Hogan KA, Chini CCS, Chini EN. The Multi-Faceted Ecto-Enzyme CD38: Roles in Immunomodulation, Cancer, Aging, and Metabolic Diseases. *Front Immunol* (2019) 10:1187. doi: 10.3389/fimmu.2019.01187
9. Katsuyama E, Suarez-Fueyo A, Bradley SJ, Mizui M, Marin AV, Mulki L, et al. The CD38/NAD/SIRTUIN1/EZH2 Axis Mitigates Cytotoxic CD8 T Cell Function and Identifies Patients With SLE Prone to Infections. *Cell Rep* (2020) 30(1):112–23.e4. doi: 10.1016/j.celrep.2019.12.014
10. Pavon EJ, Zumaquero E, Rosal-Vela A, Khoo KM, Cerezo-Wallis D, Garcia-Rodriguez S, et al. Increased CD38 Expression in T Cells and Circulating Anti-CD38 IgG Autoantibodies Differentially Correlate With Distinct Cytokine Profiles and Disease Activity in Systemic Lupus Erythematosus Patients. *Cytokine* (2013) 62(2):232–43. doi: 10.1016/j.cyto.2013.02.023
11. Cole S, Walsh A, Yin X, Wechalekar MD, Smith MD, Proudman SM, et al. Integrative Analysis Reveals CD38 as a Therapeutic Target for Plasma Cell-Rich Pre-Disease and Established Rheumatoid Arthritis and Systemic Lupus Erythematosus. *Arthritis Res Ther* (2018) 20(1):85. doi: 10.1186/s13075-018-1578-z
12. Ostendorf L, Burns M, Durek P, Heinz GA, Heinrich F, Garantziotis P, et al. Targeting CD38 With Daratumumab in Refractory Systemic Lupus Erythematosus. *N Engl J Med* (2020) 383(12):1149–55. doi: 10.1056/NEJMoa2023325
13. Garcia-Rodriguez S, Rosal-Vela A, Botta D, Cumba Garcia LM, Zumaquero E, Prados-Maniviesa V, et al. CD38 Promotes Pristane-Induced Chronic Inflammation and Increases Susceptibility to Experimental Lupus by an Apoptosis-Driven and TRPM2-Dependent Mechanism. *Sci Rep* (2018) 8 (1):3357. doi: 10.1038/s41598-018-21337-6
14. Burlock B, Richardson G, Garcia-Rodriguez S, Guerrero S, Zubiaur M, Sancho J. The Role of CD38 on the Function of Regulatory B Cells in a Murine Model of Lupus. *Int J Mol Sci* (2018) 19(10):2906. doi: 10.3390/ijms19102906
15. Viegas MS, Silva T, Monteiro MM, do Carmo A, Martins TC. Knocking Out of CD38 Accelerates Development of a Lupus-Like Disease in Lpr Mice. *Rheumatology* (2011) 50(9):1569–77. doi: 10.1093/rheumatology/ker178
16. Dominguez-Pantoja M, Lopez-Herrera G, Romero-Ramirez H, Santos-Argumedo L, Chavez-Rueda AK, Hernandez-Cueto A, et al. CD38 Protein Deficiency Induces Autoimmune Characteristics and its Activation Enhances IL-10 Production by Regulatory B Cells. *Scand J Immunol* (2018) 87:e12664. doi: 10.1111/sji.12664
17. Morris SC, Cheek RL, Cohen PL, Eisenberg RA. Autoantibodies in Chronic Graft *Versus* Host Result From Cognate T-B Interactions. *J Exp Med* (1990) 171(2):503–17. doi: 10.1084/jem.171.2.503
18. Klarquist J, Janssen EM. The Bm12 Inducible Model of Systemic Lupus Erythematosus (SLE) in C57BL/6 Mice. *J Vis Exp* (2015) 105):e53319. doi: 10.3791/53319
19. Klarquist J, Cantrell R, Lehn MA, Lampe K, Hennies CM, Hoebe K, et al. Type I IFN Drives Experimental Systemic Lupus Erythematosus by Distinct Mechanisms in CD4 T Cells and B Cells. *Immunohorizons* (2020) 4(3):140–52. doi: 10.4049/immunohorizons.2000005
20. Percie du Sert N, Hurst V, Ahluwalia A, Alam S, Avey MT, Baker M, et al. The ARRIVE Guidelines 2.0: Updated Guidelines for Reporting Animal Research. *PloS Biol* (2020) 18(7):e3000410. doi: 10.1371/journal.pbio.3000410
21. Morris SC, Cohen PL, Eisenberg RA. Experimental Induction of Systemic Lupus Erythematosus by Recognition of Foreign Ia. *Clin Immunol Immunopathol* (1990) 57(2):263–73. doi: 10.1016/0090-1229(90)90040-W
22. Shih W, Hines WH, Neilson EG. Effects of Cyclosporin A on the Development of Immune-Mediated Interstitial Nephritis. *Kidney Int* (1988) 33(6):1113–8. doi: 10.1038/ki.1988.119
23. Marquina R, Diez MA, Lopez-Hoyos M, Buelta L, Kuroki A, Kikuchi S, et al. Inhibition of B Cell Death Causes the Development of an IgA Nephropathy in (New Zealand White X C57BL/6)F(1)-Bcl-2 Transgenic Mice. *J Immunol* (2004) 172(11):7177–85. doi: 10.4049/jimmunol.172.11.7177
24. Lopez-Hoyos M, Carrio R, Merino R, Buelta L, Izui S, Nunez G, et al. Constitutive Expression of Bcl-2 in B Cells Causes a Lethal Form of Lupuslike Autoimmune Disease After Induction of Neonatal Tolerance to H-2b Alloantigens. *J Exp Med* (1996) 183(6):2523–31. doi: 10.1084/jem.183.6.2523
25. Zubiaur M, Izquierdo M, Terhorst C, Malavasi F, Sancho J. CD38 Ligation Results in Activation of the Raf-1/Mitogen-Activated Protein Kinase and the CD3-Zeta/Zeta-Associated Protein-70 Signaling Pathways in Jurkat T Lymphocytes. *J Immunol* (1997) 159(1):193–205.
26. Rosal-Vela A, Barroso A, Gimenez E, Garcia-Rodriguez S, Longobardo V, Postigo J, et al. Identification of Multiple Transferrin Species in the Spleen and Serum From Mice With Collagen-Induced Arthritis Which may Reflect Changes in Transferrin Glycosylation Associated With Disease Activity: The Role of CD38. *J Proteomics* (2016) 144:127–37. doi: 10.1016/j.jprot.2015.11.023
27. Ishihama Y, Oda Y, Tabata T, Sato T, Nagasu T, Rappsilber J, et al. Exponentially Modified Protein Abundance Index (emPAI) for Estimation of Absolute Protein Amount in Proteomics by the Number of Sequenced Peptides Per Protein. *Mol Cell Proteomics* (2005) 4(9):1265–72. doi: 10.1074/mcp.M500061-MCP200
28. Perez-Riverol Y, Csordas A, Bai J, Bernal-Llinares M, Hewapathirana S, Kundu DJ, et al. The PRIDE Database and Related Tools and Resources in 2019: Improving Support for Quantification Data. *Nucleic Acids Res* (2019) 47 (D1):D442–D50. doi: 10.1093/nar/gky1106
29. Bindea G, Mlecnik B, Hackl H, Charoentong P, Tosolini M, Kirilovsky A, et al. ClueGO: A Cytoscape Plug-in to Decipher Functionally Grouped Gene Ontology and Pathway Annotation Networks. *Bioinformatics* (2009) 25 (8):1091–3. doi: 10.1093/bioinformatics/btp101
30. Bindea G, Galon J, Mlecnik B. CluePedia Cytoscape Plugin: Pathway Insights Using Integrated Experimental and in Silico Data. *Bioinformatics* (2013) 29 (5):661–3. doi: 10.1093/bioinformatics/btt019
31. Shannon P, Markiel A, Ozier O, Baliga NS, Wang JT, Ramage D, et al. Cytoscape: A Software Environment for Integrated Models of Biomolecular Interaction Networks. *Genome Res* (2003) 13(11):2498–504. doi: 10.1101/gr.1239303
32. Prive F, Luu K, Blum MGB, McGrath JJ, Vilhjalmsson BJ. Efficient Toolkit Implementing Best Practices for Principal Component Analysis of Population Genetic Data. *Bioinformatics* (2020) 36(16):4449–57. doi: 10.1093/bioinformatics/btaa520
33. Kassambara AM F. *Factoextra: Extract and Visualize the Results of Multivariate Data Analyses. R Package Version 1.0.4* (2017). Available at: https://CRAN.R-project.org/package=factoextra.
34. Horikoshi M, Tang Y. *ggfortify: Data Visualization Tools for Statistical Analysis Results* (2018). Available at: https://CRAN.R-project.org/package=ggfortify.
35. Maechler M, Rousseeuw P, Struyf A, Hubert M, Hornik K. *Cluster: Cluster Analysis Basics and Extensions. R Package Version 2.1.2 — For New Features, See the 'Changelog' File (in the Package Source)* (2021). Available at: https://CRAN.R-project.org/package=cluster.
36. Eisenberg RA, Via CS. T Cells, Murine Chronic Graft-*Versus*-Host Disease and Autoimmunity. *J Autoimmun* (2012) 39(3):240–7. doi: 10.1016/j.jaut.2012.05.017
37. Kerfoot SM, Yaari G, Patel JR, Johnson KL, Gonzalez DG, Kleinstein SH, et al. Germinal Center B Cell and T Follicular Helper Cell Development Initiates in the Interfollicular Zone. *Immunity* (2011) 34(6):947–60. doi: 10.1016/j.immuni.2011.03.024

38. Baumjohann D, Preite S, Reboldi A, Ronchi F, Ansel KM, Lanzavecchia A, et al. Persistent Antigen and Germinal Center B Cells Sustain T Follicular Helper Cell Responses and Phenotype. *Immunity* (2013) 38(3):596–605. doi: 10.1016/j.immuni.2012.11.020
39. Rubtsova K, Rubtsov AV, Thurman JM, Mennona JM, Kappler JW, Marrack P. B Cells Expressing the Transcription Factor T-Bet Drive Lupus-Like Autoimmunity. *J Clin Invest* (2017) 127(4):1392–404. doi: 10.1172/JCI91250
40. Liu Y, Zhou S, Qian J, Wang Y, Yu X, Dai D, et al. T-Bet(+)CD11c(+) B Cells Are Critical for Antichromatin Immunoglobulin G Production in the Development of Lupus. *Arthritis Res Ther* (2017) 19(1):225. doi: 10.1186/s13075-017-1438-2
41. Stebegg M, Kumar SD, Silva-Cayetano A, Fonseca VR, Linterman MA, Graca L. Regulation of the Germinal Center Response. *Front Immunol* (2018) 9:2469. doi: 10.3389/fimmu.2018.02469
42. Mountz JD, Hsu HC, Ballesteros-Tato A. Dysregulation of T Follicular Helper Cells in Lupus. *J Immunol* (2019) 202(6):1649–58. doi: 10.4049/jimmunol.1801150
43. Sage PT, Sharpe AH. T Follicular Regulatory Cells in the Regulation of B Cell Responses. *Trends Immunol* (2015) 36(7):410–8. doi: 10.1016/j.it.2015.05.005
44. Sage PT, Tan CL, Freeman GJ, Haigis M, Sharpe AH. Defective TFH Cell Function and Increased TFR Cells Contribute to Defective Antibody Production in Aging. *Cell Rep* (2015) 12(2):163–71. doi: 10.1016/j.celrep.2015.06.015
45. Sage PT, Sharpe AH. T Follicular Regulatory Cells. *Immunol Rev* (2016) 271 (1):246–59. doi: 10.1111/imr.12411
46. Rissiek B, Haag F, Boyer O, Koch-Nolte F, Adriouch S. ADP-Ribosylation of P2X7: A Matter of Life and Death for Regulatory T Cells and Natural Killer T Cells. *Curr Top Microbiol Immunol* (2015) 384:107–26. doi: 10.1007/82_2014_420
47. Fliegert R, Heeren J, Koch-Nolte F, Nikolaev VO, Lohr C, Meier C, et al. Adenine Nucleotides as Paracrine Mediators and Intracellular Second Messengers in Immunity and Inflammation. *Biochem Soc Trans* (2019) 47 (1):329–37. doi: 10.1042/BST20180419
48. Schneider M, Schumacher V, Lischke T, Lucke K, Meyer-Schwesinger C, Velden J, et al. CD38 Is Expressed on Inflammatory Cells of the Intestine and Promotes Intestinal Inflammation. *PloS One* (2015) 10(5):e0126007. doi: 10.1371/journal.pone.0126007
49. Chen J, Chen YG, Reifsnyder PC, Schott WH, Lee CH, Osborne M, et al. Targeted Disruption of CD38 Accelerates Autoimmune Diabetes in NOD/Lt Mice by Enhancing Autoimmunity in an ADP-Ribosyltransferase 2-Dependent Fashion. *J Immunol* (2006) 176(8):4590–9. doi: 10.4049/jimmunol.176.8.4590
50. Postigo J, Iglesias M, Cerezo-Wallis D, Rosal-Vela A, Garcia-Rodriguez S, Zubiaur M, et al. Mice Deficient in CD38 Develop an Attenuated Form of Collagen Type II-Induced Arthritis. *PloS One* (2012) 7(3):e33534. doi: 10.1371/journal.pone.0033534PONE-D-11-24323
51. Facciotti F, Larghi P, Bosotti R, Vasco C, Gagliani N, Cordiglieri C, et al. Evidence for a Pathogenic Role of Extrafollicular, IL-10-Producing CCR6(+)B Helper T Cells in Systemic Lupus Erythematosus. *Proc Natl Acad Sci USA* (2020) 117(13):7305–16. doi: 10.1073/pnas.1917834117
52. Lee MH, Gallo PM, Hooper KM, Corradetti C, Ganea D, Caricchio R, et al. The Cytokine Network Type I IFN-IL-27-IL-10 Is Augmented in Murine and Human Lupus. *J Leukoc Biol* (2019) 106(4):967–75. doi: 10.1002/JLB.3AB0518-180RR
53. Yoshimoto T, Okada K, Morishima N, Kamiya S, Owaki T, Asakawa M, et al. Induction of IgG2a Class Switching in B Cells by IL-27. *J Immunol* (2004) 173 (4):2479–85. doi: 10.4049/jimmunol.173.4.2479
54. Chatterjee S, Daenthanasanmak A, Chakraborty P, Wyatt MW, Dhar P, Selvam SP, et al. CD38-NAD(+)Axis Regulates Immunotherapeutic Anti-Tumor T Cell Response. *Cell Metab* (2018) 27(1):85–100 e8. doi: 10.1016/j.cmet.2017.10.006
55. Chatterjee S, Chakraborty P, Mehrotra S. CD38-NAD(+)-Sirt1 Axis in T Cell Immunotherapy. *Aging (Albany NY)* (2019) 11(20):8743–4. doi: 10.18632/aging.102385
56. Morris SC, Cheek RL, Cohen PL, Eisenberg RA. Allotype-Specific Immunoregulation of Autoantibody Production by Host B Cells in Chronic Graft-*Versus* Host Disease. *J Immunol* (1990) 144(3):916–22.
57. Sivakumar R, Abboud G, Mathews CE, Atkinson MA, Morel L. Protective Role of Myeloid Cells Expressing a G-CSF Receptor Polymorphism in an Induced Model of Lupus. *Front Immunol* (2018) 9:1053. doi: 10.3389/fimmu.2018.01053
58. Chen L, Diao L, Yang Y, Yi X, Rodriguez BL, Li Y, et al. CD38-Mediated Immunosuppression as a Mechanism of Tumor Cell Escape From PD-1/PD-L1 Blockade. *Cancer Discov* (2018) 8(9):1156–75. doi: 10.1158/2159-8290.CD-17-1033
59. Ridderstad A, Tarlinton DM. Kinetics of Establishing the Memory B Cell Population as Revealed by CD38 Expression. *J Immunol* (1998) 160(10):4688–95.
60. Kato K, Santana-Sahagun E, Rassenti LZ, Weisman MH, Tamura N, Kobayashi S, et al. The Soluble CD40 Ligand sCD154 in Systemic Lupus Erythematosus. *J Clin Invest* (1999) 104(7):947–55. doi: 10.1172/JCI7014
61. Vakkalanka RK, Woo C, Kirou KA, Koshy M, Berger D, Crow MK. Elevated Levels and Functional Capacity of Soluble CD40 Ligand in Systemic Lupus Erythematosus Sera. *Arthritis Rheum* (1999) 42(5):871–81. doi: 10.1002/1529-0131(199905)42:5<871::AID-ANR5>3.0.CO;2-J
62. Thibault DL, Graham KL, Lee LY, Balboni I, Hertzog PJ, Utz PJ. Type I Interferon Receptor Controls B-Cell Expression of Nucleic Acid-Sensing Toll-Like Receptors and Autoantibody Production in a Murine Model of Lupus. *Arthritis Res Ther* (2009) 11(4):R112. doi: 10.1186/ar2771
63. Thibault DL, Chu AD, Graham KL, Balboni I, Lee LY, Kohlmoos C, et al. IRF9 and STAT1 Are Required for IgG Autoantibody Production and B Cell Expression of TLR7 in Mice. *J Clin Invest* (2008) 118(4):1417–26. doi: 10.1172/JCI30065
64. Jenks SA, Cashman KS, Zumaquero E, Marigorta UM, Patel AV, Wang X, et al. Distinct Effector B Cells Induced by Unregulated Toll-Like Receptor 7 Contribute to Pathogenic Responses in Systemic Lupus Erythematosus. *Immunity* (2018) 49(4):725–39 e6. doi: 10.1016/j.immuni.2018.08.015
65. Zumaquero E, Stone SL, Scharer CD, Jenks SA, Nellore A, Mousseau B, et al. IFNgamma Induces Epigenetic Programming of Human T-Bet(Hi) B Cells and Promotes TLR7/8 and IL-21 Induced Differentiation. *Elife* (2019) 8: e41641. doi: 10.7554/eLife.41641
66. Myles A, Sanz I, Cancro MP. T-Bet(+) B Cells: A Common Denominator in Protective and Autoreactive Antibody Responses? *Curr Opin Immunol* (2019) 57:40–5. doi: 10.1016/j.coi.2019.01.002
67. Russell Knode LM, Naradikian MS, Myles A, Scholz JL, Hao Y, Liu D, et al. Age-Associated B Cells Express a Diverse Repertoire of VH and Vkappa Genes With Somatic Hypermutation. *J Immunol* (2017) 198(5):1921–7. doi: 10.4049/jimmunol.1601106
68. Zhang W, Zhang H, Liu S, Xia F, Kang Z, Zhang Y, et al. Excessive CD11c(+) Tbet(+) B Cells Promote Aberrant TFH Differentiation and Affinity-Based Germinal Center Selection in Lupus. *Proc Natl Acad Sci USA* (2019) 116 (37):18550–60. doi: 10.1073/pnas.1901340116
69. Zumaquero E, Munoz P, Cobo M, Lucena G, Pavon EJ, Martin A, et al. Exosomes From Human Lymphoblastoid B Cells Express Enzymatically Active CD38 That Is Associated With Signaling Complexes Containing CD81, Hsc-70 and Lyn. *Exp Cell Res* (2010) 316(16):2692–706. doi: 10.1016/j.yexcr.2010.05.032

Conflict of Interest: The authors declare that the research was conducted in the absence of any commercial or financial relationships that could be construed as a potential conflict of interest.

frontiers in Immunology

ORIGINAL RESEARCH
published: 03 September 2021
doi: 10.3389/fimmu.2021.703574

Mouse CD38-Specific Heavy Chain Antibodies Inhibit CD38 GDPR-Cyclase Activity and Mediate Cytotoxicity Against Tumor Cells

Natalie Baum[1†], Marie Eggers[1†], Julia Koenigsdorf[1,2], Stephan Menzel[1,3], Julia Hambach[1,2], Tobias Staehler[1], Ralf Fliegert[4], Frederike Kulow[4], Gerhard Adam[2], Friedrich Haag[1], Peter Bannas[2*‡] and Friedrich Koch-Nolte[1*‡]

[1] Institute of Immunology, University Medical Center Hamburg-Eppendorf, Hamburg, Germany, [2] Department of Radiology, University Medical Center Hamburg-Eppendorf, Hamburg, Germany, [3] Mildred Scheel Cancer Career Center HaTriCS4, University Medical Center Hamburg-Eppendorf, Hamburg, Germany, [4] Department of Biochemistry and Molecular Cell Biology, University Medical Center Hamburg-Eppendorf, Hamburg, Germany

CD38 is the major NAD$^+$-hydrolyzing ecto-enzyme in most mammals. As a type II transmembrane protein, CD38 is also a promising target for the immunotherapy of multiple myeloma (MM). Nanobodies are single immunoglobulin variable domains from heavy chain antibodies that naturally occur in camelids. Using phage display technology, we isolated 13 mouse CD38-specific nanobodies from immunized llamas and produced these as recombinant chimeric mouse IgG2a heavy chain antibodies (hcAbs). Sequence analysis assigned these hcAbs to five distinct families that bind to three non-overlapping epitopes of CD38. Members of families 4 and 5 inhibit the GDPR-cyclase activity of CD38. Members of families 2, 4 and 5 effectively induce complement-dependent cytotoxicity against CD38-expressing tumor cell lines, while all families effectively induce antibody dependent cellular cytotoxicity. Our hcAbs present unique tools to assess cytotoxicity mechanisms of CD38-specific hcAbs *in vivo* against tumor cells and potential off-target effects on normal cells expressing CD38 in syngeneic mouse tumor models, i.e. in a fully immunocompetent background.

Keywords: CD38, NAD$^+$, antibody-dependent cellular cytotoxicity, complement-dependent cytotoxicity, multiple myeloma, nanobody, heavy chain antibody, antibody engineering

Edited by:
Santina Bruzzone,
University of Genoa, Italy

Reviewed by:
Michele Cea,
University of Genoa, Italy
Yongjuan Zhao,
The Chinese University of Hong Kong,
Shenzhen, China

***Correspondence:**
Friedrich Koch-Nolte
nolte@uke.de
Peter Bannas
p.bannas@uke.de

†These authors share first authorship

‡These authors share senior authorship

Specialty section:
This article was submitted to Cytokines and Soluble Mediators in Immunity, a section of the journal Frontiers in Immunology

Received: *30 April 2021*
Accepted: *04 August 2021*
Published: *03 September 2021*

Citation:
Baum N, Eggers M, Koenigsdorf J, Menzel S, Hambach J, Staehler T, Fliegert R, Kulow F, Adam G, Haag F, Bannas P and Koch-Nolte F (2021) Mouse CD38-Specific Heavy Chain Antibodies Inhibit CD38 GDPR-Cyclase Activity and Mediate Cytotoxicity Against Tumor Cells. Front. Immunol. 12:703574. doi: 10.3389/fimmu.2021.703574

Abbreviations: ADCC, antibody dependent cellular cytotoxicity; CDC, complement-dependent cytotoxicity; CDR, complementarity determining region; Fc, crystallizing fragment; hcAb, heavy chain antibody, Ig immunoglobulin; kDa, kilodalton; MM, multiple myeloma; NAD$^+$, nicotinamide adenine dinucleotide; mAb, monoclonal antibody; Nb, nanobody; VHH, variable domain of a camelid heavy chain antibody.

INTRODUCTION

NAD$^+$ is released as an endogenous danger signal from cells during inflammation (1, 2). CD38, a 43 kDa type II transmembrane protein consisting of a short intracellular N-terminal domain, a transmembrane helix and a long C-terminal extracellular catalytic domain, is the major NAD$^+$-hydrolyzing ecto-enzyme of mammals (3–6). NAD$^+$-hydrolysis by CD38 limits the availability of NAD$^+$ for extracellular-ADP-ribosyltransferases (7, 8), and generates the Ca^{2+} -mobilizing metabolites ADP-ribose and cyclic ADP-ribose (9) that can be further hydrolyzed to immunosuppressive adenosine by other ecto-enzymes (10). CD38 is highly expressed in hematological malignancies including multiple myeloma (11, 12). It has been proposed that the enzymatic activity of CD38 contributes to a microenvironment favourable for tumor survival in the bone marrow niche (13, 14).

CD38 represents a promising target for monoclonal antibody (mAb)-based immunotherapy of multiple myeloma (MM) (11, 15, 16). Several CD38-specific mAbs, including daratumumab and isatuximab, have shown encouraging results in the clinic (17–20). The anti-tumor effects of these mAbs presumably reflect their ability to induce immune effector functions, such as antibody-dependent cellular cytotoxicity (ADCC) and complement-dependent cytotoxicity (CDC) (21). However, these antibodies may also induce the depletion of CD38-expressing NK cells and may have other off-target effects on normal cells expressing CD38 (22, 23). Moreover, the use of mAbs has disadvantages that include limited tissue penetration due to their large size of approximately 150 kD (24, 25).

Nanobodies are recombinant, single antigen-binding immunoglobulin variable domains (designated VHH) derived from naturally occurring camelid heavy chain antibodies (hcAbs) (26, 27). Nanobodies have several advantages over conventional antibodies, including a 10-fold smaller size (15 kDa *vs.* 150 kDa) (28, 29). To endow immune-effector functions, nanobodies can be fused to the hinge, CH2, and CH3 domains of a conventional mouse or human IgG antibody to generate nanobody-based chimeric hcAbs (30). These chimeric hcAbs lack the CH1 domain and the light chain, resulting in approximately half the molecular size of a conventional antibody (75 kDa *vs.* 150 kDa) (30).

Both, nanobodies and hcAbs are emerging as promising theranostic molecules (31–34). For example, we have recently shown that human CD38-specific hcAbs can be used to effectively target human MM cells in xenograft mouse models of systemic human lymphoma (35). Lack of reactivity with mouse CD38, however, makes it difficult to understand and assess potential off-target effects of such therapeutic antibodies on immune cells that endogenously express CD38. Substituting three amino acid residues in the CH2 domain of mouse IgG2a or human IgG1 (L234A, L235A, P329G) eliminates complement dependent cytotoxicity (CDC) as well as CD16-mediated antibody dependent cellular toxicity (ADCC) (36). These so-called LALA-PG mutants retain the thermostability and pharmacokinetics of the parental IgG (36).

We aimed to develop mouse CD38-specific nanobodies and hcAbs, to assess their binding epitopes, and to evaluate their capacity to induce cytotoxicity against tumor cells expressing CD38 *in vitro* as a basis for future *in vivo* studies of syngeneic MM models in immunocompetent mice.

METHODS

Mice and Cells

BALB/c and C57BL/6 mice were obtained from The Jackson Laboratory or Charles River. *Cd38*$^{-/-}$ mice (3) were back-crossed onto the BALB/c and C57BL/6 backgrounds for 8 –12 generations. The mouse EL4 (C57BL76N lymphoma, ATCC TIB-39) and MOPC 315 (BALB/C myeloma, ATCC TIB-23) cell lines were obtained from the American Type Culture Collection. EL4 and MOPC 315 cells were cultured in RPMI-1640 medium (Gibco, Life Technologies, Paisley, UK) supplemented with 2 mM sodium pyruvate (Gibco), 2 mM L-glutamine (Gibco) and 10% (v/v) fetal calf serum (Gibco). Human HEK cells (ATCC CRL-1573) were transiently co-transfected with expression vectors for nuclear GFP and mouse CD38 (gene ID: 12494) or human CD38 (gene ID: 952) (37). The human NK-92 cell line (ACC 488) was obtained from the DSMZ German Collection of Microorganisms and Cell Cultures. NK-92 cells were stably transduced with mouse CD16 by retroviral transduction using the pSF91 retroviral vector (35). The sequence for CD16, i.e. the ectodomain of FcγRIII fused to the transmembrane and cytosolic domains of FcϵRI, was kindly provided by B. Clémenceau (Nantes, France). NK-92 cells were cultured in alpha MEM culture medium (Gibco) supplemented with 10% FCS (Gibco), 10% horse serum (Gibco), 100 IU/mL IL2 (Proleukin, Novartis) and 2 mM L-glutamine (Gibco). Primary spleen cells were obtained from wild type and *Cd38*$^{-/-}$ mice by passing spleen cell suspensions through a 70 µm cell strainer.

Selection and Sequencing of Mouse CD38-Specific Nanobodies

Two llamas were immunized subcutaneously by ballistic cDNA immunization with an expression vector encoding the full-length open reading frame of mouse CD38. The VHH repertoire was PCR-amplified from peripheral blood lymphocytes and cloned into the pHEN2 phagemid vector as described previously (37). Selection of specific phages was performed by sequential panning of the phage library on primary splenocytes obtained from *Cd38*$^{-/-}$ and WT mice. Following extensive washing, bound phages were eluted by trypsinization. Plasmid DNA was isolated from single colonies and subjected to sequence analyses using pHEN2-specific forward and reverse primers (37).

The coding region of selected nanobodies was subcloned using NcoI/PciI and NotI into the pCSE2.5 vector (38) (kindly provided by Thomas Schirrmann, Braunschweig, Germany) upstream of either a chimeric His6x-Myc epitope tag, the coding region for the hinge and Fc domains of mouse IgG2a, or the corresponding coding region for the LALA-PG mutant (36) of mouse IgG2a (gene ID: 404711). Recombinant myc-his tagged nanobodies and chimeric nanobody-mouse IgG2c heavy chain antibodies were produced in transiently transfected HEK-6E cells (39) (kindly provided by Ives Durocher, Ottowa, Canada) cultivated in serum-free medium. Six days post transfection, supernatants were harvested and cleared by centrifugation at 4000 rpm for 10 min. Nanobodies in cell supernatants were quantified by SDS-PAGE and Coomassie staining relative to marker proteins of known quantity as described previously (37). Yields typically ranged from 0.5–3 µg Nb or hcAb per 10 µl of HEK-6E cell supernatant. Myc-His tagged nanobodies were purified by immobilized metal affinity chromatography using Ni-NTA agarose (Sigma, St Louis, MO), hcAbs by affinity chromatography on protein A immobilized on sepharose beads (GE Healthcare) (37).

Biolayer Interferometry

The extracellular domain of mouse CD38 (aa 45–304) with intact glycosylation sites was produced as a secretory protein with a chimeric His6x-Myc epitope tag in the pCSE2.5 vector. The tagged protein was purified using immobilized metal affinity chromatography (IMAC). Affinity of hcAbs to recombinant mouse CD38 was determined by BLI-technology using a fortéBIO BLItz instrument. Assays were performed at 20°C with running buffer (PBS, 0.01% (m/v) BSA, 0.002% (v/v) Tween-20). Protein A sensors were hydrated in running buffer and loaded until saturation with hcAbs at 10 µg/ml. After washing, purified mouse CD38 (1.8 µM) was allowed to associate for 120 seconds on immobilized hcAbs, followed by dissociation for 120 seconds. Respective binding curves were referenced against antibody-loaded sensors receiving only buffer for association and dissociation steps. Curve fitting and affinity calculations were performed using Graph Pad Prism (version 7) using non-linear regression and the build-in "association then dissociation" method.

Flow Cytometry

Purified hcAbs were conjugated *via* amino groups to Alexa Fluor^{647}-fluorochrome according to the manufacturer's instructions (Molecular Probes, Thermo Fisher Scientific). For epitope mapping analyses, EL4 cells were pre-incubated with a saturating concentration (100 nM) of unconjugated hcAbs for 30 min at 4°C, followed by addition of Alexa Fluor^{647}-conjugated hcAbs (10 nM) and further incubation for 20 min at 4°C. Cells were washed and analyzed by flow cytometry on a BD-FACS Canto. Data was analyzed using the FlowJo software (Treestar). The percentage of cross-blockade was calculated from mean fluorescence intensities (MFI) as follows: (MFI in the absence of competing Abs – MFI in the presence of competing Abs): (MFI in the presence of competing Abs) x 100. Spleen cells were pre-incubated with Fc-block (BioXcell, clone 2.4G2) to minimize unspecific binding to Fc-receptors. Cells were then incubated with Alexa Fluor^{647}-conjugated hcAbs, FITC-conjugated anti-B220 (BD biosciences, clone RA3-6B2), and Alexa Fluor 750 as a viability dye (ThermoFischer). Gating was performed on Alexa Fluor 750-low cells (live cells).

Fluorometric Enzyme Assays

EL4 cells (3×10^5 cells/well) were incubated at 37°C in the dark for 20 min with hcAbs (10 or 100 µg/ml) or araF-NAD (10 µM) before fluorescence measurements. After recording for 20 cycles, NGD$^+$ (80 µM, Sigma, St Louis, MO) was added, followed by further incubation in the dark at 37°C. Production of cGDPR was monitored continuously for 50 min at 410 nm (emission wavelength) with the excitation wavelength set to 300 nm, using a Tecan Infinite M 200 microplate fluorimeter (37). Readings (EX300/EM410) from wells without cells were subtracted from all sample readings and values were plotted as Relative Fluorescence Units (RFU) *vs.* time. The rate of cGDPR production was calculated as the slope of the curves (RFU/s) during the linear phase of the reaction, i.e. t = 500-1200 s.

CDC and ADCC Assays

To analyze the complement-dependent cytotoxicity (CDC) mediated by hcAbs, EL4 or MOPC 315 cells were incubated for 10 min at 4°C with hcAbs before addition of guinea pig serum (25% v/v) as a source of complement. Cells were incubated for 120 minutes at 37°C, washed and resuspended in PBS/0.2% BSA/ propidium iodide before analysis by flow cytometry (35).

To analyze antibody dependent cellular cytotoxicity (ADCC) mediated by NK-92 cells, EL4 or MOPC 315 cells were incubated for 10 min at 4°C with hcAbs before addition of NK92 cells. In order to distinguish NK92 effector cells from target cells, NK92 cells were prelabelled with eFluor 450 (ThermoFisher) for 20 min at 4°C and washed three times before addition of hcAb-treated target cells at an effector to target ratio [E:T] of 3:1. Cells were co-incubated for 3 hours at 37°C, washed, and resuspended in PBS/ 0.2% BSA/propidium iodide before flow cytometry (35). In order to quantify cytotoxicity against target cells, gating was performed on eFluor 450-negative cells. Dead target cells were quantified using uptake of propidium iodide (PI) and decrease in forward scatter (FCS) as indicators of cell lysis. As negative controls, hcAbs carrying the ADCC and CDC abrogating LALA-PG mutations (36) were used.

Statistical Analysis

Data were analyzed using GraphPad Prism version 7.00 (GraphPad Software). For enzyme inhibition assays, statistical significance was calculated using one-way ANOVA followed by a Bonferroni *post hoc* test for multiple comparisons. with $P< 0.05$ (*), $P < 0.01$ (**), $P < 0.001$ (***), $P < 0.0001$ (****). Data for CDC and ADCC assays in bar diagrams represent the mean ± SD from three independent experiments.

RESULTS

Phage Display Selection Yields Five Families of Mouse CD38-Specific Nanobodies

We cloned the VHH-repertoire from blood lymphocytes of two llamas immunized (40) with a mouse CD38-encoding cDNA expression vector into M13 phage display libraries. Selection of CD38-specific phages was achieved by first panning the libraries on cells lacking CD38, i.e. splenocytes from CD38-deficient mice and YAC-1 lymphoma cells to remove unspecific binders. Libraries were then panned on cells expressing high levels of

CD38, i.e. splenocytes from WT mice and EL4 thymoma cells. Sequencing of selected clones revealed 13 distinct clones (JK3, JK5, JK13, JK16, NB3, NB7, NB11, NB22, NB24, NB28, NB32, NB38, NB40 and NB42) that can be subgrouped into five distinct nanobody families based on sequence similarities in the framework and complementarity determining regions, with CDR3 lengths ranging from three to 13 amino acid residues (**Table 1**).

In order to generate nanobody-based mouse heavy chain antibodies (hcAbs), the VHH-coding region was fused to the hinge, CH2 and CH3 domains of mouse IgG2a. These hcAbs were produced as secreted recombinant proteins in transiently transfected HEK cells grown in serum-free medium. Affinities of the hcAbs were determined by biolayer interferometry using the recombinant ecto-domain of mouse CD38 (**Table 1**). The results reveal moderate affinities in the two and three digit nanomolar range; family 1 nanobodies had the lowest affinities (> 400 nM), family 5 nanobodies the highest affinities (19-33 nM). In order to verify the specificity of the selected antibodies, we performed flow cytometry analyses of HEK cells co-transfected with GFP and either mouse CD38 or human CD38 (**Figure 1A**). The results show specific binding of the selected hcAbs to mouse CD38 but not to human CD38. Flow cytometry analyses of splenocytes obtained from wild type and from CD38-deficient mice confirmed the specific binding of all hcAbs to native mouse CD38 (**Figure 1B**).

Cross Blockade Analyses Reveal Binding of Nanobody-Based hcAbs to Three Non-Overlapping Epitopes of Mouse CD38

Next, we aimed to assess whether the identified anti-mouse CD38-specific hcAbs recognize overlapping or distinct epitopes on mouse CD38. To this end, we performed cross blockade flow cytometry analyses. We monitored the binding of Alexa Fluor^{647}-conjugated hcAbs (JK3-hcAb, JK5-hcAb, JK13-hcAb, JK16-hcAb) to EL4 thymoma cells in the presence of excess unlabelled hcAbs (**Table 2**). The results show that the selected hcAbs fall into three distinct binding groups. Group 1 hcAbs block binding of hcAbs derived from nanobodies JK3 and NB11 (both family 1). These nanobodies recognize an overlapping epitope designated *epitope 1*. Group 2 hcAbs block binding of hcAbs derived from nanobodies JK5 (family 2) and NB32 (family 3). These nanobodies recognize an overlapping epitope designated *epitope 2*. Group 3 hcAbs block binding of hcAbs derived from nanobodies JK13, JK16, NB3, NB7, NB22, NB24 (family 4) and NB38, NB40, and NB42 (family 5). These nanobodies recognize an overlapping epitope designated *epitope 3*. Remarkably NB32-hcAb (epitope 2), which has the shortest CDR3, seemed to enhance binding of hcAbs that bind to the epitope 1 (JK3-hcAb) and epitope 3 (JK13-hcAb, JK16-hcAb). Note that JK13-hcAb and JK16-hcAb (both epitope 3) blocked binding of JK3-hcAb (epitope 1), suggesting that these hcAbs either sterically interfere with binding of JK3-hcAb or alter the conformation of mouse CD38 so as to inhibit binding of JK3-hcAb.

TABLE 1 | Characteristics of mouse CD38-specific nanobodies.

Clone	Family	FR2	CDR3	length	K$_D$ (nM)
JK3	1	QREL	YIVPYGTGSAYTV	13	> 500
NB11	1	QREL	YIVPYGTGSAYTS	13	423
JK5	2	EREF	DLFDRLVIPREST	13	102
NB32	3	QREV	LNY	3	147
NB7	4	EREF	WPPRSASWDDYDY	13	93
NB22	4	EREF	WPPRSASWDDYDY	13	59
JK16	4	EREF	WPQRSASWDDFDY	13	60
JK13	4	EREF	WPPRAASWDDYDY	13	113
NB3	4	EREF	WPPRAASWDEYDY	13	251
NB24	4	EREF	WPPRAANWDEYDY	13	75
NB40	5	QREL	DVVDDRGLGFDDY	13	19
NB42	5	QREL	DVVDDRGLGFDDY	13	32
NB38	5	QREL	DVVDSRGLGFDDY	13	33

Families were designated according to highly similar CDR3 and shared framework sequences. Variant amino acid positions in the CDR3 within a family are highlighted in grey. Affinities (K$_D$) of nanobodies for the recombinant ecto-domain of CD38 were determined by biolayer interferometry.

Nanobody-Based hcAbs of Families 4 and 5 Inhibit the GDPR Cyclase Activity of Mouse CD38

To analyze the potential functional effects of the selected hcAbs on the enzyme activity of mouse CD38 on cells, we employed a fluorometric GDPR cyclase assay (37, 41–43). This assay uses NGD$^+$ (which carries a guanine nucleobase instead of adenine) instead of NAD$^+$ as substrate. We incubated CD38-positive EL4 cells with either CD38-specific hcAbs for 15 min before addition of NGD$^+$ and monitored the increased fluorescence of the product cGDPR by fluorimetry (44) (**Figure 2**). The results showed a continuous increase of cGDPR during incubation of EL4 cells with NGD$^+$ in the absence of antibodies. As a control, we used the NAD$^+$-analogue nicotinamide 2-deoxy-2-fluoroarabinoside adenine dinucleotide (araF-NAD$^+$), a highly specific inhibitor of mouse CD38 (7, 45). Addition of araF-NAD$^+$ effectively abrogated the increase of cGDPR, indicating that the increased fluorescence is largely due to CD38 on the surface of EL4 cells. Addition of hcAb from family 1 (JK3-hcAb), family 2 (JK5-hcAb), and family 3 (NB32-hcAb) had little if any effect on the enzyme activity of EL4 cells (**Figures 2A–C**). Addition of family 4 hcAbs (hcAbs NB3, NB7, NB22, NB24) showed significant, but varying levels of enzyme inhibition (**Figure 2D**). The most potent inhibitory effect of the GDPR cyclase activity was observed for all tested hcAbs from family 5 (hcAbs NB38, NB40, NB42) (**Figure 2E**). **Figure 2F** allows for direct visual comparison of the inhibitory effects of all tested hcAbs and demonstrates the dose dependency of the hcAbs used.

All CD38-Specific hcAbs Mediate Effective ADCC

To analyze the capacity of mouse CD38-specific hcAbs to induce ADCC, EL4 thymoma cells or MOPC 315 myeloma cells were used as target cells and NK-92 cells stably transfected with mouse Fc-receptor III (CD16) were used as effector cells. Flow cytometry analyses confirmed high expression of CD38 by EL4 and MOPC 315 cells (**Figures 3 A, B**, panel 1), while human NK-92 cells were negative for mouse CD38 (not shown). To monitor

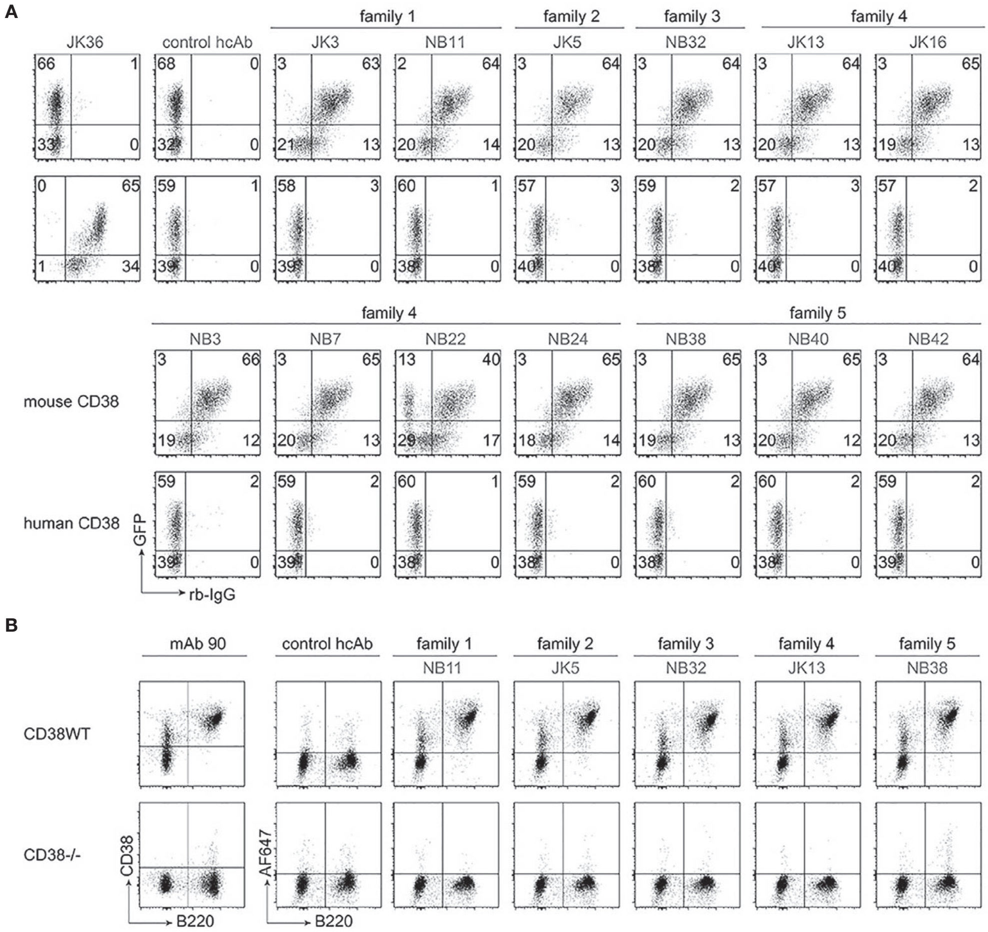

FIGURE 1 | Selected heavy chain antibodies specifically recognize mouse CD38. **(A)** HEK cells were transiently co-transfected with expression constructs for GFP and either mouse CD38 (top rows) or human CD38 (bottom rows). Twenty-four hours after transfection, cells were incubated sequentially with selected nanobody-rabbit IgG hcAbs and APC-conjugated anti-rabbit IgG. Control stainings were performed with an isotype control hcAb and with human CD38-specific JK36-hcAb. Numbers indicate the percentage of cells in the respective quadrants. Data are representative of two independent experiments. **(B)** Splenocytes from wildtype (WT) and *Cd38*$^{-/-}$ mice were incubated with Alexa Fluor ^{647}-conjugated hcAbs, a FITC-conjugated B220-specific mAb, and Alexa Fluor 750 as vitality dye. Control stainings were performed with an isotype control hcAb and a conventional mouse CD38-specific mAb (clone 90). Gating was performed on live (Alexa Fluor 750-low) cells. Data are representative of two independent experiments.

ADCC, EL4 and MOPC 315 cells were incubated with eFluor 450-labelled NK92 cells in the absence or presence of Nb-based mouse IgG2a hcAbs. To evaluate cell death, we monitored uptake of propidium iodide and decrease in forward scatter by flow cytometry (**Figures 3 A, B**, panels 2–4). The results show that all analyzed hcAbs mediated effective killing of EL4 and MOPC 315 target cells. In contrast, only background levels of cell death were observed in the presence of mouse IgG2a hcAbs carrying the three LALA-PG mutations that abrogate binding to Fc-receptors (36).

CD38-Specific hcAbs of Families 2, 4, and 5 Mediate CDC

To analyze the potential of hcAbs to induce CDC, we incubated EL4 and MOPC 315 cells with saturating amounts of mouse IgG2a hcAbs and guinea pig serum as a source of complement. As indicators of cell lysis, we monitored permeabilization of cells to the DNA-staining dye propidium iodide and decrease in forward scatter using flow cytometry (**Figure 4**). The results show that hcAbs JK5, JK13, and NB38 from families 2, 4 and 5 mediate effective CDC of EL4 and MOPC 315 target cells. In contrast, only background levels of cell death were observed when incubations were performed in the presence of the LALA-PG mutants of the corresponding hcAbs that abrogate binding of complement factor C1q (36).

DISCUSSION

From immunized llamas, we selected 13 mouse CD38-specific hcAbs that derive from five nanobody families, each of which carries a common framework region and a highly similar CDR3.

TABLE 2 | Epitope mapping of nanobody-based mouse CD38-specific hcAbs.

ep	Fam	Nb	JK3^{647}	JK5^{647}	JK13^{647}	JK16^{647}
1	1	JK3	98	17	27	18
1	1	NB11	74	5	17	29
2	2	JK5	29	97	33	5
2	3	NB32	-58	82	-22	-8
3	4	JK13	55	-5	99	100
3	4	JK16	79	25	95	98
3	4	NB3	-19	4	72	78
3	4	NB7	-22	0	71	82
3	4	NB22	-5	3	66	65
3	4	NB24	-27	0	75	79
3	5	NB38	6	15	79	83
3	5	NB40	0	14	75	77
3	5	NB42	12	13	76	75

EL4 thymoma cells were incubated for 30 min at 4 °C with unconjugated hcAbs (indicated on the left) before addition of Alexa Fluor^{647}-conjugated hcAbs (indicated on top). Cells were further incubated for 30 min at 4 °C, washed twice and analyzed by flow cytometry. Numbers indicate the percentage maximal blockade of the mean fluorescence intensity of cells labelled in the presence of competing hcAbs. Negative numbers indicate enhanced labelling of cells in the presence of the competing hcAbs. Efficiency of inhibition is indicated by different shades of grey (dark grey: > 80% inhibition, light grey: 50–80% inhibition). Self-blockade by the nanobody used for labelling is indicated by highlighted boxes in the diagonal. HcAbs that blocked binding of each other were assigned to the same epitope.

These hcAbs bind specifically to three distinct epitopes of murine CD38.

All epitope 3-directed hcAbs (i.e., families 4 and 5) inhibited the GDPR-cyclase activity in a dose dependent fashion. In contrast, hcAbs of families 1, 2 and 3 had little if any effect on the GDPR-cyclase activity. This NGD$^+$-based assay is commonly used to assess the effect of antibodies on CD38 enzyme activity (37, 43, 46). A limitation of this assay is that it only allows an estimate of the allosteric inhibitory effect of antibodies on the GDPR-cyclase, but not necessarily on the ADPR-cyclase or NAD-glycohydrolase activities of CD38. It is possible that nanobodies might affect cyclase and NADase activities differentially. Indeed, in a recent study we found that both, daratumumab and human CD38-specific hcAb 1067, inhibited the GDPR-cyclase and ADPR-cyclase activities of human CD38 (47), while neither daratumumab nor hcAb 1067 had any detectable effect on the NADase activity of CD38. It has been proposed that CD38 contributes to shaping an immunosuppressive tumor microenvironment (TME) by fuelling the conversion of NAD$^+$ to immunosuppressive adenosine (14, 48–50). Since inhibition of the NADase activity of CD38 is more relevant in this context than inhibition of its cyclase activities, there remains a need for better CD38-inhibitory antibodies.

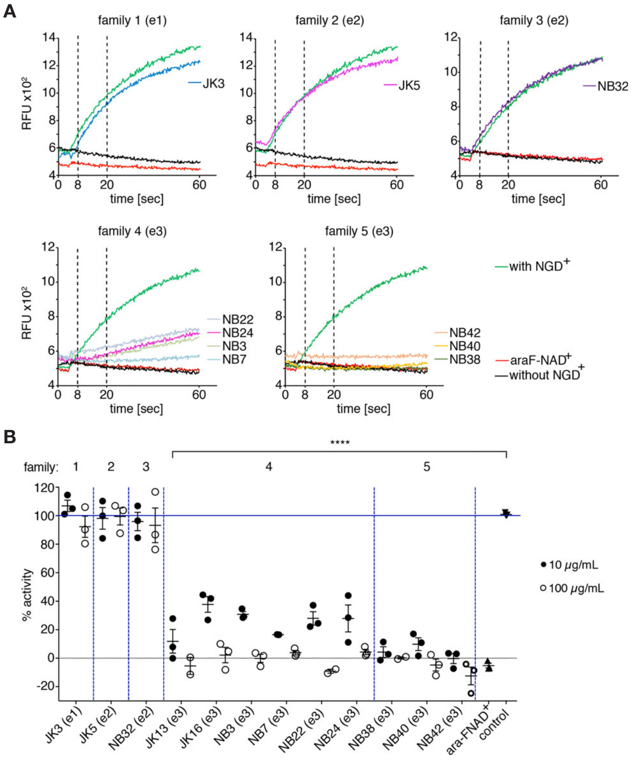

FIGURE 2 | hcAbs of families 4 and 5 inhibit the GDPR-cyclase activity of mouse CD38. EL4 thymoma cells were incubated with the indicated hcAbs or 10 µM araF-NAD$^+$ for 15 min at 37°C before fluorescence measurements with a microplate reader. After the first 20 cycles, 50 µM NGD$^+$ was added and kinetic fluorescence reading (ex/em: 300/410 nm) was continued for 60 min. **(A)** Representative fluorimetry plots for cells incubated with the indicated hcAbs. Controls included cells incubated with (green) or without (black) NGD$^+$, and cells incubated with NGD$^+$ and araF-NAD$^+$ (red). Vertical dotted lines at 8 and 20 min depict the time points used for calculation of slopes depicted in **(B)**. **(B)** Each dot indicates the slope of the curve during the linear phase (t = 8-20 min), relative to the slope of the curve obtained from control cells incubated with NGD$^+$ alone (n = 3). Statistical significance was calculated using one-way ANOVA followed by a Bonferroni *post hoc* test for multiple comparisons. ****p < 0.0001. Data are representative of three independent experiments.

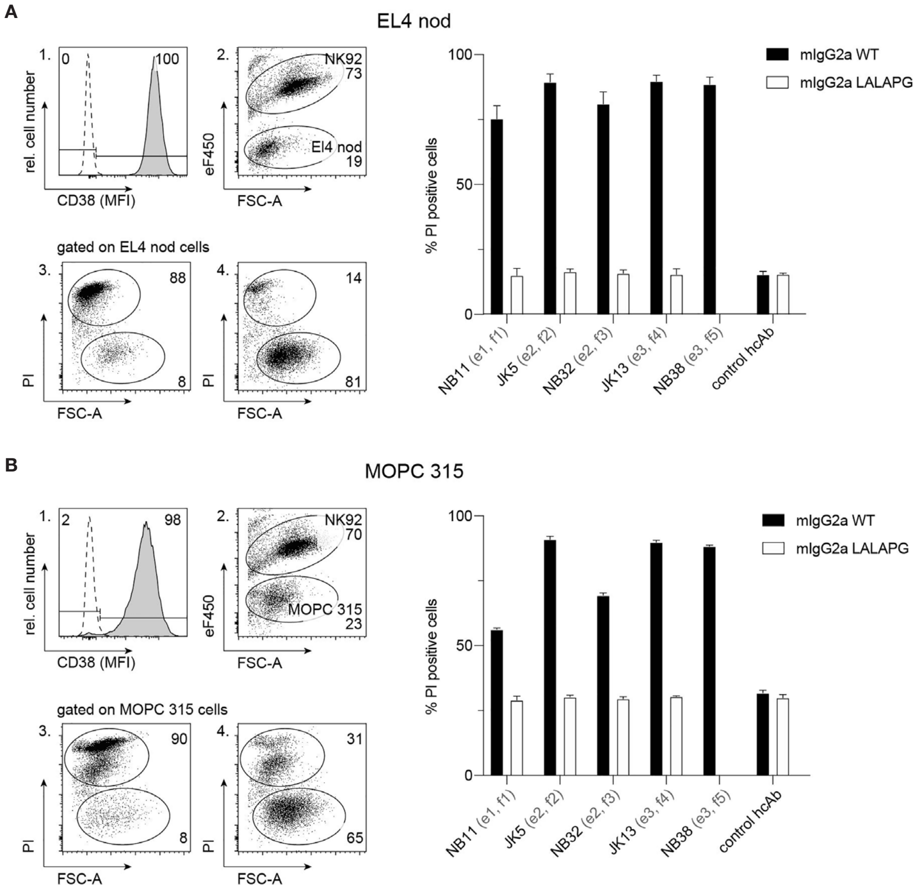

FIGURE 3 | hcAbs of all five families effectively induce antibody-dependent cellular cytotoxicity against CD38-expressing thymoma and myeloma cell lines. Cell surface expression of CD38 by EL4 thymoma **(A)** and MOPC 315 myeloma **(B)** cells was assessed by flow cytometry using a fluorochrome-conjugated mouse CD38-specific mAb and an isotype control (open histogram) (panel 1). To assess the capacity of hcAbs to induce ADCC, EL4 cells **(A)** or MOPC 315 cells **(B)** were co-cultured with eFluor 450-labelled NK-92 cells for 3h at 37°C at an effector to target ratio of 3:1 in the presence of CD38-specific mouse IgG2a hcAbs from all five nanobody families. As controls, we used the same mouse IgG2a hcAbs carrying the LALA-PG mutation that abrogate FcR-binding and a non-binding control hcAb. Cells were then incubated with propidium iodide (PI) and analyzed by flow cytometry. Representative dot plots illustrate the clear separation of eFluor 450-postive effector cells and eFluor 450-negative target cells (panel 2). To assess cytotoxicity against target cells, gating was performed on eFluor 450-negative cells (panels 3, 4). Representative dot plots in panels 3 and 4 illustrate the clear distinction of dead target cells (PI-positive, low forward scatter/FSC-A) from live target cells (PI-negative, FSC^{high}). Panel 3 shows the results of cells incubated with JK5 hcAb, panel 4 shows the results of cells incubated with the isotype control hcAb. Numbers in panels 2-4 indicate the percentage of cells in the indicated gated populations. Epitopes and nanobody families are indicated in parentheses behind the nanobody names. Data in bar diagrams represent mean ± SD from three independent experiments.

The CD38-specific hcAbs from all five families, irrespective of their binding epitopes induced potent ADCC of murine cell lines. This in line with the results of our previous studies showing that human CD38-specific nanobody-based hcAbs potently induced ADCC of several human lymphoma and myeloma cell lines, including LP-1 myeloma, CA-46 and Daudi Burkitt lymphoma (35, 51).

Members of hcAbs families 2, 4 and 5, but not of families 1 and 3 also mediated CDC. These findings differ from those of our previous studies with hcAbs directed against human CD38, in which we found that the 22 nanobody-based hcAbs directed against 3 different epitopes of human CD38 showed little if any capacity to induce CDC against different human CD38 expressing lymphoma cell lines (35, 51). Similar findings were reported for a panel of 42 human mAbs, of which only a single Ab, daratumumab, was able to induce CDC (35, 52).

The ability of daratumumab to induce CDC was strongly potentiated by point mutations of residue E345 or E430 that facilitate oligomerization of CD38-bound antibodies into ordered hexamers on the cell surface (53, 54). Similarly introduction of the E345R mutation also markedly enhanced the CDC potency of human CD38-specific hcAbs (51).

New structural insights regarding the CDC-inducing potency have recently been obtained for antibodies directed against the B-cell membrane protein CD20 (54). These Abs have been subdivided into two groups, which either recruit complement effectively (type I) or not (type II). A cryo-electron microscopy analysis of the Fab fragments of such antibodies in complex

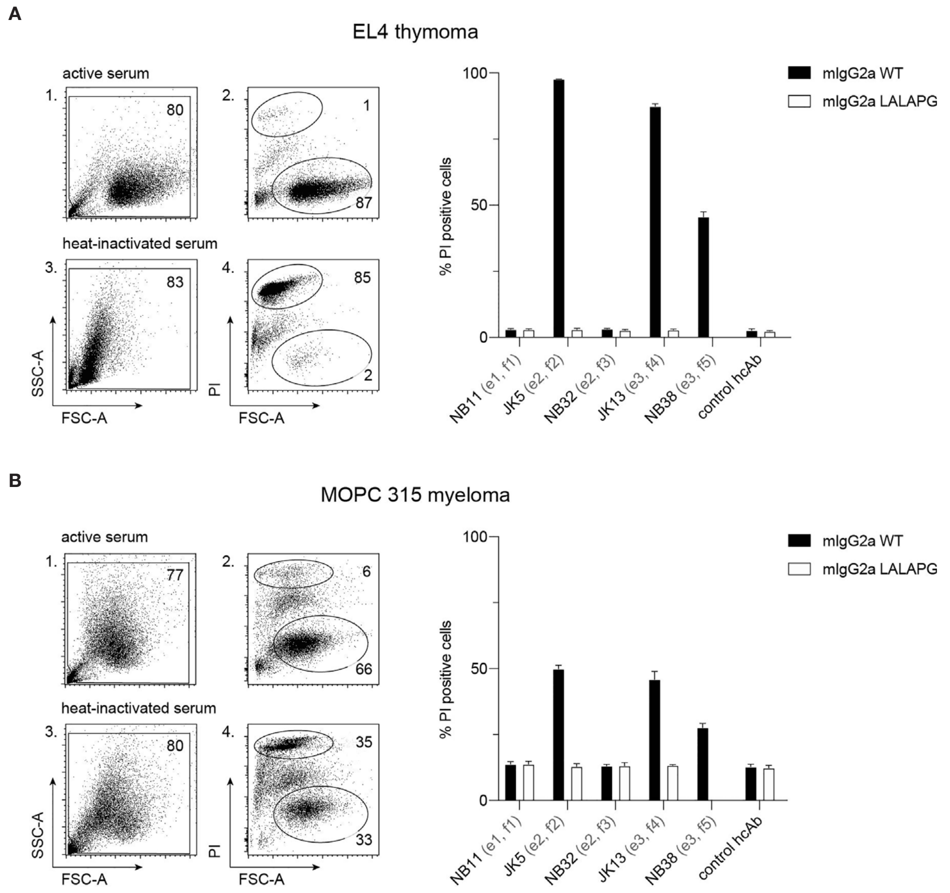

FIGURE 4 | hcAbs of families 2, 4, and 5 mediate complement-dependent cytotoxicity of cells against CD38-expressing thymoma and myeloma cell lines. EL4 thymoma **(A)** and MOPC 315 myeloma **(B)** cells were incubated for 120 min at 37°C with the indicated CD38-specific mouse IgG2a hcAbs in the presence of 25% guinea pig serum as a source of complement. The same serum was pretreated for 10 min at 70°C to inactivate complement components and used as a control (heat-inactivated serum). As additional controls, we used LALA-PG mutant hcAbs (with abrogated C1q-binding) and a non-binding control hcAb. Cells were stained with propidium iodide and analyzed by flow cytometry to quantify the percentage of dead (PI-positive, FSC^{low}) cells. Gating was performed to exclude cellular debris with very low FSC and low SSC. Numbers in panels 1-4 indicate the percentage of cells in the indicated gated populations. Data in the bar diagrams represent mean ± SD from three independent experiments.

with full length dimeric CD20 found that the CD20 dimer bound only one Fab arm of the type II mAb obinutuzumab, but two Fab fragments of the type I mAbs rituximab and ofatumumab (55). These findings indicate that type I antibodies act as molecular seeds that allow formation of oligomeric complexes, while type II antibodies preclude recruitment of additional complexes. Since CD38 can also form dimers and oligomers (6, 56), it is tempting to speculate that mouse CD38-specific hcAbs of families 2, 4, and 5 can similarly act as molecular seeds that facilitate formation of oligomeric complexes of CD38 on the cell surface and thereby enhance CDC.

In vivo studies are ultimately needed to assess the potential therapeutic efficacy of the hcAbs reported here in mouse myeloma models. Of note, we have previously shown that nanobody-based hcAbs can achieve therapeutic efficacy *in vivo* in xenograft mouse models using our previously generated hcAbs directed against human CD38 (35). These human CD38-specific hcAbs reduced the growth of a systemic lymphoma and prolonged the survival of tumor bearing SCID mice. The specificity for murine CD38 makes our hcAbs unique tools to simultaneously assess the cytotoxicity mechanisms of CD38-specific hcAbs *in vivo* against tumor cells and their potential off-target effects on normal cells expressing CD38 in syngeneic mouse tumor models, i.e. in a fully immunocompetent background.

DATA AVAILABILITY STATEMENT

The raw data supporting the conclusions of this article will be made available by the authors, without undue reservation, to any qualified researcher.

ETHICS STATEMENT

The animal study was reviewed and approved by the animal welfare commission (Amt für Verbraucherschutz, Lebensmittelsicherheit und Veterinärwesen Hamburg, Nr. A8a/694).

AUTHOR CONTRIBUTIONS

PB and FK-N conceived the project. All authors established experimental procedures. NB, PB, and FK-N wrote the manuscript. All authors contributed to the article and approved the submitted version.

FUNDING

Supported by grants SFB1328-A05 and Z02 from the Deutsche Forschungsgemeinschaft to RF, FH, and FK-N and by a grant from the Hamburger Krebsgesellschaft to ME.

ACKNOWLEDGMENTS

We thank Bianca Morgenrot and Sarah Hewald, UKE central animal facility, and Fabienne Seyfried, Dorte Wendt, Lynn Diekow and Anna Josephine Gebhardt, Institute of Immunology, for excellent technical assistance.

REFERENCES

1. Adriouch S, Haag F, Boyer O, Seman M, Koch-Nolte F. Extracellular NAD(+): A Danger Signal Hindering Regulatory T Cells. *Microbes Infect* (2012) 14 (14):1284–92. doi: 10.1016/j.micinf.2012.05.011
2. Haag F, Adriouch S, Brass A, Jung C, Moller S, Scheuplein F, et al. Extracellular NAD and ATP: Partners in Immune Cell Modulation. *Purinergic Signal* (2007) 3 (1-2):71–81. doi: 10.1007/s11302-006-9038-7
3. Cockayne DA, Muchamuel T, Grimaldi JC, Muller-Steffner H, Randall TD, Lund FE, et al. Mice Deficient for the Ecto-Nicotinamide Adenine Dinucleotide Glycohydrolase CD38 Exhibit Altered Humoral Immune Responses. *Blood* (1998) 92(4):1324–33. doi: 10.1182/blood.V92.4.1324.416k26_1324_1333
4. Lund FE, Cockayne DA, Randall TD, Solvason N, Schuber F, Howard MC, et al. CD38: A New Paradigm in Lymphocyte Activation and Signal Transduction. *Immunol Rev* (1998) 161:79–93. doi: 10.1111/j.1600-065X.1998.tb01573.x
5. Young GS, Choleris E, Lund FE, Kirkland JB. Decreased cADPR and Increased NAD+ in the Cd38-/- Mouse. *Biochem Biophys Res Commun* (2006) 346(1):188–92. doi: 10.1016/j.bbrc.2006.05.100
6. Hara-Yokoyama M, Kukimoto-Niino M, Terasawa K, Harumiya S, Podyma-Inoue KA, Hino N, et al. Tetrameric Interaction of the Ectoenzyme CD38 on the Cell Surface Enables Its Catalytic and Raft-Association Activities. *Structure* (2012) 20(9):1585–95. doi: 10.1016/j.str.2012.06.017
7. Krebs C, Adriouch S, Braasch F, Koestner W, Leiter EH, Seman M, et al. CD38 Controls ADP-Ribosyltransferase-2-Catalyzed ADP-Ribosylation of T Cell Surface Proteins. *J Immunol* (2005) 174(6):3298–305. doi: 10.4049/jimmunol.174.6.3298
8. Chen J, Reifsnyder YG, Schott PC, Lee WH, Osborne CH, Scheuplein M, et al. Targeted Disruption of CD38 Accelerates Autoimmune Diabetes in NOD/Lt Mice by Enhancing Autoimmunity in an ADP-Ribosyltransferase 2-Dependent Fashion. *J Immunol* (2006) 176(8):4590–9. doi: 10.4049/jimmunol.176.8.4590
9. Schuber F, Lund FE. Structure and Enzymology of ADP-Ribosyl Cyclases: Conserved Enzymes That Produce Multiple Calcium Mobilizing Metabolites. *Curr Mol Med* (2004) 4(3):249–61. doi: 10.2174/1566524043360708
10. Lund FE. Signaling Properties of CD38 in the Mouse Immune System: Enzyme-Dependent and -Independent Roles in Immunity. *Mol Med* (2006) 12(11-12):328–33. doi: 10.2119/2006-00099.Lund
11. Morandi F, Horenstein AL, Costa F, Giuliani N, Pistoia V, Malavasi F. CD38: A Target for Immunotherapeutic Approaches in Multiple Myeloma. *Front Immunol* (2018) 9:2722. doi: 10.3389/fimmu.2018.02722
12. Calabretta E, Carlo-Stella C. The Many Facets of CD38 in Lymphoma: From Tumor-Microenvironment Cell Interactions to Acquired Resistance to Immunotherapy. *Cells* (2020) 9(4):802. doi: 10.3390/cells9040802
13. Chillemi A, Quarona V, Antonioli L, Ferrari D, Horenstein AL, Malavasi F. Roles and Modalities of Ectonucleotidases in Remodeling the Multiple Myeloma Niche. *Front Immunol* (2017) 8:305. doi: 10.3389/fimmu.2017.00305
14. Konen JM, Fradette JJ, Gibbons DL. The Good, the Bad and the Unknown of CD38 in the Metabolic Microenvironment and Immune Cell Functionality of Solid Tumors. *Cells* (2019) 9(1):52. doi: 10.3390/cells9010052
15. van de Donk N, Richardson PG, Malavasi F. CD38 Antibodies in Multiple Myeloma: Back to the Future. *Blood* (2018) 131(1):13–29. doi: 10.1182/blood-2017-06-740944
16. Bonello F, D'Agostino M, Moscvin M, Cerrato C, Boccadoro M, Gay F. CD38 as an Immunotherapeutic Target in Multiple Myeloma. *Expert Opin Biol Ther* (2018) 18(12):1209–21. doi: 10.1080/14712598.2018.1544240
17. Lokhorst HM, Plesner T, Laubach JP, Nahi H, Gimsing P, Hansson M, et al. Targeting CD38 With Daratumumab Monotherapy in Multiple Myeloma. *N Engl J Med* (2015) 373(13):1207–19. doi: 10.1056/NEJMoa1506348
18. Frerichs KA, Nagy NA, Lindenbergh PL, Bosman P, Marin Soto J, Broekmans M, et al. CD38-Targeting Antibodies in Multiple Myeloma: Mechanisms of Action and Clinical Experience. *Expert Rev Clin Immunol* (2018) 14(3):197–206. doi: 10.1080/1744666X.2018.1443809
19. Moreno L, Perez C, Zabaleta A, Manrique I, Alignani D, Ajona D, et al. The Mechanism of Action of the Anti-CD38 Monoclonal Antibody Isatuximab in Multiple Myeloma. *Clin Cancer Res* (2019) 25(10):3176–87. doi: 10.1158/1078-0432.CCR-18-1597
20. Chong LL, Soon YY, Soekojo CY, Ooi M, Chng WJ, de Mel S. Daratumumab-Based Induction Therapy for Multiple Myeloma: A Systematic Review and Meta-Analysis. *Crit Rev Oncol Hematol* (2021) 159:103211. doi: 10.1016/j.critrevonc.2020.103211
21. Phipps C, Chen Y, Gopalakrishnan S, Tan D. Daratumumab and its Potential in the Treatment of Multiple Myeloma: Overview of the Preclinical and Clinical Development. *Ther Adv Hematol* (2015) 6(3):120–7. doi: 10.1177/2040620715572295
22. Wang Y, Zhang Y, Hughes T, Zhang J, Caligiuri MA, Benson DM, et al. Fratricide of NK Cells in Daratumumab Therapy for Multiple Myeloma Overcome by *Ex Vivo*-Expanded Autologous NK Cells. *Clin Cancer Res* (2018) 24(16):4006–17. doi: 10.1158/1078-0432.CCR-17-3117
23. Adams HC3rd, Stevenaert F, Krejcik J, Van der Borght K, Smets T, Bald J, et al. High-Parameter Mass Cytometry Evaluation of Relapsed/Refractory Multiple Myeloma Patients Treated With Daratumumab Demonstrates Immune Modulation as a Novel Mechanism of Action. *Cytometry A* (2019) 95(3):279–89. doi: 10.1002/cyto.a.23693
24. Tijink BM, Laeremans T, Budde M, Stigter-van Walsum M, Dreier T, de Haard HJ, et al. Improved Tumor Targeting of Anti-Epidermal Growth Factor Receptor Nanobodies Through Albumin Binding: Taking Advantage of Modular Nanobody Technology. *Mol Cancer Ther* (2008) 7(8):2288–97. doi: 10.1158/1535-7163.MCT-07-2384
25. Bannas P, Lenz A, Kunick V, Well L, Fumey W, Rissiek B, et al. Molecular Imaging of Tumors With Nanobodies and Antibodies: Timing and Dosage are Crucial Factors for Improved *In Vivo* Detection. *Contrast Media Mol Imaging* (2015) 10(5):367–78. doi: 10.1002/cmmi.1637
26. Muyldermans S. Nanobodies: Natural Single-Domain Antibodies. *Annu Rev Biochem* (2013) 82:775–97. doi: 10.1146/annurev-biochem-063011-092449

27. Muyldermans S. Applications of Nanobodies. *Annu Rev Anim Biosci* (2021) 9:401–21. doi: 10.1146/annurev-animal-021419-083831
28. Wesolowski J, Alzogaray V, Reyelt J, Unger M, Juarez K, Urrutia M, et al. Single Domain Antibodies: Promising Experimental and Therapeutic Tools in Infection and Immunity. *Med Microbiol Immunol* (2009) 198(3):157–74. doi: 10.1007/s00430-009-0116-7
29. Ingram JR, Schmidt FI, Ploegh HL. Exploiting Nanobodies' Singular Traits. *Annu Rev Immunol* (2018) 36:695–715. doi: 10.1146/annurev-immunol-042617-053327
30. Bannas P, Hambach J, Koch-Nolte F. Nanobodies and Nanobody-Based Human Heavy Chain Antibodies As Antitumor Therapeutics. *Front Immunol* (2017) 8:1603. doi: 10.3389/fimmu.2017.01603
31. Liu Q, Jiang L, Li K, Li H, Lv G, Lin J, et al. Immuno-PET Imaging of (68)Ga-Labelled Nanobody Nb109 for Dynamic Monitoring the PD-L1 Expression in Cancers. *Cancer Immunol Immunother* (2021) 70:1721–33. doi: 10.1007/s00262-020-02818-y
32. Hu Y, Liu C, Muyldermans S. Nanobody-Based Delivery Systems for Diagnosis and Targeted Tumor Therapy. *Front Immunol* (2017) 8:1442. doi: 10.3389/fimmu.2017.01442
33. Bannas P, Well L, Lenz A, Rissiek B, Haag F, Schmid J, et al. *In Vivo* Near-Infrared Fluorescence Targeting of T Cells: Comparison of Nanobodies and Conventional Monoclonal Antibodies. *Contrast Media Mol Imaging* (2014) 9 (2):135–42. doi: 10.1002/cmmi.1548
34. Verhaar ER, Woodham AW, Ploegh HL. Nanobodies in Cancer. *Semin Immunol* (2020) p:101425. doi: 10.1016/j.smim.2020.101425
35. Schriewer L, Schutze K, Petry K, Hambach J, Fumey W, Koenigsdorf J, et al. Nanobody-Based CD38-Specific Heavy Chain Antibodies Induce Killing of Multiple Myeloma and Other Hematological Malignancies. *Theranostics* (2020) 10(6):2645–58. doi: 10.7150/thno.38533
36. Lo M, Kim HS, Tong RK, Bainbridge TW, Vernes JM, Zhang YL, et al. Effector-Attenuating Substitutions That Maintain Antibody Stability and Reduce Toxicity in Mice. *J Biol Chem* (2017) 292(9):3900–8. doi: 10.1074/jbc.M116.767749
37. Fumey W, Koenigsdorf J, Kunick V, Menzel S, Schutze K, Unger M, et al. Nanobodies Effectively Modulate the Enzymatic Activity of CD38 and Allow Specific Imaging of CD38(+) Tumors in Mouse Models *In Vivo*. *Sci Rep* (2017) 7(1):14289. doi: 10.1038/s41598-017-14112-6
38. Jager V, Bussow K, Wagner A, Weber S, Hust M, Frenzel A, et al. High Level Transient Production of Recombinant Antibodies and Antibody Fusion Proteins in HEK293 Cells. *BMC Biotechnol* (2013) 13:52. doi: 10.1186/1472-6750-13-52
39. Zhang J, MacKenzie R, Durocher Y. Production of Chimeric Heavy-Chain Antibodies. *Methods Mol Biol* (2009) 525:323–36, xv. doi: 10.1007/978-1-59745-554-1_17
40. Koch-Nolte F, Glowacki G, Bannas P, Braasch F, Dubberke G, Ortolan E, et al. Use of Genetic Immunization to Raise Antibodies Recognizing Toxin-Related Cell Surface ADP-Ribosyltransferases in Native Conformation. *Cell Immunol* (2005) 236(1):66–71. doi: 10.1016/j.cellimm.2005.08.033
41. Horenstein AL, Bracci C, Morandi F, Malavasi F. CD38 in Adenosinergic Pathways and Metabolic Re-Programming in Human Multiple Myeloma Cells: In-Tandem Insights From Basic Science to Therapy. *Front Immunol* (2019) 10:760. doi: 10.3389/fimmu.2019.00760
42. Martin TG, Corzo K, Chiron M, Velde HV, Abbadessa G, Campana F, et al. Therapeutic Opportunities With Pharmacological Inhibition of CD38 With Isatuximab. *Cells* (2019) 8(12). doi: 10.3390/cells8121522
43. van de Donk NW, Janmaat ML, Mutis T, Lammerts van Bueren JJ, Ahmadi T, Sasser AK, et al. Monoclonal Antibodies Targeting CD38 in Hematological Malignancies and Beyond. *Immunol Rev* (2016) 270(1):95–112. doi: 10.1111/imr.12389
44. Graeff RM, Walseth TF, Hill HK, Lee HC. Fluorescent Analogs of Cyclic ADP-Ribose: Synthesis, Spectral Characterization, and Use. *Biochemistry* (1996) 35 (2):379–86. doi: 10.1021/bi952083f
45. Muller-Steffner HM, Malver O, Hosie L, Oppenheimer NJ, Schuber F. Slow-Binding Inhibition of NAD+ Glycohydrolase by Arabino Analogues of Beta-NAD. *J Biol Chem* (1992) 267(14):9606–11. doi: 10.1016/S0021-9258(19) 50133-8
46. Deckert J, Wetzel MC, Bartle LM, Skaletskaya A, Goldmacher VS, Vallee F, et al. SAR650984, A Novel Humanized CD38-Targeting Antibody, Demonstrates Potent Antitumor Activity in Models of Multiple Myeloma and Other CD38+ Hematologic Malignancies. *Clin Cancer Res* (2014) 20 (17):4574–83. doi: 10.1158/1078-0432.CCR-14-0695
47. Baum N, Fliegert R, Bauche A, Hambach J, Menzel S, Haag F, et al. Koch-Nolte, Daratumumab and Nanobody-Based Heavy Chain Antibodies Inhibit the ADPR Cyclase But Not the NAD. *Cancers (Basel)* (2020) 13(1):76. doi: 10.3390/cancers13010076
48. Vaisitti T, Arruga F, Guerra G, Deaglio S. Ectonucleotidases in Blood Malignancies: A Tale of Surface Markers and Therapeutic Targets. *Front Immunol* (2019) 10:2301. doi: 10.3389/fimmu.2019.02301
49. Morandi F, Morandi B, Horenstein AL, Chillemi A, Quarona V, Zaccarello G, et al. A Non-Canonical Adenosinergic Pathway Led by CD38 in Human Melanoma Cells Induces Suppression of T Cell Proliferation. *Oncotarget* (2015) 6(28):25602–18. doi: 10.18632/oncotarget.4693
50. Horenstein AL, Chillemi A, Zaccarello G, Bruzzone S, Quarona V, Zito A, et al. A CD38/CD203a/CD73 Ectoenzymatic Pathway Independent of CD39 Drives a Novel Adenosinergic Loop in Human T Lymphocytes. *Oncoimmunology* (2013) 2(9):e26246. doi: 10.4161/onci.26246
51. Schutze K, Petry K, Hambach J, Schuster N, Fumey W, Schriewer L, et al. CD38-Specific Biparatopic Heavy Chain Antibodies Display Potent Complement-Dependent Cytotoxicity Against Multiple Myeloma Cells. *Front Immunol* (2018) 9:2553. doi: 10.3389/fimmu.2018.02553
52. de Weers M, Tai YT, van der Veer MS, Bakker JM, Vink T, Jacobs DC, et al. Daratumumab, a Novel Therapeutic Human CD38 Monoclonal Antibody, Induces Killing of Multiple Myeloma and Other Hematological Tumors. *J Immunol* (2011) 186(3):1840–8. doi: 10.4049/jimmunol.1003032
53. Diebolder CA, Beurskens FJ, de Jong RN, Koning RI, Strumane K, Lindorfer MA, et al. Complement Is Activated by IgG Hexamers Assembled at the Cell Surface. *Science* (2014) 343(6176):1260–3. doi: 10.1126/science.1248943
54. de Jong RN, Beurskens FJ, Verploegen S, Strumane K, van Kampen MD, Voorhorst M, et al. A Novel Platform for the Potentiation of Therapeutic Antibodies Based on Antigen-Dependent Formation of IgG Hexamers at the Cell Surface. *PloS Biol* (2016) 14(1):e1002344. doi: 10.1371/journal.pbio.1002344
55. Kumar A, Planchais C, Fronzes R, Mouquet H, Reyes N. Binding Mechanisms of Therapeutic Antibodies to Human CD20. *Science* (2020) 369(6505):793–9. doi: 10.1126/science.abb8008
56. Deaglio S, Vaisitti T, Billington R, Bergui L, Omede P, Genazzani AA, et al. CD38/CD19: A Lipid Raft-Dependent Signaling Complex in Human B Cells. *Blood* (2007) 109(12):5390–8. doi: 10.1182/blood-2006-12-061812

Conflict of Interest: FH and FKN receive a share of antibody sales via MediGate GmbH, a wholly owned subsidiary of the University Medical Center Hamburg-Eppendorf. PB and FKN are coinventors on a patent application on CD38-specific nanobodies.

The remaining authors declare that the research was conducted in the absence of any commercial or financial relationships that could be construed as a potential conflict of interest.

frontiers
in Immunology

PERSPECTIVE
published: 07 September 2021
doi: 10.3389/fimmu.2021.703326

NAADP: From Discovery to Mechanism

Timothy F. Walseth[1] *and Andreas H. Guse*[2*]

[1] *Department of Pharmacology, University of Minnesota Medical School, Minneapolis, MN, United States,* [2] *The Calcium Signalling Group, Department of Biochemistry and Molecular Cell Biology, University Medical Center Hamburg-Eppendorf, Hamburg, Germany*

Nicotinic acid adenine dinucleotide 2'-phosphate (NAADP) is a naturally occurring nucleotide that has been shown to be involved in the release of Ca^{2+} from intracellular stores in a wide variety of cell types, tissues and organisms. Current evidence suggests that NAADP may function as a trigger to initiate a Ca^{2+} signal that is then amplified by other Ca^{2+} release mechanisms. A fundamental question that remains unanswered is the identity of the NAADP receptor. Our recent studies have identified HN1L/JPT2 as a high affinity NAADP binding protein that is essential for the modulation of Ca^{2+} channels.

Keywords: NAADP, HN1L/JPT2, ryanodine receptor, two-pore channel, calcium signaling

OPEN ACCESS

Edited by:
Antonio Filippini,
Sapienza University of Rome, Italy

Reviewed by:
Antony Galione,
University of Oxford, United Kingdom
Samantha Pitt,
University of St Andrews,
United Kingdom
John Parrington,
University of Oxford, United Kingdom
Francesco Di Virgilio,
University of Ferrara, Italy

***Correspondence:**
Andreas H. Guse
guse@uke.de

Specialty section:
This article was submitted to
Cytokines and Soluble
Mediators in Immunity,
a section of the journal
Frontiers in Immunology

Received: *30 April 2021*
Accepted: *19 August 2021*
Published: *07 September 2021*

Citation:
Walseth TF and Guse AH (2021)
NAADP: From Discovery to Mechanism.
Front. Immunol. 12:703326.
doi: 10.3389/fimmu.2021.703326

INTRODUCTION

Nicotinic acid adenine dinucleotide phosphate was first described in 1995 as potent Ca^{2+} mobilizing adenine nucleotide (1). NAADP's biological activity was first observed in sea urchin egg homogenates (1, 2), soon followed by reports describing NAADP evoked Ca^{2+} release in invertebrates (1, 3, 4), mammalian and human cells (5–7). Obviously, NAADP signaling was very successful in evolution since it operates in both invertebrate and vertebrates.

Here, we will highlight the steps of NAADP's discovery, the tales and mysteries of its mode of action, and finally discuss the unifying hypothesis of NAADP action that was published some years ago (8).

NAADP: DISCOVERY IN SEA URCHIN EGG HOMOGENATE

Hon Cheung Lee's laboratory at the University of Minnesota developed the sea urchin egg homogenate system in 1985 in order to study D-*myo*-inositol 1,4,5-trisphosphate (IP_3) induced Ca^{2+} mobilization *in vitro* (2). The egg homogenate system contained Ca^{2+} pumps that were able to pump Ca^{2+} into vesicles in an ATP-dependent manner and IP_3 receptors that would release Ca^{2+} from the vesicles in response to the addition of IP_3. Two important observations using the sea urchin egg homogenate system were made in 1987 (9). The first was that nicotinamide adenine dinucleotide (NAD) was able to release Ca^{2+}, but only after a lag of several minutes. This observation led to the discovery of cyclic ADP-ribose (cADPR) (10). The lag in the response to NAD was due to the conversion of NAD to cADPR by ADP-ribosyl cyclases. The second observation was that nicotinamide adenine dinucleotide (NADP) caused an immediate and robust release of Ca^{2+} from the egg homogenate (9). Further examination of the NADP-induced Ca^{2+} release revealed that the release was not due to NADP itself, but a contaminant in commercial sources of NADP that could be resolved chromatographically from NADP (1). Alkaline treatment of NADP produced a 30-fold enrichment of the active metabolite that released Ca^{2+} (1). In 1995, Aarhus and Lee demonstrated that the derivative produced by alkaline treatment of NADP was nicotinic acid adenine dinucleotide 2'-phosphate (NAADP) (1). Some of the basic properties of NAADP-induced Ca^{2+} release as determined using the sea urchin egg system are as follows. Ca^{2+} release by NAADP was saturable with an EC_{50} of 30nM, making it the most potent of the agents (IP_3 and cADPR) known to mobilize Ca^{2+} from intracellular stores (1). NAADP-induced Ca^{2+} release exhibited self-desensitization, but the action of NAADP was not desensitized by preexposure to IP_3 or cADPR (1). Antagonists of IP_3 or cADPR did not block NAADP-induced Ca^{2+} release (1). In addition, the Ca^{2+} stores sensitive to NAADP were distinct than those released by IP_3 or cADPR as indicated by density gradient fractionation of egg homogenates and stratifying live sea urchin eggs by centrifugation. While IP_3 and cADPR appear to release Ca^{2+} from endoplasmic reticulum stores, NAADP releases Ca^{2+} from a thapsigargin-insensitive store that has the properties consistent with being acidic lysosomal type organelles (11, 12). In the sea urchin egg system, NAADP displays a unique self-inactivation mechanism (13, 14). Subthreshold concentrations of NAADP inhibit subsequent Ca^{2+} release by maximal concentrations of NAADP in a time and concentration-dependent manner (13, 14). NAADP was shown to be active in intact cells as microinjection of NAADP into live sea urchin eggs resulted in Ca^{2+} mobilization and induced a cortical reaction (1). NAADP has now been shown to be active in many cell types [reviewed in references (15–18)].

NAADP: ENDO/SARCOPLASMIC RETICULUM AND RYANODINE RECEPTORS

The molecular mechanisms involved in Ca^{2+} mobilizing activity of NAADP have been a matter of many discussions in the past years: basically, two hypotheses evolved: (i) NAADP activates type 1 ryanodine receptor (RYR1) localized on endoplasmic reticulum (ER) Ca^{2+} stores, or (ii) NAADP's target organelles are acidic endo-lysosomal stores and Ca^{2+} mobilization proceeds *via* two-pore channels (TPC).

In 1999 Cancela et al. proposed a model for pancreatic acinar cells in which nanomolar concentrations of NAADP activate an unknown NAADP receptor/Ca^{2+} channel that releases trigger Ca^{2+} which then would be amplified by Ca^{2+} induced Ca^{2+} release (CICR) through RYR (19). A more direct effect of NAADP on cardiac RYR (RYR2) was reported in 2001 showing Ca^{2+} release from cardiac microsomes; further, RYR2s in lipid planar bilayers were activated by NAADP (20). However, micromolar NAADP was used in (20) while in most other studies nanomolar NAADP was sufficient to evoke Ca^{2+} release. One year later, in a similar experimental approach in lipid planar bilayers, low nanomolar NAADP (EC_{50} ~ 30 nM) increased the open probability of RYR1 from skeletal muscle of RYR1 (21). However, others did not confirm RYR activation by NAADP in lipid planar bilayers (22, 23). In 2003, in the nuclear envelope of pancreatic acinar cells, NAADP-evoked Ca^{2+} release was not affected by inhibition of lysosomal acidification, but was blocked by antagonists of RYR, ryanodine and ruthenium red, as well as by depletion of ER using SERCA inhibitor thapsigargin; accordingly, it was hypothesized that NAADP acts on RYR, but most likely indirectly *via* a NAADP binding protein (NAADP BP) (24). In 2004 and 2005, RYR was identified as major Ca^{2+} channel responding to NAADP in T cells; using a combination of NAADP microinjection during Ca^{2+} imaging, NAADP evoked local and global Ca^{2+} signaling was abolished by either pharmacological inhibition or gene silencing of RYR (25). More evidence for NAADP acting on RYR1 was obtained in partially purified RYR1 preparations where NAADP facilitated [^{3}H]ryanodine binding, while this was blocked by a novel NAADP antagonist, BZ194 (26). Collectively, these data indicated that if an unknown NAADP receptor/Ca^{2+} channel, as proposed by Cancela et al. (19), would be involved to produce trigger Ca^{2+} ahead of activation of RYR by CICR, this process must be working with very small and very fast Ca^{2+} signals. To solve this problem, at least partially, high-resolution Ca^{2+} imaging was optimized for T cells and combined with NAADP microinjections and specific gene knock-outs (27). Using high spatiotemporal resolution (25 ms, 368 nm), for the first time initial local Ca^{2+} signals of T cells were characterized; while experiments with *Ryr1*$^{-/-}$, *Orai1*$^{-/-}$, *Stim1*$^{-/-}$ and *Stim2*$^{-/-}$ T cells identified the protein products of these genes as major elements essential for NAADP evoked Ca^{2+} signaling, evidence for involvement of other ion channels was not obtained (27, 28). Though further studies from Petersen and colleagues confirmed that NAADP acts on ER stores *via* RYR in pancreatic acinar cell function, they also emphasized that acidic stores and two-pore channels (TPC) are additionally required (29).

However, as mentioned above, in a couple of systems, RYR1 did not respond to NAADP. Using overexpression of RYR1 in HEK cells and intracellular dialysis of 10 nM NAADP did not evoke Ca^{2+} signals above background (30). In a similar cell model, HEK cell overexpressing RYR1, direct activation NAADP (30 nM and 1 μM) activation of RYR1 by on-nucleus patch clamp was not observed (31).

Taken together, these studies suggest two different roles for RYR in NAADP signaling: (i) as amplifier of initial lysosomal Ca^{2+} signals, or (ii) in a more direct sense as NAADP sensitive Ca^{2+} channels. However, the latter results appear to be restricted to T cells and pancreatic acinar cells. While in pancreatic acinar cells also the endo-lysosomal system and TPCs were found to be involved in NAADP signaling, in T cells a role of endo-lysosomes remains to be confirmed (32).

NAADP: ACIDIC STORES AND TWO-PORE-CHANNELS

The second hypothesis regarding NAADP's mechanism of action is that NAADP targets organelles that are acidic endo-lysosomal stores and Ca^{2+} mobilization proceeds *via* two-pore channels (TPCs) Several laboratories have demonstrated that the two-pore channel (TPC) family of endolysosomal proteins are regulated by NAADP (33–35). The experimental approaches utilized to support the role of TPCs in NAADP signaling, include manipulation of TPC levels by overexpression (33–36) or knockdown (33, 34), as well as electrophysiological analyses (36–39). However, in some reports TPCs were found to be activated primarily by phosphatidylinositol 3,5-bisphosphate and to conduct Na^+ currents rather than Ca^{2+} currents (40–42).

An important unresolved issue is whether TPCs directly interact with NAADP. Most biological data suggest that while TPCs are required for NAADP action, NAADP does not appear to bind directly to TPCs. For instance, overexpression of mammalian TPC2 slightly increased [^{32}P]NAADP binding activity, but the increment in binding was much lower than the increase in TPC2 mRNA levels (3-fold *versus* 250-fold) (34). [^{32}P]NAADP binding activity was also found in immunoprecipitates using antibodies to sea urchin TPCs (39). The question of whether NAADP binds directly to TPCs was assessed by photoaffinity labeling. [^{32}P]-5-azido-NAADP was synthesized and characterized as a photoaffinity probe for NAADP binding sites (43–46). 5-azido-NAADP was previously shown to release Ca^{2+} from sea urchin egg homogenates and mammalian cells with high affinity (44, 47). Photoaffinity labeling of sea urchin egg homogenates with [^{32}P]-5-azido-NAADP resulted in specific labeling of proteins with molecular weights of 45, 40 and 30kDa, which are much smaller in size than the TPCs expressed in sea urchin (45). These proteins exhibited the properties of high affinity [^{32}P]-NAADP binding previously described in this system (45). The photolabeled proteins were not recognized by antibodies to sea urchin TPCs suggesting these proteins are immunologically distinct from TPCs (45). A small amount (~5%) of the photolabeled 45 and 40kDa proteins were pulled down with antibodies to sea urchin TPCs, suggesting an interaction between these proteins and TPCs (45).

Photolabeling in mammalian cell extracts with [^{32}P]-5-azido-NAADP resulted in the specific labeling of 23kDa protein(s) (44, 46). The photolabeling pattern was not changed by overexpression of TPC isoforms (44). Photolabeling was also unchanged in tissue samples form TPC1 or TPC2 knockout mice (44). Similar results were also obtained with a TPC1/TPC2 double knockout mouse model (48). The unchanged photolabeling from overexpression and knockout models indicates that the high affinity NAADP binding proteins detected by [^{32}P]-5-azido-NAADP in mammalian systems are independent of TPC proteins. Overall, the data suggest that a NAADP-sensitive complex containing the TPC channel and high affinity NAADP binding protein(s) is responsible for mediating NAADP-evoked Ca^{2+} release.

The identity of the high affinity NAADP binding proteins identified *via* photoaffinity labeling is crucial to our understanding of the mechanism by which NAADP elicits Ca^{2+} release. The next section details our efforts to accomplish this task.

NAADP: UNIFYING HYPOTHESIS

One excellent possibility to identify proteins that specifically bind small ligands is photoaffinity labelling. In 2012 independent studies reported photoaffinity labelling experiments with [^{32}P]-5-N_3-NAADP as PAL-ligand (44–46). The main, but unexpected finding of all three reports was labelling of small soluble proteins in mammalian cell extracts (44, 46). In the two reports conducted in different mammalian cell lines and tissues, a protein double band of 22/23kDa was labelled consistently by [^{32}P]-5-N_3-NAADP and specificity was demonstrated by displacement of the label by low nanomolar concentrations of ‘cold’ NAADP (44, 46).

These novel findings resulted in the ‘unifying hypothesis’ (8). The central idea of this hypothesis consists of a (small) NAADP binding protein and a Ca^{2+} channel that is activated by the NAADP binding protein in conjunction with NAADP. This idea builds on an earlier report by Petersen’s group where binding proteins for NAADP or cADPR were proposed to activate RYR (24). The ‘unifying hypothesis’ helps to explain the fact that one part of the community obtained evidence of RYR1 localized on the ER as target of NAADP, but not for lysosomal TPCs, while the other part reported data supporting TPCs localized on lysosomes as NAADP’s target channels, but did not find evidence for RYR in NAADP signaling (for details see chapters above).

The molecular identification of the protein hidden in the 22/23kDa band that was photoaffinity labelled turned out to be as complicated as the design of NAADP analogues suitable for photo-affinity labelling (48–50). Nine years after discovery of the small soluble NAADP binding proteins and formulation of the ‘unifying hypothesis’, two back-to-back studies in *Science Signaling* reported identification of a 21kDa NAADP binding protein as haematological and neurological expressed 1-like protein (HN1L)/Jupiter microtubule associated homolog 2 (JPT2) in March 2021 (51, 52). HN1L/JPT2 was purified independently from erythrocytes and Jurkat T-lymphocytes using photo-affinity labeling as selection criterion during protein purification and enrichment steps. HN1L/JPT2, also known as C16orf34, FLJ13092, KIAA1426, or L11, is a 20.1 kDa protein with broad expression in mammalian cell types (see human protein atlas.org) and with orthologues throughout the animal kingdom (51). Recombinantly expressed HN1L/JPT2 was specifically photo-affinity labelled, though displacement by ‘cold’ NAADP was somewhat shifted to higher NAADP concentrations (51, 52). Crucial experiments to validate HN1L/JPT2’s role as signal transducer in NAADP signaling were (i) decreased responsiveness of SKBR cells to microinjected NAADP upon gene silencing of HN1L/JPT2 by shRNA (44) and (ii) largely diminished initial Ca^{2+} microdomains upon knock out of *Hn1l/Jpt2* using CRISPR/Cas technology both in human Jurkat T cells or in primary rat effector T cells (51). Further, in *Hn1l/Jpt2*$^{-/-}$ rat T cells, NAADP antagonist BZ194 did not further enhance the Ca^{2+} phenotype suggesting that the same signaling pathway is affected by both interventions (52). These results confirmed the first part of the ‘unifying hypothesis’ since the NAADP binding protein is not any more a faint band on a phosphoscreen, but an identified protein to be further analysed and validated by the scientific community. But what about the second part of the 'unifying hypothesis', activation of different ion channels? Roggenkamp et al. (52) reported co-localization of HN1L/JPT2 with RYR already before T cell receptor (TCR)/CD3 stimulation using super-resolution microscopy (**Figure 1**) (52). Further, TCR/CD3-dependent re-localization of HN1L/JPT2 from the cytosol towards the plasma membrane within seconds was observed by super-resolution microscopy. Finally, HN1L/JPT2 was detected by western blot in anti-RYR immunoprecipitates from Jurkat T cells (52). Collectively these data confirm interaction of HN1L/JPT2 with RYR.

But what about other proposed target channels for NAADP? Gunaratne et al. (51) demonstrated co-immunoprecipitation of HN1L/JPT2 when TPC1, but not TPC2, was pulled down from HEK293 cells overexpressing GFP-tagged TPC1 or TPC2 demonstrating that HN1L/JPT2 may function as a switch point to direct incoming signals either to RYR1 or TPC1 activation (**Figure 2**). The fact that HN1L/JPT2 interacts with two different ion channels nicely confirms the second part of the 'unifying hypothesis' and paves the way for experiments to unravel the molecular mechanism(s) opening this bifurcation onto one or the other path.

DISCUSSION AND OUTLOOK

Despite confirmation of the main aspects of the 'unifying' hypothesis, several questions remain open. Though photoaffinity labelling of HN1L/JPT2 and specific and high affinity binding of [^{32}P]NAADP were demonstrated (51, 52), details of the molecular basis for NAADP binding to HN1L/JPT2 remain elusive. Under non-reducing conditions, recombinant HN1L/JPT2 was detected in size exclusion-HPLC mainly as dimer, though higher oligomers and monomers were observed, too (52). It is currently unclear whether this might be an artefact due to recombinant HN1L/JPT2 production, or whether there is a biological background, perhaps related to regulation of HN1L/JPT's activity in NAADP signaling. Further, the binding site of NAADP on HN1L/JPT2 so far has not been mapped. However, understanding binding of NAADP would greatly facilitate further structure-activity studies to translate the basic finding of a novel signal transducer to pharmacology and hopefully to therapy. What type of disease and therapy is meant? In 2010 it was shown that NAADP signaling is an important determinant of CNS autoimmunity (53); however, specific, high affinity compounds antagonizing NAADP's interaction with HNL1 that may be tested in multiple sclerosis animal model experimental autoimmune encephalomyelitis are not yet known.

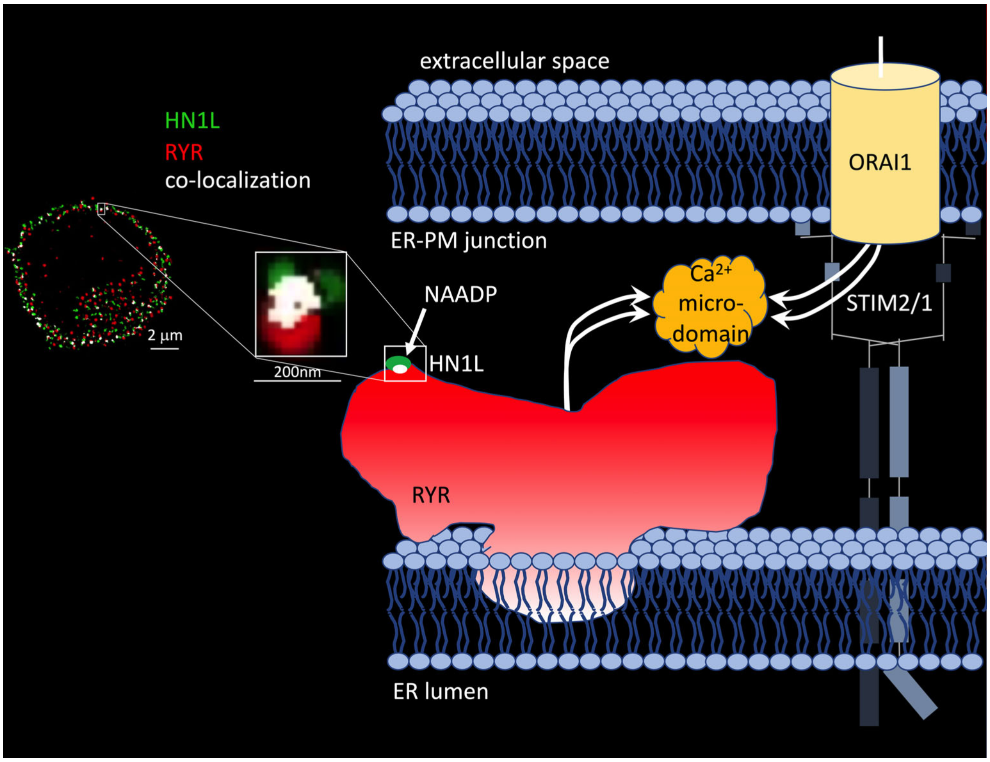

FIGURE 1 | HN1L/JPT2 co-localization with ryanodine receptors and scheme of Ca^{2+} microdomain formation by ryanodine receptors and ORAI1 channels in ER-PM junctions of T cells. Left: Co-localization of HN1L/JPT2 with RYR shown by super-resolution microscopy in a single Jurkat T cell [image taken from Figure 6 of (45)]. From (52). Reprinted with permission from AAAS. Right: scheme of Ca^{2+} microdomain formation by RYRs and ORAI1 channels in ER-PM junctions of T cells. Abbreviations used: STIM1/2, stromal interaction molecule 1 and/or 2.

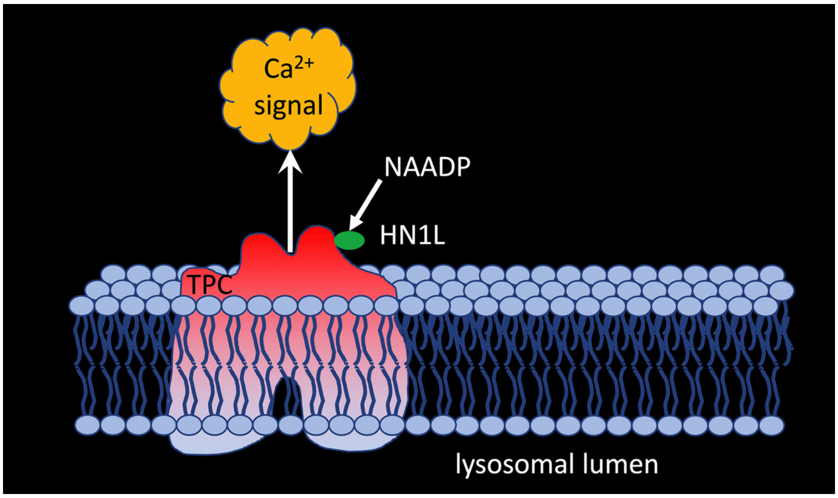

FIGURE 2 | HNL1/JPT2 interacts with TPC1 and is essential for NAADP-evoked calcium signaling *via* two pore channels.

Next open question relates to the molecular basis for HN1L/JPT2 binding to and activation of different Ca^{2+} channels. Like for NAADP binding, we do not know the binding interface of either side. However, also this protein-protein interaction would be of high translational value for the same reasons as quoted for the NAADP binding site at HN1L/JPT2 above. Another point of interest is the interaction of HN1L/JPT2 with TPC isoforms. Co-immunoprecipitation was only confirmed for TPC1, but not for TPC2 (51). However, the molecular basis for this is unclear. This differential binding of HN1L/JPT2 to TPC1, but not TPC2, also opens the question of further, still unknown members of the NAADP signalosome.

Further, the exact kinetic mechanism of NAADP-HN1L/JPT2-Ca^{2+} channel interaction is unknown. Possible would be (i) that NAADP binds HN1L/JPT2 first and afterwards to the Ca^{2+} channel or (ii) that a fraction of HN1L/JPT2 is already bound to the Ca^{2+} channel before cell activation and operates like in a "waiting position" until NAADP formation upon cell activation takes place.

It is possible that other NAADP binding proteins exist and participate in NAADP signalsome. Zhang et al. have identified Lsm12 as a high affinity NAADP binding protein that is essential for NAADP -induced TPC2 activation (54). The Lsm12 data suggest that NAADP signaling has more components that need to be identified and studied.

In conclusion, the identification of HN1L/JPT2 constitutes a milestone in Ca^{2+} signaling research, allowing for future characterization of the molecular basis as well as for translational research towards therapeutic applications. The 'unifying hypothesis' was confirmed in its major aspects, however, the current model does not explain the complexity and calls for further investigation of the NAADP signaling pathway.

DATA AVAILABILITY STATEMENT

The original contributions presented in the study are included in the article/supplementary material. Further inquiries can be directed to the corresponding author.

AUTHOR CONTRIBUTIONS

Both authors wrote the manuscript. All authors contributed to the article and approved the submitted version.

FUNDING

This work was supported by the Deutsche Forschungsgemeinschaft (DFG) (Project number 335447717; SFB1328, project A01 to AG). Research in the Guse lab is also supported by the Joachim-Herz-Foundation (Hamburg; Infectophysics consortium, project 4), NCL-Foundation (Hamburg), and EU project INTEGRATA - DLV-813284. Research in the Walseth lab is supported by NIH R15-GM131129.

REFERENCES

1. Lee HC, Aarhus R. A Derivative of NADP Mobilizes Calcium Stores Insensitive to Inositol Trisphosphate and Cyclic ADP-Ribose. *J Biol Chem* (1995) 270(5):2152–7. doi: 10.1074/jbc.270.5.2152
2. Clapper DL, Lee HC. Inositol Trisphosphate Induces Calcium Release From Nonmitochondrial Stores I Sea Urchin Egg Homogenates. *J Biol Chem* (1985) 260(26):13947–54. doi: 10.1016/S0021-9258(17)38668-4
3. Albrieux M, Lee HC, Villaz M. Calcium Signaling by Cyclic ADP-Ribose, NAADP, and Inositol Trisphosphate Are Involved in Distinct Functions in Ascidian Oocytes. *J Biol Chem* (1998) 273(23):14566–74. doi: 10.1074/jbc.273.23.14566
4. Santella L, Kyozuka K, Genazzani AA, De Riso L, Carafoli E. Nicotinic Acid Adenine Dinucleotide Phosphate-Induced Ca(2+) Release. Interactions Among Distinct Ca(2+) Mobilizing Mechanisms in Starfish Oocytes. *J Biol Chem* (2000) 275(12):8301–6. doi: 10.1074/jbc.275.12.8301

5. Berg I, Potter BV, Mayr GW, Guse AH. Nicotinic Acid Adenine Dinucleotide Phosphate [NAADP(+)] Is an Essential Regulator of T-Lymphocyte Ca (2+)-Signaling. *J Cell Biol* (2000) 150(3):581–8. doi: 10.1083/jcb.150.3.581
6. Burdakov D, Galione A. Two Neuropeptides Recruit Different Messenger Pathways to Evoke Ca2+ Signals in the Same Cell. *Curr Biol* (2000) 10 (16):993–6. doi: 10.1016/S0960-9822(00)00649-7
7. Cancela JM, Churchill GC, Galione A. Coordination of Agonist-Induced Ca2 +-Signalling Patterns by NAADP in Pancreatic Acinar Cells. *Nature* (1999) 398(6722):74–6. doi: 10.1038/18032
8. Guse AH. Linking NAADP to Ion Channel Activity: A Unifying Hypothesis. *Sci Signal* (2012) 5(221):pe18. doi: 10.1126/scisignal.2002890
9. Clapper DL, Walseth TF, Dargie PJ, Lee HC. Pyridine Nucleotide Metabolites Stimulate Calcium Release From Sea Urchin Egg Microsomes Desensitized to Inositol Trisphosphate. *J Biol Chem* (1987) 262(20):9561–8. doi: 10.1016/S0021-9258(18)47970-7
10. Lee HC, Walseth TF, Bratt GT, Hayes RN, Clapper DL. Structural Determination of a Cyclic Metabolite of NAD+ With Intracellular Ca2+ -Mobilizing Activity. *J Biol Chem* (1989) 264(3):1608–15. doi: 10.1016/S0021-9258(18)94230-4
11. Churchill GC, Okada Y, Thomas JM, Genazzani AA, Patel S, Galione A. NAADP Mobilizes Ca(2+) From Reserve Granules, Lysosome-Related Organelles, in Sea Urchin Eggs. *Cell* (2002) 111(5):703–8. doi: 10.1016/S0092-8674(02)01082-6
12. Genazzani AA, Galione A. Nicotinic Acid-Adenine Dinucleotide Phosphate Mobilizes Ca2+ From a Thapsigargin-Insensitive Pool. *Biochem J* (1996) 315 (Pt 3):721–5. doi: 10.1042/bj3150721
13. Aarhus R, Dickey DM, Graeff RM, Gee KR, Walseth TF, Lee HC. Activation and Inactivation of Ca2+ Release by NAADP+. *J Biol Chem* (1996) 271 (15):8513–6. doi: 10.1074/jbc.271.15.8513
14. Genazzani AA, Empson RM, Galione A. Unique Inactivation Properties of NAADP-Sensitive Ca2+ Release. *J Biol Chem* (1996) 271(20):11599–602. doi: 10.1074/jbc.271.20.11599
15. Guse AH, Lee HC. NAADP: A Universal Ca2+ Trigger. *Sci Signal* (2008) 1 (44):re10. doi: 10.1126/scisignal.144re10
16. Lee HC. NAADP: An Emerging Calcium Signaling Molecule. *J Membr Biol* (2000) 173(1):1–8. doi: 10.1007/s002320001001
17. Lee HC. Calcium Signaling: NAADP Ascends as a New Messenger. *Curr Biol* (2003) 13(5):R186–8. doi: 10.1016/S0960-9822(03)00120-9
18. Lee HC. Nicotinic Acid Adenine Dinucleotide Phosphate (NAADP)-Mediated Calcium Signaling. *J Biol Chem* (2005) 280(40):33693–6. doi: 10.1074/jbc.R500012200
19. Cancela JM, Churchill GC, Galione A. Coordination of Agonist-Induced Ca2 +-Signaling Patterns by NAADP in Pancreatic Acinar Cells. *Nature* (1999) 398(6722):74–6. doi: 10.1038/18032
20. Mojzisova A, Krizanova O, Zacikova L, Kominkova V, Ondrias K. Effect of Nicotinic Acid Adenine Dinucleotide Phosphate on Ryanodine Calcium Release Channel in Heart. *Pflugers Arch* (2001) 441(5):674–7. doi: 10.1007/s004240000465
21. Hohenegger M, Suko J, Gscheidlinger R, Drobny H, Zidar A. Nicotinic Acid-Adenine Dinucleotide Phosphate Activates the Skeletal Muscle Ryanodine Receptor. *Biochem J* (2002) 367(Pt 2):423–31. doi: 10.1042/bj20020584
22. Copello JA, Qi Y, Jeyakumar LH, Ogunbunmi E, Fleischer S. Lack of Effect of Cadp-Ribose and NAADP on the Activity of Skeletal Muscle and Heart Ryanodine Receptors. *Cell Calcium* (2001) 30:269–84. doi: 10.1054/ceca.2001.0235
23. Zhang F, Zhang G, Zhang AY, Koeberl MJ, Wallander E, Li PL. Production of NAADP and its Role in Ca2+ Mobilization Associated With Lysosomes in Coronary Arterial Myocytes. *Am J Physiol Heart Circ Physiol* (2006) 291: H274–82. doi: 10.1152/ajpheart.01064.2005
24. Gerasimenko JV, Maruyama Y, Yano K, Dolman NJ, Tepikin AV, Petersen OH, et al. NAADP Mobilizes Ca2+ From a Thapsigargin-Sensitive Store in the Nuclear Envelope by Activating Ryanodine Receptors. *J Cell Biol* (2003) 163 (2):271–82. doi: 10.1083/jcb.200306134
25. Langhorst MF, Schwarzmann N, Guse AH. Ca2+ Release *via* Ryanodine Receptors and Ca2+ Entry: Major Mechanisms in NAADP-Mediated Ca2+ Signaling in T-Lymphocytes. *Cell Signal* (2004) 16(11):1283–9. doi: 10.1016/j.cellsig.2004.03.013
26. Dammermann W, Zhang B, Nebel M, Cordiglieri C, Odoardi F, Kirchberger T, et al. NAADP-Mediated Ca2+ Signaling *via* Type 1 Ryanodine Receptor in T Cells Revealed by a Synthetic NAADP Antagonist. *Proc Natl Acad Sci USA* (2009) 106(26):10678–83. doi: 10.1073/pnas.0809997106
27. Wolf IM, Diercks BP, Gattkowski E, Czarniak F, Kempski J, Werner R, et al. Frontrunners of T Cell Activation: Initial, Localized Ca2+ Signals Mediated by NAADP and the Type 1 Ryanodine Receptor. *Sci Signal* (2015) 8(398):ra102. doi: 10.1126/scisignal.aab0863
28. Diercks BP, Werner R, Weidemüller P, Czarniak F, Hernandez L, Lehmann C, et al. ORAI1, STIM1/2, and RYR1 Shape Subsecond Ca(2+) Microdomains Upon T Cell Activation. *Sci Signal* (2018) 11(561):1–14. doi: 10.1126/scisignal.aat0358
29. Gerasimenko JV, Charlesworth RM, Sherwood MW, Ferdek PE, Mikoshiba K, Parrington J, et al. Both Ryrs and Tpcs Are Required for NAADP-Induced Intracellular Ca^{2+} Release. *Cell Calcium* (2015) 58:237–45. doi: 10.1016/j.ceca.2015.05.005
30. Ogunbayo OA, Zhu Y, Rossi D, Sorrentino V, Ma J, Zhu MX, et al. Cyclic Adenosine Diphosphate Ribose Activates Ryanodine Receptors, Whereas NAADP Activates Two-Pore Domain Channels. *J Biol Chem* (2011) 286:9136–40. doi: 10.1074/jbc.M110.202002
31. Wagner LE, Groom LA, Dirksen RT, Yule DI. Characterization of Ryanodine Receptor Type 1 Single Channel Activity Using “On-Nucleus” Patch Clamp. *Cell Calcium* (2014) 56:96–107. doi: 10.1016/j.ceca.2014.05.004
32. Steen M, Kirchberger T, Guse AH. NAADP Mobilizes Calcium From the Endoplasmic Reticular Ca(2+) Store in T-Lymphocytes. *J Biol Chem* (2007) 282(26):18864–71. doi: 10.1074/jbc.M610925200
33. Brailoiu E, Churamani D, Cai X, Schrlau MG, Brailoiu GC, Gao X, et al. Essential Requirement for Two-Pore Channel 1 in NAADP-Mediated Calcium Signaling. *J Cell Biol* (2009) 186(2):201–9. doi: 10.1083/jcb.200904073
34. Calcraft PJ, Ruas M, Pan Z, Cheng X, Arredouani A, Hao X, et al. NAADP Mobilizes Calcium From Acidic Organelles Through Two-Pore Channels. *Nature* (2009) 459(7246):596–600. doi: 10.1038/nature08030
35. Zong X, Schieder M, Cuny H, Fenske S, Gruner C, Rötzer K, et al. The Two-Pore Channel TPCN2 Mediates NAADP-Dependent Ca(2+)-Release From Lysosomal Stores. *Pflugers Arch* (2009) 458(5):891–9. doi: 10.1007/s00424-009-0690-y
36. Brailoiu E, Rahman T, Churamani D, Prole DL, Brailoiu GC, Hooper R, et al. An NAADP-Gated Two-Pore Channel Targeted to the Plasma Membrane Uncouples Triggering From Amplifying Ca2+ Signals. *J Biol Chem* (2010) 285 (49):38511–6. doi: 10.1074/jbc.M110.162073
37. Pitt SJ, Funnell TM, Sitsapesan M, Venturi E, Rietdorf K, Ruas M, et al. TPC2 Is a Novel NAADP-Sensitive Ca2+ Release Channel, Operating as a Dual Sensor of Luminal Ph and Ca2+. *J Biol Chem* (2010) 285(45):35039–46. doi: 10.1074/jbc.M110.156927
38. Schieder M, Rötzer K, Brüggemann A, Biel M, Wahl-Schott CA. Characterization of Two-Pore Channel 2 (TPCN2)-Mediated Ca2+ Currents in Isolated Lysosomes. *J Biol Chem* (2010) 285(28):21219–22. doi: 10.1074/jbc.C110.143123
39. Yamaguchi S, Jha A, Li Q, Soyombo AA, Dickinson GD, Churamani D, et al. Transient Receptor Potential Mucolipin 1 (TRPML1) and Two-Pore Channels are Functionally Independent Organellar Ion Channels. *J Biol Chem* (2011) 286(26):22934–42. doi: 10.1074/jbc.M110.210930
40. Wang X, Zhang X, Dong XP, Samie M, Li X, Cheng X, et al. TPC Proteins are Phosphoinositide- Activated Sodium-Selective Ion Channels in Endosomes and Lysosomes. *Cell* (2012) 151:372–83. doi: 10.1016/j.cell.2012.08.036
41. She J, Guo J, Chen Q, Zeng W, Jiang Y, Bai XC. Structural Insights Into the Voltage and Phospholipid Activation of the Mammalian TPC1 Channel. *Nature* (2018) 556:130–4. doi: 10.1038/nature26139
42. Zhang X, Chen W, Li P, Calvo R, Southall N, Hu X, et al. Agonist-Specific Voltage-Dependent Gating of Lysosomal Two-Pore Na+ Channels. *Elife* (2019) 8:e51423. doi: 10.7554/eLife.51423
43. Ruas M, Rietdorf K, Arredouani A, Davis LC, Lloyd-Evans E, Koegel H, et al. Purified TPC Isoforms Form NAADP Receptors With Distinct Roles for Ca(2+) Signaling and Endolysosomal Trafficking. *Curr Biol* (2010) 20(8):703–9. doi: 10.1016/j.cub.2010.02.049
44. Lin-Moshier Y, Walseth TF, Churamani D, Davidson SM, Slama JT, Hooper R, et al. Photoaffinity Labeling of Nicotinic Acid Adenine Dinucleotide

Phosphate (NAADP) Targets in Mammalian Cells. *J Biol Chem* (2012) 287 (4):2296–307. doi: 10.1074/jbc.M111.305813

45. Walseth TF, Lin-Moshier Y, Jain P, Ruas M, Parrington J, Galione A, et al. Photoaffinity Labeling of High Affinity Nicotinic Acid Adenine Dinucleotide Phosphate (NAADP)-Binding Proteins in Sea Urchin Egg. *J Biol Chem* (2012) 287(4):2308–15. doi: 10.1074/jbc.M111.306563
46. Walseth TF, Lin-Moshier Y, Weber K, Marchant JS, Slama JT, Guse AH. Nicotinic Acid Adenine Dinucleotide 2'-Phosphate (NAADP) Binding Proteins in T-Lymphocytes. *Messenger (Los Angel)* (2012) 1(1):86–94. doi: 10.1166/msr.2012.1008
47. Jain P, Slama JT, Perez-Haddock LA, Walseth TF. Nicotinic Acid Adenine Dinucleotide Phosphate Analogues Containing Substituted Nicotinic Acid: Effect of Modification on Ca(2+) Release. *J Med Chem* (2010) 53(21):7599–612. doi: 10.1021/jm1007209
48. Ruas M, Davis LC, Chen CC, Morgan AJ, Chuang KT, Walseth TF, et al. Expression of Ca^{2+}-Permeable Two-Pore Channels Rescues NAADP Signalling in TPC-Deficient Cells. *EMBO J* (2015) 34(13):1743–58. doi: 10.15252/embj.201490009
49. Gunaratne GS, Su P, Marchant JS, Slama JT, Walseth TF. 5-Azido-8-Ethynyl-NAADP: A Bifunctional, Clickable Photoaffinity Probe for the Identification of NAADP Receptors. *Biochim Biophys Acta Mol Cell Res* (2019) 1866 (7):1180–8. doi: 10.1016/j.bbamcr.2018.11.017
50. Su P, Bretz JD, Gunaratne GS, Marchant JS, Walseth TF, Slama JT. Chemo-Enzymatic Synthesis of Adenine Substituted Nicotinic Acid Adenine Dinucleotide Phosphate (NAADP) Analogs. *Bioorg Med Chem* (2021) 30:115901. doi: 10.1016/j.bmc.2020.115901
51. Gunaratne GS, Brailoiu E, He S, Unterwald EM, Patel S, Slama JT, et al. Essential Requirement for JPT2 in NAADP-Evoked Ca(2+) Signaling. *Sci Signal* (2021) 14(675):1–13. doi: 10.1126/scisignal.abd5605
52. Roggenkamp HG, Khansahib I, Hernandez CL, Zhang Y, Lodygin D, Krüger A, et al. HN1L/JPT2: A Signaling Protein That Connects NAADP Generation to Ca(2+) Microdomain Formation. *Sci Signal* (2021) 14(675):1–13. doi: 10.1126/scisignal.abd5647
53. Cordiglieri C, Odoardi F, Zhang B, Nebel M, Kawakami N, Klinkert WE, et al. Nicotinic Acid Adenine Dinucleotide Phosphate-Mediated Calcium Signalling in Effector T Cells Regulates Autoimmunity of the Central Nervous System. *Brain* (2010) 133(Pt 7):1930–43. doi: 10.1093/brain/awq135
54. Zhang J, Guan X, Yan J. Lsm12 Is an NAADP Receptor and a Two-Pore Channel Regulatory Protein Required for Calcium Mobilization From Acidic Organelles. *Nat Commun* (2021) 12(1):4739–52. doi: 10.1038/s41467-021-24735-z

Conflict of Interest: The authors declare that the research was conducted in the absence of any commercial or financial relationships that could be construed as a potential conflict of interest.

Advantages of publishing in Frontiers

OPEN ACCESS
Articles are free to read for greatest visibility and readership

FAST PUBLICATION
Around 90 days from submission to decision

HIGH QUALITY PEER-REVIEW
Rigorous, collaborative, and constructive peer-review

TRANSPARENT PEER-REVIEW
Editors and reviewers acknowledged by name on published articles

Frontiers
Avenue du Tribunal-Fédéral 34
1005 Lausanne | Switzerland

Visit us: www.frontiersin.org
Contact us: frontiersin.org/about/contact

REPRODUCIBILITY OF RESEARCH
Support open data and methods to enhance research reproducibility

DIGITAL PUBLISHING
Articles designed for optimal readership across devices

FOLLOW US
@frontiersin

IMPACT METRICS
Advanced article metrics track visibility across digital media

EXTENSIVE PROMOTION
Marketing and promotion of impactful research

LOOP RESEARCH NETWORK
Our network increases your article's readership